




Cite this: *Phys. Chem. Chem. Phys.*,
2017, **19**, 20320

Commensurate–incommensurate adsorption and diffusion in ordered crystalline microporous materials†

Rajamani Krishna *^a and Jasper M. van Baten^b

For homologous series of linear chain molecules, there could be either a match, or mismatch, between the characteristic periodicity of the host structure and the characteristic length of the guest molecules. The major objective of this article is to highlight the influence of commensurateness, or incommensurateness, on both the adsorption and diffusion characteristics. Published experimental data, backed by molecular simulation results, are used to highlight the attendant non-monotonicity in adsorption strengths and diffusivities. We demonstrate the possibility of separating mixtures of *n*-alkanes, *n*-alcohols, and hydrocarbon isomers by appropriate and judicious choice of the dimensions, topology, and connectivity of the crystalline host material. Of particular practical interest are entropy-based separations that manifest at pore saturation conditions, relying on differences in the saturation capacities of the constituent species; the exploiting of such entropy effects is discussed with the aid of several examples.

Received 18th June 2017,
Accepted 25th July 2017

DOI: 10.1039/c7cp04101b

rsc.li/pccp

1. Introduction

The energy consumption for conventionally used separation technologies such as distillation, absorption, and extraction accounts for more than 50% of the total energy consumption for all separations. In some cases, adsorptive separations offer energy-efficient alternatives.^{1–5} With amorphous adsorbents such as activated carbon, the most commonly used separation strategies involve distinguishing molecules on the basis of (a) size and mobility, (b) van der Waals interactions and polarizability, (c) electrostatic interactions, and (d) π -electron transfers. The use of ordered crystalline microporous materials, such as zeolites (crystalline aluminosilicates), metal–organic frameworks (MOFs), and zeolitic imidazolate frameworks (ZIFs), with channel dimensions in the 3–20 Å range, opens up new separation strategies that are not realizable with amorphous adsorbents.^{1–14}

The pore landscape, topology, and connectivity of the microporous host structures show a wide diversity.^{14–18} These include: one-dimensional (1D) channels (*e.g.* AFI, LTL, MTW, TON, MIL-47,

MIL-53, Fe₂(BDP)₃, 1D zig-zag channels (*e.g.* CoFormate, MnFormate), 1D channels with side pockets (*e.g.* MOR, FER), intersecting channels (*e.g.* MFI, BEA, BOG, Zn(bdc)dabco, Co(bdc)dabco), cavities with large windows (*e.g.* FAU, NaX, NaY, IRMOF-1, CuBTC), and cages separated by narrow windows (*e.g.* LTA, CHA, DDR, TSC, ERI, ZIF-8); see typical landscapes in Fig. 1. We also note an inherent periodicity in the pore landscape, caused due to a variety of factors.^{19–21} For example, in one-dimensional (1D) channels of AFI, MTW, MOR, and MIL-53, there is a characteristic segment length of the 1D channels. For MFI, the periodicity is governed by the distances between channel intersections. For LTA, and ZIF-8, the periodicity is dictated by the window-to-window distance. There could be either a match, or mismatch, between the characteristic periodicity of the structure and the characteristic dimensions of the guest molecules.^{19–21}

To set the scene for this article, and define its objectives, let us consider the adsorption of *n*-alkanes, with *C* numbers ranging from 1 to 7, in cobalt formate (Co-FA) framework.²¹ The Co-FA structure consists of 1D zig-zag channels; one unit cell of Co-FA comprises a total of four distinct channel “segments”; each channel segment forms part of the repeat zig-zag structure. Fig. 2 presents computational snapshots of the conformations of adsorbed *n*-alkanes molecules within the zig-zag 1D channel segments of Co-FA. Configurational-Bias Monte Carlo (CBMC) simulations^{16,21–27} of the unary adsorption isotherms of C1, C2, C3, *n*C4, *n*C5, *n*C6, and *n*C7 alkanes are presented in Fig. 3a. The hierarchy of adsorption strengths for C1, C2 and C3 is as expected; increasing chain length results in higher adsorption

^a Van 't Hoff Institute for Molecular Sciences, University of Amsterdam, Science Park 904, 1098 XH Amsterdam, The Netherlands. E-mail: r.krishna@contact.uva.nl

^b AmsterCHEM, Calle Las Rozas 32, 04618 Las Rozas, Cuevas del Almanzora, Almeria, Spain. E-mail: jasper@amsterchem.com

† Electronic supplementary information (ESI) available: (a) Detailed structural information on all of the zeolites, MOFs, and ZIFs analyzed and discussed in the article, (b) detailed derivations of the lattice model for mixture adsorption equilibrium, (c) details of IAST calculations for mixture adsorption equilibria, (d) input data on isotherm fits used in the lattice, and IAST model calculations. See DOI: 10.1039/c7cp04101b

strength; the van der Waals interactions and polarizabilities increase with increasing chain length. The saturation capacities for C1, C2, and C3 are found to be 4 molecules per unit cell (uc), corresponding to one molecule per channel segment. However, with increasing chain lengths beyond C3 we note an unusual adsorption hierarchy: $C3 > nC4 > nC5$; the length of each channel segment is commensurate with that of the propane molecule and longer molecules such as *n*-pentane (*n*C5), and *n*-hexane (*n*C6) must straddle two channel segments. The length of the *n*C6 molecule is commensurate with the length of two channel segments, and further increase in chain length, results in the expected hierarchy, *i.e.* $nC7 > nC6 > nC5$. The saturation capacities of *n*C5, *n*C6, and *n*C7 are restricted to 2 molecules uc^{-1} .

Confirmation of the unusual hierarchy in the adsorption strengths observed in Fig. 3a is provided by the experimental data of Li *et al.*²⁸ for unary isotherms of 1-propanol and 1-butanol in Co-FA, see Fig. 3b. We note that the adsorption strength of 1-propanol is higher than that of 1-butanol over the entire range of experimental pressures. This trend is the same as witnessed for *n*C3 and *n*C4 alkanes in Fig. 3a.

Due to commensurate-incommensurate adsorption, the hierarchy of adsorption strengths displays non-monotonic

characteristics in the plot of Henry coefficient *vs.* *C* chain length; see Fig. 3c. Also shown on the right *y*-axis in Fig. 3c are the Maxwell–Stefan (M–S) diffusivities at zero-loadings, $D_i(0)$, determined from Molecular Dynamics (MD) simulations.^{16,17} The diffusivity hierarchy is the mirror image of that for the Henry coefficient; incommensurate adsorption results in a higher diffusivity value. A simple physical reasoning is that commensurate adsorption implies that the molecules resides “cozily” within the channel segment, and has a low tendency to hop to a neighboring location. The converse is true for guests that adsorb incommensurately; that molecule feels “out of place” and has a tendency to escape and hop to a neighboring site.

The non-monotonous adsorption characteristics, along with differences in saturation capacities can be exploited to achieve unusual separation possibilities. Consider a mixture of C3 and *n*C6. From the pure component adsorption isotherms in Fig. 3 we note that at low pressures the adsorption strengths of C3 is nearly the same as that of *n*C6. However the saturation capacity of C3 is twice that of *n*C6. We can devise a strategy for separating C3 from *n*C6 by exploiting the differences in the saturation capacities. CBMC simulations of the component loadings for C3/*n*C6 mixtures with equal partial fluid phase



Rajamani Krishna

Rajamani Krishna received his PhD degree in Chemical Engineering in 1975 from the University of Manchester in England, and soon thereafter joined the Royal Dutch Shell Laboratories, Amsterdam in The Netherlands. He spent nine years at Shell, working on a wide range of research and developmental activities in separations and reaction processes. Subsequently, he joined the Indian Institute of Petroleum, as Director. Since 1990, he is Professor at the Van 't Hoff Institute

*for Molecular Sciences, University of Amsterdam. During his entire career, the focus of Krishna's research has been on the investigation of physico-chemical phenomena at the molecular and microscopic levels, in order to gain fundamental insights that facilitate improvements and innovations in reaction and separation technologies in the process industries. He has published more than 500 peer-reviewed journal articles, and two text books, one of which has been translated into Chinese. He holds several patents. A complete list of his research contributions can be found on Google Scholar; see <http://scholar.google.nl/citations?user=cKqtQ0MAAAAJ&hl=en>. His publications have been cited more than 31 000 times, with an *h*-index of 91. He is the recipient of the prestigious 2013 ENI award for his research theme Improving Process Technologies with Molecular Insights. Krishna is included in the 2016 list of the most Highly Cited Researchers (category: Chemistry); see <http://hcr.stateofinnovation.com/2016>. This list “represents some of the world's most influential minds as determined by a citation analysis of Web of Science data”.*



Jasper M. van Baten

Jasper van Baten, who holds a PhD from the University of Amsterdam, is a free-lance software consultant specializing in computer simulations; see <http://www.amsterchem.com>. With a focus on software development, he has a particular passion for process simulation and actively contributes to the CAPE-OPEN standard specifications. He is the principal author of the COCO simulation suite. He has co-authored over 130 refereed

articles in multiphase reactor hydrodynamics and computational chemistry.

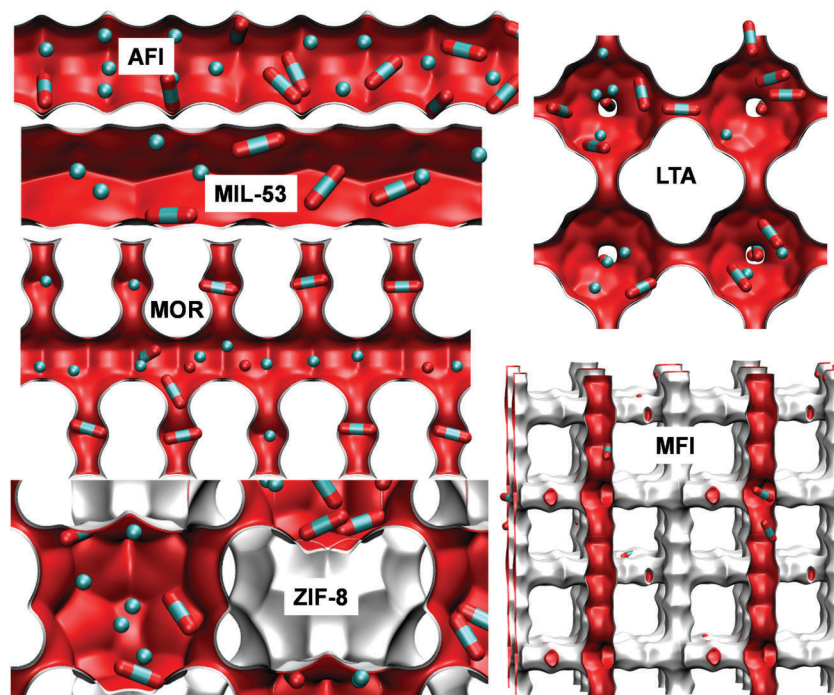


Fig. 1 Pore landscapes of AFI, MIL-53, MOR, LTA, MFI, and ZIF-8.

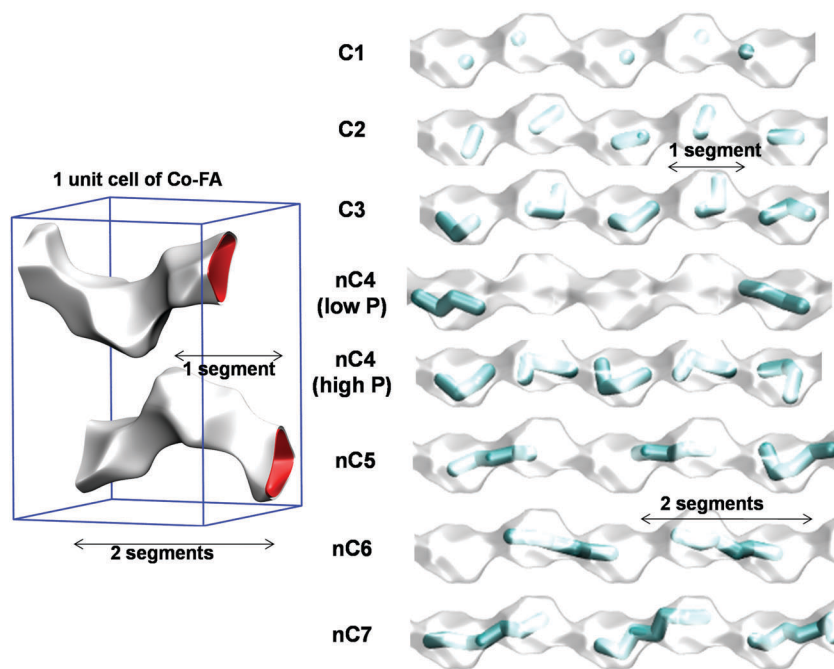


Fig. 2 Snapshots showing the location of *n*-alkanes molecules within the zig-zag 1D channel segments of Co-FA.

fugacities, $f_1 = f_2$, are shown in Fig. 4a. When operating at total fugacities $f_t = f_1 + f_2 > 1$ MPa, with a bulk liquid phase, we note that the adsorbed phase contains practically no *n*C6 and predominantly loaded with C3. The curious maximum in the *n*C6 loading at $f_t \approx 8$ kPa is particularly noteworthy. For adsorption of *n*C4/*n*C6 mixtures in Co-FA, the maximum in the *n*C6 is much more pronounced and occurs at $f_t \approx 100$ kPa

(see Fig. 4b); the selectivity reversal that manifests at $f_t > 100$ kPa is an unusual and important characteristic. The maximum in the *n*C6 loading, along with selectivity reversals, are not the exclusive province of Co-FA; these also manifest for C3/*n*C6 mixture adsorption in Mn-Formate (Mn-FA), that has a pore topology similar to that of Co-FA; see CBMC simulations data in Fig. 4c.

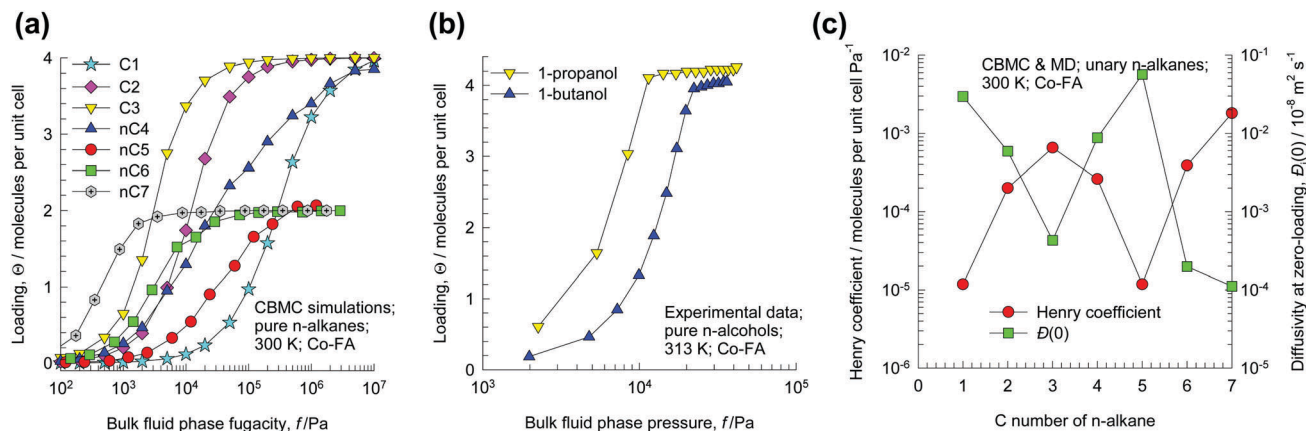


Fig. 3 (a) CBMC simulations of adsorption isotherms for C1, C2, C3, nC4, nC5, nC6 and nC7 in Co-FA at 300 K. (b) Experimental data of Li *et al.*²⁸ for unary adsorption isotherms for propanol and 1-butanol in Co-FA. (c) Henry coefficients and M - S diffusivity at zero-loading, $D_l(0)$, for n -alkanes in Co-FA as a function of C number.

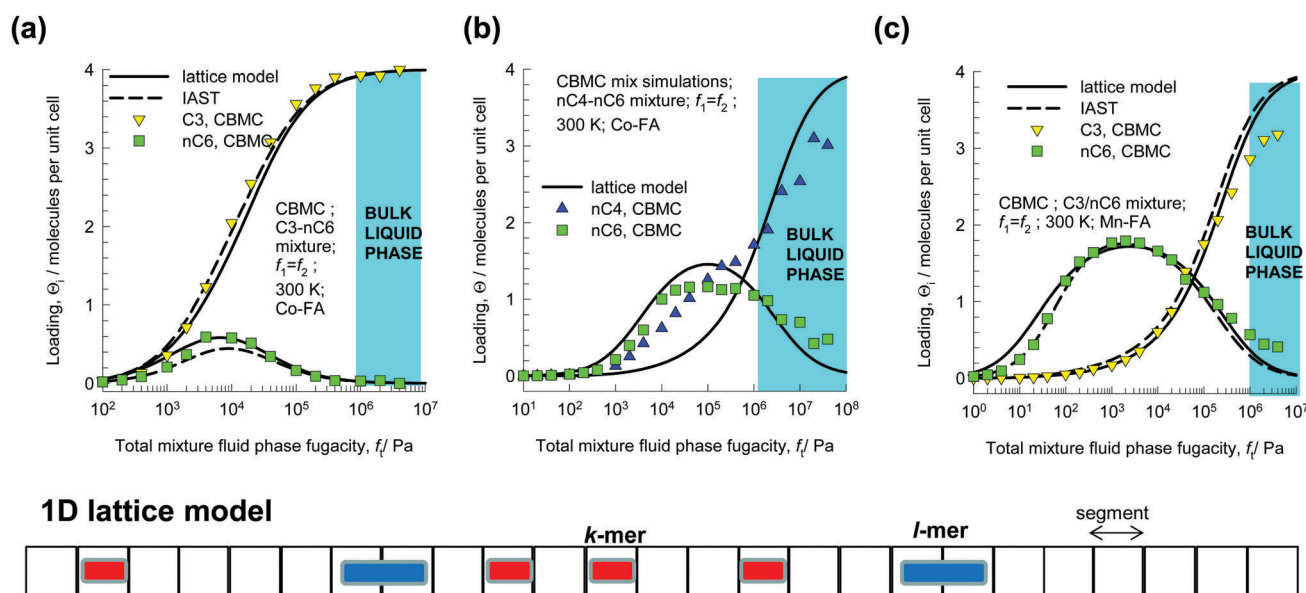


Fig. 4 (a–c) CBMC simulations (symbols) of component loadings for adsorption of (a) C3/nC6 mixtures in Co-FA, (b) nC4/nC6 mixtures in Co-FA, and (c) C3/nC6 mixtures in Mn-FA at 300 K. The continuous solid lines are the calculations using the 1D lattice model. The dashed lines are the estimations of the component loading using the Ideal Adsorbed Solution Theory (IAST). The calculation details are provided in the ESI.†

The primary objective of this article is to demonstrate that the variety of phenomena witnessed for commensurate/incommensurate adsorption of n -alkanes in Co-FA, and Mn-FA have wider consequences and applications for several other guest/host combinations. The secondary objective is to elucidate the fundamental physico-chemical principles underlying the selectivity reversals observed in Fig. 4 using the Boltzmann relationship for the entropy contribution to mixture adsorption $S = k_B \ln(W)$. The wide applications of entropy driven separations, that rely on differences in saturation capacities, rather than binding strengths, are underscored by means of several illustrative examples. Indeed, the foregoing comments and remarks pertaining to the data in Fig. 3 and 4 serve as templates for ensuing discussions and analyses.

The ESI,† provides (a) detailed structural information on all of the zeolites, MOFs, and ZIFs analyzed and discussed in the article, (b) detailed derivations of the lattice model for mixture adsorption equilibrium, (c) details of Ideal Adsorbed Solution Theory (IAST) calculations for mixture adsorption equilibria, (d) input data on isotherm fits used in the lattice, and IAST model calculations.

2. Lattice model for elucidation of entropy effects in mixture adsorption

To elucidate the unusual characteristics noted in Fig. 4, we use the model of Dávila *et al.*²⁹ for adsorption of a binary mixture of

rigid k -mers and rigid l -mers on an one-dimensional (1D) lattice. The adsorbent surface is modeled by a 1D lattice of M sites ($M \rightarrow \infty$). The k -mers (l -mers) are assumed to be composed by k (l) identical units in a linear array with constant bond length equal to the lattice dimension. The k -mers (l -mers) can only adsorb flat on the surface occupying k (l) contiguous lattice sites. Also, there are no adsorbate-adsorbate interactions. Since different particles do not interact with each other, all configurations of N_k k -mers and N_l l -mers on M sites are equally probable.

The mixture adsorption equilibrium for the 1D lattice is described by a set of two, coupled, equations:

$$\begin{aligned} (k-1) \ln \left(1 - \frac{(k-1)\theta_k}{k} - \frac{(l-1)\theta_l}{l} \right) \\ + \ln \frac{\theta_k}{k} - k \ln(1 - \theta_k - \theta_l) = \ln(b_k f_k) \\ (l-1) \ln \left(1 - \frac{(k-1)\theta_k}{k} - \frac{(l-1)\theta_l}{l} \right) \\ + \ln \frac{\theta_l}{l} - l \ln(1 - \theta_k - \theta_l) = \ln(b_l f_l) \end{aligned} \quad (1)$$

where b_k and b_l are the binding constants for the two adsorbates; f_k and f_l are the partial fugacities in the bulk fluid phase in equilibrium with the adsorbates. It is to be noted that since the eqn (1) are not explicit in terms of the occupancies, $\theta_k = \frac{kN_k}{M}$; $\theta_l = \frac{lN_l}{M}$, the set of two equations need to be solved numerically. All the calculations presented in this article were performed using the Given-Find solve block of MathCad 15.³⁰

The corresponding unary isotherms are described by the limiting cases of eqn (2):

$$\begin{aligned} (k-1) \ln \left(1 - \frac{(k-1)\theta_k}{k} \right) + \ln \frac{\theta_k}{k} - k \ln(1 - \theta_k) = \ln(b_k f) \\ (l-1) \ln \left(1 - \frac{(l-1)\theta_l}{l} \right) + \ln \frac{\theta_l}{l} - l \ln(1 - \theta_l) = \ln(b_l f) \end{aligned} \quad (2)$$

The binding constants b_k and b_l can be fitted to match the unary isotherm data. For the three systems shown in Fig. 4a-c are the values of the fitted constants are (a) $b_k = 3 \times 10^{-4}$, $b_l = 3 \times 10^{-4}$, (b) $b_k = 2 \times 10^{-5}$, $b_l = 2.5 \times 10^{-4}$, (c) $b_l = 8 \times 10^{-4}$, $b_k = 4 \times 10^{-2} \text{ Pa}^{-1}$. The linear hexane molecule (species l) adsorbs commensurately with two channel segments, and so we take $l = 2$; for the species k , C3 or n C4, adsorbs commensurately with one channel segment, we take $k = 1$; see Fig. 4.

With the fitted binding constants, eqn (1) can be used to calculate the component loadings; these are shown by the continuous solid lines in Fig. 4. The lattice model is able to quantitatively capture the n C6 maximum observed in the CBMC simulations, and as pore saturation is approached, n C6 is virtually excluded for all three systems shown in Fig. 4. The lattice model is also in good agreement with the Ideal Adsorbed Solution Theory (IAST) calculations (shown by the dashed lines in Fig. 4) for mixture adsorption equilibrium.

Particularly remarkable is C3/ n C6 adsorption in Co-FA because the binding constants are equal to each other, $b_k = b_l$, and exclusion of n C6 at high pore saturations cannot be rationalized on the basis of adsorption strengths; we now demonstrate that the selectivity is an entropy-driven phenomenon.

Dávila *et al.*²⁹ derive the following expression for the number of arrangements of N_k k -mers and N_l l -mers on M sites:

$$W = \frac{(M - (k-1)N_k - (l-1)N_l)!}{(M - kN_k - lN_l)!N_k!N_l!} \quad (3)$$

The entropy for binary mixture adsorption, $S = k_B \ln(W)$, can be calculated using the Stirling's approximation $\ln(M!) = M \ln M - M$. The expression for the dimensionless entropy per site is

$$\begin{aligned} \frac{S}{k_B M} = \left(1 - \frac{(k-1)\theta_k}{k} - \frac{(l-1)\theta_l}{l} \right) \ln \left(1 - \frac{(k-1)\theta_k}{k} - \frac{(l-1)\theta_l}{l} \right) \\ - (1 - \theta_k - \theta_l) \ln(1 - \theta_k - \theta_l) - \frac{\theta_k}{k} \ln \frac{\theta_k}{k} - \frac{\theta_l}{l} \ln \frac{\theta_l}{l} \end{aligned} \quad (4)$$

Fig. 5a presents calculations of the dimensionless entropy per site $\frac{S}{k_B M}$ for a binary mixture as a function of the proportion of

the k -mer in the adsorbed phase, $x_k = \frac{N_k}{N_k + N_l}$, for three different values of total occupancies, $\frac{N_k + N_l}{M} = 0.1, 0.3, \text{ and } 0.5$. At the lowest occupancy, $\frac{N_k + N_l}{M} = 0.1$, the maximum in the $\frac{S}{k_B M}$ occurs at the adsorbed phase mole fraction $x_k = \frac{N_k}{N_k + N_l} \approx 0.5$.

With increasing occupancies, $\frac{N_k + N_l}{M}$, the maximum in the $\frac{S}{k_B M}$ occurs at values the adsorbed composition $x_k = \frac{N_k}{N_k + N_l}$, that are

significantly richer in propane; this is because the vacancies are more efficiently filled up by molecules with the shorter chain length. Since the binding energies for C3/ n C6 adsorption in Co-FA are equal to each other, the maximum in the entropy also corresponds to the minimum in the Helmholtz free energy of adsorption $F = U - TS$ because the internal energy contribution to the free energy is not a function of composition for this specific case. In other words, the state of maximum entropy production is the preferred one that will be attained at adsorption equilibrium. The precise composition of the adsorbed phase, corresponding to the maximum entropy can be determined by setting $\frac{\partial}{\partial N_k} \left(\frac{S}{k_B M} \right) = 0$. The continuous solid black line in Fig. 5b

presents a plot of the values of $x_k = \frac{N_k}{N_k + N_l}$ corresponding to the maximum entropy, *i.e.* the preferred composition of the adsorbed mixtures as a function of the occupancy, $\frac{N_k + N_l}{M}$. As the total occupancy approaches unity, *i.e.* corresponding to pore saturation conditions, the adsorbed mixture consists predominantly of the shorter alkane, and the longer n C6 is practically excluded.

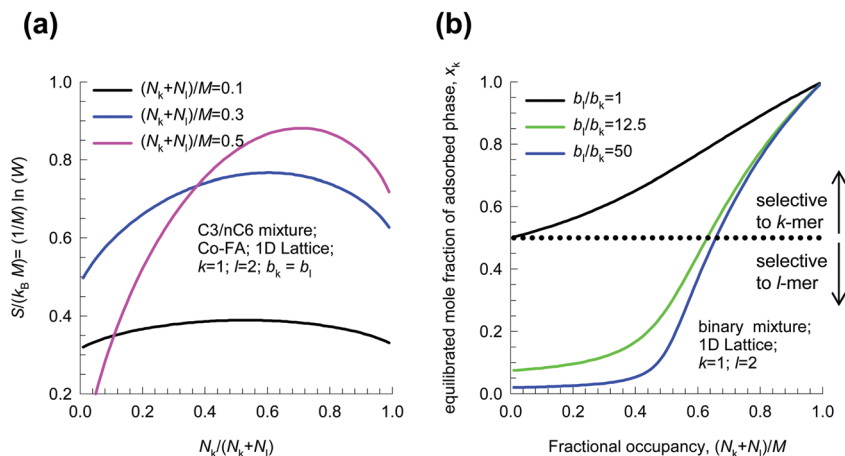


Fig. 5 Calculations of the dimensionless entropy per site, $\frac{S}{k_B M}$, for adsorption of binary C3/nC6 mixture in a 1D lattice representation of Co-FA as a function of the proportion of propane in the adsorbed phase, x_k , for three different values of total occupancies, $\frac{N_k + N_l}{M} = 0.1, 0.3, \text{ and } 0.5$. (b) Plots of the values of equilibrated compositions, x_k , in the adsorbed phase as a function of the occupancy, $\frac{N_k + N_l}{M}$, for C3/nC6/Co-FA, nC4/nC6/Co-FA, and C3/nC6/Mn-FA systems.

For nC4/nC6/Co-FA, and C3/nC6/Mn-FA systems, with $\frac{b_l}{b_k} = 12.5$, and 50, respectively, the corresponding calculations of the equilibrated adsorbed phase compositions are shown by green and blue lines; these values correspond to the minimization of the Helmholtz free energy, F . At low fractional occupancies the adsorbed phase consists predominantly of nC6 with the significantly larger binding constant. For these two systems, the entropic contribution to the Helmholtz free energy is able to override the internal energy contribution only at fractional occupancies $\frac{N_k + N_l}{M}$ higher than about 0.65.

It should be evident that entropic separations are intrinsically more potent than separations based on differences in binding strengths, because near-exclusion of the “entropically challenged” component (nC6 in these three examples) is feasible. Using the lattice model, the physico-chemical principles underlying selectivity reversal are unambiguously attributed to entropy effects favoring the smaller guest species.

For entropy effects to be fully exploited, and nC6 to be rejected, the operations must be under conditions such that pore saturation prevails; adsorption from mixtures in the liquid phase usually ensures prevalence of pore saturation conditions. For adsorption of mixtures of light gases, pore saturation is practically unrealizable, and entropic separations are not feasible.

Having established the origins of selectivity reversals in entropy driven separations of mixtures of commensurate/incommensurate species, we proceed with highlighting the exploitation of such separations for other guest/host combinations.

3. Entropic separations of linear alkanes using cage-type zeolites

Let us examine the adsorption of n -alkanes in CHA zeolite, which is a cage type zeolite that consists of cages of volume 316 \AA^3 ,

separated by $3.8 \text{ \AA} \times 4.2 \text{ \AA}$ 8-ring windows. Fig. 6 presents snapshots of the location, and conformation, of the n -alkanes within the cages of CHA at saturation conditions. We note that in all cases there appears to be no n -alkane molecules at the windows separating adjacent cages and, therefore, the cage capacity at saturation are integral numbers, decreasing from 6 molecules per cage for methane to 1 molecule per cage for n -octane (nC8). These saturation capacities are in conformity with the experimental data of Daems *et al.*³¹

For mixture adsorption near pore saturation conditions, entropy effects will strongly favor the component with the higher saturation capacity. As demonstration of this, Fig. 7a–c present CBMC simulations for the component loadings in equilibrium with equimolar C3/nC6, nC4/nC6, and nC5/nC6 fluid mixtures at 300 K. For operation at bulk fluid phase fugacities $f_t = f_1 + f_2 < 10^6 \text{ Pa}$ corresponding to bulk vapor phase, the adsorption is selective to the component with the longer chain length, *i.e.* nC6; this is because of the stronger van der Waals interactions that increase with chain length. However, for operation at fugacities $f_t > 10^6 \text{ Pa}$, corresponding to bulk liquid phase, the adsorption favors the component with the smaller chain length. If the fugacities are sufficiently high, say $f_t > 10^8 \text{ Pa}$ the nC6 is virtually excluded from the zeolite. For C3/nC6 mixture adsorption, good agreement with the CBMC simulation data is achieved using the two-dimensional (2D) lattice model of Azizian and Bashiri,³² shown by the continuous solid lines in Fig. 7a; the calculation details are provided in the ESI.† The dashed lines in Fig. 7 are the predictions of the Ideal Adsorbed Solution Theory (IAST) of Myers and Prausnitz.³³

The principle of separating mixtures on the basis of the differences in the saturation cage capacities applies also to the separation of linear alkanes in other cage type structures such as AFX (cages of 490 \AA^3 volume, separated by $3.4 \text{ \AA} \times 3.9 \text{ \AA}$ 8-ring windows; the cages are also connected to pockets of 98 \AA^3), ERI (cages of 408.7 \AA^3 volume, separated by $3.8 \text{ \AA} \times 4.9 \text{ \AA}$ 8-ring windows), and LTA (cages of 743 \AA^3 volume, separated by $4.11 \text{ \AA} \times 4.47 \text{ \AA}$ 8-ring windows). Fig. 8a compares the saturation

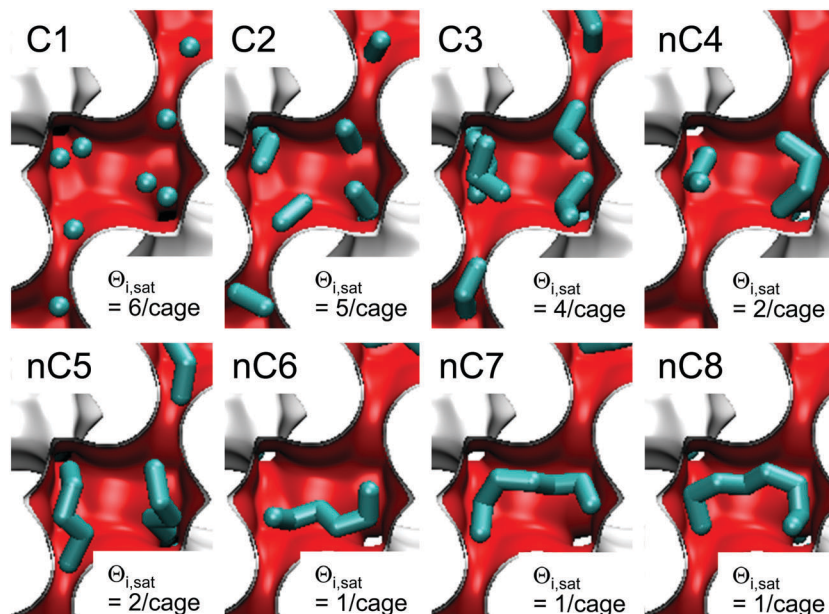


Fig. 6 Snapshots showing the conformations of *n*-alkanes in CHA at saturation conditions.

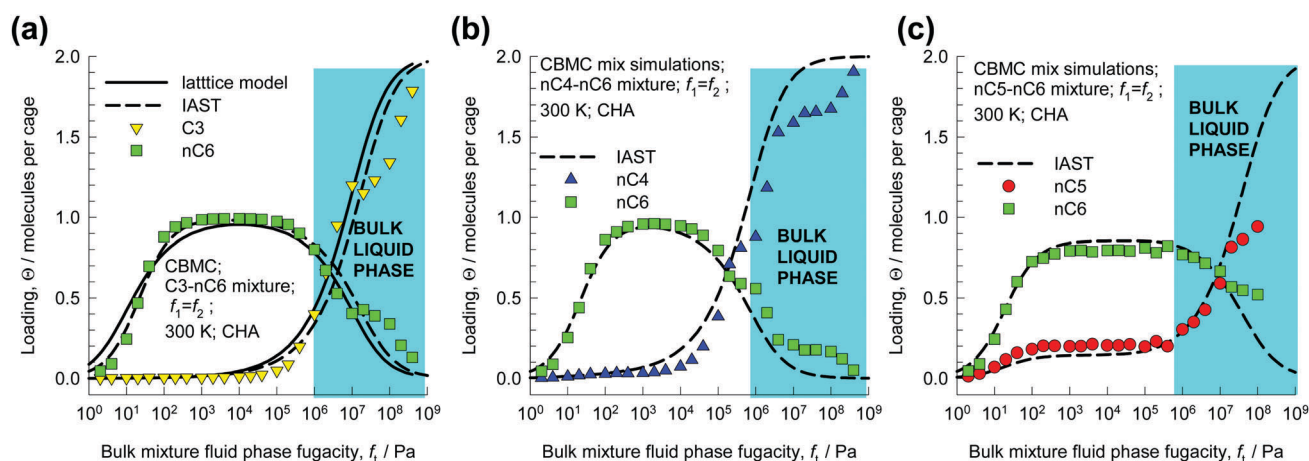


Fig. 7 CBMC mixture simulations⁵³ (symbols) for (a) C3/nC6, (b) nC4/nC6, and (c) nC5/nC6 in CHA at 300 K. The continuous solid lines in (a) are the calculations using the 2D lattice model. The dashed lines represent calculations of the IAST.⁵³ The region of liquid phase operation is indicated by the colored bar; the transition between vapor and liquid bulk phase is determined using the Peng–Robinson equation of state.

capacities for linear alkanes and linear alcohols in all-silica zeolites CHA, ERI, AFX, and LTA. For each host structure, we note that for the range of *C* numbers, the saturation loading, $\Theta_{i,\text{sat}}$, decreases in a step-wise manner with increasing chain length. The driver for entropic separations of mixtures of linear chain molecules is the difference in the saturation capacities. For binary mixture adsorption, the shorter linear alkane, or alcohol, adsorption will be favored only if there is a difference in saturation capacities; the larger the difference in the values of $\Theta_{i,\text{sat}}$, the more effective the separation.

For separation of chain molecules with *C* numbers higher than say 20, as is required in the petroleum industry in lube oil processing, we need structures with sufficiently large cages. Of particular importance in this context is all-silica TSC zeolite, with a Tschörtnerite framework, that has the largest cage volume of any known zeolite.³⁴ Each unit cell of TSC has four “LTA type cages” of

743 Å³, and four “TSC supercages” of 2553 Å³; the cages are separated by two types of windows: 4.02 Å × 4.17 Å, and 3.1 Å × 5.41 Å. As demonstration of the potential use of TSC, Fig. 8b compares the unary adsorption isotherms of nC21 and nC24 alkanes; the saturation capacities are $\Theta_{i,\text{sat}} = 16$, and 8 molecules uc⁻¹, respectively. CBMC simulations for nC21/nC24 mixture adsorption in TSC, shows that the shorter alkane is preferentially adsorbed under pore saturation conditions; see Fig. 8c.

4. Entropic separations of mixtures of linear alcohols using CHA zeolite

Consider adsorption of 1-alcohols in CHA, that consists of cages of volume 316 Å³, separated by 3.8 Å × 4.2 Å 8-ring windows.

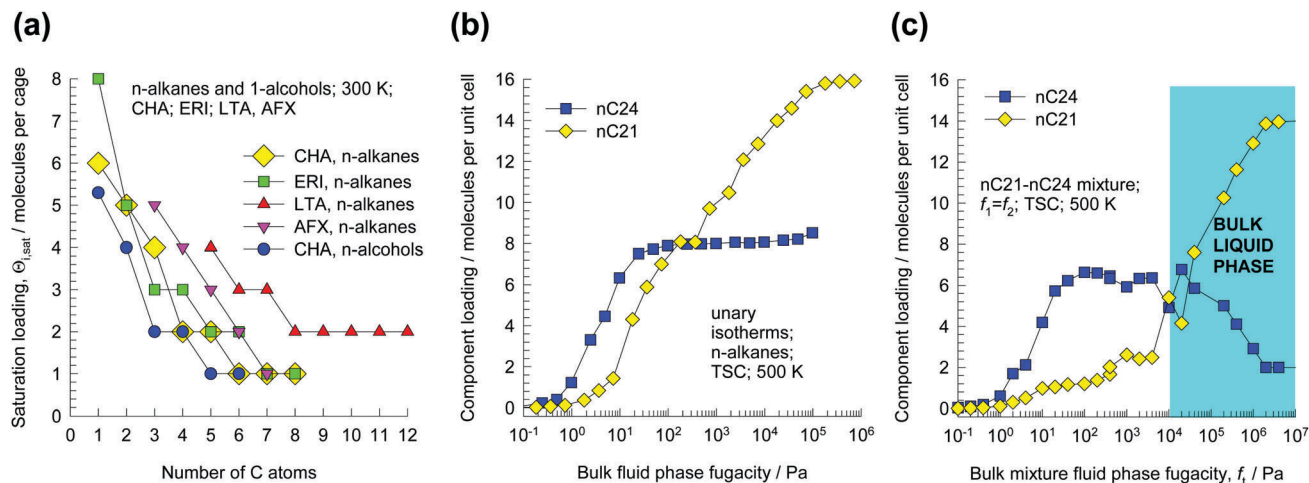


Fig. 8 (a) Saturation capacities for adsorption of *n*-alkanes and *n*-alcohols in CHA, ERI, AFX, and LTA, at 300 K. The data are based on CBMC simulations culled from the papers of Krishna and van Baten.^{53,54} (b) CBMC simulations⁵⁴ of the unary isotherms of *n*C21 and *n*C24 linear alkanes in TSC zeolite at 500 K. (c) CBMC simulations⁵⁴ of *n*C21/*n*C24 mixture adsorption in TSC at 500 K.

Fig. 9a presents snapshots of the conformations of ethanol, 1-propanol, 1-butanol, and 1-hexanol within the cages under saturation conditions. The saturation capacities are, respectively, 4, 2, 2, and 1 molecules cage⁻¹; *i.e.* the dimensions of 1-hexanol are commensurate with the size of a single cage. CBMC simulations of the unary isotherms of the 1-alcohols are shown in Fig. 9b. In the Henry regime of adsorption, the hierarchy of adsorption strengths increases with increasing chain length, as it to be expected on the basis of van der Waals interactions of 1-alcohols with the framework.

CBMC simulations of the component loadings for ethanol/1-propanol are shown in Fig. 9c. For bulk fluid phase fugacities $f_{\text{t}} = f_1 + f_2 < 5$ kPa, the component that is more strongly adsorbed is the longer chain alcohol, and the separation is governed by binding strengths and van der Waals interactions. However, for operations at bulk fugacities $f_{\text{t}} > 8$ kPa, selectivity reversal is observed and the component that is more strongly adsorbed is ethanol with the shorter chain length. Analogous selectivity reversal is experienced for adsorption of ethanol/1-hexanol mixtures; see Fig. 9d. The shaded regions in Fig. 9c and d indicate that the bulk fluid phase is in the liquid phase for the range of fugacities, f_{t} ; selectivity reversal is ensured when adsorption is from the liquid phase mixture.

A further point to note is that the data in Fig. 9c and d are analogous to that for binary mixtures of *n*-alkanes in CHA (*cf.* Fig. 7a–c); the phenomenon of selectivity reversal and exclusion of the longer molecule is valid for both linear alkanes and alcohols.

Experimental confirmation of the selectivity reversal phenomena observed in Fig. 9c and d are provided by Remy *et al.*³⁵ who report data transient breakthroughs of ethanol/1-propanol and ethanol/1-hexanol mixtures in a fixed bed adsorber packed with SAPO-34, that has the same structural topology as CHA zeolite; see Fig. 10a and b. The experiments show that the component that is eluted first from the adsorber is the alcohol with the longer chain length. In other words, the separations are not dictated by the

binding strengths in the Henry regime. Rather, the breakthroughs confirm the selectivity reversal phenomena and preferential adsorption of the shorter 1-alcohol.

5. Commensurate adsorption and diffusion in MFI zeolite

MFI zeolite (also called silicalite-1) has a topology consisting of a set of intersecting straight channels, and zig-zag (or sinusoidal) channels of approximately 5.5 Å size. The length of an *n*-hexane molecule is commensurate with the distance between intersections of MFI zeolite (*cf.* snapshot in Fig. 11a). The *n*-heptane molecule, on the other hand, has a length that is slightly longer than the distance between channel intersections (see Fig. 11b). Due to configurational considerations, the mono-branched 2-methylpentane (2MP) cannot be located within the channels, but is forced to reside at the channel intersections; *i.e.* it adsorbs commensurately with the channel intersections; see Fig. 11c.

The commensurate/incommensurate nature of adsorption strongly influences both adsorption and diffusion characteristics. Fig. 12a shows CBMC simulation data^{23,36–38} on unary adsorption isotherms for *n*C6, *n*C7, and 2MP in MFI zeolite at 300 K. Due to commensurate adsorption of *n*C6, the saturation capacity of *n*C6, Θ_{sat} , is precisely equal to 8 molecules uc⁻¹. Since there are 4 intersection sites per unit cell of MFI, the commensurate adsorption of 2MP at the intersections restricts its saturation capacity to 4 molecules uc⁻¹. For adsorption of *n*C7, the isotherm exhibits strong inflection characteristics at a loading corresponding to 4 molecules uc⁻¹; this implies that an additional “push” is required to position the incommensurate *n*C7 within the channels of MFI because it feels “out of place”. The saturation capacity of *n*C7 is restricted to $\Theta_{\text{sat}} = 7$ molecules uc⁻¹.

Fig. 12b shows the experimental data of Talu *et al.*³⁹ for the diffusivity of *n*-alkanes for *C* numbers ranging from 1 to 9. There is a sharp minimum in the diffusivity of the commensurate *n*C6.

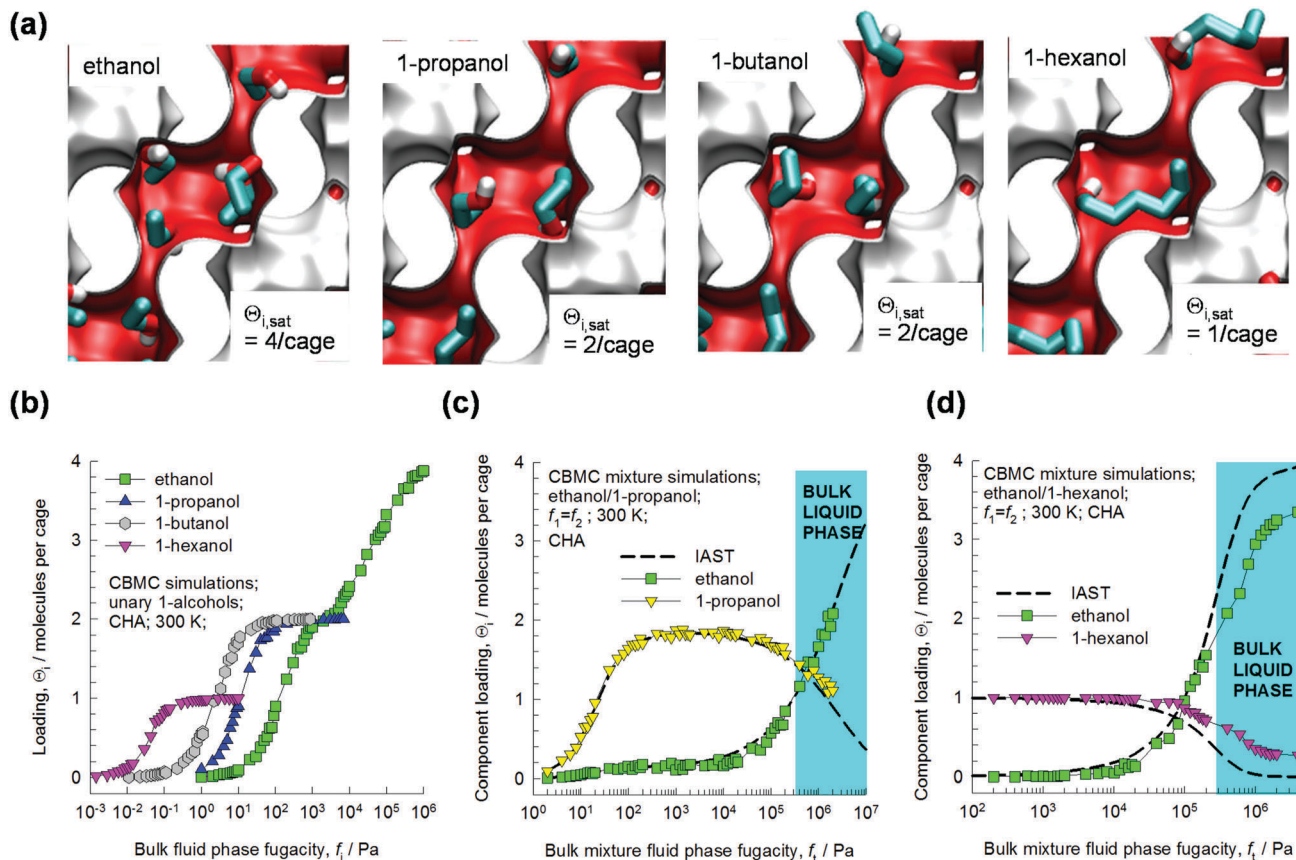


Fig. 9 (a) Snapshots showing the conformations of ethanol, 1-propanol, 1-butanol, and 1-hexanol in CHA at saturation conditions in CHA zeolite. (b) CBMC simulations⁵⁴ of unary adsorption isotherms for 1-alcohols in CHA at 300 K. (c and d) CBMC mixture simulations for (c) ethanol/1-propanol, and (d) ethanol/1-hexanol mixtures in CHA at 300 K. The partial fugacities in the bulk fluid phase are equal to each other, *i.e.* $f_1 = f_2$. The dashed lines are the IAST calculations of mixture adsorption equilibrium.

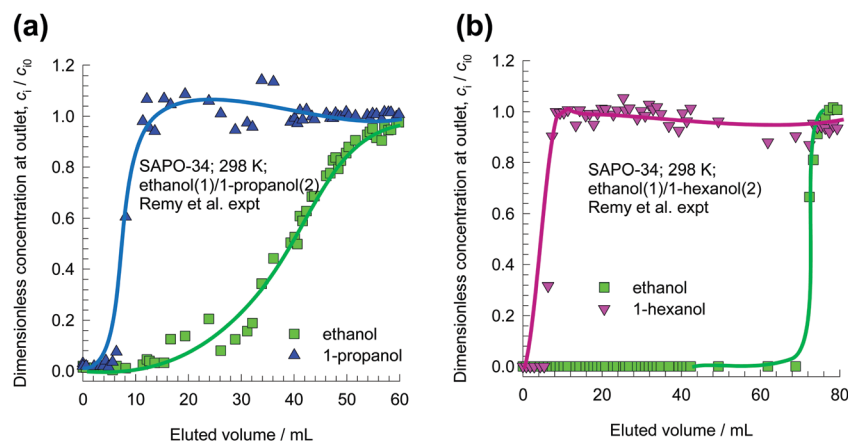


Fig. 10 (a and b) Transient breakthrough experimental data of Remy *et al.*³⁵ for separation of (a) ethanol/1-propanol, and (b) ethanol/1-hexanol mixtures in a fixed bed adsorber packed with SAPO-34.

Remarkably, *n*C7 has a higher diffusivity due to its incommensurate positioning within the channels.

Fig. 12c presents CBMC simulations⁴⁰ of loadings in the adsorbed phase in equilibrium with equimolar binary gas phase containing a mixture of *n*C6 and 2MP with equal partial fugacities $f_1 = f_2$ in the bulk fluid phase. Up to total hydrocarbons fugacities

$f_t = f_1 + f_2 = 2$ Pa, the component loadings Θ_i of each component increases in an expected manner; increasing f_t leads to a corresponding increase in the component loadings Θ_i of both *n*C6 and 2MP. At $f_t = 2$ Pa, the total loading $\Theta_t = 4 \text{ uc}^{-1}$, signifying that all the intersection sites are fully occupied. For bulk fugacities $f_t > 50$ Pa, the adsorbed phase contains

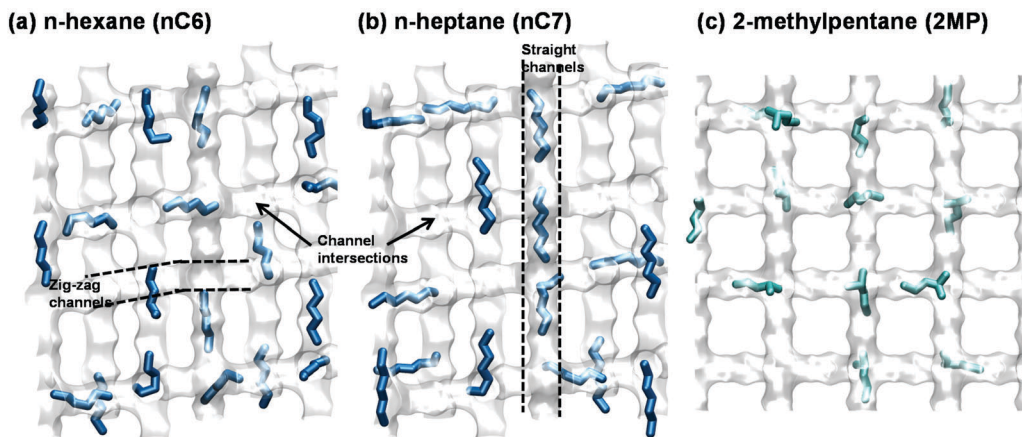


Fig. 11 (a–c) Snapshots showing the locations of (a) *n*C6, (b) *n*C7, and (c) 2MP within the intersecting channels of MFI zeolite.

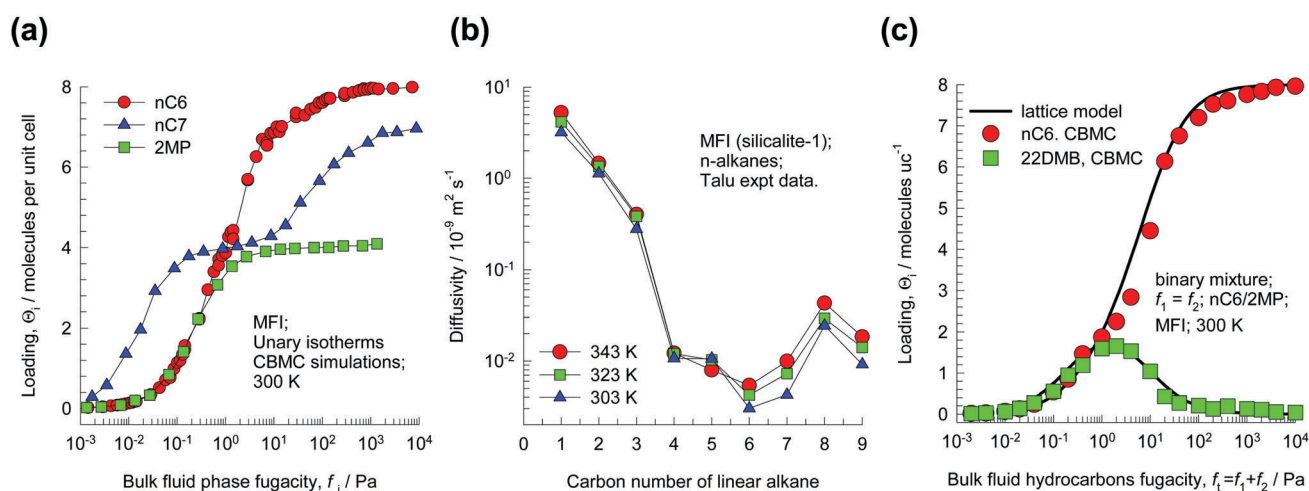


Fig. 12 (a) CBMC simulations^{23,36–38} of unary adsorption isotherms for *n*C6, *n*C7, and 2MP in MFI zeolite at 300 K. (b) Experimental data of Talu *et al.*³⁹ for the chain length dependence of diffusivities of *n*-alkanes in MFI zeolite; these data are not at constant loading; the loadings increase with increasing chain length because of stronger adsorption. (c) CBMC simulations of loadings in the adsorbed phase in equilibrium with binary *n*C6/2MP mixture with partial fugacities $f_1 = f_2$ in the bulk gas phase at 298 K. The continuous solid lines are the calculations using the 2D lattice model; the calculation details are provided in the ESI.†

predominantly *n*C6, and 2MP is virtually excluded from the channels of MFI; experimental evidence of this exclusion has been provided by Titze *et al.*⁴⁰ For *n*C6/2MP adsorption in MFI zeolite, the exclusion of the mono-branched isomer (*cf.* Fig. 12c) is ascribable to entropy effects; excellent agreement with the CBMC simulation data is achieved using the two-dimensional lattice model of Azizian and Bashiri,³² shown by the continuous solid lines.

6. The “window” effect and “resonant” diffusion

For cage-window type structures such as LTA, CHA, DDR, ERI zeolites, the window-to-window distances and cage volumes have important consequences for the adsorption and diffusion of guest species. The Quasi-Elastic Neutron Scattering (QENS) data of Jobic *et al.*⁴¹ for diffusivity in LTA-5A with increasing

n-alkane chain length displays a minimum value for *n*C8 (see Fig. 13a); the non-monotonicity in the variation of the diffusivity with chain length has been termed the “window” effect.⁴² Snapshots of the conformations of *n*C8 and *n*C13 molecules within the cages of LTA-5A provide a rationale for the non-monotonicity. The volume of each cage of LTA-5A is 743 Å³; *n*-octane can nestle comfortably within a single cage, whereas *n*C13 is too long, *i.e.* incommensurate with the cage size, and straddles two adjacent cages. An incommensurate scenario leads to a higher diffusivity because the molecule does not feel “too comfortable” and has a tendency to hop with increased frequency from cage to cage.

The experimental data of Yoo *et al.*⁴³ for diffusivity of *n*-alkanes in MTW zeolite (with 1D 12-ring channels of size 5.6 Å × 6.8 Å) show a periodicity in the diffusivity *vs.* chain length characteristics. The characteristics for the *C* number range 1–6 appear to be repeated for the range of 7–12; see Fig. 14. This periodicity been termed “resonant diffusion”.^{43–45}

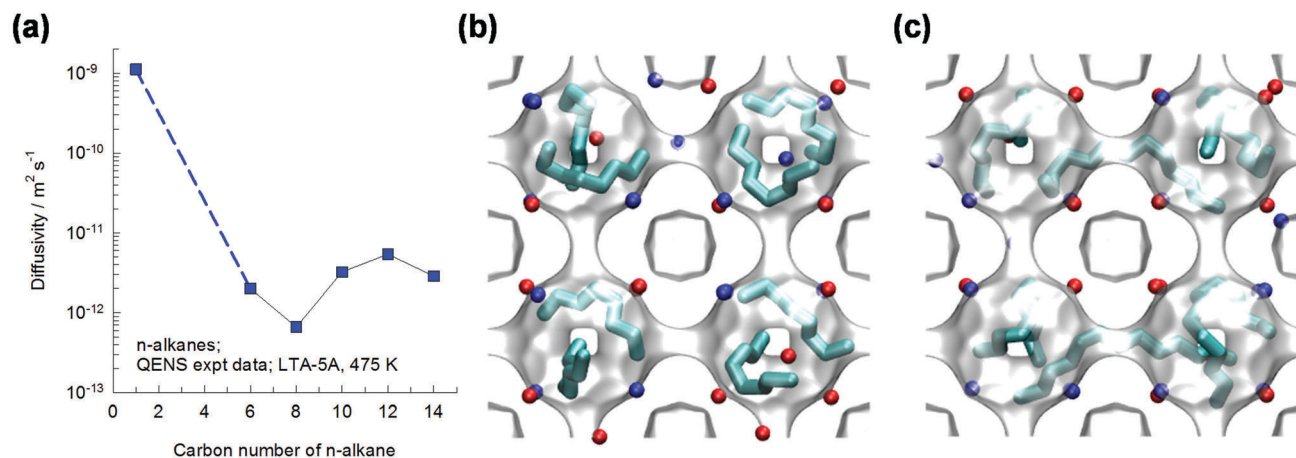


Fig. 13 (a) QENS data of Jobic *et al.*⁴¹ for diffusivity of *n*-alkanes in LTA-5A. (b and c) Snapshots showing the conformations of (b) *n*C8, and (c) *n*C13 alkanes within the cages of LTA-5A.

To rationalize their experimental observations, computational snapshots of the conformations of *n*-alkanes are also shown in Fig. 14. Normal hexane, with the pivotal *C* number, appears to align commensurately with one channel segment.

The experimental data of Yoo *et al.*⁴³ for diffusivity of *n*-alkanes in LTL zeolite (with 1D 12-ring 7.1 Å channels) also show an analogous periodicity (see Fig. 15). For LTL zeolite, the *n*-alkanes can configure themselves circumferentially within the “grooves” of the 1D channels. The “head-on” snapshots show that *n*-hexane can align commensurately with one-quarter of the circumference; this offers a qualitative rationalization of the experimental observations of resonant diffusion.

7. Commensurate/incommensurate stacking of mixtures of aromatics in 1D channels

The xylene isomers, *o*-xylene, *m*-xylene, *p*-xylene, are important chemical intermediates. The separation of mixtures of xylene

isomers, also containing ethylbenzene, is of great significance in the petrochemical industries. The height and width of the C8 aromatics are: *o*-xylene: 8 Å × 7.4 Å; *m*-xylene: 8.9 Å × 7.4 Å; *p*-xylene: 9.3 Å × 6.7 Å; ethylbenzene: 9.5 Å × 6.7 Å; see dimensions provided in Fig. 16a. Due to the differences in the molecular dimensions of the xylene isomers, the efficiencies with which the xylene isomers stack within the channels of different dimensions are different. We can deliberately choose an adsorbent material with a specified channel dimension in order to allow the commensurate stacking of one or other of the xylene isomers. Stacking xylenes within 1D channels of MOFs is analogous to stacking books within bookshelves.^{15,38}

The computational snapshots¹⁵ in Fig. 16b, show commensurate stacking of *o*-xylene within 8.5 Å channels of MIL-47. Experimental data^{46–48} for MIL-47 and MIL-53 with 1D rhombohedral channels of 8.5 Å confirm that these MOFs are selective to adsorption of *o*-xylene when operating at conditions close to pore saturation. Within the one-dimensional 10 Å channels of MAF-X8, we have commensurate stacking of *p*-xylene; see Fig. 16c.¹⁵ Commensurate stacking within 1D channels of MAF-X8, results in strong selectivity in the favor of the *p*-xylene as saturation conditions are approached.

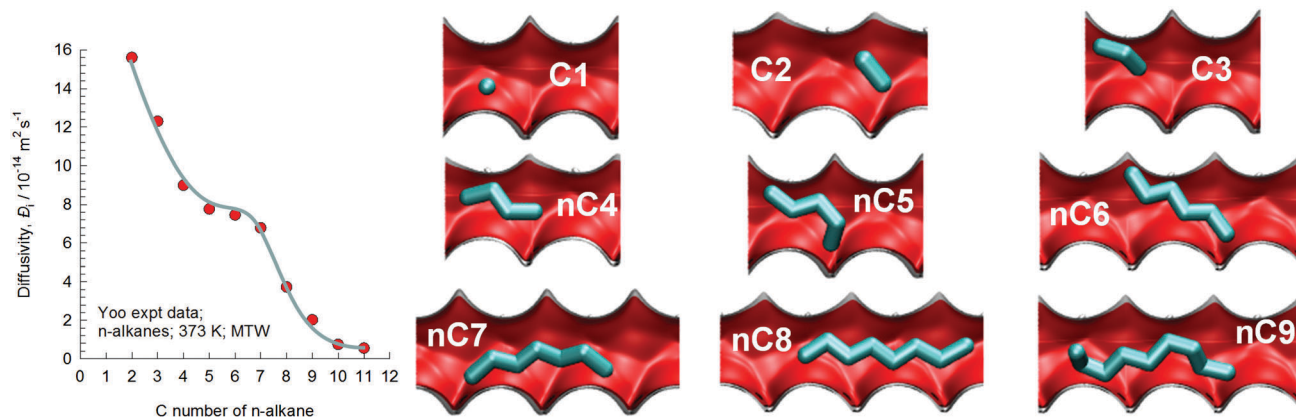


Fig. 14 Experimental data of Yoo *et al.*⁴³ for diffusivity of *n*-alkanes in MTW zeolite. Also shown are snapshots of the conformations of linear alkanes with *C* numbers ranging from 1–9 in MTW zeolite.

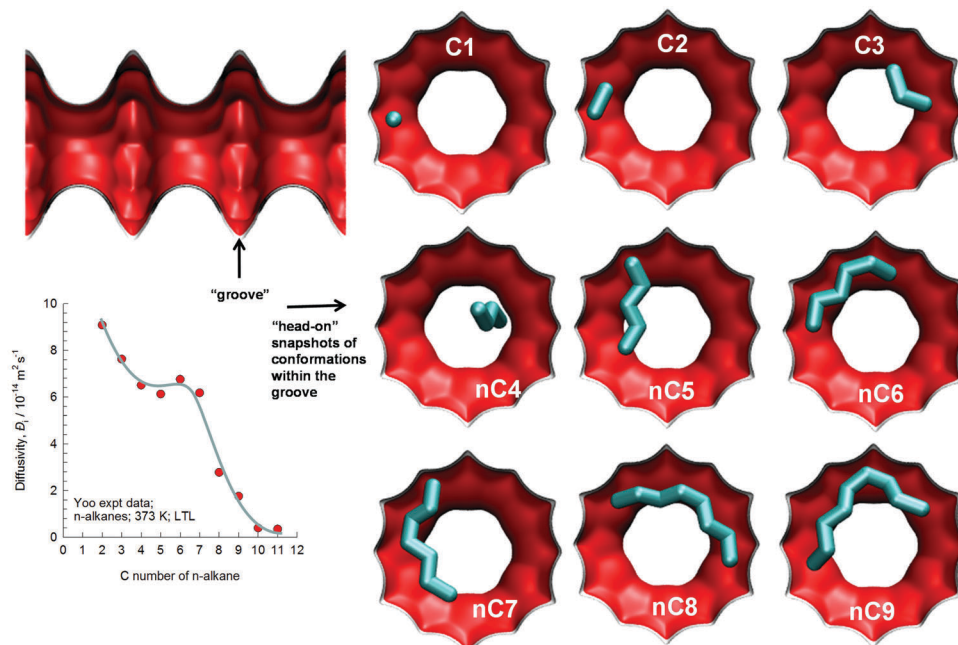


Fig. 15 Experimental data of Yoo *et al.*⁴³ for diffusivity of *n*-alkanes in LTL zeolite. Also shown are snapshots (head-on view) of the conformations of linear alkanes with C numbers ranging from 1–9 in LTL zeolite.

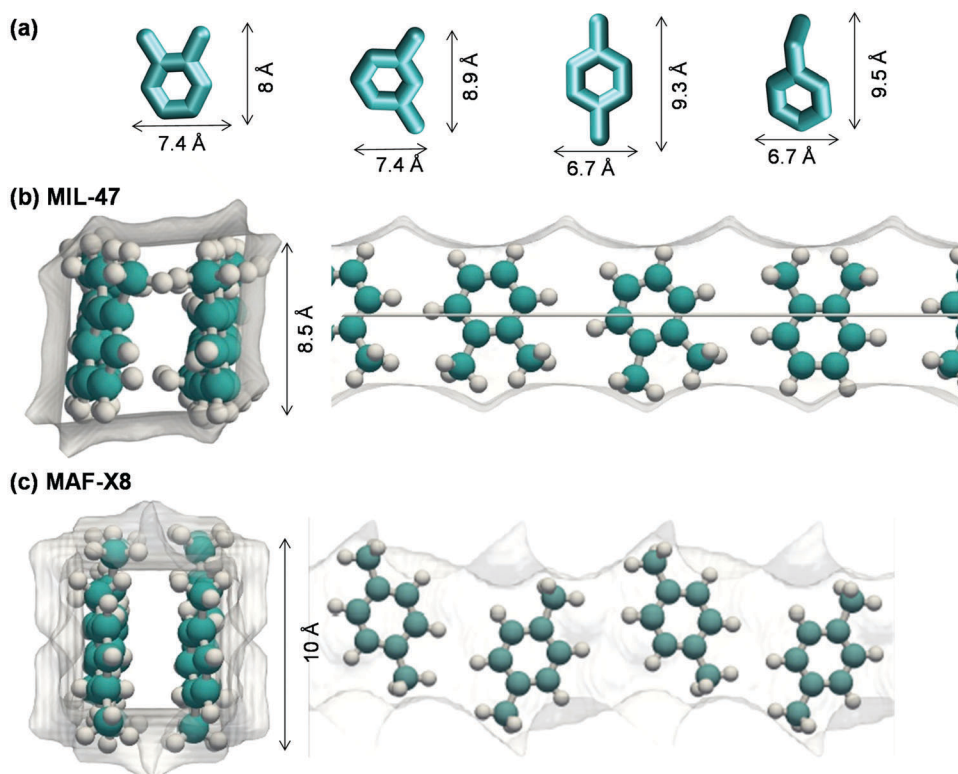


Fig. 16 (a) The molecular dimensions of C8 aromatics, culled from Torres-Knoop *et al.*¹⁵ (b and c) Computational snapshots¹⁵ showing the stacking of (b) *o*-xylene within 8.5 Å channels of MIL-47, and (c) *p*-xylene within 10 Å channels of MAF-X8.

In the study of Torres-Knoop *et al.*,¹⁵ MAF-X8 emerged as the best MOF for separation of 4-component *o*-xylene/*m*-xylene/*p*-xylene/ethylbenzene mixtures.

The stacking of xylene isomers within the 1D corrugated channels of $\text{AlPO}_4\text{-5}$ (with AFI zeolite topology) occurs in a different manner. For *m*-xylene, and *p*-xylene, either the “height”

or “width” is too large to allow vertical alignment; the orientation of these isomers occurs at an inclination; see snapshots in Fig. 17. By contrast, the molecular dimensions of *o*-xylene allow the molecules to be stacked vertically within the 8.4 Å “grooves”; this face-to-face stacking is akin to the packing of potato crisps in cylindrical tubes as marketed by Pringles. An important consequence of the differences in the orientation of isomers is that the “footprints” of *o*-xylene molecules is significantly shorter than the footprints of *m*-xylene, and *p*-xylene molecules. Shorter footprints result in higher saturation capacities, as evidenced in the isotherm data reported by Chiang *et al.*⁴⁹

Torres-Knoop *et al.*^{13,50} have also provided other examples in which optimum face-to-face stacking of aromatic molecules can lead to uncommonly effective separations. Within triangular channels of a structure such as Fe₂(BDP)₃, 1,3,5 tri-chlorobenzene (TCB) can be selectively separated from the 1,2,3 and 1,3,5 TCB isomers; the preferential adsorption of the 1,3,5 isomer is due to optimum face-to-face stacking; see computational snapshots in Fig. 18. Fig. 19a shows CBMC simulations for unary isotherms of 1,2,3 tri-chlorobenzene (TCB), 1,2,4 TCB, and 1,3,5 TCB in modified Fe₂(BDP)₃ at 433 K. Due to optimal face-to-face stacking, the 1,3,5 isomer has the highest saturation capacity. For adsorption of ternary mixtures of the three isomers under saturation conditions, the adsorbed phase is practically devoid of the 1,2,3 and 1,2,4 isomers due to entropy effects that favor 1,3,5 TCB with the smallest footprint; see Fig. 19b.

8. Entropic separations of alkane isomers exploiting differences in molecular footprints

The selective adsorption of components with the smallest “footprint” within 1D channels can be effectively exploited for separation of alkane isomers. Below, we discuss three different zeolites, MOR, AFI, and TON that can be utilized for this purpose.

MOR zeolite (Mordenite) consists of 12-ring (7.0 Å × 6.5 Å) 1D channels, connected to 8-ring (5.7 Å × 2.6 Å) pockets. Some representative snapshots⁵¹ showing the siting and conformation of hexane isomers along one of the 12-ring channels, 8 unit cells long, are presented in Fig. 20 for a total bulk fluid phase fugacity $f_t = 1000$ kPa. Within the same channel length we find five *n*C6 molecules, seven 2MP molecules and nine 22DMB molecules. The higher loading with increased degree of branching is due to increased degree of compactness of the molecules, *i.e.* smaller footprint. The more compact the molecule, the higher the packing efficiency within the one-dimensional channels. This point is emphasized further by determining the projected lengths of the molecules of the hexane isomers on the *z*-axis for $f_t = 1$ MPa; the data on the distribution of molecular lengths are shown in Fig. 21a. The projected lengths are obtained by monitoring the positions of each of the pseudo-atoms in the alkane molecules and determining the maximum span of the molecule by projecting the positions of the pseudo-atoms along

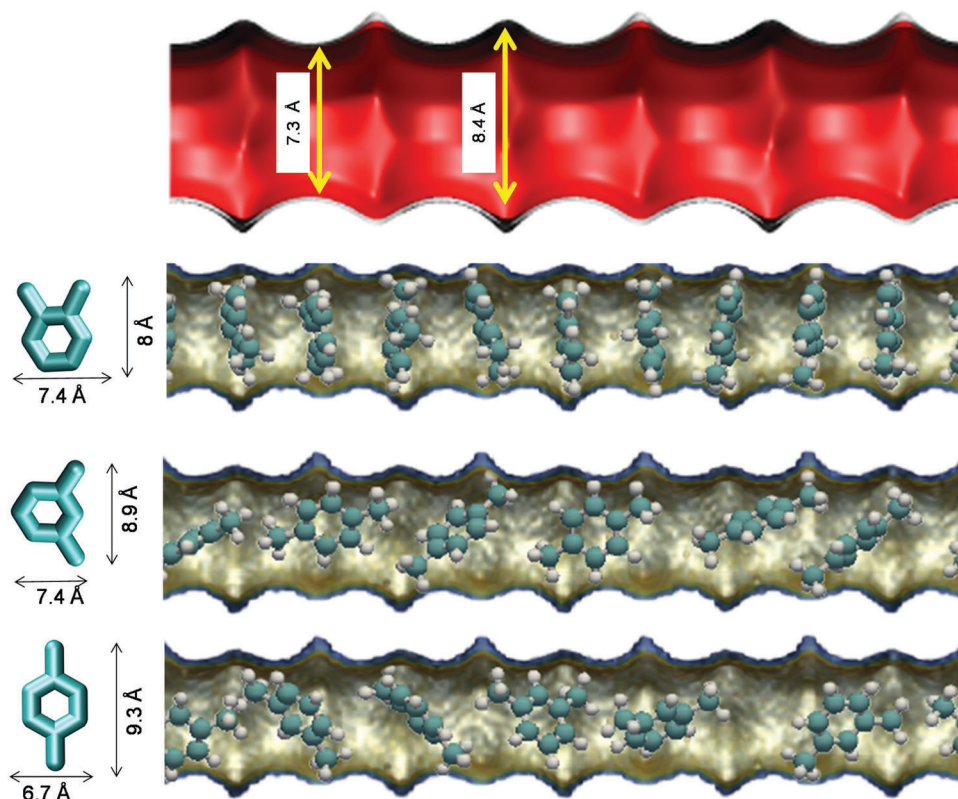


Fig. 17 Computational snapshots¹³ showing the orientations of *o*-xylene, *m*-xylene, and *p*-xylene as they stack within the corrugated 1D channel of AFI zeolite.

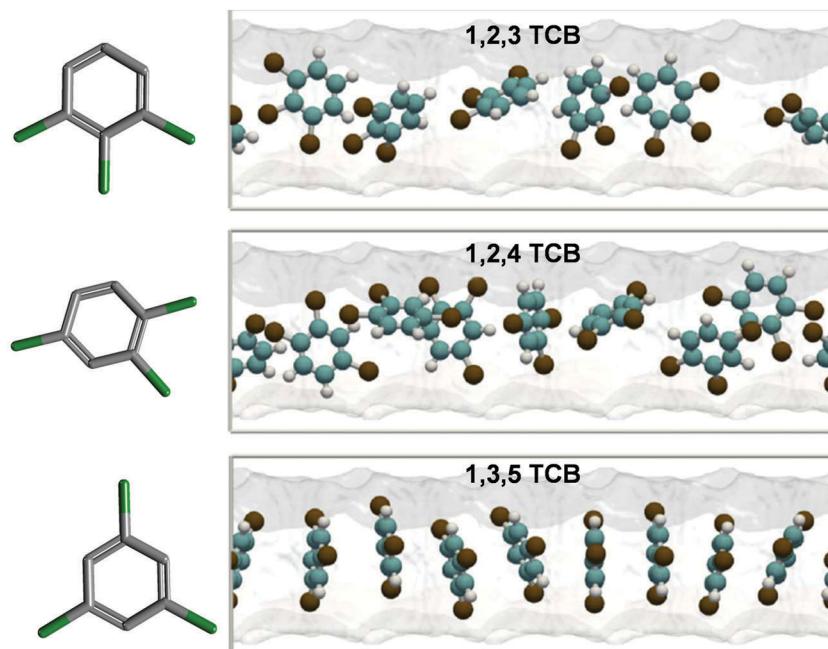


Fig. 18 Computational snapshots¹³ showing conformations and stacking of 1,2,3-trichlorobenzene (TCB), 1,2,4-TCB, and 1,3,5-TCB within the triangular channels of modified $\text{Fe}_2(\text{BDP})_3$. From Torres-Knoop *et al.*,¹³ reprinted with permission from John Wiley and Sons.

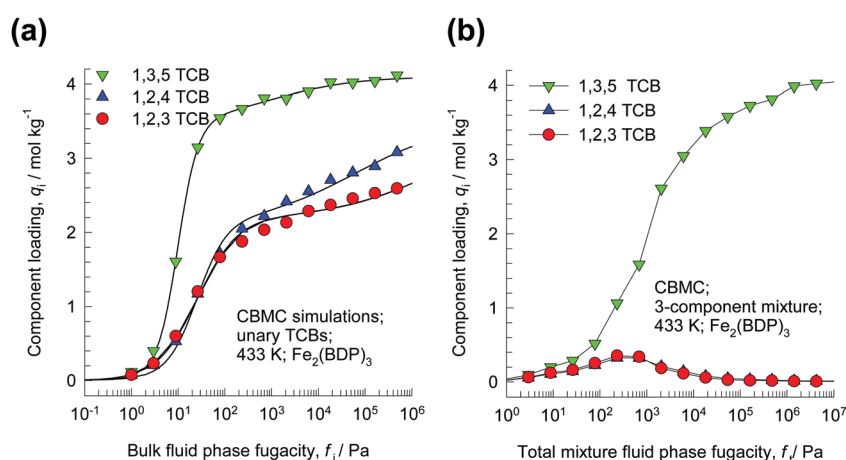


Fig. 19 (a) CBMC simulations for unary isotherms of 1,2,3-trichlorobenzene (TCB), 1,2,4-TCB, and 1,3,5-TCB in modified $\text{Fe}_2(\text{BDP})_3$ at 433 K. (b) CBMC simulations of component loadings for adsorption of equimolar ternary TCB mixtures in modified $\text{Fe}_2(\text{BDP})_3$ at 433 K.

the direction of the 12-ring channels. The mean lengths of the hexane isomers are 5.2 Å, 4.3 Å and 3 Å for *n*C6, 2MP and 22DMB respectively. These data also explain why the saturation capacity for 22DMB is significantly higher ($\theta_{\text{sat}} = 2$ molecules uc^{-1}), compared to that for 2MP ($\theta_{\text{sat}} = 1.7$ molecules uc^{-1}) and *n*C6 ($\theta_{\text{sat}} = 1.5$ molecules uc^{-1}); see Fig. 21b.

CBMC simulations for *n*C6/22DMB mixture adsorption shows that for total fugacities, $f_t = f_1 + f_2 > 100$ kPa, the selectivity is heavily in favor of the di-branched isomer and the linear isomer is virtually excluded from the 1D channels of MOR; see Fig. 21c. The lattice model, using eqn (1), is able to quantitatively capture the phenomenon of *n*C6 exclusion from MOR zeolite due to entropy effects.

Consider the adsorption of a mixture of hexane isomers *n*-hexane (*n*C6), 2-methylpentane (2MP), and 2,2-dimethylbutane (22DMB) within the 12-ring 7.3 Å 1D channels of AFI zeolite. The CBMC simulation results for unary isotherms are presented in Fig. 22a. Near pore saturation conditions, the hierarchy of adsorption strengths is $n\text{C6} < 2\text{MP} \ll 22\text{DMB}$; the hierarchy is primarily dictated by the molecular “footprints”. The linear *n*C6 has a longer “footprint” and occupies a longer segment of the channel. 22DMB is the most compact molecules and has the smallest footprint; consequently, a larger number of di-branched isomers can be located within a given length of the channels when compared to *n*C6. Mono-branched isomers 2MP and 3-methylpentane (3MP) have footprints that are intermediate in length.

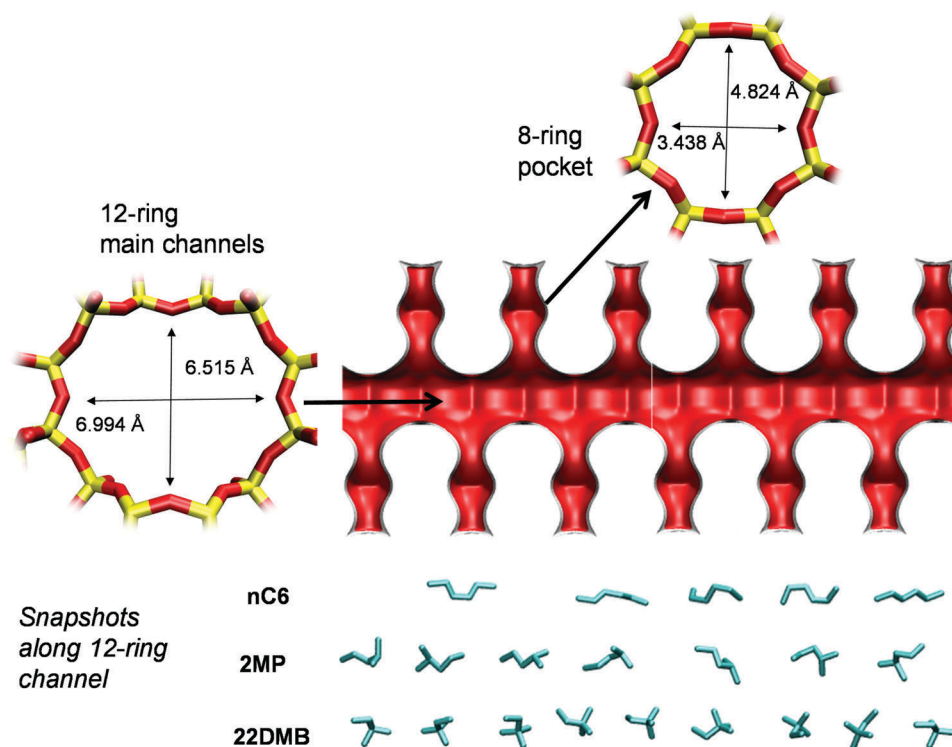


Fig. 20 Pore landscape of MOR zeolite.⁵¹ Snapshots of the conformation and siting of *n*C6, 2MP, and 22DMB along 1D 12-ring channel, 8 unit cells long.

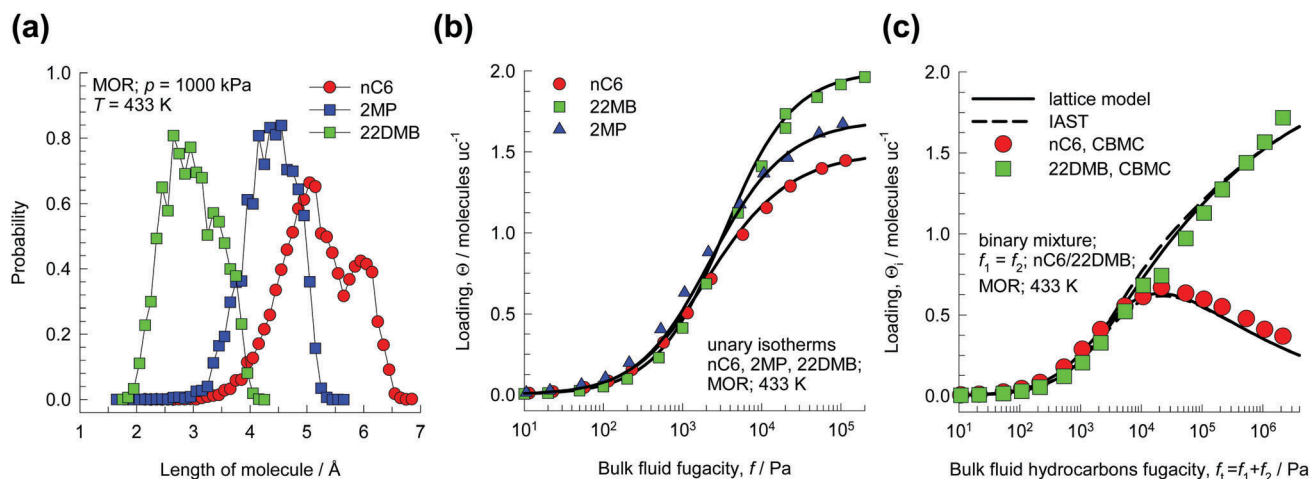


Fig. 21 (a) Distribution of lengths of hexane isomers ($f_1 = 1$ MPa, $T = 433$ K) along the z -direction of MOR obtained from CBMC simulations. (b) CBMC simulations⁵¹ of the unary isotherms for hexane isomers *n*C6, 2MP, 22DMB in MOR at 433 K. (c) Comparison of the CBMC simulations (shown by symbols) for *n*C6/22DMB mixture adsorption with the estimations of the 1D lattice model (shown by continuous solid lines), described by eqn (1). The dashed lines are the estimations of the component loadings using the Ideal Adsorbed Solution Theory (IAST).

For adsorption of ternary mixtures of linear, mono-branched, and di-branched isomers, the adsorption loading becomes increasingly in favor of the di-branched isomer as the channel becomes increasingly occupied; see Fig. 22b and c for adsorption of equimolar *n*C6/2MP/22DMB and *n*C6/3MP/23DMB mixtures.⁵ The selective adsorption of the di-branched isomer is due to the higher packing efficiency, *i.e.* this is an entropy effect. It is noteworthy that entropy effects can cause virtual exclusion of the linear isomer from AFI zeolite.

TON zeolite consists of 10-ring $5.6 \text{ \AA} \times 5.3 \text{ \AA}$ 1D channels. Fig. 23a shows CBMC simulations⁵² for unary isotherms for heptane isomers *n*-heptane (*n*C7), 3-methylhexane (3MH), and 2,3-dimethylpentane (23DMP) in TON. The saturation capacity of the di-branched isomer is significantly higher than that of the linear and mono-branched isomers. The rationalization for the higher saturation capacity is to be found in the molecular footprints within the channels, as elucidated by the snapshots. The more compact 23DMP has a shorter footprint, and as a

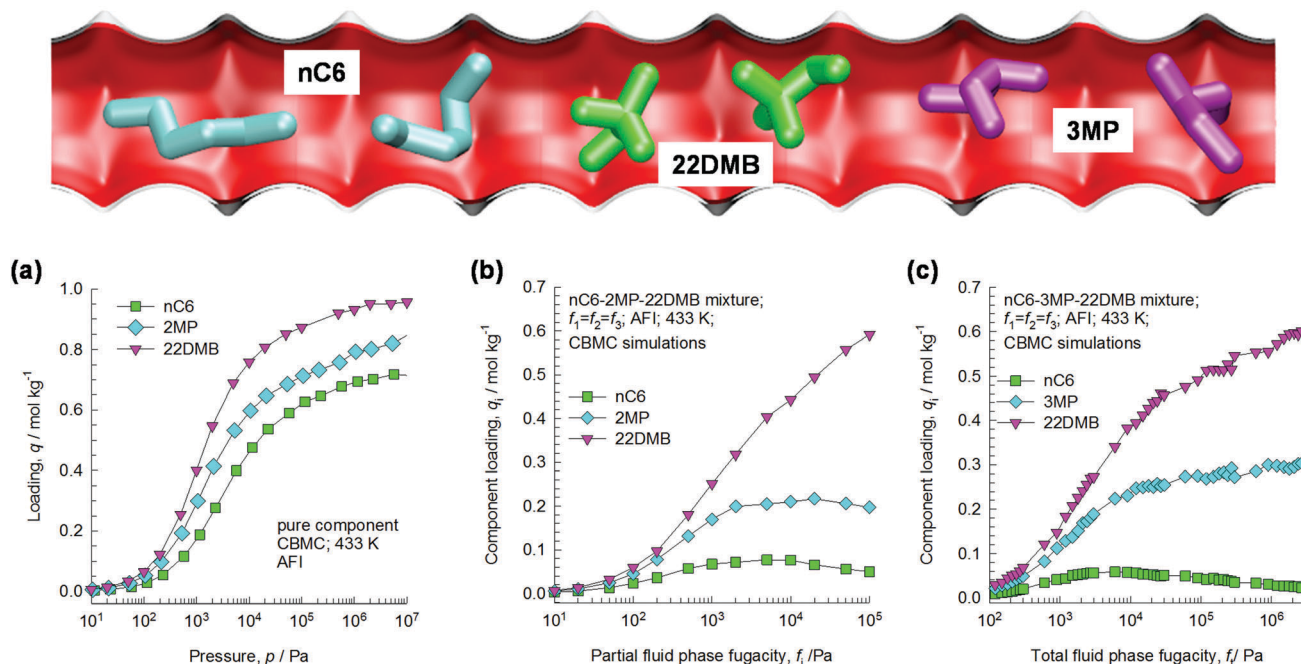


Fig. 22 Snapshots showing the molecular conformations of *n*C6, 3MP, and 22DMB within 1D channels of AFI zeolite.⁵ (a) CBMC simulations for unary isotherms of *n*C6, 2MP, and 22DMB in AFI zeolite at 433 K. (b and c) CBMC simulations for adsorption of equimolar (b) *n*C6/2MP/22DMB, and (c) *n*C6/3MP/22DMB mixtures in AFI zeolite at 433 K.⁵

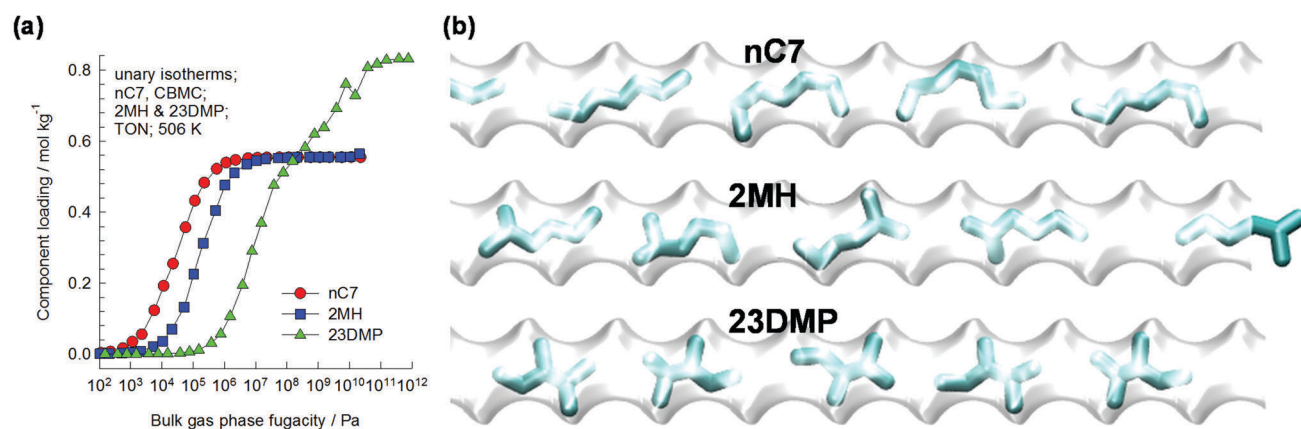


Fig. 23 (a) CBMC simulations⁵² for unary isotherms for heptane isomers *n*-pentane (*n*C7), 3-methylhexane (3MH), and 2,3-dimethylpentane (23DMP) in TON zeolite at 506 K. (b) Snapshots showing the molecular configurations of *n*C7, 3MH, and 23DMP within 1D channels of TON zeolite.

consequence more molecules can be packed into a channel of a given length. Mixture adsorption at saturation conditions will be in favor of the di-branched isomer; there are important consequences in TON-catalyzed hydrocracking processes.⁵²

9. Conclusions

The following major conclusions emerge from our analysis of commensurate/incommensurate adsorption in microporous crystalline materials.

(1) For homologous series of linear chain molecules, either alkanes or 1-alcohols, there could be either a match (commensurate), or mismatch (incommensurate), between the characteristic

periodicity of the host structure and the characteristic length of the guest molecules. Commensurate/incommensurate adsorption often results in non-monotonicity in the saturation capacities, adsorption strengths, and diffusivities as a function of the chain length. Such non-monotonicity can be gainfully exploited to achieve highly selective separations at conditions corresponding to pore saturation conditions.

(2) Commensurate/incommensurate adsorption phenomena can also be gainfully exploited to separate mixtures of hydrocarbon isomers. The adsorption selectivity favors the component that has smallest “footprint” in the channels.

(3) For separation of mixtures of aromatics, such as xylenes, choice of the appropriate channel dimension and cross-sectional

geometry allows optimal, commensurate, face-to-face stacking of one component, resulting in the highest saturation loadings.

(4) Separations at conditions close to pore saturation are significantly influenced by differences in saturation capacities, that are a direct reflection of the efficiencies by which molecules pack, or stack, themselves within the microporous channels. The adsorption selectivity is strongly in favor of the component that packs more efficiently, often commensurately, within the pore landscape. The component that adsorbs less efficiently, often incommensurately, is almost totally excluded from the pores at saturation conditions. This exclusion can be simply, and elegantly, elucidated using simple 1D and 2D lattice model descriptions of mixture adsorption, along with the Boltzmann relation, $S = k_B \ln(W)$. The underlying physical reasoning is that there are many more molecular configurations and arrangements, W , realizable if the adsorbed phase is predominantly richer in the component that adsorbs commensurately. Entropic separations are also quantitatively predicted by the IAST calculations.

(5) Using molecular simulations, backed in some cases by experiments, it is demonstrated that entropy effects can be exploited in one-dimensional channels, cage-type structures, and in structures with intersecting channels.

Notation

b	Binding constant, Pa^{-1}
c_i	Molar concentration of species i in gas mixture, mol m^{-3}
c_{i0}	Molar concentration of species i in gas mixture at inlet to adsorber, mol m^{-3}
D_i	Maxwell–Stefan diffusivity, $\text{m}^2 \text{s}^{-1}$
f_i	Partial fugacity of species i , Pa
f_t	Total fugacity of bulk fluid mixture, Pa
F	Helmholtz free energy, J mol^{-1}
k_B	Boltzmann constant, $1.38 \times 10^{-23} \text{ J molecule}^{-1} \text{ K}^{-1}$
n	Number of species in the mixture, dimensionless
M	Number of sites on lattice, dimensionless
N_k	Number of k -mers, dimensionless
N_l	Number of l -mers, dimensionless
S	Entropy, $\text{J mol}^{-1} \text{ K}^{-1}$
T	Absolute temperature, K
U	Internal energy, J mol^{-1}
x_i	Component mole fraction in adsorbed phase, i , mol kg^{-1}

Greek letters

θ_i	Fractional occupancy for mixture adsorption, dimensionless
Θ_i	Loading of species i , molecules per unit cage, or per unit cell
$\Theta_{i,\text{sat}}$	Saturation loading of species i , molecules per unit cage, or per unit cell
Θ_t	Total mixture loading, molecules per unit cage, or per unit cell

Subscripts

i	Referring to component i
t	Referring to total mixture

References

- Z. Bao, G. Chang, H. Xing, R. Krishna, Q. Ren and B. Chen, *Energy Environ. Sci.*, 2016, **9**, 3612–3641.
- Y. He, R. Krishna and B. Chen, *Energy Environ. Sci.*, 2012, **5**, 9107–9120.
- K. Sumida, D. L. Rogow, J. A. Mason, T. M. McDonald, E. D. Bloch, Z. R. Herm, T.-H. Bae and J. R. Long, *Chem. Rev.*, 2012, **112**, 724–781.
- J.-R. Li, J. Sculley and H.-C. Zhou, *Chem. Rev.*, 2012, **112**, 869–932.
- R. Krishna and J. M. van Baten, *Phys. Chem. Chem. Phys.*, 2011, **13**, 10593–10616.
- H. Wu, Q. Gong, D. H. Olson and J. Li, *Chem. Rev.*, 2012, **112**, 836–868.
- Y. J. Colón and R. Q. Snurr, *Chem. Soc. Rev.*, 2014, **43**, 5735–5749.
- C. E. Wilmer, M. Leaf, C. Y. Lee, O. K. Farka, B. G. Hauser, J. T. Hupp and R. Q. Snurr, *Nat. Chem.*, 2012, **4**, 83–89.
- N. S. Bobbitt, J. Chen and R. Q. Snurr, *J. Phys. Chem. C*, 2016, **120**, 27328–27341.
- R. Krishna, *Phys. Chem. Chem. Phys.*, 2015, **17**, 39–59.
- R. Krishna, *RSC Adv.*, 2015, **5**, 52269–52295.
- R. Krishna, *RSC Adv.*, 2017, **7**, 35724–35737.
- A. Torres-Knoop, S. R. G. Balestra, R. Krishna, S. Calero and D. Dubbeldam, *ChemPhysChem*, 2015, **16**, 532–535.
- D. Dubbeldam, R. Krishna, S. Calero and A. Ö. Yazaydın, *Angew. Chem., Int. Ed.*, 2012, **51**, 11867–11871.
- A. Torres-Knoop, R. Krishna and D. Dubbeldam, *Angew. Chem., Int. Ed.*, 2014, **53**, 7774–7778.
- R. Krishna, *J. Phys. Chem. C*, 2009, **113**, 19756–19781.
- R. Krishna, *Chem. Soc. Rev.*, 2012, **41**, 3099–3118.
- C. Baerlocher, W. M. Meier and D. H. Olson, *Atlas of Zeolite Framework Types*, Elsevier, Amsterdam, 5th edn, 2002.
- D. Dubbeldam, S. Calero, T. L. M. Maesen and B. Smit, *Angew. Chem., Int. Ed.*, 2003, **42**, 3624–3626.
- D. Dubbeldam, S. Calero, T. L. M. Maesen and B. Smit, *Phys. Rev. Lett.*, 2003, **90**(24), 245901.
- R. Krishna and J. M. van Baten, *Mol. Simul.*, 2009, **35**, 1098–1104.
- R. Krishna and J. M. van Baten, *J. Phys. Chem. B*, 2005, **109**, 6386–6396.
- R. Krishna and J. M. van Baten, *Microporous Mesoporous Mater.*, 2008, **109**, 91–108.
- D. Dubbeldam, S. Calero, T. J. H. Vlucht, R. Krishna, T. L. M. Maesen and B. Smit, *J. Phys. Chem. B*, 2004, **108**, 12301–12313.
- T. J. H. Vlucht, R. Krishna and B. Smit, *J. Phys. Chem. B*, 1999, **103**, 1102–1118.
- D. Frenkel and B. Smit, *Understanding Molecular Simulations: From Algorithms to Applications*, 2nd edn, Academic Press, San Diego, 2002.
- B. Smit and R. Krishna, *Chem. Eng. Sci.*, 2003, **58**, 557–568.
- K. Li, D. H. Olson, J. Y. Lee, W. Bi, K. Wu, T. Yuen, Q. Xu and J. Li, *Adv. Funct. Mater.*, 2008, **18**, 2205–2214.
- M. Dávila, J. L. Riccardo and A. J. Ramirez-Pastor, *Chem. Phys. Lett.*, 2009, **477**, 402–405.
- PTC, MathCad, 15.0, PTC Corporate Headquarters, Needham, <http://www.ptc.com/>, 3 November 2015.

- 31 I. Daems, R. Singh, G. V. Baron and J. F. M. Denayer, *Chem. Commun.*, 2007, 1316–1318.
- 32 S. Azizian and H. Bashiri, *Langmuir*, 2009, **25**, 2309–2312.
- 33 A. L. Myers and J. M. Prausnitz, *AIChE J.*, 1965, **11**, 121–130.
- 34 M. D. Foster, I. Rivin, M. M. J. Treacy and O. D. Friedrichs, *Microporous Mesoporous Mater.*, 2006, **90**, 32–38.
- 35 T. Remy, J. C. Saint-Remi, R. Singh, P. A. Webley, G. V. Baron and J. F. M. Denayer, *J. Phys. Chem. C*, 2011, **115**, 8117–8125.
- 36 R. Krishna and J. M. van Baten, *Chem. Eng. Technol.*, 2007, **30**, 1235–1241.
- 37 R. Krishna and J. M. van Baten, *Microporous Mesoporous Mater.*, 2008, **107**, 296–298.
- 38 R. Krishna, *Microporous Mesoporous Mater.*, 2014, **185**, 30–50.
- 39 O. Talu, M. S. Sun and D. B. Shah, *AIChE J.*, 1998, **44**, 681–694.
- 40 T. Titze, C. Chmelik, J. Kärger, J. M. van Baten and R. Krishna, *J. Phys. Chem. C*, 2014, **118**, 2660–2665.
- 41 H. Jobic, A. Methivier, G. Ehlers, B. Farago and W. Haeussler, *Angew. Chem., Int. Ed.*, 2004, **43**, 364–366.
- 42 R. L. Goring, *J. Catal.*, 1973, **31**, 13–26.
- 43 K. Yoo, R. Tsekov and P. G. Smirniotis, *J. Phys. Chem. B*, 2003, **107**, 13593–13596.
- 44 R. C. Runnebaum and E. J. Maginn, *J. Phys. Chem. B*, 1997, **101**, 6394–6408.
- 45 H. Jobic and D. N. Theodorou, *Microporous Mesoporous Mater.*, 2006, **102**, 21–50.
- 46 R. El Osta, A. Carlin-Sinclair, N. Guillou, R. I. Walton, F. Vermoortele, M. Maes, D. De Vos and F. Millange, *Chem. Mater.*, 2012, **24**, 2781–2791.
- 47 V. Finsy, H. Verelst, L. Alaerts, D. De Vos, P. A. Jacobs, G. V. Baron and J. F. M. Denayer, *J. Am. Chem. Soc.*, 2008, **130**, 7110–7118.
- 48 T. Remy, G. V. Baron and J. F. M. Denayer, *Langmuir*, 2011, **27**, 13064–13071.
- 49 A. S. T. Chiang, C.-K. Lee and Z.-H. Chang, *Zeolites*, 1991, **11**, 380–386.
- 50 A. Torres-Knoop and D. Dubbeldam, *ChemPhysChem*, 2015, **16**, 2046–2067.
- 51 J. M. van Baten and R. Krishna, *Microporous Mesoporous Mater.*, 2005, **84**, 179–191.
- 52 T. L. M. Maesen, R. Krishna, J. M. van Baten, B. Smit, S. Calero and J. M. Castillo Sanchez, *J. Catal.*, 2008, **256**, 95–107.
- 53 R. Krishna and J. M. van Baten, *Sep. Purif. Technol.*, 2008, **60**, 315–320.
- 54 R. Krishna and J. M. van Baten, *Sep. Purif. Technol.*, 2011, **76**, 325–330.

Electronic Supplementary Information (ESI) to accompany:

Commensurate-Incommensurate Adsorption and Diffusion in Ordered Crystalline Microporous Materials

Rajamani Krishna*, Jasper M. van Baten

Van 't Hoff Institute for Molecular Sciences, University of Amsterdam, Science Park 904,

1098 XH Amsterdam, The Netherlands

*Tel +31 20 6270990; Fax: + 31 20 5255604;

email: r.krishna@contact.uva.nl

Table of Contents

1. Preamble	3
2. Structural topology and connectivity of some common zeolites, MOFs, and ZIFs	3
3. The Ideal Adsorbed Solution Theory (IAST) for calculation of mixture adsorption equilibrium.....	7
4. IAST model: Langmuir isotherms	10
5. IAST model: Langmuir isotherms with equal saturation capacities.....	12
6. Statistical thermodynamics for 1D lattice model for mixture adsorption equilibrium.....	13
7. Statistical thermodynamics for 2D lattice model for mixture adsorption equilibrium.....	16
8. Commensurate-incommensurate adsorption in Manganese Formate.....	18
9. Commensurate-incommensurate adsorption in Cobalt Formate	21
10. Commensurate-incommensurate adsorption/diffusion in cage-type zeolites	25
11. Entropic separations of mixtures of linear alcohols using CHA zeolite	30
12. Entropic separations of mixtures of linear molecules using cage-type zeolites	33
13. Commensurate adsorption-diffusion in MFI zeolite.....	34
14. Separating hexane isomers using MFI zeolite	35
15. Entropy effects for n-alkane separations in ISV zeolite	39
16. The “window” effect and “resonant” diffusion	40
17. Separations xylene isomers by commensurate adsorption.....	41
18. Commensurate face-to-face stacking of aromatic molecules	42
19. Separating hexane isomers by exploiting differences in molecular footprints in 1D channels of MOR zeolite	44
20. Separating hexane isomers by exploiting differences in molecular footprints in 1D channels of AFI zeolite	48
21. Separating heptane isomers by exploiting differences in molecular footprints in 1D channels of TON zeolite	49
22. Notation.....	50
23. References.....	55
24. Captions for Figures.....	59

1. Preamble

This ESI accompanying our review article *Commensurate-Incommensurate Adsorption and Diffusion in Ordered Crystalline Microporous Materials* provides (a) detailed structural information on all of the zeolites, MOFs, and ZIFs analyzed and discussed in the article, (b) detailed derivations of the lattice model for mixture adsorption equilibrium, (c) details of IAST calculations for mixture adsorption equilibria, (d) input data on isotherm fits used in the lattice, and IAST model calculations.

For ease of reading, this ESI is written as a stand-alone document; as a consequence, there is some overlap of material with the main manuscript.

2. Structural topology and connectivity of some common zeolites, MOFs, and ZIFs

The pore dimensions, surface area, and pore volumes, and crystal densities of microporous adsorbents vary over a wide range; see Figure 1. The commonly used LTA-5A zeolite, for example, has 743 Å³ size cages separated by 4 Å windows, pore volume of 0.31 cm³ g⁻¹, and surface area of 896 m² g⁻¹. The accessible pore volumes of MOFs are commonly in the 0.5 – 2 cm³ g⁻¹ range. Significantly larger surface areas are available with MOFs; for example, Co(BDP) has an surface area of 2150 m² g⁻¹. The pore dimensions of MOFs cover a wide range: ZIF-77 has one dimensional 4.5 Å channels, and MgMOF-74 has 1D hexagonal shaped 11 Å channels.

The pore landscape, topology, and connectivity of the microporous host structures also show a wide diversity. These include: one-dimensional (1D) channels (e.g. AFI, LTL, MTW, TON, MIL-47, MIL-53, Co(BDP), Fe₂(BDP)₃), 1D zig-zag channels (e.g. CoFormate, MnFormate), 1D channels with side pockets (e.g. MOR, FER), intersecting channels (e.g. MFI, BEA, BOG,

Zn(bdc)dabco, Co(bdc)dabco), cavities with large windows (e.g. FAU, NaX, NaY, IRMOF-1, CuBTC), and cages separated by narrow windows (e.g. LTA, CHA, DDR, TSC, ERI, ZIF-8); see typical landscapes in Figure 2. We also note an inherent periodicity in the pore landscape, caused due to a variety of factors. For example, in one-dimensional channels of AFI, MTW, MOR, and MIL-53, there is a characteristic segment length of the 1D channels. For MFI, the periodicity is introduced by the distances between channel intersections. For LTA, and ZIF-8, the periodicity is introduced by the window-to-window distance.

The crystallographic data are available on the zeolite atlas website of the International Zeolite Association (IZA).^{1,2} Further details on the structure, landscape, pore dimensions of a very wide variety of micro-porous materials are available in the published literature.³⁻¹⁰

The pore topology and structural details of the crystalline structures that are discussed and analyzed in this article are provided in the accompanying Figures as indicated below; further details are provided by Krishna and van Baten.¹¹⁻¹³

One-dimensional (1D) channels

AFI (Figures 3, 4)

LTL (see Figures 5, 6)

MTW (see Figures 7, 8)

TON (see Figures 9, 10)

Co-Formate (Figure 11). Its synthesis is reported by Li et al.¹⁴ The network exhibits diamondoid connectivity and the overall framework gives rise to zig-zag channels along the *b* axis. The effective pore size of these one-dimensional channels is 5 – 6 Å; one unit cell of Co-

FA comprises a total of four distinct channel “segments”; each channel segment forms part of the repeat zig-zag structure.

Mn-Formate (Figures 12) has a topology is similar to that of Co-Formate.

The pore landscape and structural details for MIL-47 are provided in Figures 13, 14.

The structural information for Co(BDP) with (BDP²⁻ = 1,4-benzenedipyrazolate) is from Choi et al.¹⁵ and Salles et al.¹⁶ The structural data, and pore landscapes along are provided in Figures 15, 16.

For Fe₂(BDP)₃ (BDP²⁻ = 1,4-benzenedipyrazolate), the channels are triangular in shape, with a pore size of 4.9 Å. The structural data, and pore landscapes are provided in Figures 17, 18.

1D channels with side pockets

MOR (see Figures 19, 20)

Cages separated by narrow windows

AFX zeolite consists of cages of volume 490 Å³, separated by 3.4 Å × 3.9 Å windows; the cages are also connected to pockets of 98 Å³ by 3.1 Å × 4.62 Å windows; see Figures 21, and 22.

CHA zeolite consists of cages of volume 316 Å³, separated by 3.8 Å × 4.2 Å 8-ring windows as shown in Figures 23, and 24. SAPO-34 has the same structural topology of CHA zeolite.

DDR (cages of 277.8 \AA^3 volume, separated by $3.65 \text{ \AA} \times 4.37 \text{ \AA}$ 8-ring windows; the pore landscapes and structural details are provided in Figures 25, and 26).

ERI (cages of 408.7 \AA^3 volume, separated by $3.8 \text{ \AA} \times 4.9 \text{ \AA}$ 8-ring windows; the pore landscapes and structural details are provided in Figures 27, and 28).

LTA, LTA-5A, LTA-4A (cages of 743 \AA^3 volume, separated by $4.11 \text{ \AA} \times 4.47 \text{ \AA}$ 8-ring windows; the pore landscapes and structural details are provided in Figures 29, 30, 31, and 32), and

TSC zeolite, with a Tschörtnerite framework, has the largest cage volume of any known zeolite;¹⁷ the pore landscape and structural details are provided in Figures 33, 34, and 35. Each unit cell of TSC has four “LTA type cages” of 743 \AA^3 , and four “TSC supercages” of 2553 \AA^3 ; the cages are separated by two types of windows: $4.02 \text{ \AA} \times 4.17 \text{ \AA}$, and $3.1 \text{ \AA} \times 5.41 \text{ \AA}$.

ZIF-8 (cages of 1168 \AA^3 volume, separated by 3.3 \AA windows; the pore landscapes and structural details are provided in Figures 36, 37).

Intersecting channels

MFI zeolite (also called silicalite-1) has a topology consisting of a set of intersecting straight channels, and zig-zag (or sinusoidal) channels of approximately 5.5 \AA size. The pore landscapes and structural details are provided in Figures 38, and 39.

The pore landscapes and structural details for ISV zeolite are provided in Figures 40, 41.

3. The Ideal Adsorbed Solution Theory (IAST) for calculation of mixture adsorption equilibrium

Within microporous crystalline materials, the guest molecules exist in the adsorbed phase. The Gibbs adsorption equation¹⁸ in differential form is

$$Ad\pi = \sum_{i=1}^n q_i d\mu_i \quad (1)$$

The quantity A on the left side of Equation (1) is the surface area per kg of framework, with units of m^2 per kg of the framework of the crystalline material; q_i is the molar loading of component i in the adsorbed phase with units moles per kg of framework; μ_i is the molar chemical potential of component i . The spreading pressure π has the same units as surface tension, i.e. N m^{-1} .

The chemical potential of any component in the adsorbed phase, μ_i , equals that in the bulk fluid phase. If the partial fugacities in the bulk fluid phase are f_i , we have

$$d\mu_i = RTd \ln f_i \quad (2)$$

where R is the gas constant ($= 8.314 \text{ J mol}^{-1} \text{ K}^{-1}$).

Briefly, the basic equation of Ideal Adsorbed Solution Theory (IAST) theory of Myers and Prausnitz¹⁹ is the analogue of Raoult's law for vapor-liquid equilibrium, i.e.

$$f_i = P_i^0 x_i; \quad i = 1, 2, \dots, n \quad (3)$$

where x_i is the mole fraction in the adsorbed phase

$$x_i = \frac{q_i}{q_1 + q_2 + \dots + q_n} \quad (4)$$

and P_i^0 is the pressure for sorption of every component i , which yields the same spreading pressure, π for each of the pure components, as that for the mixture:

$$\frac{\pi A}{RT} = \int_0^{P_1^0} \frac{q_1^0(f)}{f} df = \int_0^{P_2^0} \frac{q_2^0(f)}{f} df = \int_0^{P_3^0} \frac{q_3^0(f)}{f} df = \dots \quad (5)$$

where $q_i^0(f)$ is the *pure* component adsorption isotherm. The unary isotherm may be described by say the 1-site Langmuir isotherm

$$q^0(f) = q_{sat} \frac{bf}{1+bf}; \quad \theta = \frac{bf}{1+bf} \quad (6)$$

where we define the fractional *occupancy* of the adsorbate molecules, $\theta = q^0(f)/q_{sat}$. The superscript 0 is used to emphasize that $q^0(f)$ relates the *pure component* loading to the bulk fluid fugacity. More generally, the unary isotherms may need to be described by the dual-Langmuir-Freundlich model

$$q^0(f) = q_{A,sat} \frac{b_A f^{vA}}{1+b_A f^{vA}} + q_{B,sat} \frac{b_B f^{vB}}{1+b_B f^{vB}} \quad (7)$$

The units of $\frac{\pi A}{RT}$, also called the adsorption potential,²⁰ are mol kg⁻¹.

Each of the integrals in Equation (5) can be evaluated analytically. For the Langmuir isotherm, the integration yields for any component i :

$$\int_{f=0}^P \frac{q_i^i(f)}{f} df = q_{i,sat} \ln(1+b_i P) \quad (8)$$

The right hand side of equation (8) is a function of P . For multicomponent mixture adsorption, each of the equalities on the right hand side of Equation (5) must be satisfied. These constraints

may be solved using a suitable root-finder, to yield the set of values of $P_1^0, P_2^0, P_3^0, \dots, P_n^0$, all of which satisfy Equation (5). The corresponding values of the integrals using these as upper limits of integration must yield the same value of $\frac{\pi A}{RT}$ for each component; this ensures that the obtained solution is the correct one.

The adsorbed phase mole fractions x_i are then determined from

$$x_i = \frac{f_i}{P_i^0}; \quad i = 1, 2, \dots, n \quad (9)$$

A key assumption of the IAST is that the enthalpies and surface areas of the adsorbed molecules do not change upon mixing. If the total mixture loading is q_t , the area covered by the adsorbed mixture is $\frac{A}{q_t}$ with units of $\text{m}^2 (\text{mol mixture})^{-1}$. Therefore, the assumption of no surface

area change due to mixture adsorption translates as $\frac{A}{q_t} = \frac{Ax_1}{q_1^0(P_1^0)} + \frac{Ax_2}{q_2^0(P_2^0)} + \dots + \frac{Ax_n}{q_n^0(P_n^0)}$; the total mixture loading is q_t is calculated from

$$q_t = q_1 + q_2 + \dots + q_n = \frac{1}{\frac{x_1}{q_1^0(P_1^0)} + \frac{x_2}{q_2^0(P_2^0)} + \dots + \frac{x_n}{q_n^0(P_n^0)}} \quad (10)$$

in which $q_1^0(P_1^0), q_2^0(P_2^0), \dots, q_n^0(P_n^0)$ are determined from the unary isotherm fits, using the sorption pressures for each component $P_1^0, P_2^0, P_3^0, \dots, P_n^0$ that are available from the solutions to equations (9), and (10).

The set of equations (3), (4), (5), (6) or (7), (8), (9), and (10) need to be solved numerically to obtain the loadings, q_i of the individual components in the mixture.

4. IAST model: Langmuir isotherms

The IAST procedure for estimation mixture adsorption will be explained in a step-by-step manner for binary mixture adsorption in which the unary isotherms are described by the 1-site Langmuir model. The objective is to determine the molar loadings, q_1 , and q_2 , in the adsorbed phase.

Performing the integration of Equation (5) results in an expression relating the sorption pressures P_i^0 of the two species

$$\begin{aligned} \frac{\pi A}{RT} &= q_{1,sat} \ln(1 + b_1 P_1^0) = q_{2,sat} \ln(1 + b_2 P_2^0) \\ b_1 P_1^0 &= \exp\left(\frac{\pi A}{q_{1,sat} RT}\right) - 1; \quad b_2 P_2^0 = \exp\left(\frac{\pi A}{q_{2,sat} RT}\right) - 1 \end{aligned} \quad (11)$$

The adsorbed phase mole fractions of component 1, and component 2 are given by equation (9):

$$x_1 = \frac{f_1}{P_1^0}; \quad x_2 = 1 - x_1 = \frac{f_2}{P_2^0} \quad (12)$$

Since the mole fractions add to unity, we may combine equations (11), and (12) to obtain

$$\begin{aligned} \frac{f_1}{P_1^0} + \frac{f_2}{P_2^0} &= 1 \\ \frac{b_1 f_1}{\exp\left(\frac{\pi A}{q_{1,sat} RT}\right) - 1} + \frac{b_2 f_2}{\exp\left(\frac{\pi A}{q_{2,sat} RT}\right) - 1} &= 1 \end{aligned} \quad (13)$$

We can combine equations (11) and (12) to yield an equation in just *one* unknown, x_1 :

$$\frac{\pi A}{RT} = q_{1,sat} \ln\left(1 + b_1 \frac{f_1}{x_1}\right) = q_{2,sat} \ln\left(1 + b_2 \frac{f_2}{1 - x_1}\right) \quad (14)$$

Equation (14) is a non-linear equation

$$q_{1,sat} \ln\left(1 + b_1 \frac{f_1}{x_1}\right) - q_{2,sat} \ln\left(1 + b_2 \frac{f_2}{1-x_1}\right) = 0 \quad (15)$$

The partial fugacities of the two components in the bulk gas phase are known, and equation (15) needs to be solved using a root finder (programmable in say Excel) to solve for the unknown, x_1 .

Once x_1 , and $x_2 = 1 - x_1$ are determined, the sorption pressures can be calculated using equation (12)

$$P_1^0 = \frac{f_1}{x_1}; \quad P_2^0 = \frac{f_2}{x_2} = \frac{f_2}{1-x_1} \quad (16)$$

The total amount adsorbed, $q_t = q_1 + q_2$ can be calculated from equation (10):

$$q_t = q_1 + q_2 = \frac{1}{\frac{x_1}{q_1^0(P_1^0)} + \frac{x_2}{q_2^0(P_2^0)}} \quad (17)$$

in which $q_1^0(P_1^0)$, and $q_2^0(P_2^0)$ are determined from the Langmuir parameters along with the sorption pressures, determined from equation (16).

The component loadings, q_1 , and q_2 are then determined from

$$q_1 = q_t x_1; \quad q_2 = q_t (1 - x_1) \quad (18)$$

LeVan and Vermeulen²¹ have developed explicit expressions for the component loadings for binary mixture adsorption for which the unary isotherms are described by the Langmuir and Freundlich isotherms. Their procedure involves developing a Taylor expansion for $\frac{\pi A}{RT}$. They

provide explicit formulae for the calculation of the component loadings for cases in which the Taylor series is approximated by (1) one term, (2) two terms, and (3) three terms.

We have tested the accuracy of the “three-term” solution and found the accuracy to be inadequate for describing the wide variety of selectivity reversal phenomena that are the main focus of this article.

5. IAST model: Langmuir isotherms with equal saturation capacities

For the special case of binary mixture adsorption with equal saturation capacities, the component loadings can be determined explicitly. Equation (15) can be solved explicitly to obtain the adsorbed phase mole fractions

$$\frac{x_1}{x_2} = \frac{q_1}{q_2} = \frac{b_1 f_1}{b_2 f_2}; \quad x_1 = \frac{q_1}{q_t} = \frac{b_1 f_1}{b_1 f_1 + b_2 f_2}; \quad x_2 = \frac{q_2}{q_t} = \frac{b_2 f_2}{b_1 f_1 + b_2 f_2} \quad (19)$$

Equation (11) simplifies to yield

$$\frac{\pi A}{RT} = q_{sat} \ln(1 + b_1 P_1^0) = q_{sat} \ln(1 + b_2 P_2^0)$$

$$b_1 P_1^0 = b_2 P_2^0 = \exp\left(\frac{\pi A}{q_{sat} RT}\right) - 1 = \exp\left(\frac{\pi A}{q_{sat} RT}\right) - 1$$

From equation (16) we get

$$b_1 P_1^0 = \frac{b_1 f_1}{x_1} = b_2 P_2^0 = \frac{b_2 f_2}{x_2} = b_1 f_1 + b_2 f_2$$

$$1 + b_1 P_1^0 = 1 + b_2 P_2^0 = 1 + b_1 f_1 + b_2 f_2$$

From equation (17) we get

$$\frac{q_{sat}}{q_t} = \frac{x_1}{b_1 P_1^0} (1 + b_1 P_1^0) + \frac{x_2}{b_2 P_2^0} (1 + b_2 P_2^0) = \frac{1 + b_1 f_1 + b_2 f_2}{b_1 f_1 + b_2 f_2} \quad (20)$$

$$q_t = q_{sat} \frac{b_1 f_1 + b_2 f_2}{1 + b_1 f_1 + b_2 f_2}$$

Combining equation (19) and (20) we obtain

$$\theta_1 = \frac{q_1}{q_{sat}} = \frac{b_1 f_1}{b_1 f_1 + b_2 f_2}; \quad \theta_2 = \frac{q_2}{q_{sat}} = \frac{b_2 f_2}{b_1 f_1 + b_2 f_2} \quad (21)$$

Equation (21) is commonly referred to as the mixed-gas Langmuir model.

6. Statistical thermodynamics for 1D lattice model for mixture adsorption equilibrium

We begin by deriving the Langmuir isotherm using a two-dimensional lattice representation for the surface of the solid (see Figure 42); the derivations are based on treatment in Chapter 27 of Dill and Bromberg.²² The adsorption of the N particles (= molecules) from the gas phase on the M lattice sites takes place at the potential energy wells. The number of arrangements of the particles (= molecules) is $W = \frac{M!}{N!(M-N)!}$. The Boltzmann relation $S = k_B \ln(W)$, where $W =$

Wahrscheinlichkeit, along with the Stirling approximation $\ln(M!) = M \ln M - M$ can be used to calculate the translation entropy of adsorption; see Figure 43. The calculation of the Helmholtz free energy of adsorption $F = U - TS$ is the following step; see Figure 44. Equating the chemical potentials in the gas phase to that of the adsorbed solid phase leads to the Langmuir isotherm

(see Figure 45), $\theta = \frac{bp}{1+bp}$ in which $b = \frac{q_{surf}}{p_{int}^0} \exp\left(-\frac{w}{k_B T}\right)$ is the binding constant.

The adsorption of a binary mixture of rigid k -mers and rigid l -mers on one-dimensional (1D) lattices is described by Dávila et al.²³ The adsorbent surface is modeled by a 1D lattice of M sites ($M \rightarrow \infty$); see schematic in Figure 46. The k -mers are assumed to be composed by k identical units in a linear array with constant bond length equal to the lattice dimension. The k -mers can only adsorb flat on the surface occupying k contiguous lattice sites. Analogously, the l -mers are assumed to be composed by l identical units in a linear array with constant bond length equal to the lattice constant a . The l -mers can only adsorb flat on the surface occupying l contiguous

lattice sites. For adsorption of methane/ethane mixtures, for example, $k = 1$, $l = 2$. Furthermore, double site occupancy is not disallowed and only mono-layer adsorption is considered. Also, there are no adsorbate-adsorbate interactions. Since different particles do not interact with each other, all configurations of N_k k -mers and N_l l -mers on M sites are equally probable.

Dávila et al.²³ derive the following expression for the number of arrangements of N_k k -mers and N_l l -mers on M sites:

$$W = \frac{(M - (k-1)N_k - (l-1)N_l)!}{(M - kN_k - lN_l)! N_k! N_l!} \quad (22)$$

Of particular interest in this article is the calculation of the entropy for binary mixture adsorption $S = k_B \ln(W)$; this can be calculated using the Stirling's approximation $\ln(M!) = M \ln M - M$. The expression for the dimensionless entropy per site for a 1D lattice is

$$\begin{aligned} \frac{S}{k_B M} = & \left(1 - \frac{(k-1)kN_k}{kM} - \frac{(l-1)lN_l}{lM}\right) \ln\left(1 - \frac{(k-1)kN_k}{kM} - \frac{(l-1)lN_l}{lM}\right) \\ & - \left(1 - \frac{kN_k}{M} - \frac{lN_l}{M}\right) \ln\left(1 - \frac{kN_k}{M} - \frac{lN_l}{M}\right) - \frac{kN_k}{M} \ln \frac{kN_k}{M} - \frac{lN_l}{M} \ln \frac{lN_l}{M} \end{aligned} \quad (23)$$

Defining, the fractional occupancies $\theta_k = \frac{kN_k}{M}$; $\theta_l = \frac{lN_l}{M}$, we obtain, on simplification of equation (23), the following expression for the dimensionless entropy per site

$$\begin{aligned} \frac{S}{k_B M} = & \left(1 - \frac{(k-1)\theta_k}{k} - \frac{(l-1)\theta_l}{l}\right) \ln\left(1 - \frac{(k-1)\theta_k}{k} - \frac{(l-1)\theta_l}{l}\right) \\ & - (1 - \theta_k - \theta_l) \ln(1 - \theta_k - \theta_l) - \frac{\theta_k}{k} \ln \frac{\theta_k}{k} - \frac{\theta_l}{l} \ln \frac{\theta_l}{l} \end{aligned} \quad (24)$$

The mixture adsorption equilibrium for a 1D lattice is described by a set of two, coupled, equations:

$$\begin{aligned}
(k-1)\ln\left(1-\frac{(k-1)}{k}\theta_k-\frac{(l-1)}{l}\theta_l\right)+\ln\frac{\theta_k}{k}-k\ln(1-\theta_k-\theta_l)&=\ln(b_k f_k) \\
(l-1)\ln\left(1-\frac{(k-1)}{k}\theta_k-\frac{(l-1)}{l}\theta_l\right)+\ln\frac{\theta_l}{l}-l\ln(1-\theta_k-\theta_l)&=\ln(b_l f_l)
\end{aligned}
\tag{25}$$

where b_k and b_l are the binding constants for the two adsorbates; f_k and f_l are the partial fugacities in the bulk fluid phase in equilibrium with the adsorbates. It is to be noted that since the equations (25) are not explicit in terms of the occupancies, $\theta_k = \frac{kN_k}{M}$; $\theta_l = \frac{lN_l}{M}$, the set of two equations need to be solved numerically. All the calculations presented in this article were performed using the Given-Find solve block of MathCad 15.²⁴

The corresponding *unary isotherms* are described by the limiting cases of equations (26):

$$\begin{aligned}
(k-1)\ln\left(1-\frac{(k-1)}{k}\theta_k\right)+\ln\frac{\theta_k}{k}-k\ln(1-\theta_k)&=\ln(b_k f) \\
(l-1)\ln\left(1-\frac{(l-1)}{l}\theta_l\right)+\ln\frac{\theta_l}{l}-l\ln(1-\theta_l)&=\ln(b_l f)
\end{aligned}
\tag{26}$$

The binding constants b_k and b_l can be fitted to match the unary isotherm data. In applying the 1D lattice model to rationalize the selectivity reversal phenomena observed for binary mixture adsorption in zeolites and MOFs, we may also interpret the parameters k and l to be representative of the inverse saturation capacities of the unary isotherms. For example, we arbitrarily set $k=1$, and take $l = \frac{q_{k,sat}}{q_{l,sat}}$. Alternatively, we set $l=1$, and take $k = \frac{q_{l,sat}}{q_{k,sat}}$. There is no strict requirement to restrict the values of k and l to integer values.

7. Statistical thermodynamics for 2D lattice model for mixture adsorption equilibrium

Azizian and Bashiri²⁵ consider a two-dimensional lattice of M sites for binary adsorption of A and B molecules. N_k and N_l molecules of A and B are adsorbed on the surface, respectively, in such a way that each A molecule occupies k lattice sites and each B molecule occupies l lattice sites. It is assumed that there are no adsorbate-adsorbate interactions, consistent with the assumptions in the classical Langmuir model. The number of configurations that are possible for arrangement of N_k and N_l molecules on M sites of the 2D lattice is given by equation (1) of Azizian and Bashiri.²⁵

$$W = \frac{(M - (k-1)N_k - (l-1)N_l)!}{(M - kN_k - lN_l)! N_k! N_l!} \quad (27)$$

Using the Stirling approximation, the following expression can be derived for the entropy per site

$$\begin{aligned} \frac{S}{k_B M} = & \left(1 - \frac{(k-1)kN_k}{kM} - \frac{(l-1)lN_l}{lM}\right) \ln \left(1 - \frac{(k-1)kN_k}{kM} - \frac{(l-1)lN_l}{lM}\right) \\ & - \left(1 - \frac{kN_k}{M} - \frac{lN_l}{M}\right) \ln \left(1 - \frac{kN_k}{M} - \frac{lN_l}{M}\right) - \frac{kN_k}{M} \ln \frac{kN_k}{M} - \frac{lN_l}{M} \ln \frac{lN_l}{M} \end{aligned} \quad (28)$$

Formally, equation (28) is identical to the corresponding expression (24), derived by Dávila et al.²³ for adsorption of N_k k -mers and N_l l -mers on M sites on an 1D lattice.

Defining, the fractional coverages of A and B molecules, $\theta_k = \frac{kN_k}{M}$; $\theta_l = \frac{lN_l}{M}$, we obtain, on simplification of equation (23), the following expression for the dimensionless entropy per site

$$\begin{aligned} \frac{S}{k_B M} = & \left(1 - \frac{(k-1)}{k} \theta_k - \frac{(l-1)}{l} \theta_l\right) \ln \left(1 - \frac{(k-1)}{k} \theta_k - \frac{(l-1)}{l} \theta_l\right) \\ & - (1 - \theta_k - \theta_l) \ln(1 - \theta_k - \theta_l) - \frac{\theta_k}{k} \ln \frac{\theta_k}{k} - \frac{\theta_l}{l} \ln \frac{\theta_l}{l} \end{aligned} \quad (29)$$

The mixture adsorption equilibrium for a 2D lattice is described by a set of two, coupled, equations:

$$\begin{aligned} (k-1) \ln \left(1 - \frac{(k-1)}{k} \theta_k - \frac{(l-1)}{l} \theta_l\right) + \ln \frac{\theta_k}{k} - k \ln(1 - \theta_k - \theta_l) &= \ln(b_k f_k) \\ (l-1) \ln \left(1 - \frac{(k-1)}{k} \theta_k - \frac{(l-1)}{l} \theta_l\right) + \ln \frac{\theta_l}{l} - l \ln(1 - \theta_k - \theta_l) &= \ln(b_l f_l) \end{aligned} \quad (30)$$

where b_k and b_l are the binding constants for the two adsorbates; f_k and f_l are the partial fugacities in the bulk fluid phase in equilibrium with the adsorbates. Equation (30) is formally identical to the equation (26) for the 1D lattice model. It is to be noted that since the equations (30) are not explicit in terms of the occupancies, $\theta_k = \frac{kN_k}{M}$; $\theta_l = \frac{lN_l}{M}$, the set of two equations need to be solved numerically. All the calculations presented in this article were performed using the Given-Find solve block of MathCad 15.²⁴

The corresponding *unary isotherms* are described by the limiting cases of equations (30)

$$\begin{aligned} (k-1) \ln \left(1 - \frac{(k-1)}{k} \theta_k\right) + \ln \frac{\theta_k}{k} - k \ln(1 - \theta_k) &= \ln(b_k f) \\ (l-1) \ln \left(1 - \frac{(l-1)}{l} \theta_l\right) + \ln \frac{\theta_l}{l} - l \ln(1 - \theta_l) &= \ln(b_l f) \end{aligned} \quad (31)$$

The binding constants b_k and b_l can be fitted to match the unary isotherm data.

For the special case, $k=1$, $l=1$, equations (31) reduce to the Langmuir isotherms

$$\frac{\theta_k}{(1 - \theta_k)} = b_k f; \quad \frac{\theta_l}{(1 - \theta_l)} = b_l f \quad (32)$$

Furthermore, for $k=1, l=1$, equations (30) reduce to

$$\frac{\theta_k}{(1-\theta_k-\theta_l)} = b_k f_k; \quad \frac{\theta_l}{(1-\theta_k-\theta_l)} = b_l f_l \quad (33)$$

It is easy to check that equation (33) is precisely equivalent to Equation (21), the mixed-gas Langmuir model.

Equation (29), the dimensionless entropy per site, for $k=1, l=1$, simplifies to

$$\frac{S}{k_B M} = -(1-\theta_k-\theta_l)\ln(1-\theta_k-\theta_l) - \theta_k \ln \theta_k - \theta_l \ln \theta_l \quad (34)$$

Equation (34) should be compared to the entropy of mixing for binary *fluid* mixtures

$$\frac{S}{k_B} = -x_k \ln x_k - x_l \ln x_l \quad \text{where } x_k \text{ and } x_l \text{ are the mole fractions.}$$

8. Commensurate-incommensurate adsorption in Manganese Formate

We consider adsorption of linear alkanes in manganese formate (Mn-FA) framework.²⁶ The Mn-FA structure consists of 1D zig-zag channels; see the pore landscapes in Figure 12.

Figure 47 presents computational snapshots showing the location and conformation of propane (C3) and n-hexane (nC6) molecules within the zig-zag 1D channel segments of Mn-FA; one unit cell of Mn-FA contains four channel segments.

Configurational-Bias Monte Carlo (CBMC) simulations²⁶ of the unary adsorption isotherms of C3 and nC6 are presented in Figure 48a. The saturation capacity for C3 is found to be 4 molecules per unit cell (uc), corresponding to one molecule per channel segment; the length of each channel segment is commensurate with that of the propane molecule. Longer alkane molecules such as nC6 must straddle two channel segments; the length of the nC6 molecule is

commensurate with the length of two channel segments. The saturation capacities of nC6 is restricted to 2 molecules uc^{-1} .

Consider a mixture of C3 and nC6. CBMC simulations of the component loadings for a mixture with equal partial fluid phase fugacities, $f_1=f_2$, are shown in Figure 48b. When operating at total fugacities $f_t = f_1 + f_2 > 100$ kPa, we note that the adsorbed phase composition is richer in the shorter alkane. Increase in f_t beyond 100 kPa causes a progressive increase in the component loading of propane, with a concomitant decrease in the loading of nC6.

To elucidate the reasons behind the selectivity reversal that occurs at $f_t \approx 100$ kPa, we use the model of Dávila et al.²³ for a 1D lattice. Since C3 (species k) adsorbs commensurately with one channel segment, we take $k=1$. The linear hexane (species l) adsorbs commensurately with two channel segments, and so we take $l=2$. To determine the component loadings in the units of molecules per unit cell, we take $M = 4$. The component loading of C3, in molecules per unit cell, is given by $N_k = \theta_k \frac{M}{k}$. The component loading of nC6, in molecules per unit cell, is given by

$$N_l = \theta_l \frac{M}{l}.$$

For a quantitative analysis of mixture adsorption, we need to first determine the binding constants, using equations (26) and the CBMC simulated data on unary isotherms. A reasonably good match between equations (26) and the CBMC simulations of the unary isotherms is obtained with the choice $b_k = 8 \times 10^{-4} \text{ Pa}^{-1}$, and $b_l = 4 \times 10^{-2} \text{ Pa}^{-1}$; see Figure 48a.

With the fitted binding constants, the component loadings for mixture adsorption can be calculated using equations (25); the results are shown by the continuous solid lines in Figure 48b. The lattice model is able to quantitatively capture the selectivity reversal phenomenon.

The lattice model is in good agreement with the IAST calculations (shown by the dashed lines in Figure 48b) for mixture adsorption equilibrium, using Langmuir fits of the unary isotherms of C3 and nC6. For C3, the Langmuir binding constant is the same as for the lattice model, i.e. $b_{C3} = 8 \times 10^{-4} \text{ Pa}^{-1}$; $\Theta_{C3,sat} = 4 \text{ uc}^{-1}$. For nC6, the Langmuir binding constant, $b_{nC6} = 3 \times 10^{-2} \text{ Pa}^{-1}$, $\Theta_{nC6,sat} = 2 \text{ uc}^{-1}$.

Figure 49a presents calculations of the dimensionless entropy per site $\frac{S}{k_B M}$, using equation (24), for a binary mixture of C3 ($k=1$), and nC6 ($l=2$) in 1D lattice as a function of the proportion

of propane in the adsorbed phase, $x_k = \frac{N_k}{N_k + N_l}$, for three different values of total occupancies,

$\frac{N_k + N_l}{M} = 0.1, 0.3, \text{ and } 0.5$. At the lowest occupancy, $\frac{N_k + N_l}{M} = 0.1$, the maximum in the $\frac{S}{k_B M}$

occurs at the adsorbed composition $x_k = \frac{N_k}{N_k + N_l} \approx 0.5$. With increasing occupancies, $\frac{N_k + N_l}{M}$,

the maximum in the $\frac{S}{k_B M}$ occurs at values the adsorbed composition $x_k = \frac{N_k}{N_k + N_l}$, that are

significantly richer in propane, the shorter alkane. This is because the vacancies are more efficiently filled up by molecules with the shorter chain length. The precise composition of the adsorbed phase, corresponding to the maximum entropy can be determined by setting

$\frac{\partial}{\partial N_k} \left(\frac{S}{k_B M} \right) = 0$. The continuous solid black line Figure 49b presents a plot of the values of

$x_k = \frac{N_k}{N_k + N_l}$ corresponding to the maximum entropy as a function of the occupancy, $\frac{N_k + N_l}{M}$.

The corresponding calculations for the minimum in the Helmholtz free energy of adsorption $F = U - TS$, is shown by the continuous solid blue line. The entropic contribution to the Helmholtz

free energy is able to override the internal energy contribution only at fractional occupancies

$\frac{N_k+N_l}{M}$ higher than about 0.6.

For the special case, $k=1$, $l=1$, the entropy maximum occurs at $x_k = \frac{N_k}{N_k + N_l} = 0.5$ for all

values of the occupancies $\frac{N_k+N_l}{M}$.

For entropy effects to be fully exploited and nC6 to be totally rejected, the operations must be under conditions such that pore saturation prevails; adsorption from mixtures in the liquid phase usually ensures prevalence of pore saturation conditions.

9. Commensurate-incommensurate adsorption in Cobalt Formate

Consider the adsorption of n-alkanes, with C numbers ranging from 1 to 7, in cobalt formate (Co-FA) framework.²⁶ The Co-FA structure consists of 1D zig-zag channels; see the pore landscapes in Figure 11. The network exhibits diamondoid connectivity and the overall framework gives rise to zig-zag channels along the b axis. The effective pore size of these one-dimensional channels is 5 – 6 Å; one unit cell of Co-FA comprises a total of four distinct channel “segments”; each channel segment forms part of the repeat zig-zag structure. The pore topology of Co-FA is analogous to that of Mn-FA. Figure 50 presents computational snapshots of the conformations of adsorbed n-alkanes molecules within the zig-zag 1D channel segments of Co-FA. One unit cell of Co-FA contains four channel segments.

Configurational-Bias Monte Carlo (CBMC) simulations of the unary adsorption isotherms of C1, C2, C3, nC4, nC5, nC6, and nC7 alkanes are presented in Figure 51a. The hierarchy of adsorption strengths for C1, C2 and C3 is as expected; increasing chain length results in higher adsorption strength. The saturation capacity for C1, C2, and C3 are found to be 4 molecules per

unit cell (uc), corresponding to one molecule per channel segment. However, with increasing chain lengths beyond C3 we note an unusual adsorption hierarchy: $C3 > nC4 > nC5$; the length of each channel segment is commensurate with that of the propane molecule and longer molecules such as n-pentane (nC5), and n-hexane (nC6) must straddle two channel segments. The length of the nC6 molecule is commensurate with the length of two channel segments, and further increase in chain length, results in the expected hierarchy, i.e. $nC7 > nC6 > nC5$. The saturation capacities of nC5, nC6, and nC7 are restricted to 2 molecules uc^{-1} .

Some confirmation of the unusual hierarchy in the adsorption hierarchy observed in Figure 51a is provided by the experimental data of Li et al.¹⁴ for unary isotherms of 1-propanol and 1-butanol in Co-FA, see Figure 51b. We note that the adsorption strength of 1-propanol is higher than that of 1-butanol over the entire range of experimental pressures. This trend is the same as witnessed for nC3 and nC4 alkanes in Figure 51a.

Due to commensurate-incommensurate adsorption, the hierarchy of adsorption strengths displays non-monotonic characteristics in the plot of Henry coefficient vs C chain length (cf. Figure 51c). Also shown on the right y-axis in Figure 51c are the Maxwell-Stefan (M-S) diffusivities at zero-loadings, $D_i(0)$, determined from Molecular Dynamics (MD) simulations. The diffusivity hierarchy is the mirror image of that for the Henry coefficient; incommensurate adsorption results in a higher diffusivity value. A simple physical reasoning is that commensurate adsorption implies that the molecules resides “cozily” within the channel segment, and has a low tendency to hop to a neighboring location. The converse is true for guests that adsorb incommensurately; that molecule feels “out of place” and has a tendency to escape and hop to a neighboring site.

The non-monotonous adsorption characteristics, along with differences in saturation capacities can be exploited to achieve unusual separation possibilities. Consider a mixture of C3 and nC6. From the pure component adsorption isotherms in Figure 51a we note that at low pressures the adsorption strengths of C3 is nearly the same as that of nC6. However the saturation capacity of C3 is twice that of nC6. We can devise a strategy for separating C3 from nC6 by exploiting the differences in the saturation capacities. CBMC simulations of the component loadings for a C3/nC6 mixture with equal partial fluid phase fugacities, $f_1=f_2$, are shown in Figure 51d. When operating at fugacities $f_t = f_1 + f_2 > 100$ kPa, we note that the adsorbed phase contains practically no nC6 and predominantly loaded with C3. The preferential adsorption of C3 is due to entropy effects that favor the molecule with the higher saturation capacity, i.e. higher “packing efficiency”.

To elucidate the reasons behind the exclusion of nC6 at fugacities $f_t > 1$ MPa, we use the model of Dávila et al.²³ for a 1D lattice. Since C3 (species k) adsorbs commensurately with one channel segment, we take $k=1$. The linear hexane (species l) adsorbs commensurately with two channel segments, and so we take $l=2$. To determine the component loadings in the units of molecules per unit cell, we take $M = 4$. The component loading of C3, in molecules per unit cell, is given by $N_k = \theta_k \frac{M}{k}$. The component loading of nC6, in molecules per unit cell, is given by

$$N_l = \theta_l \frac{M}{l}.$$

For a quantitative analysis of mixture adsorption, we need to first determine the binding constants, using equations (26) and the CBMC simulated unary isotherm data. A reasonably good match between equations (26) and the CBMC simulations of the unary isotherms is obtained with the choice $b_k = 3 \times 10^{-4} \text{ Pa}^{-1}$, and $b_l = 3 \times 10^{-4} \text{ Pa}^{-1}$; see Figure 52a.

With the fitted binding constants, the component loadings for mixture adsorption can be calculated using equations (25); the results are shown by the continuous solid lines in Figure 52b. The lattice model is able to quantitatively capture the phenomenon of nC6 exclusion from Co-FA as pore saturation is approached.

The lattice model is in good agreement with the IAST calculations (shown by the dashed lines in Figure 52b) for mixture adsorption equilibrium, using Langmuir fits of the unary isotherms of C3 and nC6. For C3, the Langmuir binding constant is the same as for the lattice model, i.e. $b_{C3} = 3 \times 10^{-4} \text{ Pa}^{-1}$; $\Theta_{C3,sat} = 4 \text{ uc}^{-1}$. For nC6, the Langmuir binding constant, $b_{nC6} = 2.65 \times 10^{-4} \text{ Pa}^{-1}$, $\Theta_{nC6,sat} = 2 \text{ uc}^{-1}$.

Figure 53a presents calculations of the dimensionless entropy per site $\frac{S}{k_B M}$, using equation (24), for a binary mixture of C3 ($k=1$), and nC6 ($l=2$) in 1D lattice as a function of the proportion of propane in the adsorbed phase, $x_k = \frac{N_k}{N_k + N_l}$, for three different values of total occupancies, $\frac{N_k + N_l}{M} = 0.1, 0.3, \text{ and } 0.5$. At the lowest occupancy, $\frac{N_k + N_l}{M} = 0.1$, the maximum in the $\frac{S}{k_B M}$ occurs at the adsorbed composition $x_k = \frac{N_k}{N_k + N_l} \approx 0.5$. Since the binding energies for C3/nC6 adsorption in Co-FA are equal to each other, the maximum in the entropy also corresponds to the minimum in the Helmholtz free energy of adsorption $F = U - TS$ because the internal energy contribution to the free energy is not a function of composition for this case. In other words, the state of maximum entropy production is the preferred one that will be attained at adsorption equilibrium. With increasing occupancies, $\frac{N_k + N_l}{M}$, the maximum in the $\frac{S}{k_B M}$ occurs at values

the adsorbed composition $x_k = \frac{N_k}{N_k + N_l}$, that are significantly richer in propane, the shorter alkane. This is because the vacancies are more efficiently filled up by molecules with the shorter chain length. The precise composition of the adsorbed phase, corresponding to the maximum entropy can be determined by setting $\frac{\partial}{\partial N_k} \left(\frac{S}{k_B M} \right) = 0$. Figure 53b presents a plot of the values of $x_k = \frac{N_k}{N_k + N_l}$ corresponding to the maximum entropy, i.e. the preferred composition of the adsorbed mixtures as a function of the occupancy, $\frac{N_k + N_l}{M}$. As the total occupancy approaches unity, i.e. at pore saturation, the adsorbed mixture consists predominantly of the shorter alkane, and the longer nC6 is practically excluded. The calculations of the adsorbed phase compositions corresponding to a minimum in the Helmholtz free energy is identical to that for the maximum entropy because the fitted binding constants of C3 and nC6 are equal to each other $b_k = b_l = 3 \times 10^{-4} \text{ Pa}^{-1}$.

For entropy effects to be exploited, the operations must be under conditions such that pore saturation prevails; adsorption from liquid mixtures usually ensures prevalence of pore saturation conditions.

10. Commensurate-incommensurate adsorption/diffusion in cage-type zeolites

Let us examine the adsorption of n-alkanes in CHA zeolite, which is a cage type zeolite that consists of cages of volume 316 \AA^3 , separated by $3.8 \text{ \AA} \times 4.2 \text{ \AA}$ 8-ring windows. The pore landscapes and structural details are provided in Figures 23, and 24.

We first investigate the potential of CHA for separation of n-alkanes by performing CBMC simulations of the pure component isotherms for n-alkanes, carried out to bulk fluid phase fugacities high enough to ensure that saturation of the cages is realized; see Figure 54a.

The saturation capacity of methane is 6 molecules per cage. For ethane, the saturation capacity remains 4 cage⁻¹ up to a fugacity of 10¹² Pa, and increases to 5/cage on further increase of fugacity to 10¹⁵ Pa. For propane, the saturation capacity remains 2/cage up to a fugacity of 10¹² Pa, and increases to 4 cage⁻¹ on further increase of fugacity to 10¹⁵ Pa. For nC4, and nC5, the saturation capacities are 2 cage⁻¹. For nC6, nC7, and nC8, the saturation capacities are 1 cage⁻¹. These saturation capacities, determined from CBMC simulations, are in good agreement with the experimental data of Daems et al.²⁷; see Figure 54b. A perfect agreement is not to be expected because in the experimental work of Daems et al.²⁷, the CHA that they used had a Si/Al ratio of 2.59. The presence of cations within the zeolite will have a quantitative influence on the adsorption characteristics, but will not alter the separation principle to be developed below.

Figure 55 presents snapshots of the location, and conformation, of the n-alkanes within the cages of CHA at saturation conditions. We note that in all cases there appears to be no n-alkane molecules at the window between two cages and, therefore, the cage capacity at saturation must be an integral number.

Another point to note is that due to limitations of cage capacity, linear alkanes with C numbers larger than 8 must straddle two cages, resulting in a saturation capacity less than 1 molecule cage⁻¹. As illustration, Figures 56a,b compare the conformations of nC8 and nC12 alkanes in CHA. Normal octane adsorbs commensurately; one molecule can comfortably nestle inside a cage. The longer alkane nC12 alkane cannot fit into one cage and straddles two cages.

Consider adsorption of a fluid mixture of C1 and C2 in CHA. The saturation capacities are 6 and 5 molecules per cage, respectively. CBMC simulations on the component loadings in equilibrium with an equimolar C1/C2 mixture are shown in Figure 57a for varying bulk fluid phase fugacities, $f_t = f_1 + f_2$. At $f_t < 10^8$ Pa, the selectivity is in favor of the component with the longer chain length, C2. However, for $f_t > 10^8$ Pa selectivity reversal occurs and the smaller chain length, i.e. C1, is preferentially adsorbed due to its higher packing efficiency. An analogous selectivity reversal is found for a mixture of C2 and C3; see Figure 57b.

For mixtures with longer chain lengths, the selectivity reversal occurs at pressures that are relatively easier to achieve in practice. CBMC simulations for the component loadings in equilibrium with equimolar C3/nC6, nC4/nC6, and nC5/nC6 fluid mixtures and CHA are shown in Figures 57c,d,e. For these mixtures, for operation at fugacities $f_t < 10^6$ Pa corresponding to bulk *vapor* phase, the adsorption is selective to the component with the longer chain length, i.e. nC6. However, for operation at fugacities $f_t > 10^6$ Pa, corresponding to bulk *liquid* phase, the adsorption in CHA favors the component with the smaller chain length. If the fugacities are sufficiently high, say $f_t > 10^8$ Pa the nC6 is virtually excluded from the zeolite. This exclusion is almost complete for C3/nC6 and nC4/nC6 mixtures.

The dashed lines in Figure 57 are the predictions of the Ideal Adsorbed Solution Theory (IAST) of Myers and Prausnitz¹⁹ using pure component isotherm fits as input data. The IAST calculations have been presented here to demonstrate that selectivity reversal is not an unexpected phenomenon, but is a natural result that is obtained for a mixture of two species having (1) lower adsorption strength, but higher saturation capacity, and (2) higher adsorption strength, but lower saturation capacity. When saturation conditions are approached the component with the higher saturation capacity is invariably preferred. This is due to the fact that

vacant “sites” are more easily filled by the smaller molecule at near-saturation conditions. The selectivity reversals observed for C1/C2, and C2/C3 mixtures in CHA are however difficult to exploit because the fugacities required are prohibitively high, i.e. $f_i > 10^8$ Pa.

To demonstrate that the selectivity reversals for mixture adsorption as witnessed in the five sets of mixture adsorption simulations presented in Figure 57 are engendered by entropy considerations, we use the model of Azizian and Bashiri²⁵ for a 2D lattice consisting of cages to model mixture adsorption. As an example, we consider C3/nC6 mixture adsorption, each cage consisting of 2 adsorption sites; we take $M = 2$. Since the saturation capacity of C3 (species k) is 2 molecules cage⁻¹ (this value corresponds to the capacity at a total fluid fugacity of 10^{12} Pa) we take $k=1$. Since the saturation capacity of nC6 (species l) is 1 molecule cage⁻¹, we take we take $l=2$. The component loading of C3, in molecules per cage, is given by $N_k = \theta_k \frac{M}{k}$. The component loading of nC6, in molecules per cage, is given by $N_l = \theta_l \frac{M}{l}$.

For a quantitative analysis of mixture adsorption, we need to first determine the binding constants, using equations (31) and the CBMC simulations of the unary isotherms. A reasonably good match between equations (31) and the CBMC simulations of the unary isotherms is obtained with the choice $b_k = 2 \times 10^{-4}$ Pa⁻¹, and $b_l = 1 \times 10^{-1}$ Pa⁻¹; see Figure 58a.

With the fitted binding constants, the component loadings for mixture adsorption can be calculated using equations (30); the results are shown by the continuous solid lines in Figure 58b. The lattice model is able to quantitatively capture the phenomenon of nC6 exclusion from CHA zeolite as the cages become increasingly occupied.

The lattice model is also in good agreement with the IAST calculations (shown by the dashed lines in Figure 58b) for mixture adsorption equilibrium.

This reversal of selectivity is entropy-based and is ascribable to the significantly higher saturation capacity of C3 (2 molecules cage⁻¹) in comparison to that of nC6 (1 molecule cage⁻¹).

Figure 59a presents calculations of the dimensionless entropy per site $\frac{S}{k_B M}$, using equation (29), for a binary mixture of C3 ($k=1$), and nC6 ($l=2$) on a 2D lattice as a function of the proportion of C3 in the adsorbed phase, $x_k = \frac{N_k}{N_k + N_l}$, for three different values of total occupancies, $\frac{N_k + N_l}{M} = 0.1, 0.5, \text{ and } 0.6$. At the lowest occupancy, $\frac{N_k + N_l}{M} = 0.1$, the maximum in the $\frac{S}{k_B M}$ occurs at the adsorbed composition $x_k = \frac{N_k}{N_k + N_l} \approx 0.5$. With increasing occupancies, $\frac{N_k + N_l}{M}$, the maximum in the $\frac{S}{k_B M}$ occurs at values the adsorbed composition $x_k = \frac{N_k}{N_k + N_l}$, that are significantly richer in C3, the component with the higher saturation capacity. This is because the vacancies within cage are more efficiently filled up by the smaller propane molecules. The precise composition of the adsorbed phase, corresponding to the maximum entropy can be determined by setting $\frac{\partial}{\partial N_k} \left(\frac{S}{k_B M} \right) = 0$.

The continuous solid black line Figure 59b presents a plot of the values of $x_k = \frac{N_k}{N_k + N_l}$ corresponding to the maximum entropy as a function of the occupancy, $\frac{N_k + N_l}{M}$. The corresponding calculations for the minimum in the Helmholtz free energy of adsorption $F = U - TS$, is shown by the continuous solid blue line. The entropic contribution to the Helmholtz free energy is able to override the internal energy contribution only at fractional occupancies

$\frac{N_k+N_l}{M}$ higher than about 0.7. As the total occupancy approaches unity, i.e. at pore saturation, the adsorbed mixture consists predominantly of C3; nC6 is practically excluded at high occupancies.

11. Entropic separations of mixtures of linear alcohols using CHA zeolite

Let us examine the adsorption of 1-alcohols in CHA, which is a cage type zeolite that consists of cages of volume 316 \AA^3 , separated by $3.8 \text{ \AA} \times 4.2 \text{ \AA}$ 8-ring windows. The pore landscapes and structural details are provided in Figures 23, and 24. SAPO-34 has the same structural topology of CHA zeolite. Figure 60a presents snapshots of the conformations of the 1-alcohols within the cages, at saturation conditions. CBMC simulations of unary 1-alcohols with C atoms in the 1 – 6 range in CHA at 300 K, as reported in the work of Krishna and van Baten,¹² are shown in Figure 60b. The saturation capacities, $\Theta_{i,\text{sat}}$, decreases from 5.4 molecules cage⁻¹ for methanol to 1 molecule cage⁻¹ for 1-hexanol; see data in Figure 60c. Except for methanol, the saturation cage capacity has an integer value because 1-alcohol molecules cannot locate at the window regions. For 1-butanol, the cage capacity is restricted to 2 molecules cage⁻¹; for 1-hexanol, the cage capacity is 1 molecule cage⁻¹. This difference in the cage capacities can be exploited to separate binary 1-butanol/1-hexanol mixtures. CBMC simulations for 1-butanol/1-hexanol mixtures are shown in Figure 60d. For total fluid phase fugacities, $f_t < 500 \text{ Pa}$, the adsorption selectivity is strongly in favor of the longer 1-hexanol molecule. However, when the total fluid phase fugacities, f_t exceed 1 kPa, we find a reversal of selectivity.

To elucidate the reasons behind the exclusion of 1-hexanol at fugacities $f_t > 1 \text{ kPa}$, we use the model of Azizian and Bashiri²⁵ for a 2D lattice consisting of cages, with each cage containing 2 sites; $M = 2$. Since the saturation capacity of 1-butanol (species k) is 2 molecules cage⁻¹, we take

$k=1$. Since the saturation capacity of 1-hexanol (species l) is 1 molecule cage⁻¹, we take $l=2$. The component loading of 1-butanol, in molecules per cage, is given by $N_k = \theta_k \frac{M}{k}$. The component loading of 1-hexanol, in molecules per cage, is given by $N_l = \theta_l \frac{M}{l}$.

For a quantitative analysis of mixture adsorption, we need to first determine the binding constants, using equations (31) and the CBMC simulations of the unary isotherms. A reasonably good match between equations (31) and the CBMC simulations of the unary isotherms is obtained with the choice $b_k = 4 \times 10^{-1} \text{ Pa}^{-1}$, and $b_l = 20 \text{ Pa}^{-1}$; see Figure 61a.

With the fitted binding constants, the component loadings for mixture adsorption can be calculated using equations (30); the results are shown by the continuous solid lines in Figure 61b. The lattice model is able to quantitatively capture the phenomenon of 1-hexanol exclusion from CHA zeolite as the cages become increasingly occupied.

The lattice model is in good agreement with the IAST calculations (shown by the dashed lines in Figure 61b) for mixture adsorption equilibrium.

This reversal of selectivity is entropy-based and is ascribable to the significantly higher saturation capacity of 1-butanol (2 molecules cage⁻¹) in comparison to that of 1-hexanol (1 molecule cage⁻¹).

Figure 62a presents calculations of the dimensionless entropy per site $\frac{S}{k_B M}$, using equation (29), for a binary mixture of 1-butanol ($k=1$), and 1-hexanol ($l=2$) on a 2D lattice as a function of the proportion of 1-butanol in the adsorbed phase, $x_k = \frac{N_k}{N_k + N_l}$, for three different values of total occupancies, $\frac{N_k + N_l}{M} = 0.1, 0.5, \text{ and } 0.6$. At the lowest occupancy, $\frac{N_k + N_l}{M} = 0.1$, the

maximum in the $\frac{S}{k_B M}$ occurs at the adsorbed composition $x_k = \frac{N_k}{N_k + N_l} \approx 0.5$. With increasing

occupancies, $\frac{N_k + N_l}{M}$, the maximum in the $\frac{S}{k_B M}$ occurs at values the adsorbed composition

$x_k = \frac{N_k}{N_k + N_l}$, that are significantly richer in 1-butanol, the component with the higher saturation

capacity. This is because the vacancies within cage are more efficiently filled up by the smaller 1-alcohol. The precise composition of the adsorbed phase, corresponding to the maximum

entropy can be determined by setting $\frac{\partial}{\partial N_k} \left(\frac{S}{k_B M} \right) = 0$.

The continuous solid black line Figure 62b presents a plot of the values of $x_k = \frac{N_k}{N_k + N_l}$ corresponding to the maximum entropy as a function of the occupancy, $\frac{N_k + N_l}{M}$. The

corresponding calculations for the minimum in the Helmholtz free energy of adsorption $F = U - TS$, is shown by the continuous solid blue line. The entropic contribution to the Helmholtz free energy is able to override the internal energy contribution only at fractional occupancies $\frac{N_k + N_l}{M}$ higher than about 0.7. As the total occupancy approaches unity, i.e. at pore saturation,

the adsorbed mixture consists predominantly of C3; nC6 is practically excluded at high occupancies.

Experimental confirmation of the selectivity reversal is observed in the experiments reported by Remy et al.²⁸ for transient breakthroughs of ethanol/1-hexanol mixtures in a fixed bed adsorber packed with SAPO-34, that has the same structural topology as CHA. The component that is eluted first from the adsorber is the alcohol with the longer chain length. The

rationalization of these experimental data can be traced to the entropy effects that favor the shorter alcohols under pore saturation conditions.

12. Entropic separations of mixtures of linear molecules using cage-type zeolites

The principle of separation mixtures on the basis of the differences in the saturation cage capacities applies also to the separation of both linear alkanes in other cage type structures such as DDR (cages of 277.8 \AA^3 volume, separated by $3.65 \text{ \AA} \times 4.37 \text{ \AA}$ 8-ring windows; the pore landscapes and structural details are provided in Figures 25, and 26), ERI (cages of 408.7 \AA^3 volume, separated by $3.8 \text{ \AA} \times 4.9 \text{ \AA}$ 8-ring windows; the pore landscapes and structural details are provided in Figures 27, and 28), AFX (cages of 490 \AA^3 volume, separated by $3.4 \text{ \AA} \times 3.9 \text{ \AA}$ 8-ring windows; the cages are also connected to pockets of 98 \AA^3), LTA, LTA-5A, LTA-4A (cages of 743 \AA^3 volume, separated by $4.11 \text{ \AA} \times 4.47 \text{ \AA}$ 8-ring windows; the pore landscapes and structural details are provided in Figures 29, 30, 31, and 32), and ZIF-8 (cages of 1168 \AA^3 volume, separated by 3.3 \AA windows; the pore landscapes and structural details are provided in Figures 36, 37); further details are provided by Krishna and van Baten.¹¹⁻¹³ The driver for entropic separations of mixtures of linear chain molecules is the difference in the saturation capacities. For binary mixture adsorption, the shorter linear alkane, or alcohol, adsorption will be favored only if there is a difference in saturation capacities; the larger the difference in the values of $\Theta_{i,\text{sat}}$, the more effective the separation.

Figure 63a compares the saturation capacities for linear alkanes and linear alcohols in all-silica zeolites CHA, ERI, AFX, and LTA. For each host structure, we note that for the range of C numbers, the saturation loading, $\Theta_{i,\text{sat}}$, decreases in a step-wise manner with increasing chain length.

Figure 63b shows snapshots of propane (C3) and n-hexane (nC6) at saturation conditions in ERI zeolite. The saturation capacities are 3, and 2 molecules cage⁻¹, respectively. The CBMC simulations for adsorption of equimolar C3/nC6 mixtures shows selectivity reversal in favor of the shorter alkane for partial fugacities exceeding 1 MPa, corresponding to adsorption for mixtures in the liquid phase (Figure 63c).

For separation of chain molecules with C numbers higher than say 20, as is required in the petroleum industry in lube oil processing, we need structures with sufficiently large cages. Of particular importance in this context is all-silica TSC zeolite, with a Tschörtnerite framework, that has the largest cage volume of any known zeolite;¹⁷ the pore landscape and structural details are provided in Figures 33, 34, and 35. Each unit cell of TSC has four “LTA type cages” of 743 Å³, and four “TSC supercages” of 2553 Å³; the cages are separated by two types of windows: 4.02 Å × 4.17 Å, and 3.1 Å × 5.41 Å.

As demonstration of the potential use of TSC, Figure 64a compares the unary adsorption isotherms of nC21 and nC24 alkanes; the saturation capacities are $\Theta_{i,\text{sat}} = 16$, and 8 molecules uc⁻¹, respectively. CBMC simulations for nC21/nC24 mixture adsorption in TSC, shows that the shorter alkane is preferentially adsorbed under pore saturation conditions; see Figure 64b.

13. Commensurate adsorption-diffusion in MFI zeolite

MFI zeolite (also called silicalite-1) has a topology consisting of a set of intersecting straight channels, and zig-zag (or sinusoidal) channels of approximately 5.5 Å size. The pore landscapes and structural details are provided in Figures 38, and 39. The length of an n-hexane molecule is commensurate with the distance between intersections of MFI zeolite (cf. snapshot in Figure 65a). The n-heptane molecule, on the other hand, has a length that is slightly longer than the distance between channel intersections (see Figure 65b). The subtle differences in molecular

lengths of nC6 (commensurate) and nC7 (incommensurate) have a profound influence on the adsorption and diffusion characteristics. Figure 65c show CBMC simulations of the unary adsorption isotherms of C1, C2, C3, nC4, nC5, nC6, and nC7 alkanes at 300 K. Due to commensurate adsorption of nC6, the saturation capacity of nC6, $\Theta_{i,\text{sat}}$, is precisely equal to 8 molecules uc^{-1} . The incommensurate adsorption of nC7 restricts the saturation capacity to $\Theta_{i,\text{sat}} \approx 7$ molecules uc^{-1} ; for bulk fluid phase fugacities exceeding 1 Pa, the loading of nC6 exceeds that of nC7, because of the more efficient packing of nC6 within the channels.

Figure 66a presents MD simulations for the Maxwell-Stefan diffusivities, D_i , of linear alkanes as a function of loading, Θ_i . The values of the M-S diffusivities at zero-loading, $D_i(0)$, for the series on n-alkanes are plotted in Figure 66b as a function of the C number. There is a minimum at a C number of 6, because of commensurate adsorption of nC6. The experimental data of Talu et al.²⁹ provides confirmation of this minimum in the diffusivity of nC6; see Figure 66c.

14. Separating hexane isomers using MFI zeolite

Separations of hexane isomers with MFI are based on the exploitation of the differences in molecular configurations. Linear molecules such as n-hexane (nC6) can locate anywhere along the channels, as illustrated in the computational snapshots in Figure 67. The length of nC6 is commensurate with the distance between adjoining intersections;³⁰ consequently, nC6 can be packed very efficiently within the channel network with a saturation loading $\Theta_{i,\text{sat}} = 8$ molecules per unit cell. Branched molecules such as iso-butane (iC4), 2-methylpentane (2MP), 3-methylpentane (3MP), 2,2 dimethylbutane (22DMB), and 2,3 dimethylbutane (23DMB) are bulkier; these locate preferentially at the intersections that afford extra “leg room”. The availability of intersection sites is limited to a total of 4 per unit cell of MFI. Indeed, the saturation capacities of 22DMB and 23DMB correspond to $\Theta_{i,\text{sat}} = 4$ molecules per unit cell,

significantly lower than that of the linear isomer nC6. Figure 68 compares CBMC simulations of pure component isotherms for 2MP with the experimental data; the strong inflection in the 2MP isotherm is a direct evidence of configurational differences. Loadings in excess of 4/uc of 2MP can only be achieved with an “extra push”, i.e. with vastly increased pressures.

The differences in the packing efficiencies of linear and branched isomers, often referred to as configuration entropy effects,³⁰⁻³² can be usefully exploited for separation of the hexane isomers to obtain different products with different degrees of branching.^{4, 32-34}

To illustrate this separation principle, let us consider CBMC simulations of component loadings in the adsorbed phase in equilibrium with equimolar binary gas phase containing a mixture of nC6 and 2MP with equal partial fugacities $f_1 = f_2$ in the bulk fluid phase; see Figure 69a. Up to total hydrocarbons fugacities $f_t = f_1 + f_2 = 2$ Pa, the component loadings Θ_i of each component increases in an expected manner; increasing f_t leads to a corresponding increase in the component loading Θ_i . At $f_t = 2$ Pa, the total loading $\Theta_t = 4/uc$, signifying that all the intersection sites are fully occupied. To further adsorb 2MP we need to provide an extra “push”. Energetically, it is more efficient to obtain higher mixture loadings by “replacing” the 2MP with nC6; this *configurational entropy* effect is the reason behind the curious maxima in the 2MP loading in the mixture. The experimentally determined loadings from IRM³⁵ are also plotted in Figure 69a. There is good agreement of the IRM data and the CBMC mixture simulations. The IRM experiments offer direct experimental verification of the configurational entropy effects in mixture adsorption for nC6/2MP that was first observed on the basis of CBMC mixture simulations.^{30, 31}

Figure 69a also shows the IAST calculations (continuous solid lines) with CBMC simulations of component loadings of binary nC6/2MP mixtures. The IAST estimations of the component

loadings are of good accuracy. The influence of configurational entropy effects on separations is best quantified by the *adsorption selectivity* S_{ads} , defined by

$$S_{ads} = \frac{\Theta_1/\Theta_2}{f_1/f_2} \quad (35)$$

For equimolar binary fluid phase mixtures, Equation (35) simplifies to yield

$$S_{ads} = \frac{\Theta_1}{\Theta_2} \quad (\text{for equimolar gas mixture with } f_1 = f_2) \quad (36)$$

The calculations of S_{ads} are shown in Figure 69b. We note that for total loadings $\Theta_t < 4/uc$, $S_{ads} \approx 1$, suggesting that adsorptive separations of nC6/2MP are not feasible for fugacities $f_t = f_1 + f_2 < 2$ Pa. However, when the total loadings of the adsorbed phase Θ_t exceeds $4/uc$, the values of S_{ads} increase significantly to values by 10 - 100. This implies that sharp separations of the linear and branched hexanes are possible provided the operating conditions correspond to total mixture loadings $\Theta_t > 4/uc$.

To elucidate the reasons behind 2MP exclusion at fugacities $f_t > 2$ Pa, we use the model of Azizian and Bashiri²⁵ for a 2D lattice 8 sites; $M = 8$. Since the saturation capacity of nC6 (species k) is 8 molecules uc^{-1} , we take $k=1$. Since the saturation capacity of 2NP (species l) is 4 molecules uc^{-1} , we take $l=2$. The component loading of nC6, in molecules per uc , is given by

$$N_k = \theta_k \frac{M}{k}. \quad \text{The component loading of 2MP, in molecules per } uc, \text{ is given by } N_l = \theta_l \frac{M}{l}.$$

For a quantitative analysis of mixture adsorption, we need to first determine the binding constants, using equations (31) and the CBMC simulations of the unary isotherms. A reasonably good match between equations (31) and the CBMC simulations of the unary isotherms is obtained with the choice $b_k = 1.5 \text{ Pa}^{-1}$, and $b_l = 3 \text{ Pa}^{-1}$; see Figure 70a.

With the fitted binding constants, the component loadings for mixture adsorption can be calculated using equations (30); the results are shown by the continuous solid lines in Figure 70b. The lattice model is able to quantitatively capture the phenomenon of 2MP exclusion from MFI zeolite as the channels become increasingly occupied.

This reversal of selectivity is entropy-based and is ascribable to the significantly higher saturation capacity of bC6 (8 molecules uc⁻¹) in comparison to that of 2MP (4 molecules uc⁻¹).

Figure 71a presents calculations of the dimensionless entropy per site $\frac{S}{k_B M}$, using equation (29), for a binary mixture of nC6 ($k=1$), and 2MP ($l=2$) on a 2D lattice as a function of the proportion of nC6 in the adsorbed phase, $x_k = \frac{N_k}{N_k + N_l}$, for three different values of total

occupancies, $\frac{N_k + N_l}{M} = 0.2, 0.4, \text{ and } 0.7$. At the lowest occupancy, $\frac{N_k + N_l}{M} = 0.1$, the maximum

in the $\frac{S}{k_B M}$ occurs at the adsorbed composition $x_k = \frac{N_k}{N_k + N_l} \approx 0.5$. With increasing

occupancies, $\frac{N_k + N_l}{M}$, the maximum in the $\frac{S}{k_B M}$ occurs at values the adsorbed composition

$x_k = \frac{N_k}{N_k + N_l}$, that are significantly richer in nC6, the component with the higher saturation

capacity. This is because the vacancies within cage are more efficiently filled up by nC6. The precise composition of the adsorbed phase, corresponding to the maximum entropy can be

determined by setting $\frac{\partial}{\partial N_k} \left(\frac{S}{k_B M} \right) = 0$.

The continuous solid black line Figure 71b presents a plot of the values of $x_k = \frac{N_k}{N_k + N_l}$ corresponding to the maximum entropy as a function of the occupancy, $\frac{N_k + N_l}{M}$. The corresponding calculations for the minimum in the Helmholtz free energy of adsorption $F = U - TS$, is shown by the continuous solid blue line. The entropic contribution to the Helmholtz free energy is able to override the internal energy contribution at fractional occupancies $\frac{N_k + N_l}{M}$ higher than about 0.5. As the total occupancy approaches unity, i.e. at pore saturation, the adsorbed mixture consists predominantly of nC6.

15. Entropy effects for n-alkane separations in ISV zeolite

Entropy effects also manifest for mixtures of linear alkanes in ISV zeolite that has intersecting channels of ISV zeolite; see the pore landscapes and structural details in Figures 40, 41. Figure 72 shows snapshots showing the location of CH₄ and C₂H₆ within the intersecting channels of ISV zeolites. The CBMC simulations of the unary isotherms of CH₄ and C₂H₆ in ISV zeolite at 300 K are well described by the 3-site Langmuir-Freundlich model fits of unary isotherms; see Figure 72a. The CBMC simulations of component loadings in the adsorbed phase in equilibrium with binary CH₄/C₂H₆ mixtures with partial fugacities $f_1 = f_2$ in the bulk gas phase at 300 K are shown by the symbols in Figure 72b. The selectivity reversal is experienced at a total hydrocarbons fugacity $f_t = f_1 + f_2 > 10^{11}$ Pa; this selectivity reversal is the consequence of entropy effects that favor methane and is quantitatively predicted by the IAST, shown by the continuous solid lines in Figure 72b.

16. The “window” effect and “resonant” diffusion

The Quasi-Elastic Neutron Scattering (QENS) data of Jobic et al.³⁶ for diffusivity in LTA-5A with increasing n-alkane chain length displays a minimum value for nC8; see Figure 73a. The non-monotonicity in the variation of the diffusivity with chain length has been termed the “window” effect.³⁷ Snapshots of the conformations of nC8 and nC13 molecules within the cages of LTA-5A provide a rationale for the non-monotonicity. Normal octane can nestle comfortably within a single cage, whereas nC13 is too long, i.e. incommensurate with the window-to-window distance, and straddles two adjacent cages. An incommensurate scenario leads to a higher diffusivity because the molecule does not feel “too comfortable” and has a tendency to hop with increased frequency from cage to cage.

The experimental data of Yoo et al.³⁸ for diffusivity of n-alkanes in MTW zeolite (with 1D 12-ring channels of size 5.6 Å × 6.8 Å; the pore landscapes and structural details are provided in Figures 7, 8) show a periodicity in the diffusivity vs chain length characteristics. The characteristics for the C number range 1-6 appear to be repeated for the range of 7-12; see Figure 74. This periodicity has been termed “resonant diffusion”.³⁸⁻⁴⁰ To rationalize their experimental observations, computational snapshots of the conformations of n-alkanes are also shown in Figure 74. Normal hexane, with the pivotal C number, appears to align commensurately with one channel segment.

The experimental data of Yoo et al.³⁸ for diffusivity of n-alkanes in LTL zeolite (with 1D 12-ring 7.1 Å channels; the pore landscapes and structural details are provided in Figures 5, 6) also show an analogous periodicity (see Figure 75). For LTL zeolite, the n-alkanes can configure themselves circumferentially within the “grooves” of the 1D channels. The “head-on” snapshots

show that n-hexane can align commensurately with *one-quarter* of the circumference; this offers a qualitative rationalization of the experimental observations of resonant diffusion.

17. Separations xylene isomers by commensurate adsorption

Aromatic hydrocarbons, that are valuable feedstocks in the petrochemical industries, are most commonly obtained from catalytic reforming of naphtha. The xylene isomers, o-xylene, m-xylene and in particular p-xylene, are important chemical intermediates. Ortho-xylene is oxidized to make phthalic anhydride which is used to make phthalate plasticizers among other things. Meta-xylene is oxidized to produce isophthalic acid, which is used in unsaturated polyester resin. However, p-xylene has the largest market of the three isomers; the demand for p-xylene is several times that of m-xylene and o-xylene. The largest use of p-xylene is in its oxidation to make terephthalic acid, that is used in turn to make polymers such as polyethylene terephthalate (PET) and polybutylene terephthalate (PBT). PET is one of the largest volume polymers in the world, and is used to produce fibers, resins, films, and blown beverage bottles.

A common feature of all the aromatics separation is that the operation conditions are such that the pores are nearly saturated with guest molecules. Therefore, molecular packing and entropy effects are of primary importance in the separations. Aromatic molecules that pack, or stack, most efficiently within the zeolite or MOF channels are the ones that are selectively adsorbed. For any adsorbent material, the packing efficiencies of any aromatic molecule are dictated by a combination of two factors: (a) molecular dimensions, and (b) departures from planarity.

The height and width of the C₈ aromatics are: o-xylene: 8 Å × 7.4 Å; m-xylene: 8.9 Å × 7.4 Å; p-xylene: 9.3 Å × 6.7 Å; ethylbenzene: 9.5 Å × 6.7 Å; styrene: 9.3 Å × 6.7 Å; see dimensions provided in Figure 76. A further point to note is that xylene isomers are flat; these isomers can align themselves parallel to the channel walls, affording better van der Waals interactions with

the framework atoms. By contrast, ethylbenzene is not a flat molecule; the ethyl branch is not in the same plane as the benzene ring.

Due to the differences in the molecular dimensions of the xylene isomers, the efficiencies with which the xylene isomers stack within the channels of different dimensions are different. We can deliberately choose an adsorbent material with a specified channel dimension in order to allow the optimum stacking of one or other of the xylene isomers. Stacking xylenes within 1D channels of MOFs is analogous to stacking books within bookshelves.^{4,41}

The computational snapshots⁴¹ in Figure 77, obtained from CBMC simulations, clearly show the optimal, commensurate, stacking of o-xylene within 8.5 Å channels of MIL-47. Experimental data⁴²⁻⁴⁴ for MIL-47 and MIL-53 with 1D rhombohedral channels of 8.5 Å confirm that these MOFs are selective to adsorption of o-xylene when operating at conditions close to pore saturation.

Co(BDP), that has 10 Å square-shaped 1D channels of Co(BDP), also allows p-xylene to stack vertically (cf. Figure 78), resulting in selectivity in favor of p-xylene.⁴¹ Within the one-dimensional 10 Å channels of MAF-X8, we have commensurate stacking of p-xylene; see snapshots in Figure 79;⁴¹ commensurate stacking within 1D channels of MAF-X8, results in strong selectivity in the favor of the p-xylene as saturation conditions are approached. In the study of Torres-Knoop et al.,⁴¹ MAF-X8 emerged as the best MOF for separation of 4-component o-xylene/m-xylene/p-xylene/ethylbenzene mixtures.

18. Commensurate face-to-face stacking of aromatic molecules

Let us examine the experimental data reported by Chiang et al.⁴⁵ on the unary isotherms of o-, m-, and p-xylenes in aluminophosphate AlPO₄-5 (with AFI zeolite topology); the pore landscapes and structural details are provided in Figures 3, and 4.

The hierarchy of saturation capacities is o-xylene > p-xylene = m-xylene. On the basis of molecular dimensions of the isomers, Chiang et al.⁴⁵ have argued that the differences in the saturation capacities reflect differences in packing arrangements within the 1D channels of AlPO₄-5. For m-xylene, and p-xylene, either the “height” or “width” is too large to allow vertical alignment; the orientation of these isomers occurs at an inclination. By contrast, the molecular dimensions of o-xylene allow the molecules to be stacked vertically, face-to-face, that is akin to the packing of potato crisps in cylindrical tubes as marketed by Pringles. An important consequence of the differences in the orientation of isomers is that the “footprints” of o-xylene molecules is significantly shorter than the footprints of m-xylene, and p-xylene molecules. Shorter footprints result in higher saturation capacities, as evidenced in the isotherm data in Figure 80a. Using configurational-bias Monte Carlo (CBMC) simulations, Torres-Knoop et al.⁴⁶ have produced computational snapshots (see Figure 80b), confirming that o-xylene is able to stack vertically within the 8.4 Å “grooves” of AFI zeolite. Put another way, o-xylene “packs” more efficiently than its isomers. The commensurate stacking of o-xylene also gets reflected in the fact that the isosteric heat of adsorption of o-xylene is higher than that of m-xylene, and p-xylene; see Figure 80c.

Differences in packing efficiencies can be exploited to adsorb the ortho isomer preferentially from a mixture of xylenes. IAST calculations for adsorption equilibrium for 3-component o-xylene(1)/m-xylene(2)/p-xylene(3) mixtures at 303 K are shown in Figure 81. We note that AlPO₄-5 becomes strongly o-xylene selective as pore saturation is approached. The preferential adsorption of the o-xylene is attributable to entropy effects that favor the isomer with the smaller footprint.

Torres-Knoop et al.^{46, 47} have also provided other examples in which optimum face-to-face stacking of aromatic molecules can lead to uncommonly effective separations. Within triangular channels of a structure such as $\text{Fe}_2(\text{BDP})_3$, but with larger channel dimensions, 1,3,5 tri-chlorobenzene (TCB) can be selectively separated from the 1,2,3 and 1,2,4 TCB isomers; the preferential adsorption of the 1,3,5 isomer is due to optimum face-to-face stacking; see computational snapshots in Figure 82. Figure 83a shows CBMC simulations for unary isotherms of 1,2,3 tri-chlorobenzene (TCB), 1,2,4 TCB, and 1,3,5 TCB in modified $\text{Fe}_2(\text{BDP})_3$ at 433 K. Due to optimal face-to-face stacking, the 1,3,5 isomer has the highest saturation capacity. For adsorption of ternary mixtures of the three isomers under saturation conditions, the adsorbed phase is practically devoid of the 1,2,3 and 1,2,4 isomers due to entropy effects that favor the component with the smallest footprint; see Figure 83b.

Torres-Knoop et al.^{46, 47} have suggested the possibility of deliberately choosing the channel geometry to cater for optimum face-to-face stacking of a specific guest aromatic molecules; see cartoons (not molecular simulations) in Figure 84: (a) cylindrical or (b) hexagonal shaped channels for adsorption of benzene, (c) triangular channels for adsorption of 1,3,5 TCB, (d) elliptical or (e) lozenge shaped channel for adsorption of p-xylene, and (f) cuboid boxes for stacking of benzene.

19. Separating hexane isomers by exploiting differences in molecular footprints in 1D channels of MOR zeolite

The selective adsorption of components with the smallest “footprint” within 1D channels can be effectively exploited for separation of alkane isomers. Below, we discuss three different zeolites, MOR, AFI, and TON that can be utilized for this purpose.

MOR zeolite (Mordenite) consists of 12-ring ($7.0 \text{ \AA} \times 6.5 \text{ \AA}$) 1D channels, connected to 8-ring ($5.7 \text{ \AA} \times 2.6 \text{ \AA}$) pockets; the pore landscapes and structural details are provided in Figures 19, and 20.

Some representative snapshots⁴⁸ showing the siting and conformation of hexane isomers along one of the 12-ring channels, 8 unit cells long, are presented in Figure 85 for a total bulk fluid phase fugacity $f_t = 1 \text{ MPa}$. Within the same channel length we find five nC6 molecules, seven 2MP molecules and nine 22DMB molecules. The higher loading with increased degree of branching is due to increased degree of compactness of the molecules, i.e. smaller footprint. The more compact the molecule, the higher the packing efficiency within the one-dimensional channels. This point is emphasized further by determining the projected lengths of the molecules of the hexane isomers on the z -axis for $f_t = 1 \text{ MPa}$; the data on the distribution of molecular lengths are shown in Figure 86a. The projected lengths are obtained by monitoring the positions of each of the pseudo-atoms in the alkane molecules and determining the maximum span of the molecule by projecting the positions of the pseudo-atoms along the direction of the 12-ring channels. The mean lengths of the hexane isomers are 5.2 \AA , 4.3 \AA and 3 \AA for nC6, 2MP and 22DMB respectively. This data also explains why the saturation capacity for 22DMB is significantly higher ($\Theta_{\text{sat}} = 2 \text{ molecules uc}^{-1}$), compared to that for 2MP ($\Theta_{\text{sat}} = 1.7 \text{ molecules uc}^{-1}$) and nC6 ($\Theta_{\text{sat}} = 1.5 \text{ molecules uc}^{-1}$); see Figure 86b.

CBMC simulations for nC6/22DMB mixture adsorption shows that for total fugacities, $f_t = f_1 + f_2 > 100 \text{ kPa}$, the selectivity is heavily in favor of the di-branched isomer and the linear isomer is virtually excluded from the 1D channels of MOR; see Figure 86c.

To elucidate the reasons for the selectivity reversal at bulk fluid fugacities $f_t > 50 \text{ kPa}$, we use the model of Dávila et al.²³ for a 1D lattice. The ratio of the “effective lengths” of nC6 (species

k) and 22DMB (species l) is taken to be inversely proportional to the saturation capacities, i.e. 2:1.5. We take $k=1.333$, and $l=1$. To determine the component loadings in the units of molecules per unit cell, we take $M = 2$. The component loading of nC6, in molecules per unit cell, is given by $N_k = \theta_k \frac{M}{k}$. The component loading of 22DMB, in molecules per unit cell, is given by

$$N_l = \theta_l \frac{M}{l}.$$

For a quantitative analysis of mixture adsorption, we need to first determine the binding constants, using equations (26) and the unary isotherm data. A good match between equations (26) and the CBMC simulations of the unary isotherms is obtained with the choice $b_k = 4 \times 10^{-4} \text{ Pa}^{-1}$, and $b_l = 3 \times 10^{-4} \text{ Pa}^{-1}$; Figure 87a.

With the fitted binding constants, the component loadings for mixture adsorption can be calculated using equations (25); the results are shown by the continuous solid lines in Figure 87b. The lattice model is able to quantitatively capture the phenomenon of nC6 exclusion from MOR zeolite due to entropy effects.

The lattice model is in good agreement with the IAST calculations (shown by the dashed lines in Figure 87b) for mixture adsorption equilibrium, using Langmuir fits of the unary isotherms of nC6 and 22DMB. For 22DMB, the Langmuir binding constant is the same as for the lattice model, i.e. $b_{22\text{DMB}} = 3 \times 10^{-4} \text{ Pa}^{-1}$; $\Theta_{\text{C3,sat}} = 2 \text{ uc}^{-1}$. For nC6, the Langmuir binding constant, $b_{\text{nC6}} = 45 \times 10^{-4} \text{ Pa}^{-1}$, $\Theta_{\text{nC6,sat}} = 1.5 \text{ uc}^{-1}$.

It is important to note that the mixed-gas Langmuir model

$$\Theta_1 = \Theta_{1,\text{sat}} \frac{b_1 f_1}{1 + b_1 f_1 + b_2 f_2}; \quad \Theta_2 = \Theta_{2,\text{sat}} \frac{b_2 f_2}{1 + b_1 f_1 + b_2 f_2} \quad (37)$$

Does not anticipate any selectivity reversal; indeed for the fitted Langmuir parameters, equation (37) predicts $q_1 = q_2$, because $\Theta_{1,sat}b_1 = \Theta_{2,sat}b_2$; see Table 2. Equation (37) is thermodynamically inconsistent if the saturation capacities are unequal to each other; this point has been stressed also by Sircar.⁴⁹

Figure 88a presents calculations of the dimensionless entropy per site $\frac{S}{k_B M}$, using equation (24), for a binary mixture of nC6 ($k=1.333$), and 22DMB ($l=1$) in 1D lattice of MOR zeolite as a function of the proportion of nC6 in the adsorbed phase, $x_k = \frac{N_k}{N_k + N_l}$, for three different values of total occupancies, $\frac{N_k+N_l}{M} = 0.15, 0.6, \text{ and } 0.8$. At the lowest occupancy, $\frac{N_k+N_l}{M} = 0.15$, the maximum in the $\frac{S}{k_B M}$ occurs at the adsorbed composition $x_k = \frac{N_k}{N_k + N_l} \approx 0.5$. With increasing occupancies, $\frac{N_k+N_l}{M}$, the maximum in the $\frac{S}{k_B M}$ occurs at values the adsorbed composition $x_k = \frac{N_k}{N_k + N_l}$, that are significantly richer in 22DMB, the d-branched isomer. This is because the vacancies are more efficiently filled up by molecules with the shorter footprint. The precise composition of the adsorbed phase, corresponding to the maximum entropy can be determined

by setting $\frac{\partial}{\partial N_k} \left(\frac{S}{k_B M} \right) = 0$.

The continuous solid black line Figure 88b presents a plot of the values of $x_k = \frac{N_k}{N_k + N_l}$ corresponding to the maximum entropy as a function of the occupancy, $\frac{N_k+N_l}{M}$. The corresponding calculations for the minimum in the Helmholtz free energy of adsorption $F = U -$

TS, is shown by the continuous solid blue line. As the total occupancy approaches unity, i.e. at pore saturation, the adsorbed mixture consists predominantly of 22DMB.

For entropy effects to be exploited, the operations must be under conditions such that pore saturation prevails; adsorption from liquid mixtures usually ensures prevalence of pore saturation conditions.

20. Separating hexane isomers by exploiting differences in molecular footprints in 1D channels of AFI zeolite

Consider the adsorption of a mixture of hexane isomers n-hexane (nC6), 2-methylpentane (2MP), and 2,2-dimethylbutane (22DMB) within the 12-ring 7.3 Å 1D channels of AFI zeolite. The CBMC simulation results for unary isotherms are presented in Figure 89a. Near pore saturation conditions, the hierarchy of adsorption strengths is $nC6 < 2MP \ll 22DMB$.⁵⁰ The hierarchy of component loadings is primarily dictated by the molecular “footprints”. The linear nC6 has a longer “footprint” and occupies a longer segment of the channel. 22DMB is the most compact molecules and has the smallest footprint; consequently, a larger number of di-branched isomers can be located within a given length of the channels when compared to nC6. Mono-branched isomers 2MP and 3-methylpentane (3MP) have footprints that are intermediate in length. For adsorption of ternary mixtures of linear, mono-branched, and di-branched isomers, the adsorption loading becomes increasingly in favor of the di-branched isomer as the channel becomes increasingly occupied; see Figures 89b,c for adsorption of equimolar nC6/2MP/22DMB and nC6/3MP/23DMB mixtures.⁵⁰ The selective adsorption of the di-branched isomer is due to the higher packing efficiency, i.e. this is an entropy effect. It is noteworthy that entropy effects can cause virtual exclusion of the linear isomer from AFI zeolite.

21. Separating heptane isomers by exploiting differences in molecular footprints in 1D channels of TON zeolite

TON zeolite consists of 10-ring $5.6 \text{ \AA} \times 5.3 \text{ \AA}$ 1D channels; the pore landscapes and structural details are provided in Figures 9, and 10. Figure 90a shows CBMC simulations⁵¹ for unary isotherms for heptane isomers n-heptane (nC7), 3-methylhexane (3MH), and 2,3-dimethylpentane (23DMP) in TON. The saturation capacity of the di-branched isomer is significantly higher than that of the linear and mono-branched isomers. The rationalization for the higher saturation capacity is to be found in the molecular footprints within the channels, as elucidated by the snapshots. The more compact 23DMP has a shorter footprint, and as a consequence more molecules can be packed into a channel of a given length. Mixture adsorption at saturation conditions will be in favor of the di-branched isomer; there are important consequences in TON-catalyzed hydrocracking processes.⁵¹

22. Notation

A	surface area per kg of framework, $\text{m}^2 \text{kg}^{-1}$
b	binding constant, Pa^{-1}
b_A	dual-Langmuir-Freundlich constant for species i at adsorption site A, $\text{Pa}^{-\nu_i}$
b_B	dual-Langmuir-Freundlich constant for species i at adsorption site B, $\text{Pa}^{-\nu_i}$
c_i	molar concentration of species i in gas mixture, mol m^{-3}
c_{i0}	molar concentration of species i in gas mixture at inlet to adsorber, mol m^{-3}
D_i	Maxwell-Stefan diffusivity, $\text{m}^2 \text{s}^{-1}$
f_i	partial fugacity of species i , Pa
f_t	total fugacity of bulk fluid mixture, Pa
F	Helmholtz free energy, J mol^{-1}
k_B	Boltzmann constant, $1.38 \times 10^{-23} \text{ J molecule}^{-1} \text{ K}^{-1}$
M	number of sites on lattice, dimensionless
N_k	number of k -mers, dimensionless
N_l	number of l -mers, dimensionless
n	number of species in the mixture, dimensionless
p_i	partial pressure of species i in mixture, Pa
p_t	total system pressure, Pa
P_i^0	sorption pressure, Pa
q_i	component molar loading of species i , mol kg^{-1}
q_t	total molar loading for mixture adsorption, mol kg^{-1}
$q_{i,\text{sat}}$	molar loading of species i at saturation, mol kg^{-1}
r_c	radius of crystallite, m
R	gas constant, $8.314 \text{ J mol}^{-1} \text{ K}^{-1}$

S	entropy, $\text{J mol}^{-1} \text{K}^{-1}$
T	absolute temperature, K
U	internal energy, J mol^{-1}
W	probability (= <i>Wahrscheinlichkeit</i>), dimensionless
x_i	component mole fraction in adsorbed phase, i , mol kg^{-1}

Greek letters

μ_i	molar chemical potential of component i , J mol^{-1}
π	spreading pressure, N m^{-1}
θ_i	fractional occupancy of component i , dimensionless
θ_v	fractional vacancy, $\theta_v = 1 - \theta_1 - \theta_2$, dimensionless
Θ_i	loading of species i , molecules per unit cage, or per unit cell
$\Theta_{i,\text{sat}}$	saturation loading of species i , molecules per unit cage, or per unit cell
Θ_t	total mixture loading, molecules per unit cage, or per unit cell
ν	exponent in dual-Langmuir-Freundlich isotherm, dimensionless
ρ	framework density, kg m^{-3}

Subscripts

i	referring to component i
t	referring to total mixture

Table 1. Three-site Langmuir parameters for pure component isotherms at 300 K. The saturation capacity Θ_{sat} has the units of molecules per cage. The Langmuir parameters b_i , have the units of Pa^{-1} .

$$\Theta = \frac{\Theta_{\text{sat},A} b_A f}{1 + b_A f} + \frac{\Theta_{\text{sat},B} b_B f}{1 + b_B f} + \frac{\Theta_{\text{sat},C} b_C f}{1 + b_C f}$$

Zeolite	Molecule	Temperature, T/K	Three-Site Langmuir parameters					
			b_A	$\Theta_{\text{sat},A}$	b_B	$\Theta_{\text{sat},B}$	b_C	$\Theta_{\text{sat},C}$
CHA	C1	300	1.6×10^{-6}	2.09	2.24×10^{-8}	3.08	5.58×10^{-10}	0.83
CHA	C2	300	2.28×10^{-5}	2	1.66×10^{-9}	2	2.11×10^{-14}	1
CHA	C3	300	1.45×10^{-4}	2	1.79×10^{-13}	0.8	5.88×10^{-16}	1.2
CHA	nC4	300	1.27×10^{-3}	1.3	9.81×10^{-2}	0.07	1.21×10^{-4}	0.63
CHA	nC5	300	1.52×10^{-2}	1	6.07×10^{-7}	1	-	-
CHA	nC6	300	9.02×10^{-2}	1	-	-	-	-
AFX	C3	300	1.77×10^{-4}	3	1.69×10^{-6}	1	7.28×10^{-10}	1
AFX	nC4	300	7.21×10^{-4}	3	7.49×10^{-9}	1	-	-
AFX	nC5	300	7.81×10^{-3}	1.5	6.64×10^{-5}	0.5	6.26×10^{-8}	1
AFX	nC6	300	8.58×10^{-2}	1	3.42×10^{-4}	1	-	-
ERI	C3	300	1.16×10^{-3}	2	6.92×10^{-7}	1	-	-
ERI	nC4	300	4.38×10^{-3}	2	2.87×10^{-9}	1	-	-
ERI	nC5	300	6.88×10^{-2}	1	1.2×10^{-4}	1	-	-
ERI	nC6	300	7.42×10^{-1}	1	4.08×10^{-8}	0.5	4.45×10^{-9}	0.5

Table 2. Langmuir parameters for hexane isomers in MOR at 433 K. The fits correspond to CBMC simulations. Note that the saturation capacities are specified in molecules per unit cell. Multiply these by 0.34673 to obtain the loading values in mol per kg framework.

$\Theta = \frac{\Theta_{sat} bf}{1 + bf}$	$\Theta_{sat}/\text{molecules uc}^{-1}$	b/Pa^{-1}
nC ₆	1.5	4×10^{-4}
2MP	1.7	4×10^{-4}
2DMB	2	3×10^{-4}

Table 3. Dual-site Langmuir-Freundlich parameters for pure component isotherms for nC6 and 2MP in MFI at 298 K.

	Site A			Site B		
	$\Theta_{i,A,sat}$ molecules uc^{-1}	$b_{i,A}$ Pa^{-v_i}	$v_{i,A}$ dimensionless	$\Theta_{i,B,sat}$ molecules uc^{-1}	$b_{i,B}$ Pa^{-v_i}	$v_{i,B}$ dimensionless
nC6	6.6	0.708	0.83	1.4	16.6	1.5
2MP	4	4.51	1.05	4	7.92×10^{-6}	1.13

23. References

- (1) Baerlocher, C.; Meier, W. M.; Olson, D. H. *Atlas of Zeolite Framework Types*; 5th Edition, Elsevier: Amsterdam, 2002.
- (2) Baerlocher, C.; McCusker, L. B. Database of Zeolite Structures. <http://www.iza-structure.org/databases/>, International Zeolite Association, 10 January 2002.
- (3) Krishna, R. Diffusion in Porous Crystalline Materials. *Chem. Soc. Rev.* **2012**, *41*, 3099-3118.
- (4) Krishna, R. The Maxwell-Stefan Description of Mixture Diffusion in Nanoporous Crystalline Materials. *Microporous Mesoporous Mater.* **2014**, *185*, 30-50.
- (5) Krishna, R. Describing the Diffusion of Guest Molecules inside Porous Structures. *J. Phys. Chem. C* **2009**, *113*, 19756-19781.
- (6) Krishna, R.; van Baten, J. M. Investigating the Relative Influences of Molecular Dimensions and Binding Energies on Diffusivities of Guest Species Inside Nanoporous Crystalline Materials *J. Phys. Chem. C* **2012**, *116*, 23556-23568.
- (7) Krishna, R.; van Baten, J. M. Investigating the Influence of Diffusional Coupling on Mixture Permeation across Porous Membranes *J. Membr. Sci.* **2013**, *430*, 113-128.
- (8) Krishna, R.; van Baten, J. M. Influence of Adsorption Thermodynamics on Guest Diffusivities in Nanoporous Crystalline Materials. *Phys. Chem. Chem. Phys.* **2013**, *15*, 7994-8016.
- (9) Krishna, R.; van Baten, J. M. Insights into diffusion of gases in zeolites gained from molecular dynamics simulations. *Microporous Mesoporous Mater.* **2008**, *109*, 91-108.
- (10) Krishna, R.; van Baten, J. M. Diffusion of alkane mixtures in MFI zeolite. *Microporous Mesoporous Mater.* **2008**, *107*, 296-298.
- (11) Krishna, R.; van Baten, J. M. Separating n-alkane mixtures by exploiting differences in the adsorption capacity within cages of CHA, AFX and ERI zeolites. *Sep. Purif. Technol.* **2008**, *60*, 315-320.
- (12) Krishna, R.; van Baten, J. M. Entropy-based Separation of Linear Chain Molecules by Exploiting Differences in the Saturation Capacities in Cage-type Zeolites. *Sep. Purif. Technol.* **2011**, *76*, 325-330.
- (13) Krishna, R. Separating Mixtures by Exploiting Molecular Packing Effects in Microporous Materials. *Phys. Chem. Chem. Phys.* **2015**, *17*, 39-59.
- (14) Li, K.; Olson, D. H.; Lee, J. Y.; Bi, W.; Wu, K.; Yuen, T.; Xu, Q.; Li, J. Multifunctional Microporous MOFs Exhibiting Gas/Hydrocarbon Adsorption Selectivity, Separation Capability and Three-Dimensional Magnetic Ordering. *Adv. Funct. Mater.* **2008**, *18*, 2205-2214.
- (15) Choi, H. J.; Dincă, M.; Long, J. R. Broadly Hysteretic H₂ Adsorption in the Microporous Metal-Organic Framework Co(1,4-benzenedipyrazolate). *J. Am. Chem. Soc.* **2008**, *130*, 7848-7850.
- (16) Salles, F.; Maurin, G.; Serre, C.; Llewellyn, P. L.; Knöfel, C.; Choi, H. J.; Filinchuk, Y.; Oliviero, L.; Vimont, A.; Long, J. R.; Férey, G. Multistep N₂ Breathing in the Metal-Organic Framework Co(1,4-benzenedipyrazolate). *J. Am. Chem. Soc.* **2010**, *132*, 13782-13788.

- (17) Foster, M. D.; Rivin, I.; Treacy, M. M. J.; Friedrichs, O. D. A geometric solution to the largest-free-sphere problem in zeolite frameworks. *Microporous Mesoporous Mater.* **2006**, *90*, 32-38.
- (18) Ruthven, D. M. *Principles of Adsorption and Adsorption Processes*; John Wiley: New York, 1984.
- (19) Myers, A. L.; Prausnitz, J. M. Thermodynamics of Mixed Gas Adsorption. *A.I.Ch.E.J.* **1965**, *11*, 121-130.
- (20) Siperstein, F. R.; Myers, A. L. Mixed-Gas Adsorption. *A.I.Ch.E.J.* **2001**, *47*, 1141-1159.
- (21) LeVan, M. D.; Vermeulen, T. Binary Langmuir and Freundlich Isotherms for Ideal Adsorbed Solutions. *J. Phys. Chem.* **1981**, *85*, 3247-3250.
- (22) Dill, K. A.; Bromberg, S. *Molecular Driving Forces*; Garland Science: New York, 2003.
- (23) Dávila, M.; Riccardo, J. L.; Ramirez-Pastor, A. J. Exact Statistical Thermodynamics of Alkane Binary Mixtures in Zeolites: New Interpretation of the Adsorption Preference Reversal Phenomenon from Multisite-Occupancy Theory. *Chem. Phys. Lett.* **2009**, *477*, 402-405.
- (24) PTC MathCad 15.0. <http://www.ptc.com/>, PTC Corporate Headquarters, Needham, 3 November 2015.
- (25) Azizian, S.; Bashiri, H. A New Isotherm for Multisite Occupancy Adsorption of Binary Gaseous Mixtures. *Langmuir* **2009**, *25*, 2309-2312.
- (26) Krishna, R.; van Baten, J. M. A molecular simulation study of commensurate – incommensurate adsorption of n-alkanes in cobalt formate frameworks. *Molecular Simulation* **2009**, *35*, 1098-1104.
- (27) Daems, I.; Singh, R.; Baron, G. V.; Denayer, J. F. M. Length exclusion in the adsorption of chain molecules on chabazite type zeolites. *Chem. Commun.* **2007**, 1316-1318.
- (28) Remy, T.; Saint-Remi, J. C.; Singh, R.; Webley, P. A.; Baron, G. V.; Denayer, J. F. M. Adsorption and Separation of C1-C8 Alcohols on SAPO-34. *J. Phys. Chem. C* **2011**, *115*, 8117-8125.
- (29) Talu, O.; Sun, M. S.; Shah, D. B. Diffusivities of n-alkanes in silicalite by steady-state single-crystal membrane technique. *A.I.Ch.E.J.* **1998**, *44*, 681-694.
- (30) Vlught, T. J. H.; Krishna, R.; Smit, B. Molecular Simulations of Adsorption Isotherms for Linear and Branched Alkanes and Their Mixtures in Silicalite. *J. Phys. Chem. B* **1999**, *103*, 1102-1118.
- (31) Krishna, R.; Smit, B.; Vlught, T. J. H. Sorption-induced Diffusion-selective Separation of Hydrocarbon Isomers Using Silicalite. *J. Phys. Chem. A* **1998**, *102*, 7727-7730.
- (32) Krishna, R. Exploiting Configurational Entropy Effects for Separation of Hexane Isomers Using Silicalite-1. *Chem. Eng. Res. Des.* **2001**, *79*, 182-194.
- (33) Dubbeldam, D.; Krishna, R.; Calero, S.; Yazaydin, A. Ö. Computer-Assisted Screening of Ordered Crystalline Nanoporous Adsorbents for Separation of Alkane Isomers. *Angew. Chem. Int. Ed.* **2012**, *51*, 11867-11871.
- (34) Herm, Z. R.; Wiers, B. M.; Van Baten, J. M.; Hudson, M. R.; Zajdel, P.; Brown, C. M.; Maschiochi, N.; Krishna, R.; Long, J. R. Separation of Hexane Isomers in a Metal-Organic Framework with Triangular Channels *Science* **2013**, *340*, 960-964.
- (35) Titze, T.; Chmelik, C.; Kärger, J.; van Baten, J. M.; Krishna, R. Uncommon Synergy Between Adsorption and Diffusion of Hexane Isomer Mixtures in MFI Zeolite Induced by Configurational Entropy Effects *J. Phys. Chem. C* **2014**, *118*, 2660-2665.

- (36) Jobic, H.; Methivier, A.; Ehlers, G.; Farago, B.; Haeussler, W. Accelerated diffusion of long-chain alkanes between nanosized cavities. *Angew. Chem.-Int. Edit.* **2004**, *43*, 364-366.
- (37) Goring, R. L. Diffusion of Normal Paraffins in Zeolite T. Occurrence of Window Effect. *J. Catal.* **1973**, *31*, 13-26.
- (38) Yoo, K.; Tsekov, R.; Smirniotis, P. G. Experimental Proof for Resonant Diffusion of Normal Alkanes in LTL and ZSM-12 Zeolites. *J. Phys. Chem. B* **2003**, *107*, 13593-13596.
- (39) Runnebaum, R. C.; Maginn, E. J. Molecular dynamics simulations of alkanes in the zeolite silicalite: Evidence for resonant diffusion effects. *J Phys Chem B* **1997**, *101*, 6394-6408.
- (40) Jobic, H.; Theodorou, D. N. Quasi-elastic neutron scattering and molecular dynamics simulation as complementary techniques for studying diffusion in zeolites. *Microporous Mesoporous Mater.* **2006**, *102*, 21-50.
- (41) Torres-Knoop, A.; Krishna, R.; Dubbeldam, D. Separating Xylene Isomers by Commensurate Stacking of p-Xylene within Channels of MAF-X8. *Angew. Chem. Int. Ed.* **2014**, *53*, 7774-7778.
- (42) El Osta, R.; Carlin-Sinclair, A.; Guillou, N.; Walton, R. I.; Vermoortele, F.; Maes, M.; De Vos, D.; Millange, F. Liquid-Phase Adsorption and Separation of Xylene Isomers by the Flexible Porous Metal–Organic Framework MIL-53(Fe). *Chem. Mater.* **2012**, *24*, 2781-2791.
- (43) Finsy, V.; Verelst, H.; Alaerts, L.; De Vos, D.; Jacobs, P. A.; Baron, G. V.; Denayer, J. F. M. Pore-Filling-Dependent Selectivity Effects in the Vapor-Phase Separation of Xylene Isomers on the Metal-Organic Framework MIL-47. *J. Am. Chem. Soc.* **2008**, *130*, 7110-7118.
- (44) Remy, T.; Baron, G. V.; Denayer, J. F. M. Modeling the Effect of Structural Changes during Dynamic Separation Processes on MOFs. *Langmuir* **2011**, *27*, 13064-13071.
- (45) Chiang, A. S. T.; Lee, C.-K.; Chang, Z.-H. Adsorption and diffusion of aromatics in AlPO₄-5. *Zeolites* **1991**, *11*, 380-386.
- (46) Torres-Knoop, A.; Balestra, S. R. G.; Krishna, R.; Calero, S.; Dubbeldam, D. Entropic Separations of Mixtures of Aromatics by Selective Face-to-Face Molecular Stacking in One-Dimensional Channels of Metal–Organic Frameworks and Zeolites. *ChemPhysChem* **2015**, *16*, 532-535.
- (47) Torres-Knoop, A.; Dubbeldam, D. Exploiting Large-Pore Metal–Organic Frameworks for Separations through Entropic Molecular Mechanisms. *ChemPhysChem* **2015**, *16*, 2046-2067.
- (48) van Baten, J. M.; Krishna, R. Entropy effects in adsorption and diffusion of alkane isomers in mordenite: An investigation using CBMC and MD simulations. *Microporous Mesoporous Mater.* **2005**, *84*, 179-191.
- (49) Rao, M. B.; Sircar, S. Thermodynamic consistency for binary gas adsorption equilibria. *Langmuir* **1999**, *15*, 7258-7267.
- (50) Krishna, R.; van Baten, J. M. In silico screening of metal-organic frameworks in separation applications. *Phys. Chem. Chem. Phys.* **2011**, *13*, 10593-10616.
- (51) Maesen, T. L. M.; Krishna, R.; van Baten, J. M.; Smit, B.; Calero, S.; Castillo Sanchez, J. M. Shape-selective n-alkane hydroconversion at exterior zeolite surfaces. *J. Catal.* **2008**, *256*, 95-107.
- (52) Krishna, R.; van Baten, J. M. Loading dependence of self-diffusivities of gases in zeolites. *Chem. Eng. Technol.* **2007**, *30*, 1235-1241.
- (53) Krishna, R.; van Baten, J. M. Influence of isotherm inflection on the diffusivities of C₅-C₈ linear alkanes in MFI zeolite. *Chem. Phys. Lett.* **2005**, *407*, 159-165.

(54) Zhu, W.; Kapteijn, F.; van der Linden, B.; Moulijn, J. A. Equilibrium adsorption of linear and branched C₆ alkanes on silicalite-1 studied by the tapered element oscillating microbalance. *Phys. Chem. Chem. Phys.* **2001**, *3*, 1755-1761.

(55) Krishna, R. Evaluation of Procedures for Estimation of the Isothermic Heat of Adsorption in Microporous Materials. *Chem. Eng. Sci.* **2015**, *123*, 191-196.

24. Captions for Figures

Figure 1. Comparison of surface area, pore volumes, framework densities, and characteristic dimensions of some representative zeolites, MOFs and ZIFs.

Figure 2. Pore landscapes of AFI, MIL-53, MOR, LTA, MFI, and ZIF-8.

Figure 3. Pore landscape of all-silica AFI zeolite.

Figure 4. Structural details for AFI zeolite.

Figure 5. Pore landscape of all-silica LTL zeolite.

Figure 6. Structural details for LTL zeolite.

Figure 7. Pore landscape of all-silica MTW zeolite.

Figure 8. Structural details for MTW zeolite.

Figure 9. Pore landscape of all-silica TON zeolite.

Figure 10. Structural details for TON zeolite.

Figure 11. Pore landscape, and structural details of Co-Formate.

Figure 12. Pore landscape, and structural details of Mn-Formate.

Figure 13. Pore landscape and structural data for MIL-47.

Figure 14. Pore landscape and structural data for MIL-47.

Figure 15. Pore landscape and structural data for Co(BDP).

Figure 16. Pore landscape and structural data for Co(BDP).

Figure 17. Pore landscape and structural data for $\text{Fe}_2(\text{BDP})_3$.

Figure 18. Pore landscape and structural data for $\text{Fe}_2(\text{BDP})_3$.

Figure 19. Pore landscape of all-silica MOR zeolite.

Figure 20. Structural details for MOR zeolite.

Figure 21. Pore landscape of all-silica AFX zeolite.

Figure 22. Structural details for AFX zeolite.

Figure 23. Pore landscape of all-silica CHA zeolite.

Figure 24. Structural details for CHA zeolite.

Figure 25. Pore landscape of all-silica DDR zeolite.

Figure 26. Structural details for DDR zeolite.

Figure 27. Pore landscape of all-silica ERI zeolite.

Figure 28. Structural details for ERI zeolite.

Figure 29. Pore landscape of all-silica LTA zeolite.

Figure 30. Structural details for all-silica LTA zeolite.

Figure 31. Structural details for LTA-5A zeolite.

Figure 32. Structural details for LTA-4A zeolite.

Figure 33. Pore landscape of all-silica TSC zeolite.

Figure 34. Pore landscape of all-silica TSC zeolite.

Figure 35. Structural details for TSC zeolite.

Figure 36. Pore landscape and structural data for ZIF-8.

Figure 37. Pore landscape and structural data for ZIF-8.

Figure 38. Pore landscape and structural data for MFI zeolite.

Figure 39. Pore landscape and structural data for MFI zeolite.

Figure 40. Pore landscape and structural data for ISV zeolite.

Figure 41. Pore landscape and structural data for ISV zeolite.

Figure 42. Two-dimensional lattice model for gas adsorption on surface of solid. There are a total of M sites on the surface, corresponding to potential energy wells.

Figure 43. Calculation of the translation entropy of adsorption using the Boltzmann equation, along with the Stirling approximation for the factorials.

Figure 44. Calculation of the Helmholtz free energy $F = U - TS$.

Figure 45. Equating the chemical potentials in the gas phase to that of the adsorbed solid phase to derive the Langmuir isotherm.

Figure 46. Schematic showing the adsorption of binary mixture of k -mers ($k=1$), and l -mers ($l=2$) on 1D and 2D (square) lattices.

Figure 47. Snapshots showing the location of propane (C3) and n-hexane (nC6) molecules within the zig-zag 1D channel segments of Mn-FA.

Figure 48. (a) CBMC data (symbols) for unary isotherms of C3 and nC6 in Mn-FA, compared with the fits of the 1D lattice model, described by equation (26). (b) Comparison of the CBMC simulations (shown by symbols) for mixture adsorption with the estimations of the 1D lattice model (shown by continuous solid lines), described by equations (25). The dashed lines are the estimations of the component loading using the Ideal Adsorbed Solution Theory (IAST), with the unary isotherms of C3 and nC6 fitted with the single-site Langmuir isotherms.

Figure 49. Calculations of the dimensionless entropy per site, $\frac{S}{k_B M}$, for adsorption of binary mixture of C3 ($k=1$), and nC6 ($l=2$) in a 1D lattice representation of Mn-FA as a function of the proportion of propane in the adsorbed phase, $\frac{N_k}{N_k + N_l}$, for three different values of total occupancies, $\frac{N_k + N_l}{M} = 0.1, 0.3, \text{ and } 0.5$. (b) Plot of the values of $\frac{N_k}{N_k + N_l}$ corresponding to the maximum entropy (black line), and minimum free energy (blue line), as a function of the occupancy, $\frac{N_k + N_l}{M}$.

Figure 50. Snapshots showing the location of n-alkanes molecules within the zig-zag 1D channel segments of Co-FA.

Figure 51. (a) CBMC simulations of adsorption isotherms for C1, C2, C3, nC4, nC5, nC6 and nC7 in Co-FA at 300 K. (b) Experimental data of Li et al.¹⁴ for unary adsorption isotherms for propanol and 1-butanol in Co-FA. (c) Henry coefficients and M-S diffusivity at zero-loading, $D_i(0)$, for n-alkanes in Co-FA as a function of C number. (d) CBMC simulations of component loadings for C3/nC6 mixture adsorption in Co-FA at 300 K.

Figure 52. (a) CBMC data for unary isotherms of C3 and nC6 in Co-FA, compared with the fits of the 1D lattice model, described by equation (26). (b) Comparison of the CBMC simulations (shown by symbols) for mixture adsorption with the estimations of the 1D lattice model (shown by continuous solid lines), described by equations (25). The dashed lines are the estimations of the component loading using the Ideal Adsorbed Solution Theory (IAST).

Figure 53. (a) Calculations of the dimensionless entropy per site, $\frac{S}{k_B M}$, for adsorption of binary mixture of C3 ($k=1$), and nC6 ($l=2$) in a 1D lattice representation of Co-FA as a function of the

proportion of propane in the adsorbed phase, $\frac{N_k}{N_k + N_l}$, for three different values of total occupancies, $\frac{N_k + N_l}{M} = 0.1, 0.3, \text{ and } 0.5$. (b) Plot of the values of $\frac{N_k}{N_k + N_l}$ corresponding to the maximum entropy, as a function of the occupancy, $\frac{N_k + N_l}{M}$.

Figure 54. (a) CBMC simulations¹¹ of pure component adsorption isotherms for n-alkanes in CHA at 300 K. (b) Saturation capacities for adsorption n-alkanes in CHA at 300 K. The CBMC simulation results¹¹ are compared with the experimental data of Daems et al.²⁷

Figure 55. Comparison of the snapshots showing the conformations of n-alkanes in CHA at saturation conditions.

Figure 56. Snapshots showing the location of (b) nC8, and (c) nC12 alkane molecules within the cages of CHA.

Figure 57. Comparison of CBMC mixture simulations¹¹ (symbols) for (a) C1/C2, (b) C2/C3, (c) C3/nC6, (d) nC4/nC6, and (e) nC4/nC6 in CHA at 300 K with the IAST predictions. The dashed

lines represent calculations of the IAST,¹⁹ using 3-site Langmuir fits of pure component isotherms with fitted parameter values as given in Table 1. The region of liquid phase operation is indicated by the colored bar; the transition between vapor and liquid bulk phase is determined using the Peng-Robinson equation of state.

Figure 58. (a) CBMC data¹¹ for unary isotherms of C3 and nC6 alkanes in CHA zeolite, compared with the fits of the 2D lattice model, (b) Comparison of the CBMC simulations¹¹ (shown by symbols) for mixture adsorption with the estimations of the lattice model (shown by continuous solid lines). The dashed lines are the estimations of the component loading using the Ideal Adsorbed Solution Theory (IAST).

Figure 59. (a) Calculations of the dimensionless entropy per site, $\frac{S}{k_B M}$, for adsorption of binary mixture of propane ($k=1$), and n-hexane ($l=2$) on 2D lattice representation of CHA zeolite as a function of the proportion of propane in the adsorbed phase, $\frac{N_k}{N_k + N_l}$, for three different values of total occupancies, $\frac{N_k + N_l}{M} = 0.1, 0.5, \text{ and } 0.6$. (b) Plot of the values of $\frac{N_k}{N_k + N_l}$ corresponding to the maximum entropy (black line), and minimum free energy (blue line), as a function of the occupancy, $\frac{N_k + N_l}{M}$.

Figure 60. (a) Snapshots showing the conformations of ethanol, 1-propanol, 1-butanol, and 1-hexanol in CHA at saturation conditions in CHA zeolite. (b) CBMC simulations¹² of pure component adsorption isotherms for 1-alcohols in CHA at 300 K. (c) Saturation capacities for adsorption of 1-alcohols in CHA at 300 K. (d) CBMC mixture simulations for 1-butanol/1-hexanol in CHA at 300 K. The partial fugacities in the bulk fluid phase are taken to be equal, i.e. $f_1=f_2$. The dashed lines are the IAST calculations of mixture adsorption equilibrium; the isotherm fit parameters are provided by Krishna and van Baten.¹²

Figure 61. (a) CBMC data for unary isotherms of 1-butanol and 1-hexanol in CHA zeolite, compared with the fits of the lattice model. (b) Comparison of the CBMC simulations (shown by symbols) for mixture adsorption with the estimations of the lattice model (shown by continuous solid lines). The dashed lines are the estimations of the component loading using the Ideal Adsorbed Solution Theory (IAST).

Figure 62. (a) Calculations of the dimensionless entropy per site, $\frac{S}{k_B M}$, for adsorption of binary mixture of 1-butanol ($k=1$), and 1-hexanol ($l=2$) on 2D lattice representation of CHA zeolite, as a function of the proportion of 1-butanol in the adsorbed phase, $\frac{N_k}{N_k + N_l}$, for three different

values of total occupancies, $\frac{N_k+N_l}{M} = 0.1, 0.5, \text{ and } 0.6$. (b) Plot of the values of $\frac{N_k}{N_k+N_l}$ corresponding to the maximum entropy (black line), and minimum free energy (blue line), as a function of the occupancy, $\frac{N_k+N_l}{M}$.

Figure 63. (a) Saturation capacities for adsorption of n-alkanes and n-alcohols in CHA, ERI, AFX, and LTA, at 300 K. The data are based on CBMC simulations culled from the papers of Krishna and van Baten.^{11, 12} (b) Snapshots showing the conformations of propane (C3) and n-hexane (nC6) at saturation conditions in ERI zeolite. (c) CBMC simulations¹¹ for C3/nC6 mixture adsorption in ERI at 300 K. The partial fugacities in the bulk fluid phase are taken to be equal, i.e. $f_1=f_2$. The range of liquid phase operation is indicated by the shaded region; the transition between vapor and liquid bulk phase is determined using the Peng-Robinson equation of state.

Figure 64. (a) CBMC simulations¹² of the unary isotherms of nC21 and nC24 linear alkanes in TSC zeolite at 500 K. (b) CBMC simulations¹² of nC21/nC24 mixture adsorption in TSC at 500 K.

Figure 65. (a, b) Snapshots showing the locations of (a) nC6, and (b) nC7 within the intersecting channels of MFI zeolite at a loading of 4 molecules per unit cell. (c) CBMC simulations of adsorption isotherms for C1, C2, C3, nC4, nC5, nC6 and nC7 in MFI at 300 K. The CBMC data are culled from the papers of Krishna and van Baten.^{4, 9, 10, 52}

Figure 66. (a) MD data, culled from the papers of Krishna and van Baten,^{4, 5, 9, 10, 52, 53} for Maxwell-Stefan (M-S) diffusivities of linear alkanes in MFI zeolite, plotted as a function of the loading. (b) Zero-loading M-S diffusivities $D_i(0)$, plotted as a function of the C number of the n-alkane. (c) Experimental data of Talu et al.²⁹ for the chain length dependence of diffusivities of n-alkanes in MFI zeolite; these data are not at constant loading; the loadings increase with increasing chain length because of stronger adsorption.

Figure 67. The isotherm data for nC6 at 298 K determined from Infra-Red Microscopy (IRM)³⁵ are compared with the corresponding CBMC simulations for nC6; the CBMC data are fitted with the dual-Langmuir-Freundlich parameters specified in Table 3. Also shown are snapshots showing the location of nC6 molecules within the straight and zig-zag channels of MFI.

Figure 68. CBMC simulations of pure component isotherm for 2-methylpentane (= 2MP) compared with the experimental data obtained from IRM,³⁵ and from experimental data of Zhu et al.⁵⁴ at 303 K. The CBMC simulations for 2MP are fitted with the dual-Langmuir-Freundlich

parameters specified in Table 3. Also shown are snapshots of 2MP molecules located within MFI.

Figure 69. (a) CBMC simulations of loadings in the adsorbed phase in equilibrium with binary nC6/2MP mixture with partial fugacities $f_1 = f_2$ in the bulk gas phase at 298 K. Also shown (using open symbols) are IRM experimental data.³⁵ The continuous solid lines are IAST calculations using the pure component isotherm fits in Table 3. (b) Calculations of the adsorption selectivity, S_{ads} , using Equation (35). Also shown are snapshots showing the location of nC6 ($\Theta_1 = 2/\text{uc}$) and 2MP ($\Theta_2 = 2/\text{uc}$) molecules at a total loading $\Theta_t = 4/\text{uc}$.

Figure 70. (a) CBMC data for unary isotherms of nC6 and 2MP in MFI zeolite at 298 K, compared with the fits of the 1D lattice model, described by equation (26). (b) Comparison of the CBMC simulations (shown by symbols) for nC6/2MP mixture adsorption with the estimations of the 2D lattice model (shown by continuous solid lines), described by equations (25).

Figure 71. (a) Calculations of the dimensionless entropy per site $\frac{S}{k_B M}$ for a binary mixture of nC6 ($k=1$), and 2MP ($l=2$) in 2D lattice representation of MFI zeolite as a function of the proportion of nC6 in the adsorbed phase, $\frac{N_k}{N_k + N_l}$, for three different values of total

occupancies, $\frac{N_k+N_l}{M} = 0.2, 0.4, \text{ and } 0.7$. (b) Plot of the values of $\frac{N_k}{N_k+N_l}$ corresponding to the maximum entropy (black line), and minimum free energy (blue line), as a function of the occupancy, $\frac{N_k+N_l}{M}$.

Figure 72. Snapshots showing the location of CH₄ and C₂H₆ within the intersecting channels of ISV zeolites. (a) CBMC simulations of the unary isotherms of CH₄ and C₂H₆ in ISV zeolite at 300 K. The continuous solid lines are the 3-site Langmuir-Freundlich fits of unary isotherms. (b) CBMC simulations of loadings in the adsorbed phase in equilibrium with binary CH₄/C₂H₆ mixtures with partial fugacities $f_1 = f_2$ in the bulk gas phase at 300 K. The continuous solid lines are the IAST calculations.

Figure 73. (a) QENS data of Jobic et al.³⁶ for diffusivity of n-alkanes in LTA-5A. (b, c) Snapshots showing the conformations of (b) nC8, and (c) nC13 alkanes within the cages of LTA-5A.

Figure 74. Experimental data of Yoo et al.³⁸ for diffusivity of n-alkanes in MTW zeolite. Also shown are snapshots of the conformations of linear alkanes with C numbers ranging from 1 – 9 in MTW zeolite.

Figure 75. Experimental data of Yoo et al.³⁸ for diffusivity of n-alkanes in LTL zeolite. Also shown are snapshots (head-on view) of the conformations of linear alkanes with C numbers ranging from 1 – 9 in LTL zeolite.

Figure 76. The molecular dimensions of xylene isomers, ethylbenzene and styrene culled from Torres-Knoop et al.⁴¹

Figure 77. Computational snapshots⁴¹ showing the stacking of o-xylene within 8.5 Å channels of MIL-47.

Figure 78. Computational snapshots⁴¹ showing the stacking of p-xylene within 10 Å channels of Co(BDP).

Figure 79. Computational snapshots⁴¹ showing the stacking of p-xylene within 10 Å channels of MAF-X8.

Figure 80. (a) Experimental data of Chiang et al.⁴⁵ for pure component isotherms for xylene isomers in $\text{AlPO}_4\text{-5}$ at 303 K. (b) Computational snapshots⁴⁶ showing the orientations of o-xylene, m-xylene, and p-xylene as they stack within the corrugated 1D channel of AFI zeolite. (c) Calculations of the isosteric heats of adsorption of xylene isomers in $\text{AlPO}_4\text{-5}$.⁵⁵

Figure 81. Calculations using the Ideal Adsorbed Solution Theory (IAST) of Myers and Prausnitz¹⁹ for adsorption equilibrium in a 3-component o-xylene/m-xylene/p-xylene in $\text{AlPO}_4\text{-5}$ at 303 K.

Figure 82. Computational snapshots showing conformations and stacking of 1,2,3 tri-chlorobenzene (TCB), 1,2,4 TCB, and 1,3,5 TCB within the triangular channels of modified $\text{Fe}_2(\text{BDP})_3$. From Torres-Knoop et al.⁴⁶; reprinted with permission from John Wiley and Sons.

Figure 83. (a) CBMC simulations for unary isotherms of 1,2,3 tri-chlorobenzene (TCB), 1,2,4 TCB, and 1,3,5 TCB in modified $\text{Fe}_2(\text{BDP})_3$ at 433 K. (b) CBMC simulations of component loadings for adsorption of equimolar ternary TCB mixtures in modified $\text{Fe}_2(\text{BDP})_3$ at 433 K.

Figure 84. Face-to-face stacking of molecules that have shapes that are commensurate with the channel cross-section. (a) cylindrical channels for molecules such as benzene, (b) honeycomb

channels for hexagonal molecules (e.g. benzene), (c) triangular channels for triangular molecules (e.g. 1,3,5 tri-chlorobenzene, cyclo-propane, aluminum hydroxide). (d) elliptical channels for face-to-face stacking of p-xylene, (e) diamond-like channels that allow face-to-face stacking of para-xylene (f) cuboid channels.

Figure 85. Pore landscape of MOR zeolite.⁴⁸ Snapshots of the conformation and siting of siting of nC6, 2MP, and 22DMB along 1D 12-ring channel, 8 unit cells long.

Figure 86. (a) Distribution of lengths of hexane isomers ($f_t = 1000$ kPa, $T = 433$ K) along the z -direction of MOR obtained from CBMC simulations. (b) CBMC simulations⁴⁸ of the sorption isotherms for pure hexane isomers nC6, 2MP, 22DMB in MOR at 433 K. (c) CBMC simulations⁴⁸ for equimolar binary mixture nC6/22DMB in MOR at $T = 433$ K.

Figure 87. (a) CBMC data for unary isotherms of nC6 and 22DMB in MOR zeolite, compared with the fits of the 1D lattice model, described by equation (26). (b) Comparison of the CBMC simulations (shown by symbols) for nC6/22DMB mixture adsorption with the estimations of the 1D lattice model (shown by continuous solid lines), described by equations (25). The dashed lines are the estimations of the component loading using the Ideal Adsorbed Solution Theory

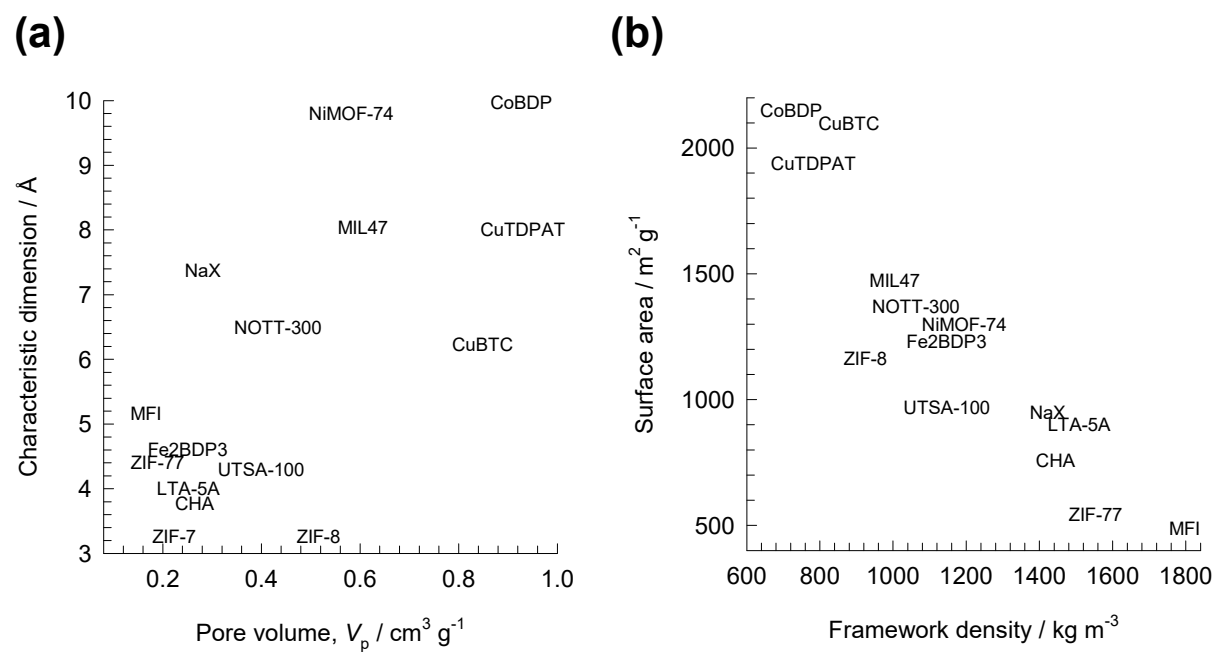
(IAST), with the unary isotherms of nC6 and 22DMB fitted with the single-site Langmuir isotherms; the Langmuir parameters are provided in Table 2.

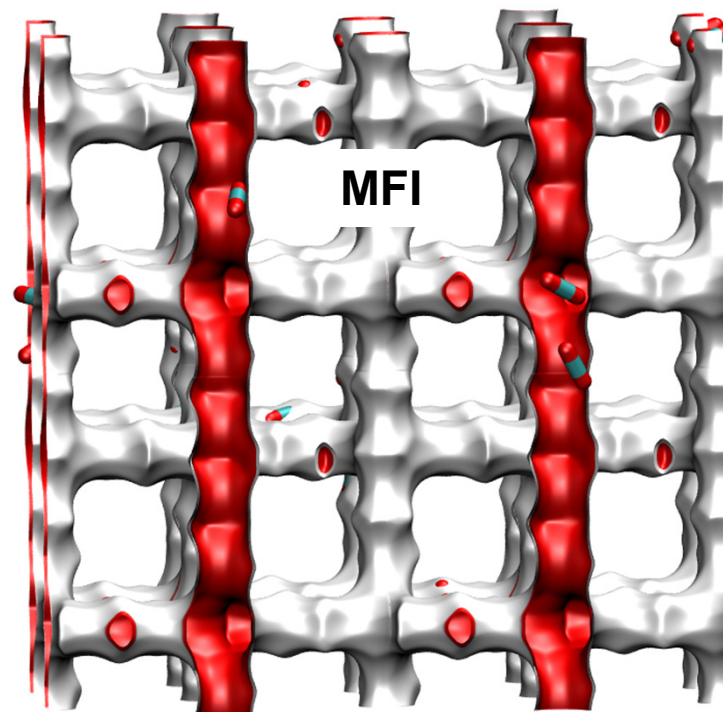
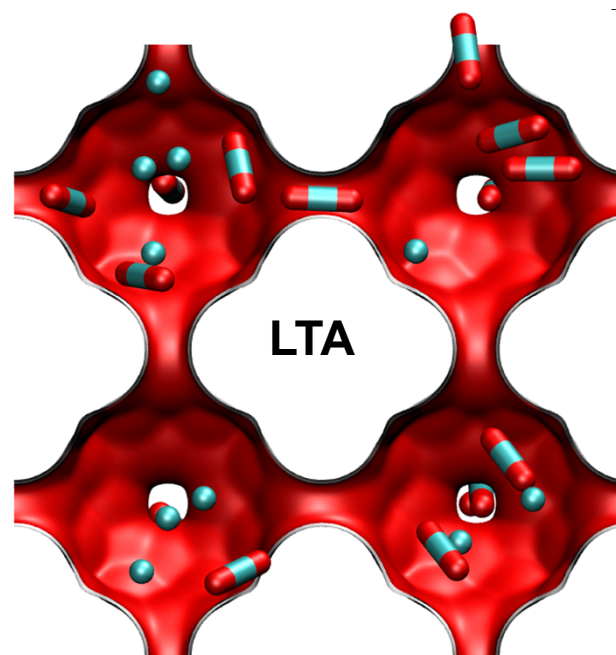
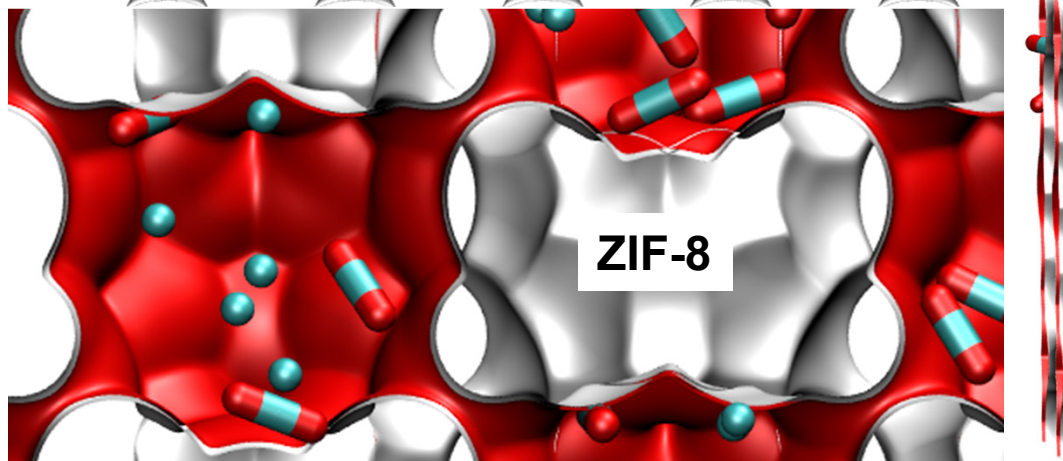
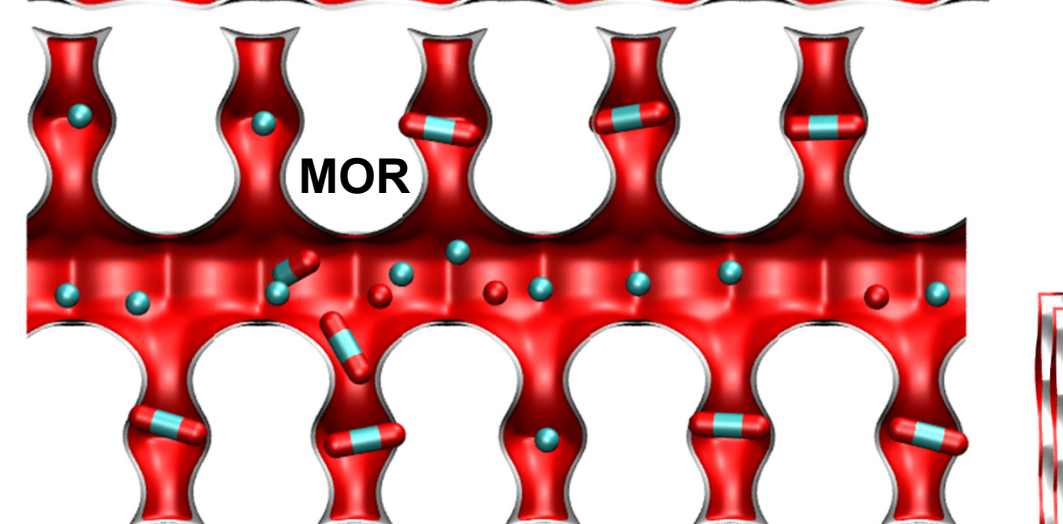
Figure 88. (a) Calculations of the dimensionless entropy per site $\frac{S}{k_B M}$ for a binary mixture of nC6 ($k=1.333$), and 22DMB ($l=1$) in 1D lattice representation of MOR zeolite as a function of the proportion of nC6 in the adsorbed phase, $\frac{N_k}{N_k + N_l}$, for three different values of total occupancies, $\frac{N_k + N_l}{M} = 0.15, 0.6, \text{ and } 0.8$. (b) Plot of the values of $\frac{N_k}{N_k + N_l}$ corresponding to the maximum entropy (black line), and minimum free energy (blue line), as a function of the occupancy, $\frac{N_k + N_l}{M}$.

Figure 89. Snapshots showing the molecular conformations of nC6, 3MP, and 22DMB within 1D channels of AFI zeolite.⁵⁰ (a) CBMC simulations for unary isotherms of nC6, 2MP, and 22DMB in AFI zeolite at 403 K. (b, c) CBMC simulations for adsorption of equimolar (b) nC6/2MP/22DMB, and (c) nC6/3MP/22DMB mixtures in AFI zeolite at 433 K.⁵⁰

Figure 90. CBMC simulations⁵¹ for unary isotherms for heptane isomers n-pentane (nC7), 3-methylhexane (3MH), and 2,3-dimethylpentane (23DMP) in TON zeolite. Snapshots showing the molecular configurations of nC7, 3MH, and 23DMP within 1D channels of TON zeolite.

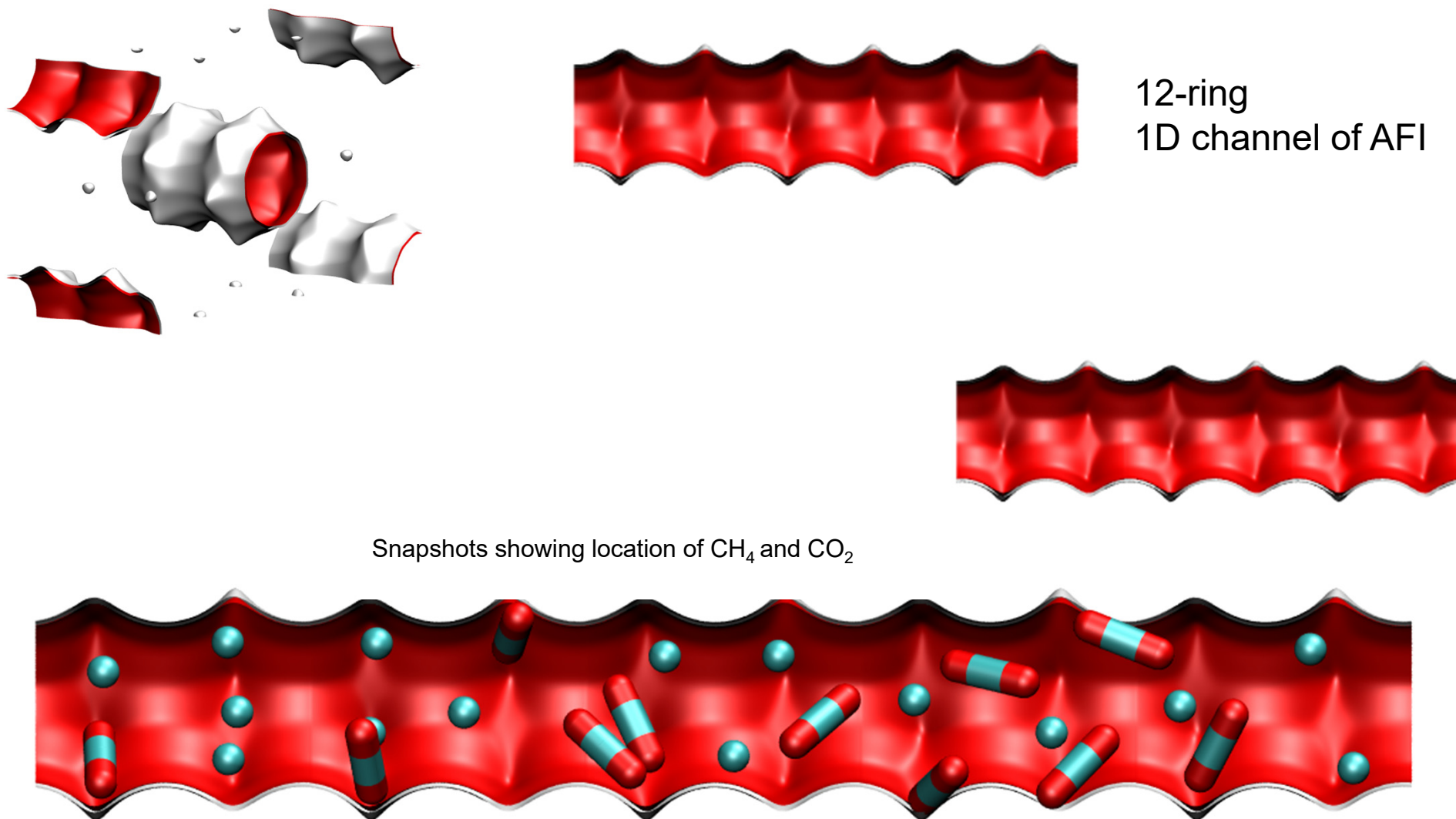
Structural data: zeolites, MOFs, ZIFs





AFI landscapes

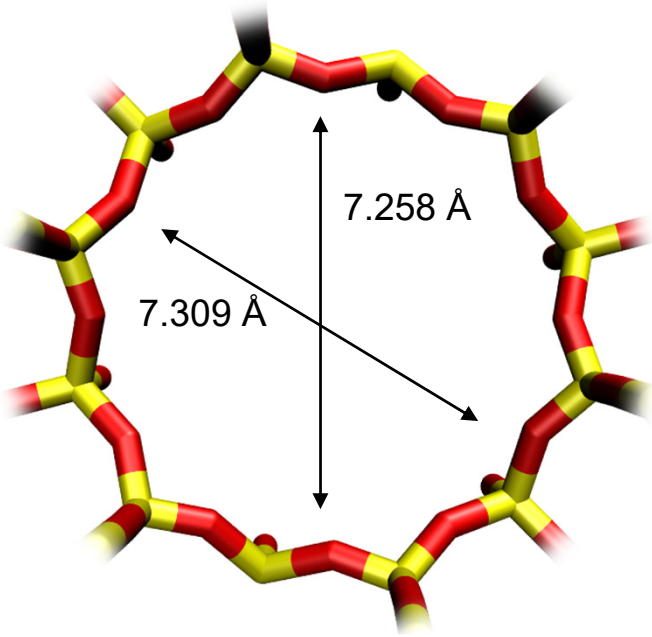
Fig. S3



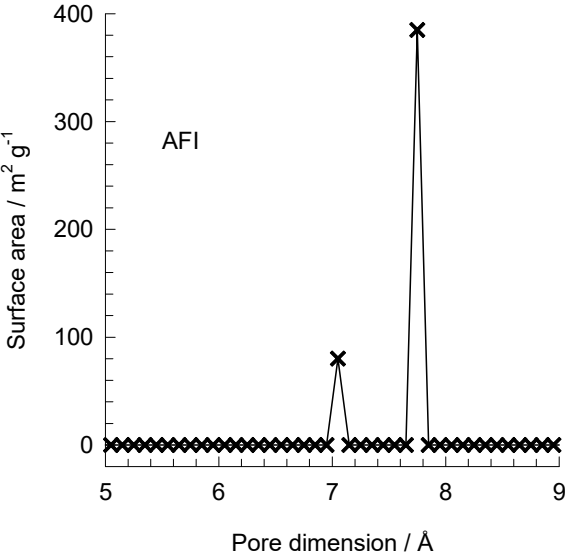
Structural information from: C. Baerlocher, L.B. McCusker, Database of Zeolite Structures, International Zeolite Association, <http://www.iza-structure.org/databases/>

Fig. S4

AFI pore dimensions



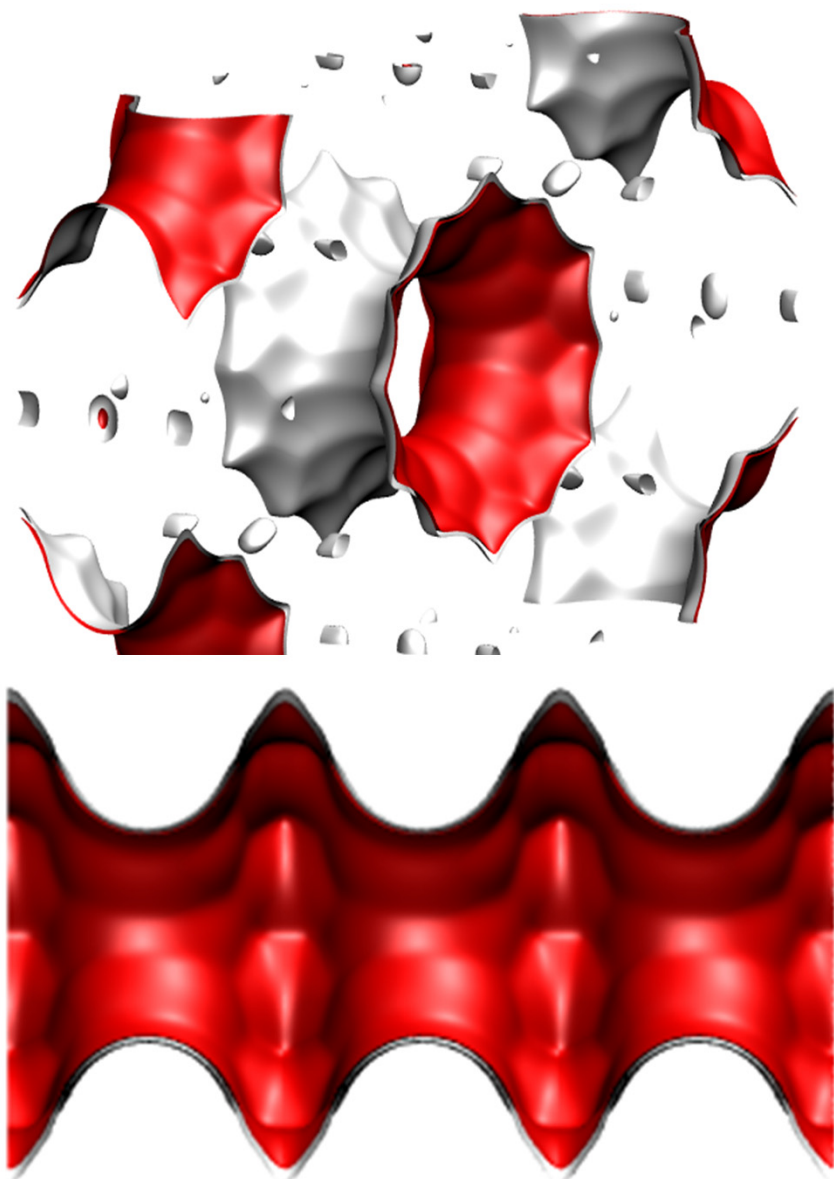
	AFI
$a / \text{Å}$	23.774
$b / \text{Å}$	13.726
$c / \text{Å}$	8.484
Cell volume / Å^3	2768.515
conversion factor for [molec/uc] to [mol per kg Framework]	0.3467
conversion factor for [molec/uc] to [kmol/m ³]	2.1866
ρ [kg/m ³]	1729.876
MW unit cell [g/mol(framework)]	2884.07
ϕ , fractional pore volume	0.274
open space / $\text{Å}^3/\text{uc}$	759.4
Pore volume / cm^3/g	0.159
Surface area / m^2/g	466.0
DeLaunay diameter / Å	7.26



This plot of surface area versus pore dimension is determined using a combination of the DeLaunay triangulation method for pore dimension determination, and the procedure of Dürren for determination of the surface area.

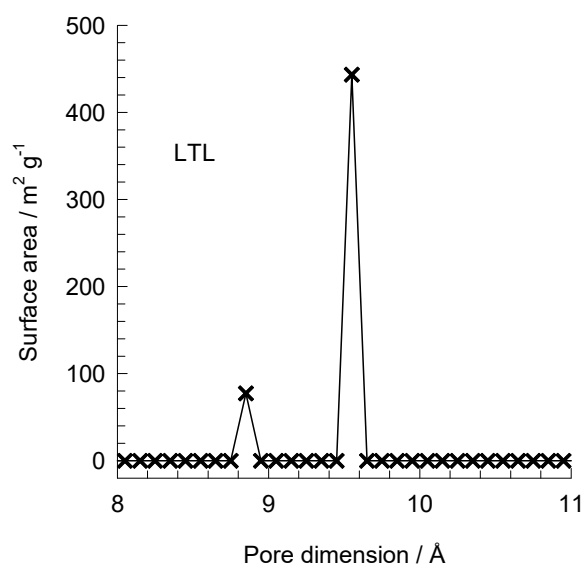
LTL pore landscapes

Fig. S5



LTL pore dimensions

Fig. S6



This plot of surface area versus pore dimension is determined using a combination of the DeLaunay triangulation method for pore dimension determination, and the procedure of Dürren for determination of the surface area.

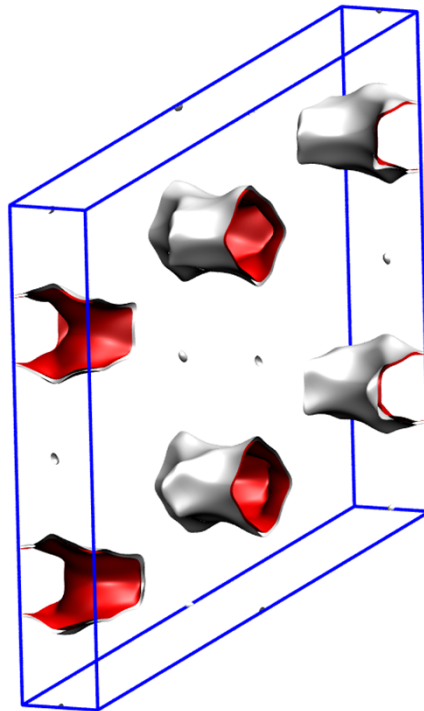
	LTL
$a / \text{Å}$	31.984
$b / \text{Å}$	18.466
$c / \text{Å}$	7.476
Cell volume / Å^3	4415.449
conversion factor for [molec/uc] to [mol per kg Framework]	0.2312
conversion factor for [molec/uc] to [kmol/m ³]	1.3597
ρ [kg/m ³]	1626.965
MW unit cell [g/mol/framework]	4326.106
ϕ , fractional pore volume	0.277
open space / $\text{Å}^3/\text{uc}$	1221.3
Pore volume / cm ³ /g	0.170
Surface area / m ² /g	521.0
DeLaunay diameter / Å	7.47

MTW pore landscape

Fig. S7

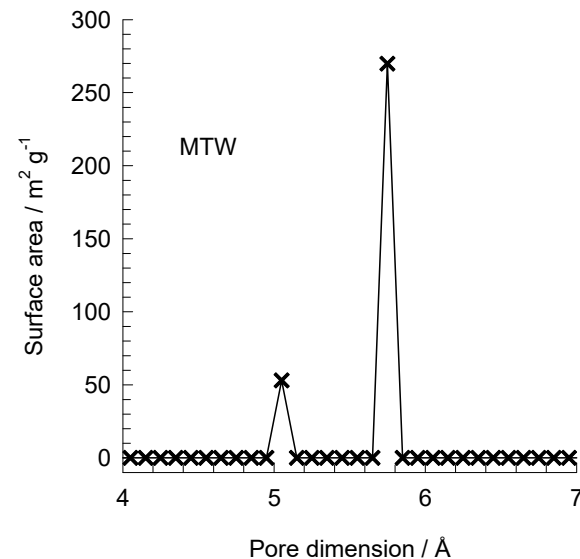


MTW has 1D, 12-ring channels

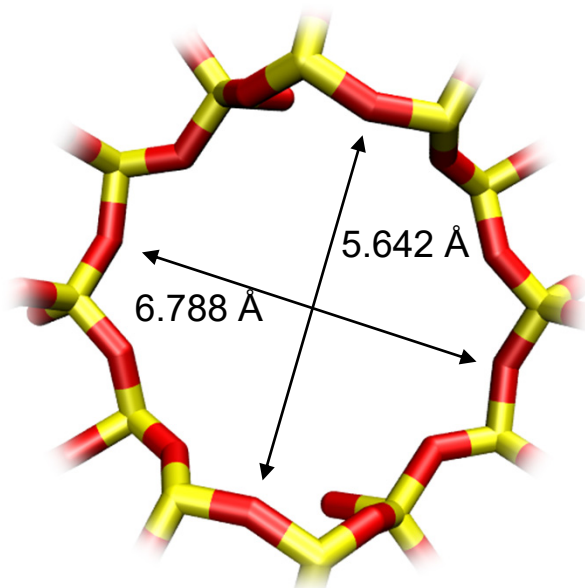


MTW pore dimensions

This plot of surface area versus pore dimension is determined using a combination of the DeLaunay triangulation method for pore dimension determination, and the procedure of Dürren for determination of the surface area.



MTW has 1D, 12-ring channels



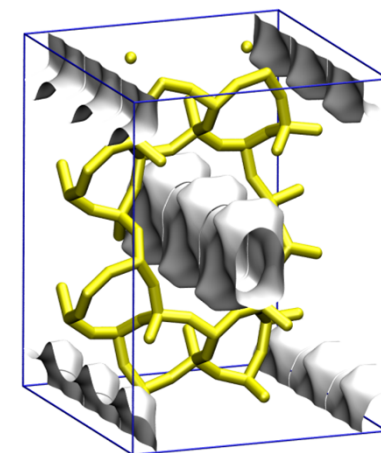
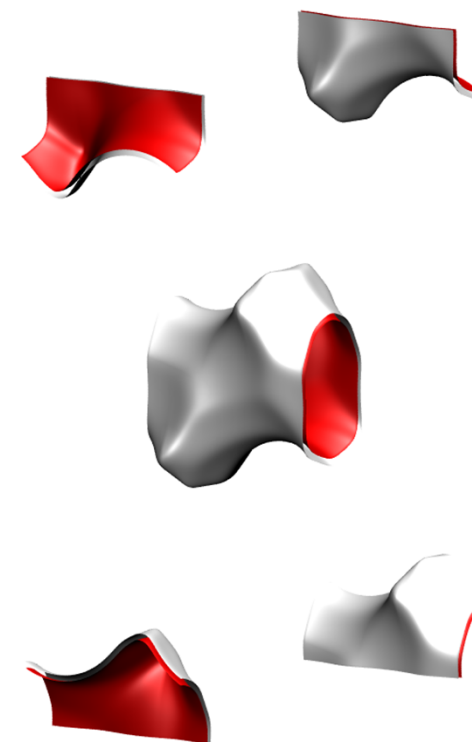
	MTW
$a / \text{Å}$	24.863
$b / \text{Å}$	5.012
$c / \text{Å}$	24.326
Cell volume / Å^3	2887.491
conversion factor for [molec/uc] to [mol per kg Framework]	0.2972
conversion factor for [molec/uc] to [kmol/m ³]	2.6759
ρ [kg/m ³]	1935.031
MW unit cell [g/mol(framework)]	3364.749
ϕ , fractional pore volume	0.215
open space / $\text{Å}^3/\text{uc}$	620.6
Pore volume / cm^3/g	0.111
Surface area / m^2/g	323.0
DeLaunay diameter / Å	5.69

TON pore landscape



10-ring channel of TON

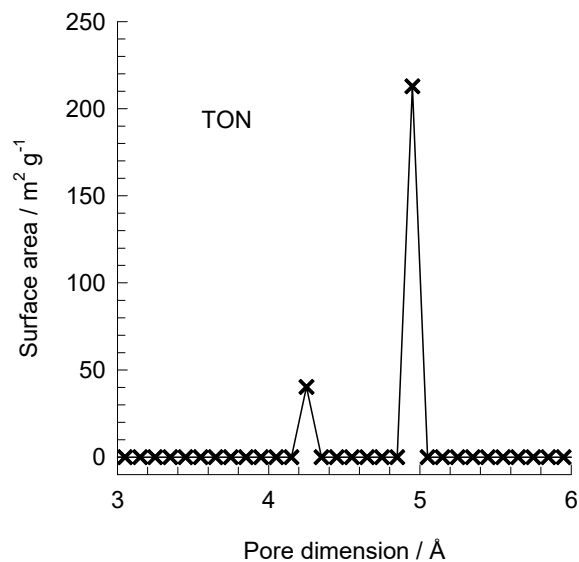
Fig. S9



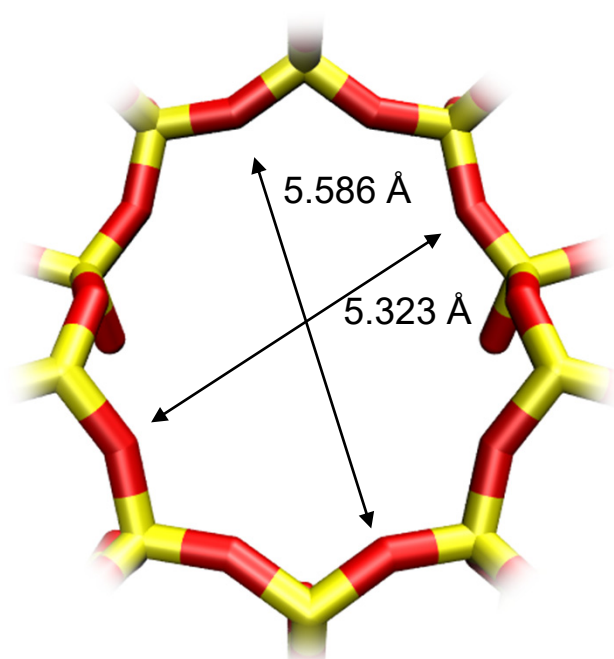
TON pore dimensions

Fig. S10

This plot of surface area versus pore dimension is determined using a combination of the DeLaunay triangulation method for pore dimension determination, and the procedure of Dürren for determination of the surface area.



10-ring channel of TON

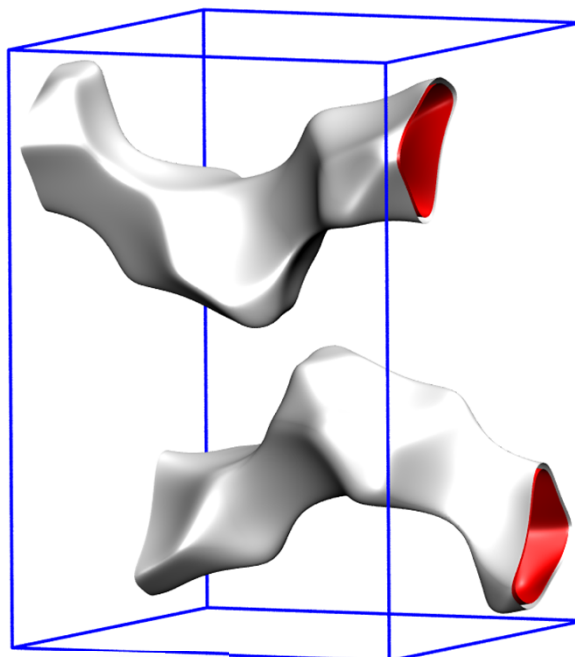


	TON
$a / \text{Å}$	13.859
$b / \text{Å}$	17.42
$c / \text{Å}$	5.038
Cell volume / Å^3	1216.293
conversion factor for [molec/uc] to [mol per kg Framework]	0.6935
conversion factor for [molec/uc] to [kmol/m ³]	7.1763
ρ [kg/m ³]	1968.764
MW unit cell [g/mol(framework)]	1442.035
ϕ , fractional pore volume	0.190
open space / $\text{Å}^3/\text{uc}$	231.4
Pore volume / cm^3/g	0.097
Surface area / m^2/g	253.0
DeLaunay diameter / Å	4.88

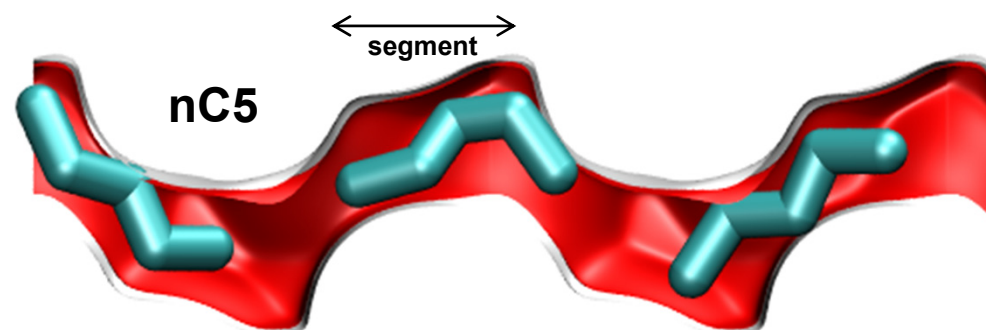
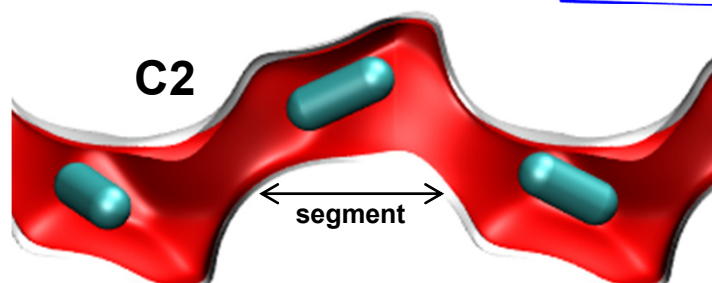
Co-Formate pore landscapes

Fig. S11

1 unit cell of Co-FA



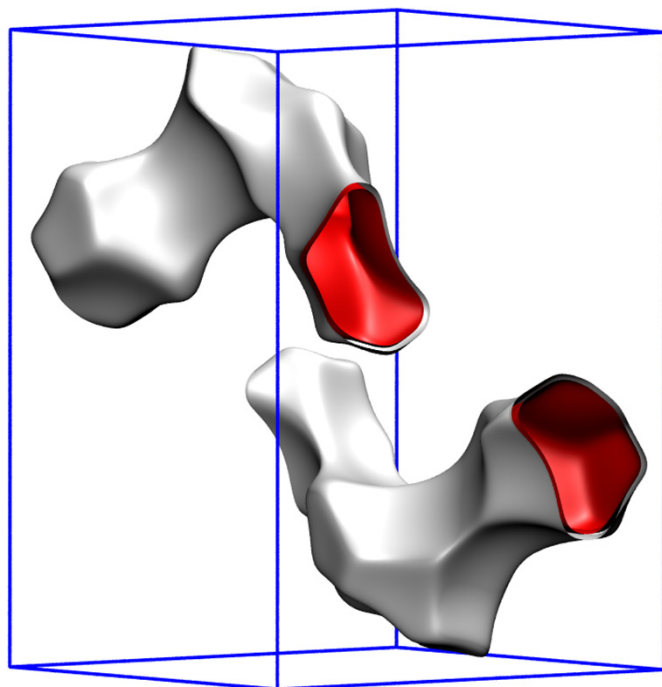
	Co-FA
$a / \text{\AA}$	11.3834
$b / \text{\AA}$	9.9292
$c / \text{\AA}$	14.4324
Cell volume / \AA^3	1631.27
conversion factor for [molec/uc] to [mol per kg Framework]	0.5595
ρ [kg/m ³]	1819.46
MW unit cell [g/mol(framework)]	1787.36
Pore volume / cm ³ /g	0.139



Mn-Formate pore landscapes

Fig. S12

1 unit cell of Mn-FA



	Mn-FA
$a / \text{\AA}$	11.715
$b / \text{\AA}$	10.248
$c / \text{\AA}$	15.159
Cell volume / \AA^3	1819.92
conversion factor for [molec/uc] to [mol per kg Framework]	0.5749
ρ [kg/m ³]	1587.11
MW unit cell [g/mol/framework]	1739.42
Pore volume / cm ³ /g	0.190

MIL-47 pore landscape

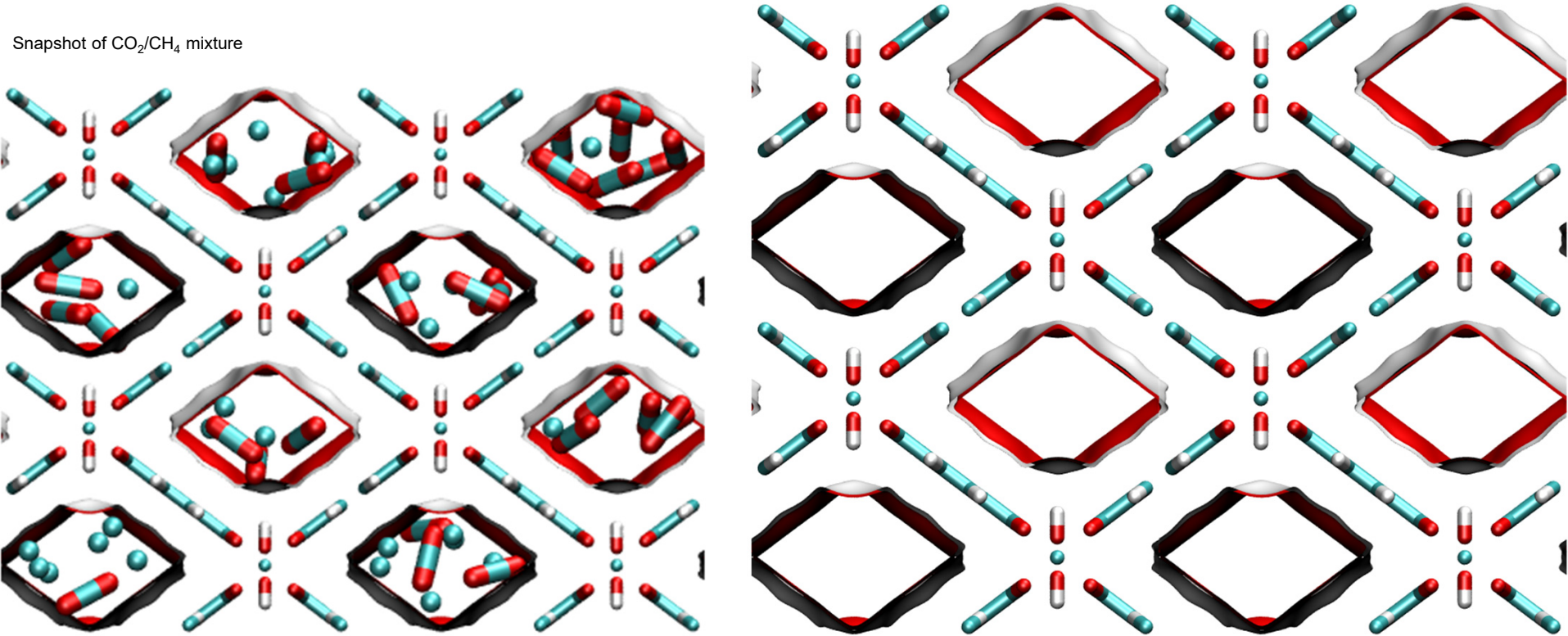
The structural information for MIL-47 was taken from

L. Alaerts, C.E.A. Kirschhock, M. Maes, M. van der Veen, V. Finsy, A. Depla, J.A. Martens, G.V. Baron, P.A. Jacobs, J.F.M. Denayer, D. De Vos, Selective Adsorption and Separation of Xylene Isomers and Ethylbenzene with the Microporous Vanadium(IV) Terephthalate MIL-47, *Angew. Chem. Int. Ed.* 46 (2007) 4293-4297.

V. Finsy, H. Verelst, L. Alaerts, D. De Vos, P.A. Jacobs, G.V. Baron, J.F.M. Denayer, Pore-Filling-Dependent Selectivity Effects in the Vapor-Phase Separation of Xylene Isomers on the Metal-Organic Framework MIL-47, *J. Am. Chem. Soc.* 130 (2008) 7110-7118.

K. Barthelet, J. Marrot, D. Riou, G. Férey, A Breathing Hybrid Organic - Inorganic Solid with Very Large Pores and High Magnetic Characteristics, *Angew. Chem. Int. Ed.* 41 (2007) 281-284.

Snapshot of CO₂/CH₄ mixture



MIL-47 dimensions

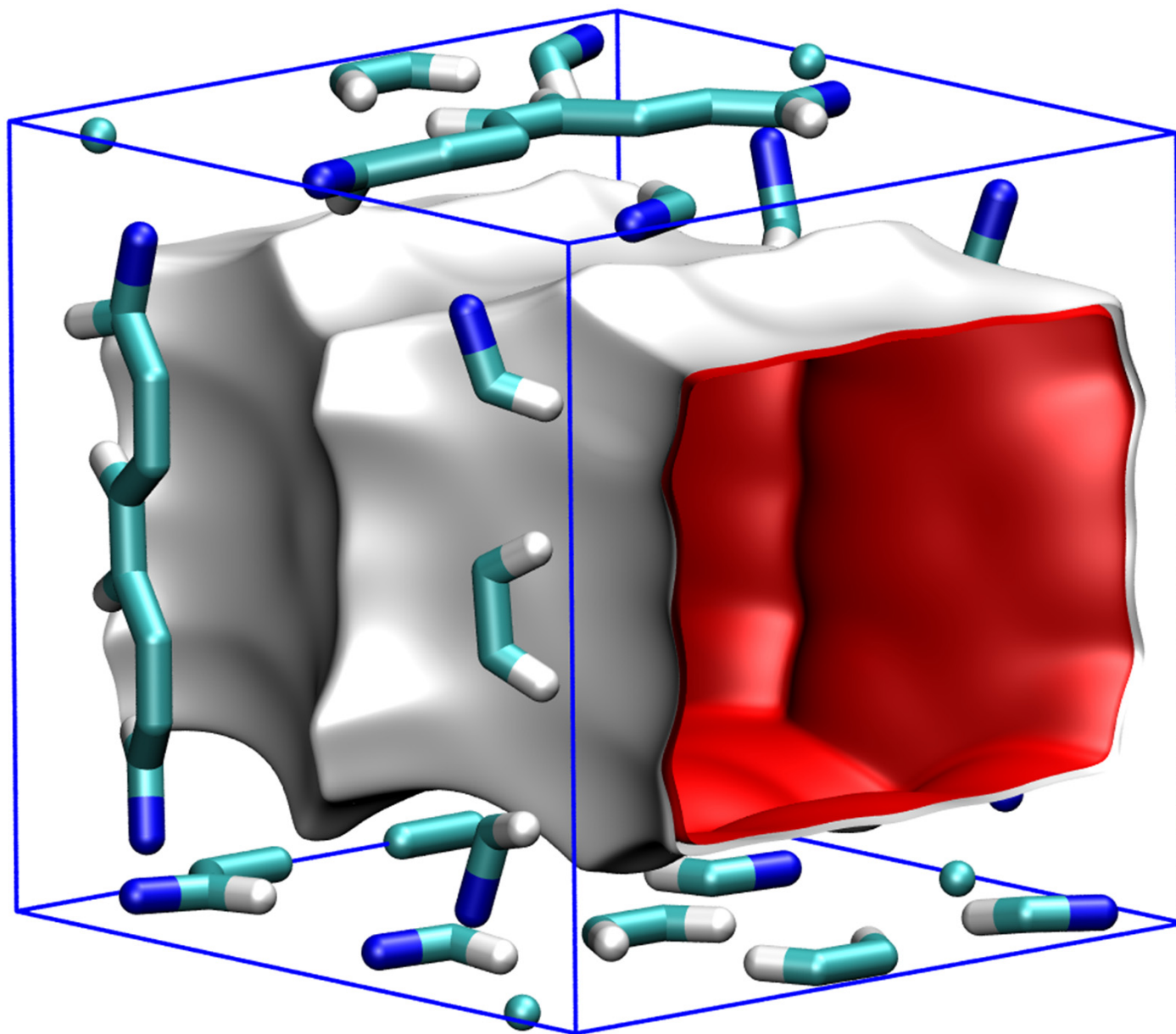
Fig. S14

	MIL-47
$a / \text{\AA}$	6.808
$b / \text{\AA}$	16.12
$c / \text{\AA}$	13.917
Cell volume / \AA^3	1527.321
conversion factor for [molec/uc] to [mol per kg Framework]	1.0824
conversion factor for [molec/uc] to [kmol/m ³]	1.7868
ρ [kg/m ³]	1004.481
MW unit cell [g/mol(framework)]	923.881
ϕ , fractional pore volume	0.608
open space / $\text{\AA}^3/\text{uc}$	929.3
Pore volume / cm ³ /g	0.606
Surface area /m ² /g	1472.8
DeLaunay diameter / \AA	8.03

One-dimensional diamond-shaped channels with free internal diameter of 8 \AA

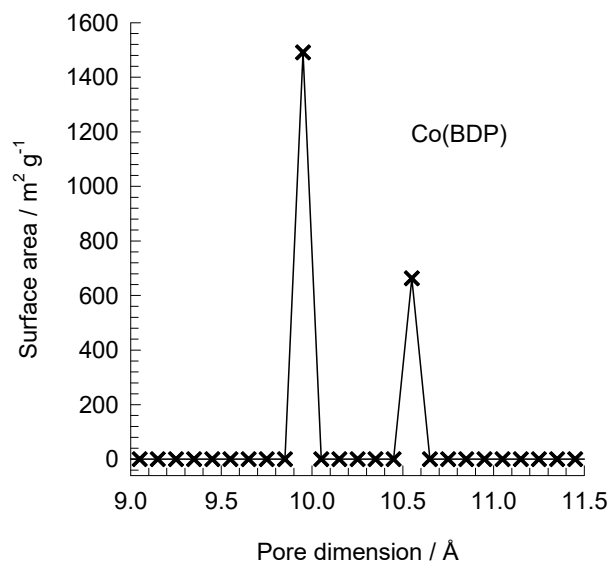
Co(BDP) pore landscapes

Fig. S15



Co(BDP) pore dimensions

Fig. S16

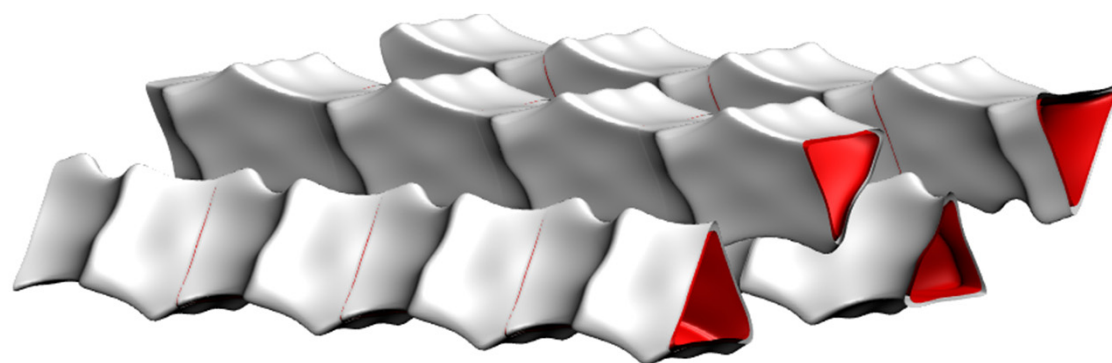
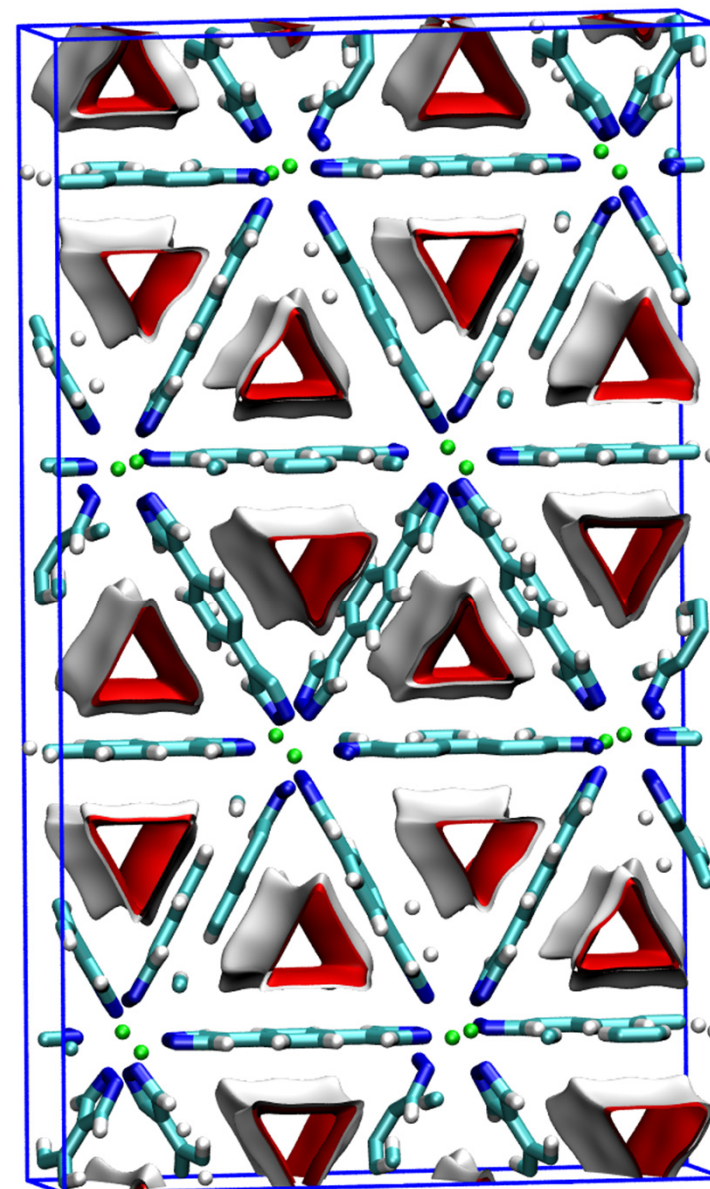
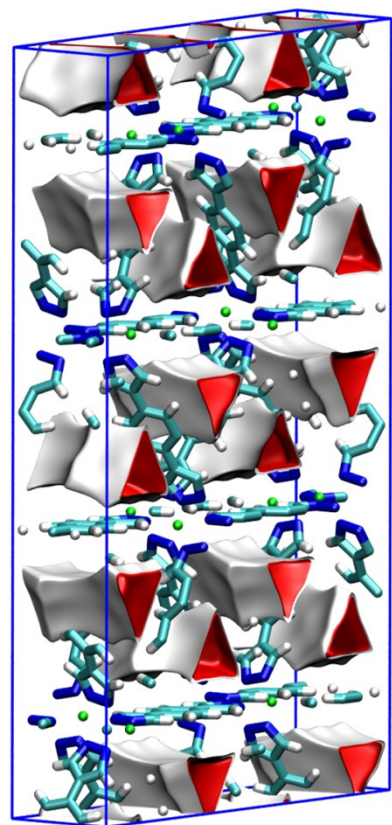


This plot of surface area versus pore dimension is determined using a combination of the DeLaunay triangulation method for pore dimension determination, and the procedure of Dürren for determination of the surface area.

	CoBDP
$a / \text{Å}$	13.2529
$b / \text{Å}$	13.253
$c / \text{Å}$	13.995
Cell volume / Å^3	2458.091
conversion factor for [molec/uc] to [mol per kg Framework]	0.9362
conversion factor for [molec/uc] to [kmol/m ³]	1.0102
ρ [kg/m ³]	721.5517
MW unit cell [g/mol(framework)]	1068.094
ϕ , fractional pore volume	0.669
open space / $\text{Å}^3/\text{uc}$	1643.9
Pore volume / cm ³ /g	0.927
Surface area / m ² /g	2148.8
DeLaunay diameter / Å	10

$\text{Fe}_2(\text{BDP})_3$ pore landscapes

Fig. S17



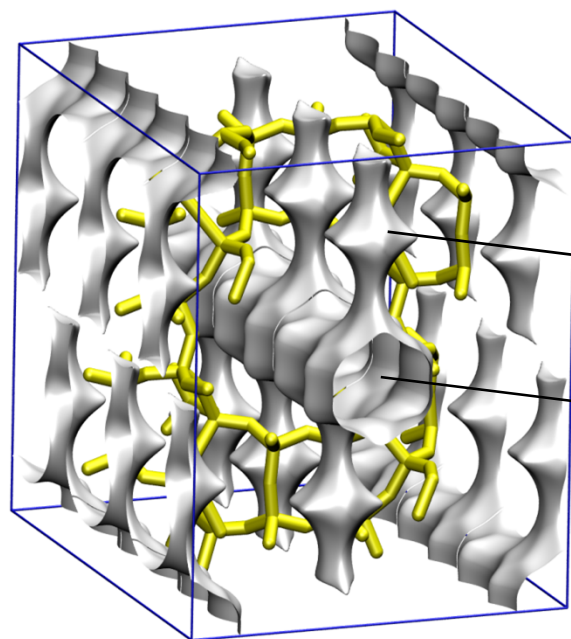
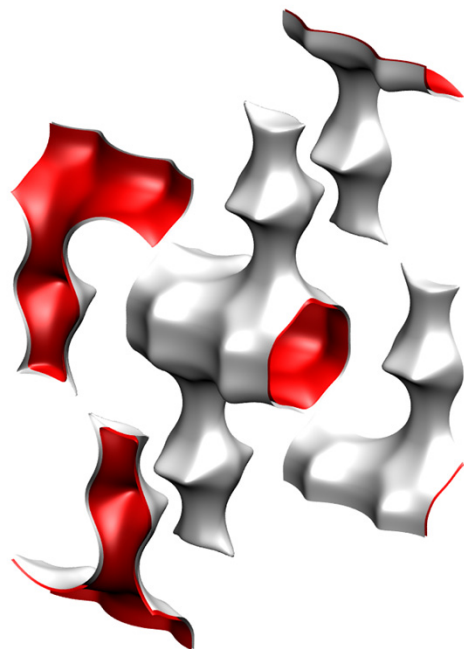
$\text{Fe}_2(\text{BDP})_3$ pore dimensions

Fig. S18

	$\text{Fe}_2(\text{BDP})_3$
$a / \text{\AA}$	7.104
$b / \text{\AA}$	26.491
$c / \text{\AA}$	45.353
Cell volume / \AA^3	8535.33
ρ [kg/m ³]	1145.46
Pore volume / cm ³ /g	0.4
Surface area/ cm ² /g	1230
DeLaunay diameter / \AA	4.9

MOR pore landscape

Fig. S19



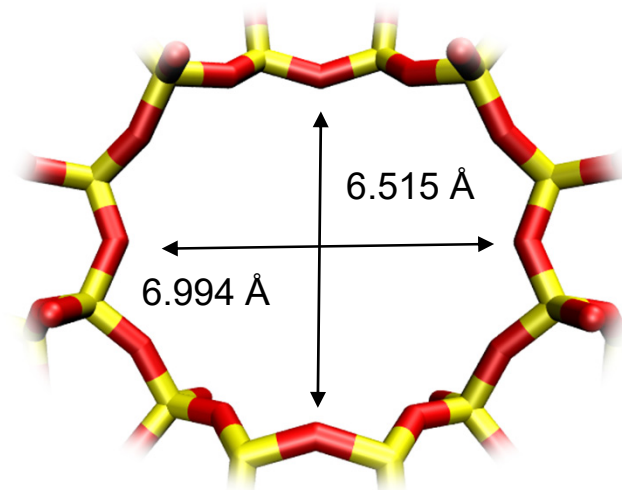
8 ring
side pocket

12 ring
channel

	MOR
$a / \text{\AA}$	18.094
$b / \text{\AA}$	20.516
$c / \text{\AA}$	7.524
Cell volume / \AA^3	2793.033
conversion factor for [molec/uc] to [mol per kg Framework]	0.3467
conversion factor for [molec/uc] to [kmol/m ³]	2.0877
ρ [kg/m ³]	1714.691
MW unit cell [g/mol/framework]	2884.07
ϕ , fractional pore volume	0.285
open space / $\text{\AA}^3/\text{uc}$	795.4
Pore volume / cm ³ /g	0.166
Surface area / m ² /g	417.0
DeLaunay diameter / \AA	6.44

MOR pore dimensions

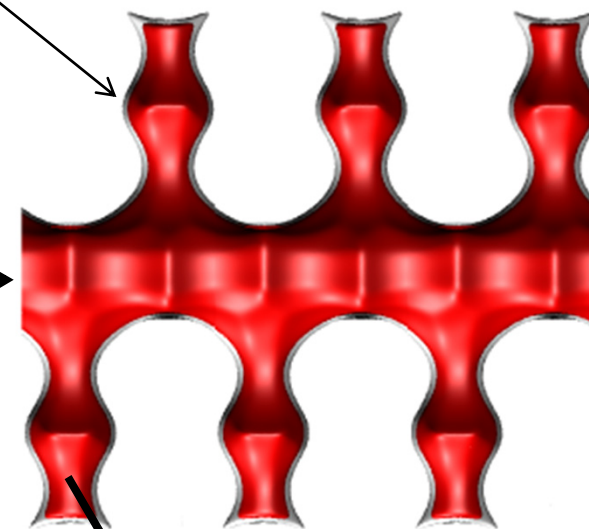
Fig. S20



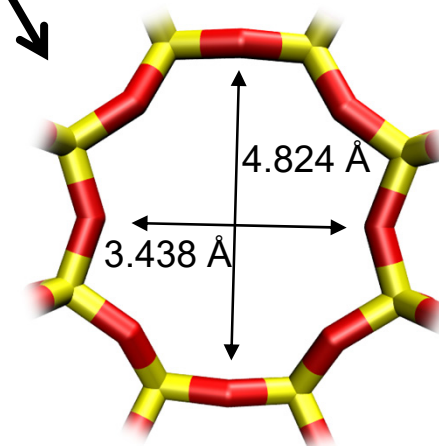
MOR Channel [1 0 0]

12-ring
main channels

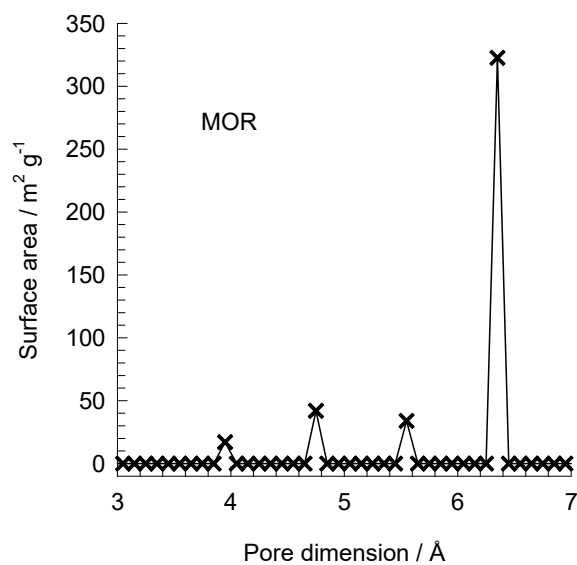
8 ring
side pocket



8 ring
side pocket



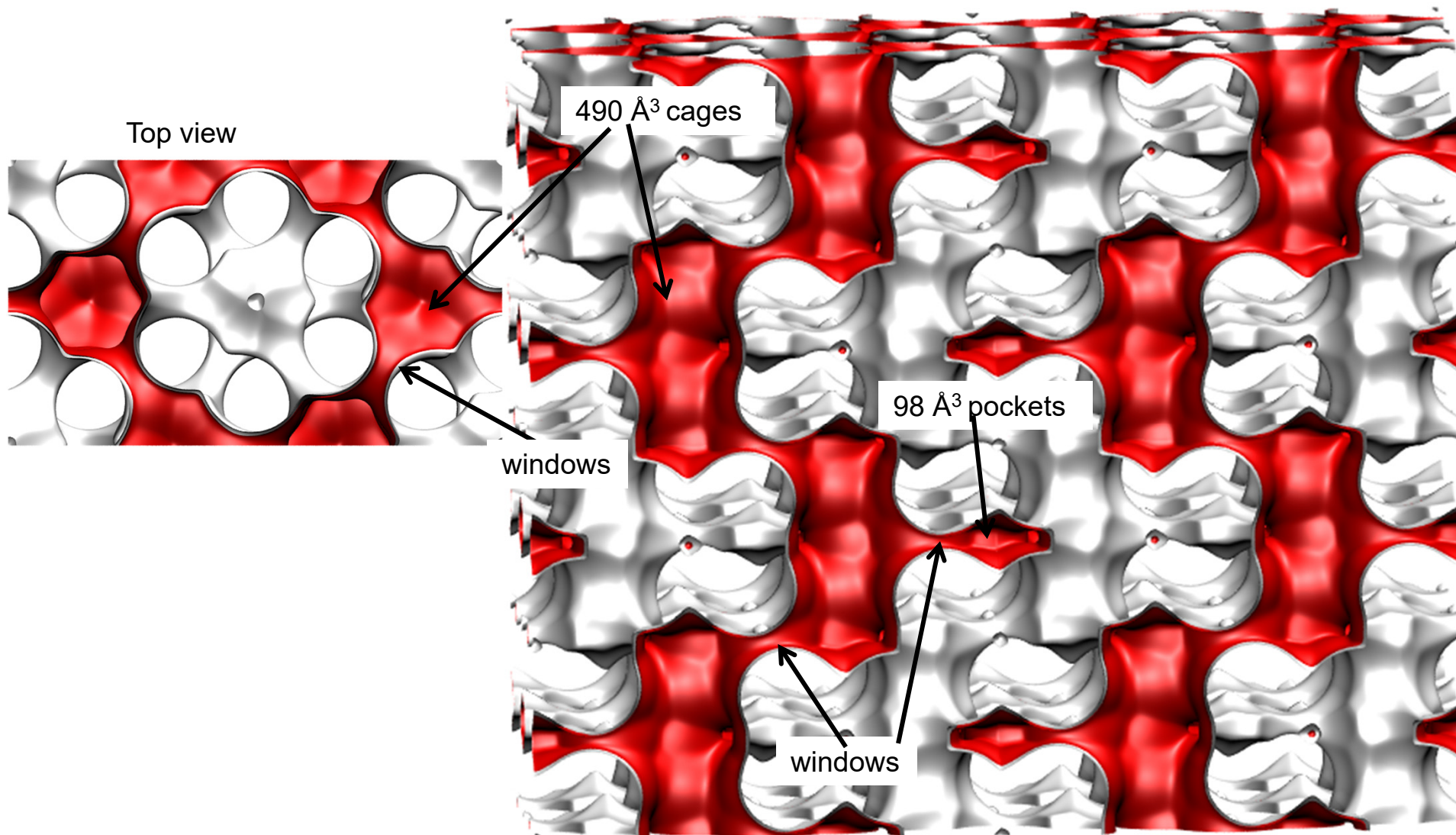
MOR [0 1 0]



This plot of surface area versus pore dimension is determined using a combination of the DeLaunay triangulation method for pore dimension determination, and the procedure of Düren for determination of the surface area.

AFX pore landscape

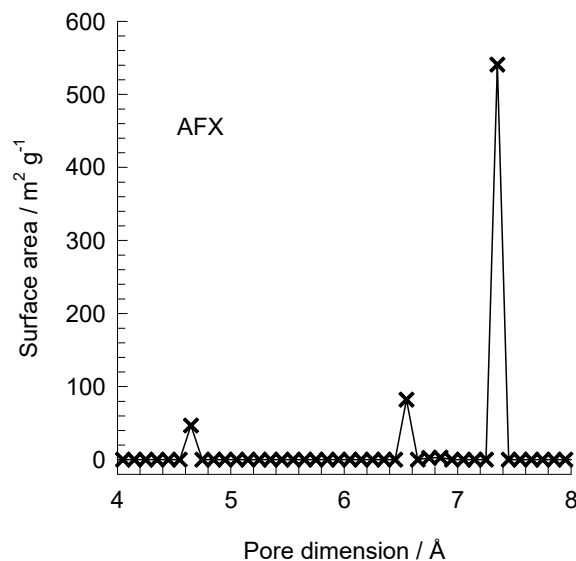
Fig. S21



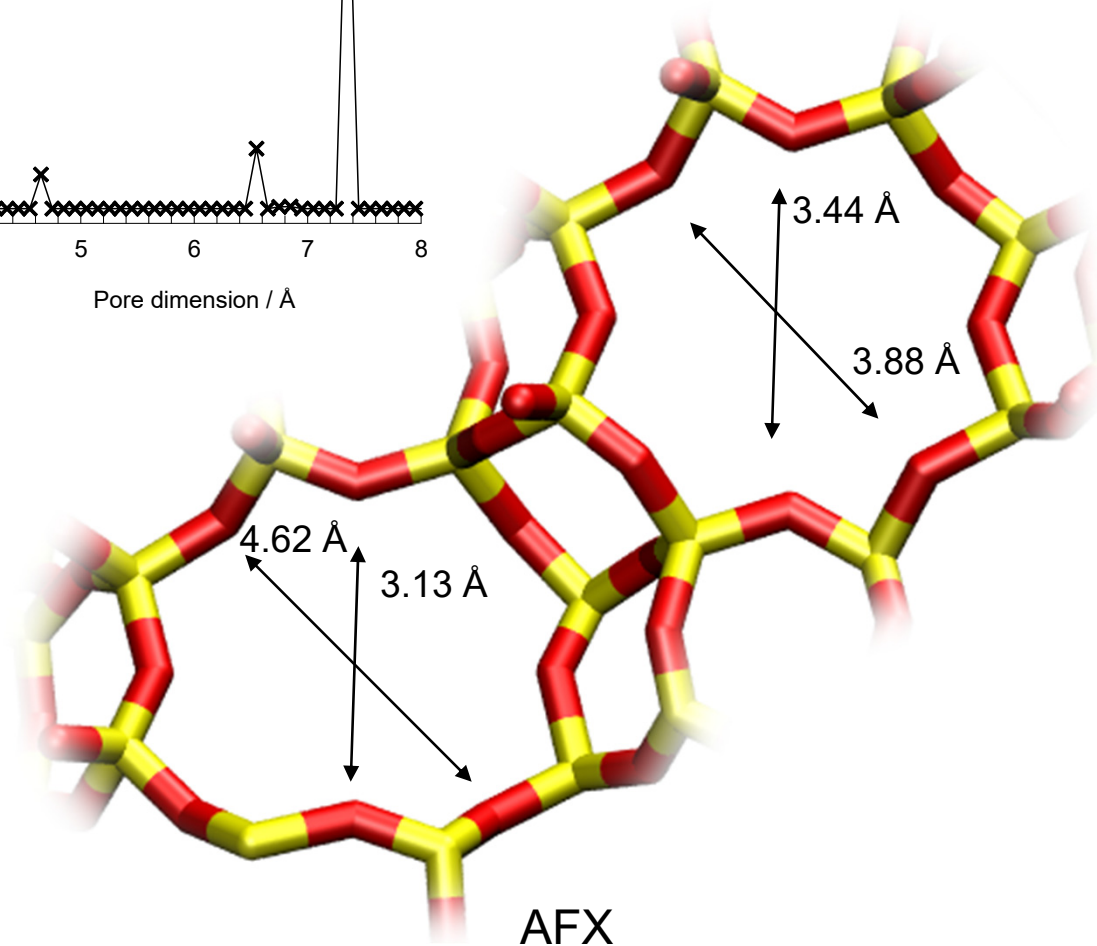
Structural information from: C. Baerlocher, L.B. McCusker, Database of Zeolite Structures, International Zeolite Association, <http://www.iza-structure.org/databases/>

AFX window sizes and pore dimensions

Fig. S22

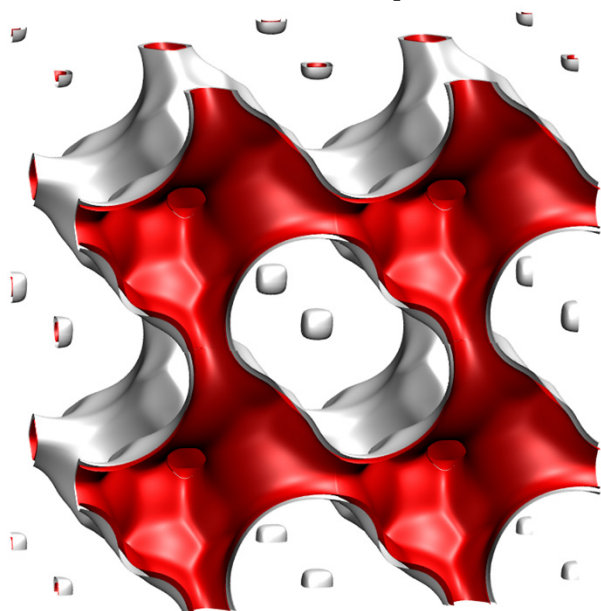


	AFX
$a / \text{Å}$	23.836
$b / \text{Å}$	13.762
$c / \text{Å}$	19.949
Cell volume / Å^3	6543.891
conversion factor for [molec/uc] to [mol per kg Framework]	0.1734
conversion factor for [molec/uc] to [kmol/m ³]	0.7059
ρ [kg/m ³]	1463.713
MW unit cell [g/mol/framework]	5768.141
ϕ , fractional pore volume	0.359
open space / $\text{Å}^3/\text{uc}$	2352.5
Pore volume / cm^3/g	0.246
Surface area / m^2/g	674.0
DeLaunay diameter / Å	3.44

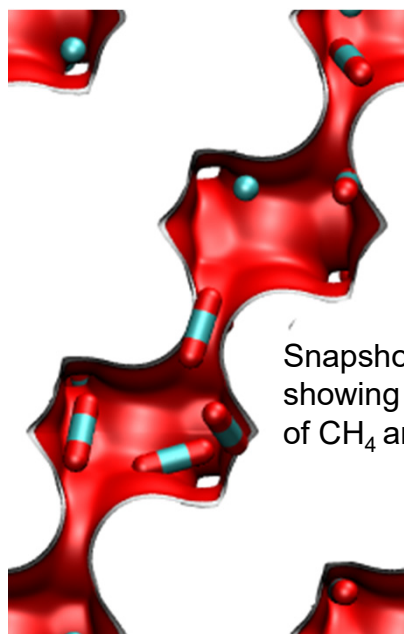
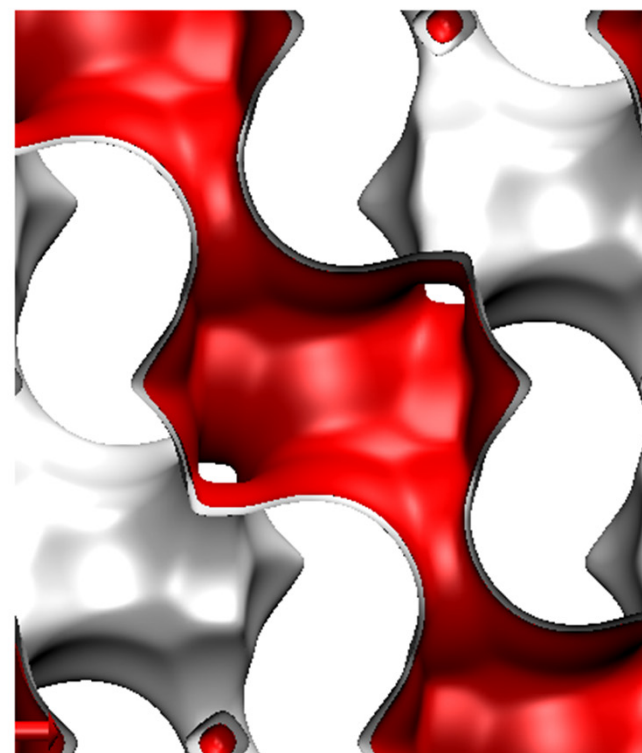


The window dimension calculated using the van der Waals diameter of framework atoms = 2.7 Å are indicated above by the arrows.

CHA landscape



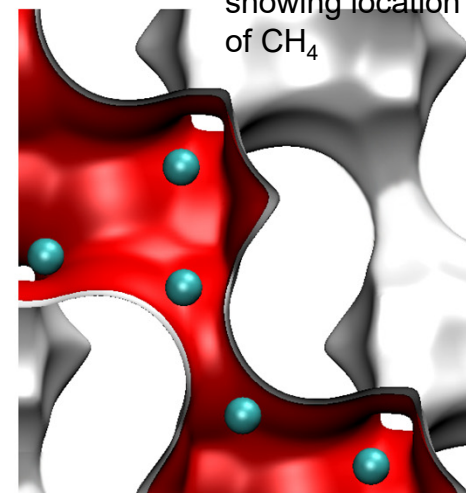
There are 6 cages per unit cell. The volume of one CHA cage is 316.4 \AA^3 , slightly larger than that of a single cage of DDR (278 \AA^3), but significantly lower than FAU (786 \AA^3).



Snapshots showing location of CH_4 and CO_2



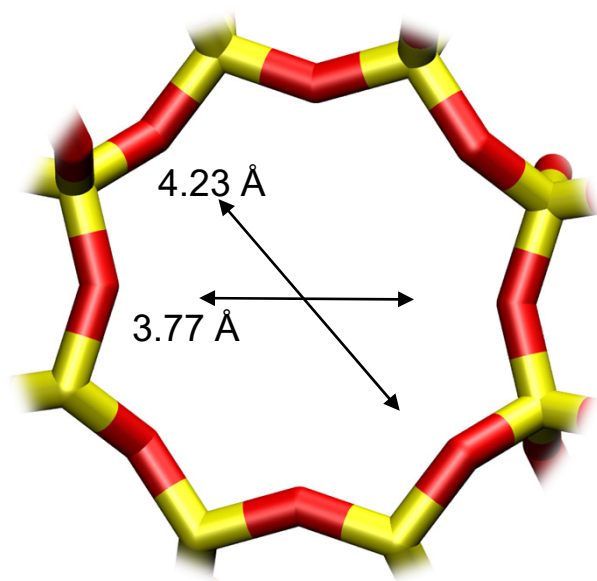
Snapshots showing location of CH_4



Structural information from: C. Baerlocher, L.B. McCusker, Database of Zeolite Structures, International Zeolite Association, <http://www.iza-structure.org/databases/>

CHA window and pore dimensions

Fig. S24



CHA

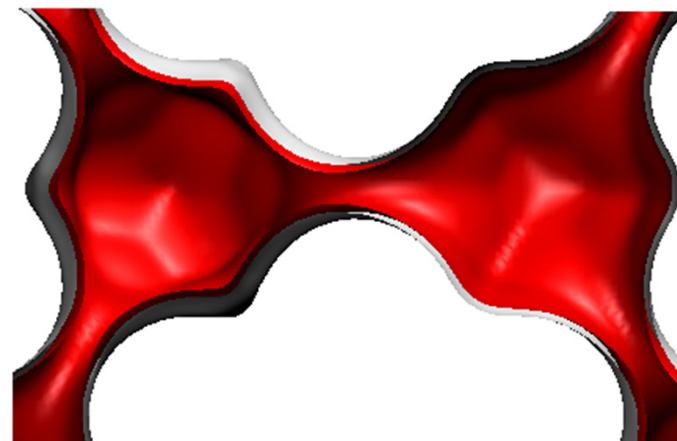
The window dimensions calculated using the van der Waals diameter of framework atoms = 2.7 Å are indicated above by the arrows.

	CHA
$a / \text{Å}$	15.075
$b / \text{Å}$	23.907
$c / \text{Å}$	13.803
Cell volume / Å^3	4974.574
conversion factor for [molec/uc] to [mol per kg Framework]	0.2312
conversion factor for [molec/uc] to [kmol/m ³]	0.8747
ρ [kg/m ³]	1444.1
MW unit cell [g/mol(framework)]	4326.106
ϕ , fractional pore volume	0.382
open space / $\text{Å}^3/\text{uc}$	1898.4
Pore volume / cm^3/g	0.264
Surface area / m^2/g	758.0
DeLaunay diameter / Å	3.77

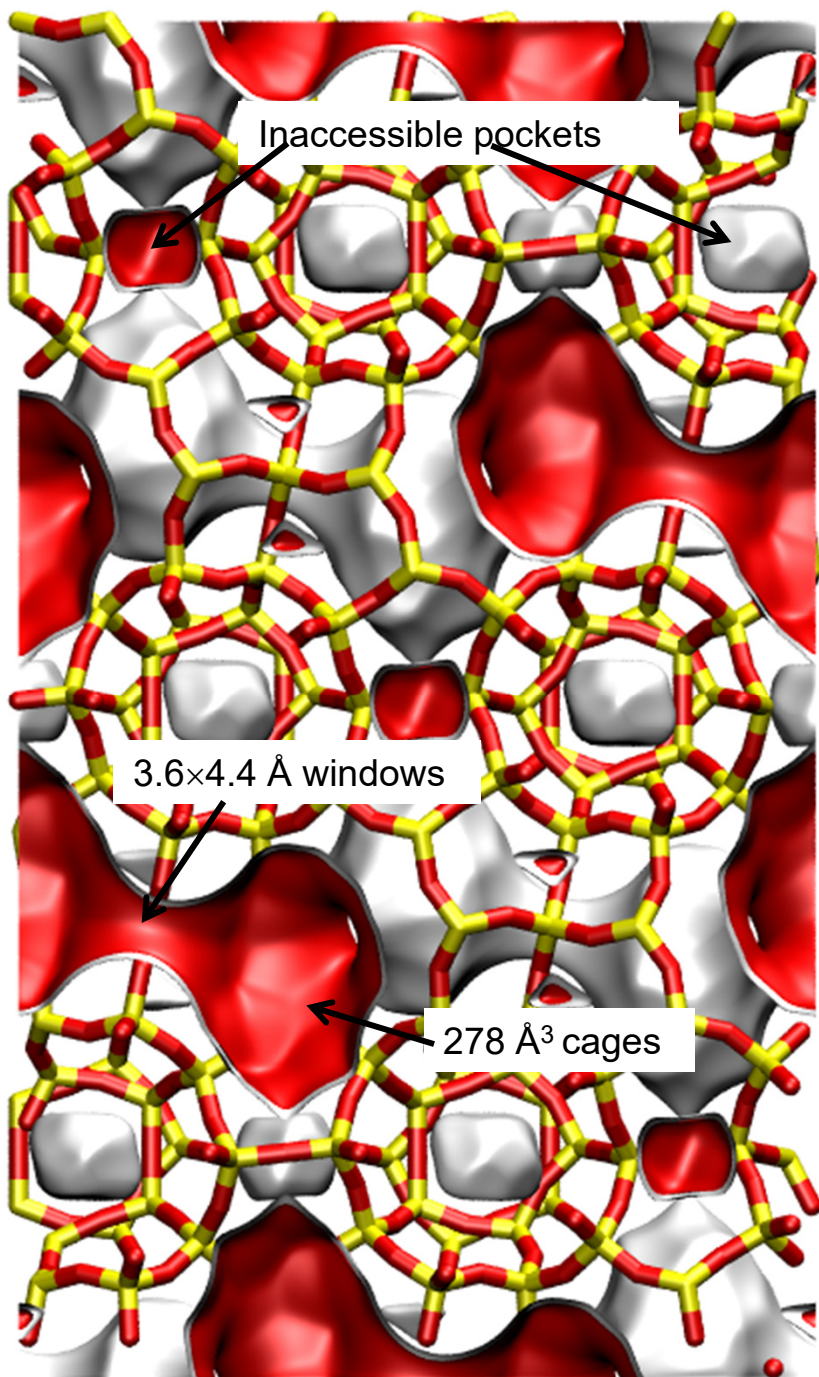
DDR landscape

To convert from molecules per unit cell to mol kg⁻¹, multiply by 0.06936.
The pore volume is 0.182 cm³/g.

There are 12 cages per unit cell.
The volume of one DDR cage is 278 Å³, significantly smaller than that of a single cage of FAU (786 Å³), or ZIF-8 (1168 Å³).

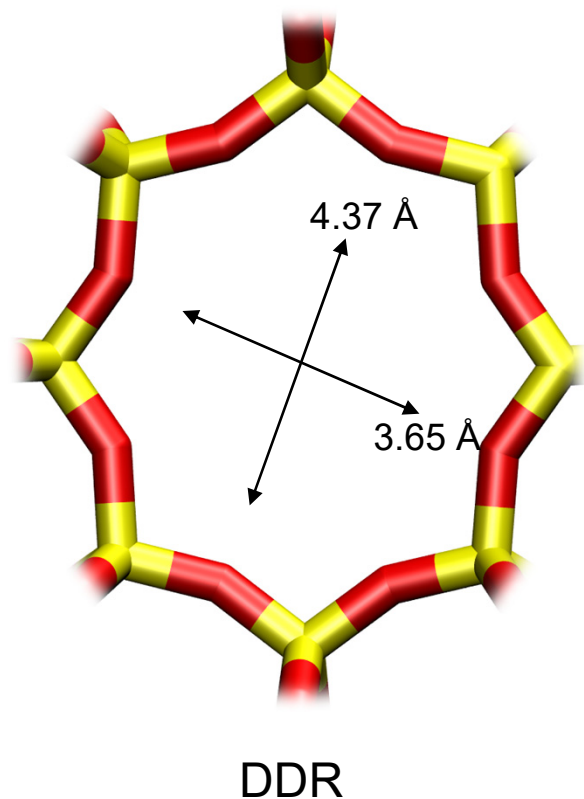


Structural information from: C. Baerlocher, L.B. McCusker, Database of Zeolite Structures, International Zeolite Association, <http://www.iza-structure.org/databases/>



DDR window and pore dimensions

Fig. S26



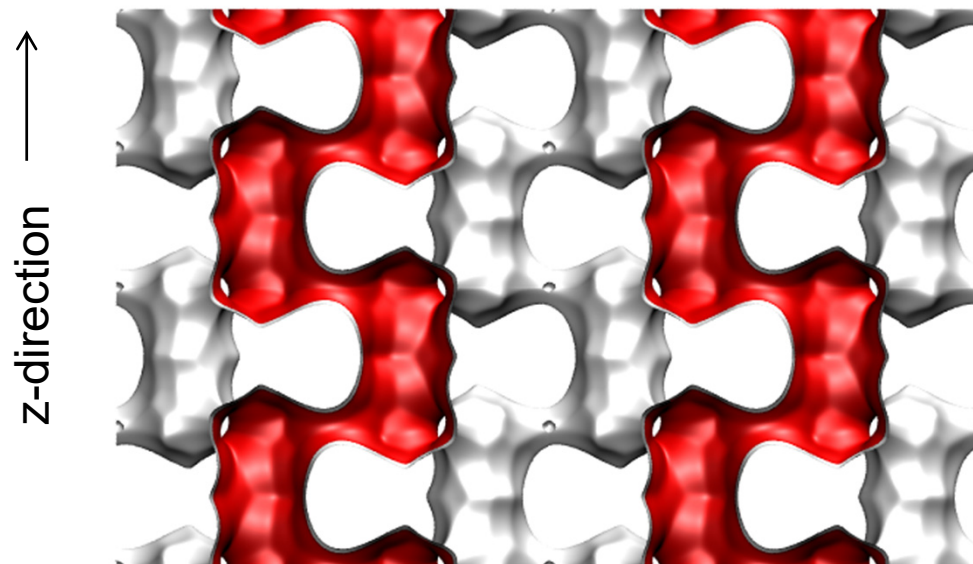
The window dimensions calculated using the van der Waals diameter of framework atoms = 2.7 Å are indicated above by the arrows.

	DDR
$a / \text{Å}$	24.006
$b / \text{Å}$	13.86
$c / \text{Å}$	40.892
Cell volume / Å^3	13605.72
conversion factor for [molec/uc] to [mol per kg Framework]	0.0693
conversion factor for [molec/uc] to [kmol/m^3]	0.4981
ρ [kg/m^3]	1759.991
MW unit cell [g/mol(framework)]	14420.35
ϕ , fractional pore volume	0.245
open space / $\text{Å}^3/\text{uc}$	3333.5
Pore volume / cm^3/g	0.139
Surface area / m^2/g	350.0
DeLaunay diameter / Å	3.65

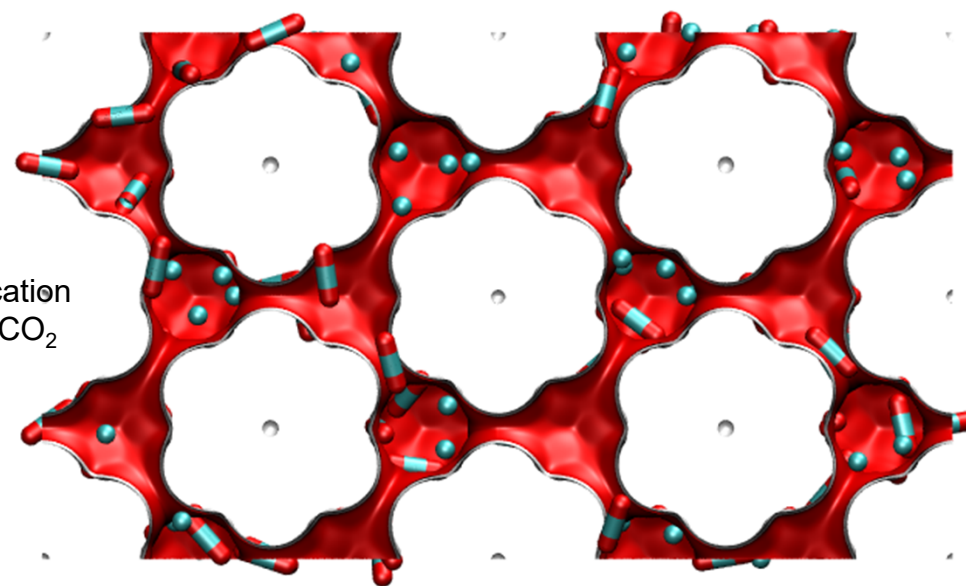
ERI pore landscape

Fig. S27

There are 4 cages per unit cell.
The volume of one ERI cage is 408.7 \AA^3 ,
significantly smaller than that of a single cage
of FAU-Si (786 \AA^3), or ZIF-8 (1168 \AA^3).



x-y projection

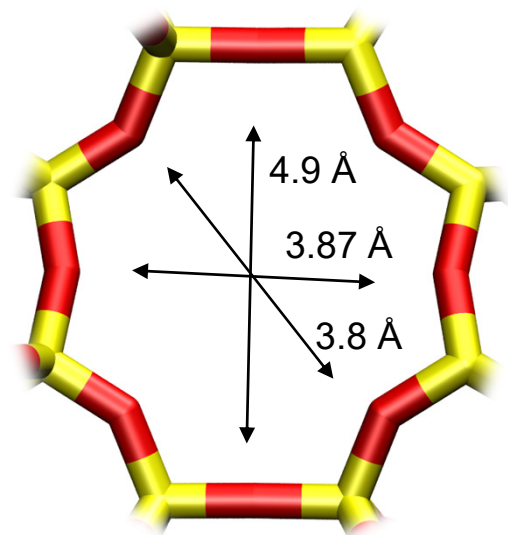


Snapshots
showing location
of CH₄ and CO₂

Structural information from: C. Baerlocher, L.B. McCusker, Database of Zeolite Structures, International Zeolite Association, <http://www.iza-structure.org/databases/>

ERI window and pore dimensions

Fig. S28



ERI

The window dimensions calculated using the van der Waals diameter of framework atoms = 2.7 Å are indicated above by the arrows.

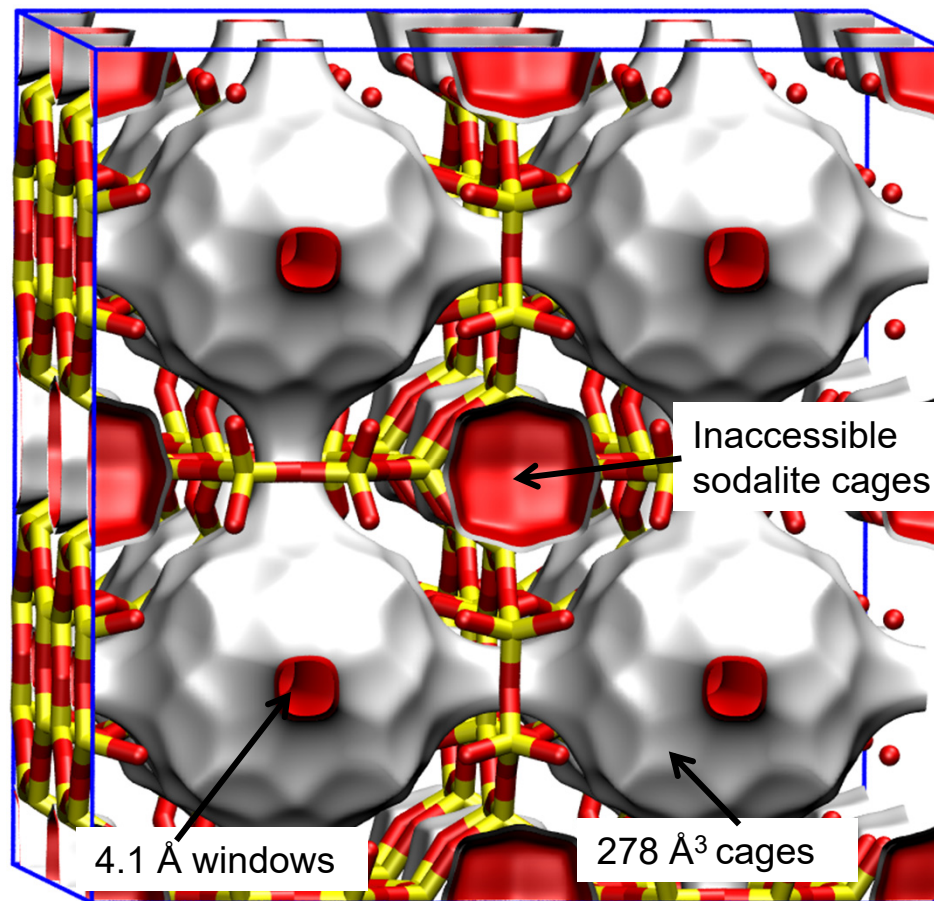
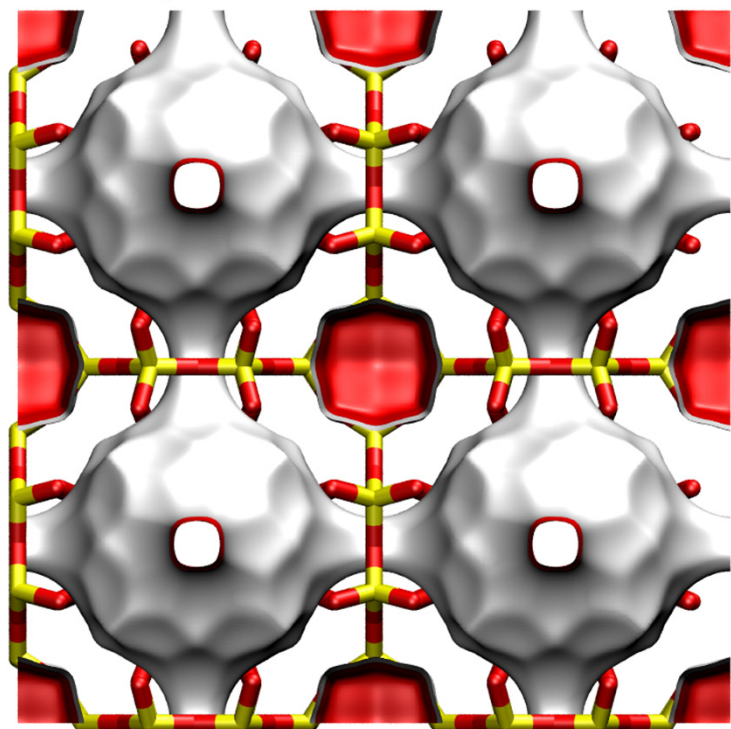
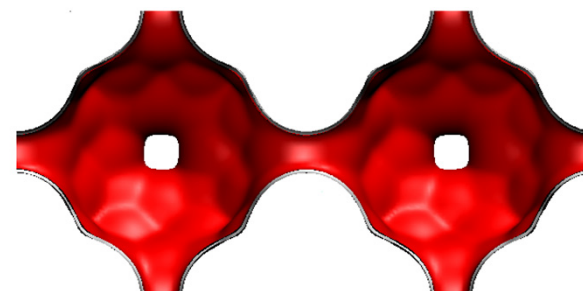
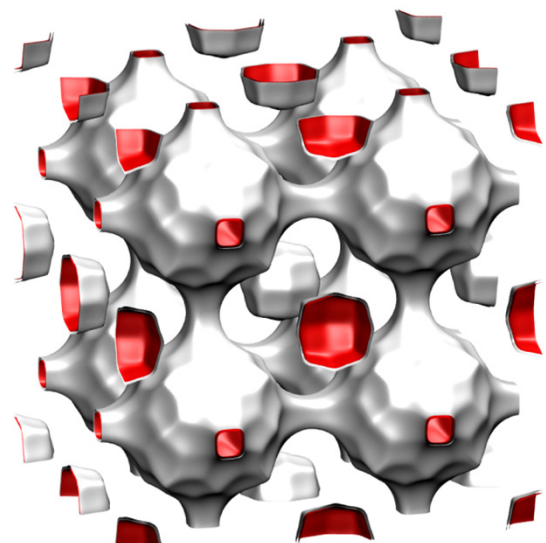
	ERI
$a / \text{Å}$	22.953
$b / \text{Å}$	13.252
$c / \text{Å}$	14.81
Cell volume / Å^3	4504.804
conversion factor for [molec/uc] to [mol per kg Framework]	0.2312
conversion factor for [molec/uc] to [kmol/m^3]	1.0156
ρ [kg/m^3]	1594.693
MW unit cell [$\text{g}/\text{mol}(\text{framework})$]	4326.106
ϕ , fractional pore volume	0.363
open space / $\text{Å}^3/\text{uc}$	1635.0
Pore volume / cm^3/g	0.228
Surface area / m^2/g	635.0
DeLaunay diameter / Å	3.81

LTA-Si landscapes

Fig. S29

This is a *hypothetical* structure constructed from dealuminized LTA-5A structure

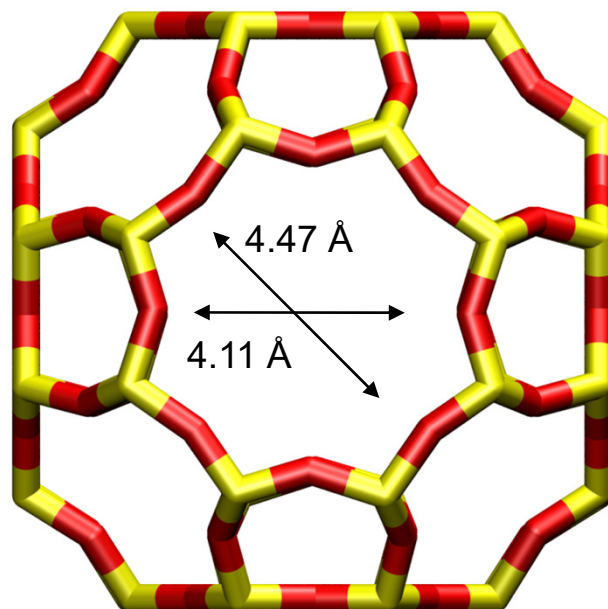
There are 8 cages per unit cell. The volume of one LTA cage is 743 \AA^3 , intermediate in size between a single cage of ZIF-8 (1168 \AA^3) and of DDR (278 \AA^3).



LTA-Si window and pore dimensions

Fig. S30

8-ring
window
of LTA

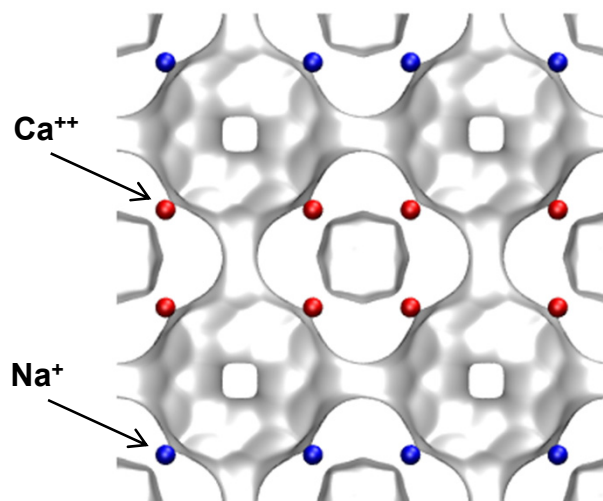


The window dimension calculated using the van der Waals diameter of framework atoms = 2.7 Å is indicated above by the arrows.

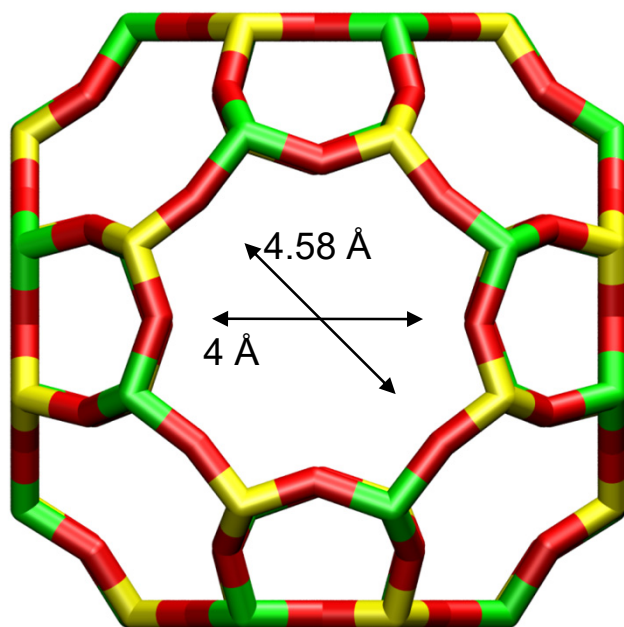
	LTA-Si
$a / \text{Å}$	24.61
$b / \text{Å}$	24.61
$c / \text{Å}$	24.61
Cell volume / Å^3	14905.1
conversion factor for [molec/uc] to [mol per kg Framework]	0.0867
conversion factor for [molec/uc] to [kmol/m^3]	0.2794
ρ [kg/m^3]	1285.248
MW unit cell [g/mol(framework)]	11536.28
ϕ , fractional pore volume	0.399
open space / $\text{Å}^3/\text{uc}$	5944.4
Pore volume / cm^3/g	0.310
Surface area / m^2/g	896.0
DeLaunay diameter / Å	4.10

LTA-5A

Fig. S31



LTA-5A (32 Na+, 32 Ca++)



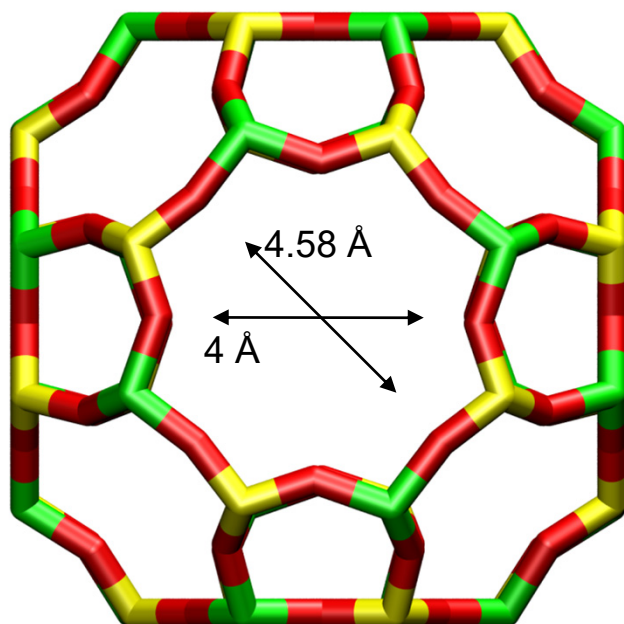
LTA-5A

The window dimension calculated using the van der Waals diameter of framework atoms = 2.7 Å is indicated above by the arrow.

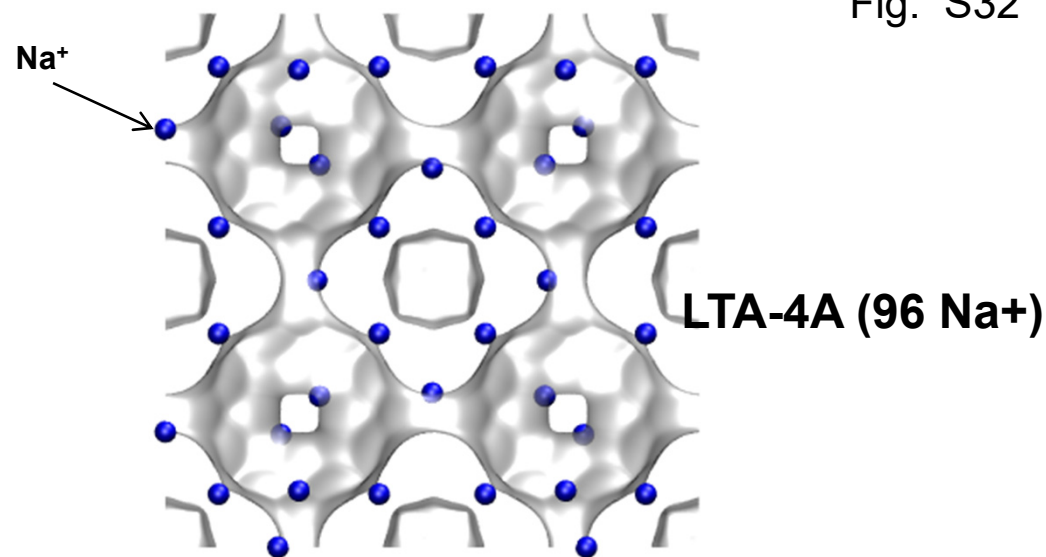
	LTA-5A
$a / \text{Å}$	24.555
$b / \text{Å}$	24.555
$c / \text{Å}$	24.555
Cell volume / Å^3	14805.39
conversion factor for [molec/uc] to [mol per kg Framework]	0.0744
conversion factor for [molec/uc] to [kmol/m^3]	0.2955
ρ [kg/m^3] (with cations)	1508.376
MW unit cell [g/mol(framework+cations)]	13448.48
ϕ , fractional pore volume	0.380
open space / $\text{Å}^3/\text{uc}$	5620.4
Pore volume / cm^3/g	0.252
Surface area / m^2/g	
DeLaunay diameter / Å	4.00

LTA-4A

Fig. S32



LTA-4A



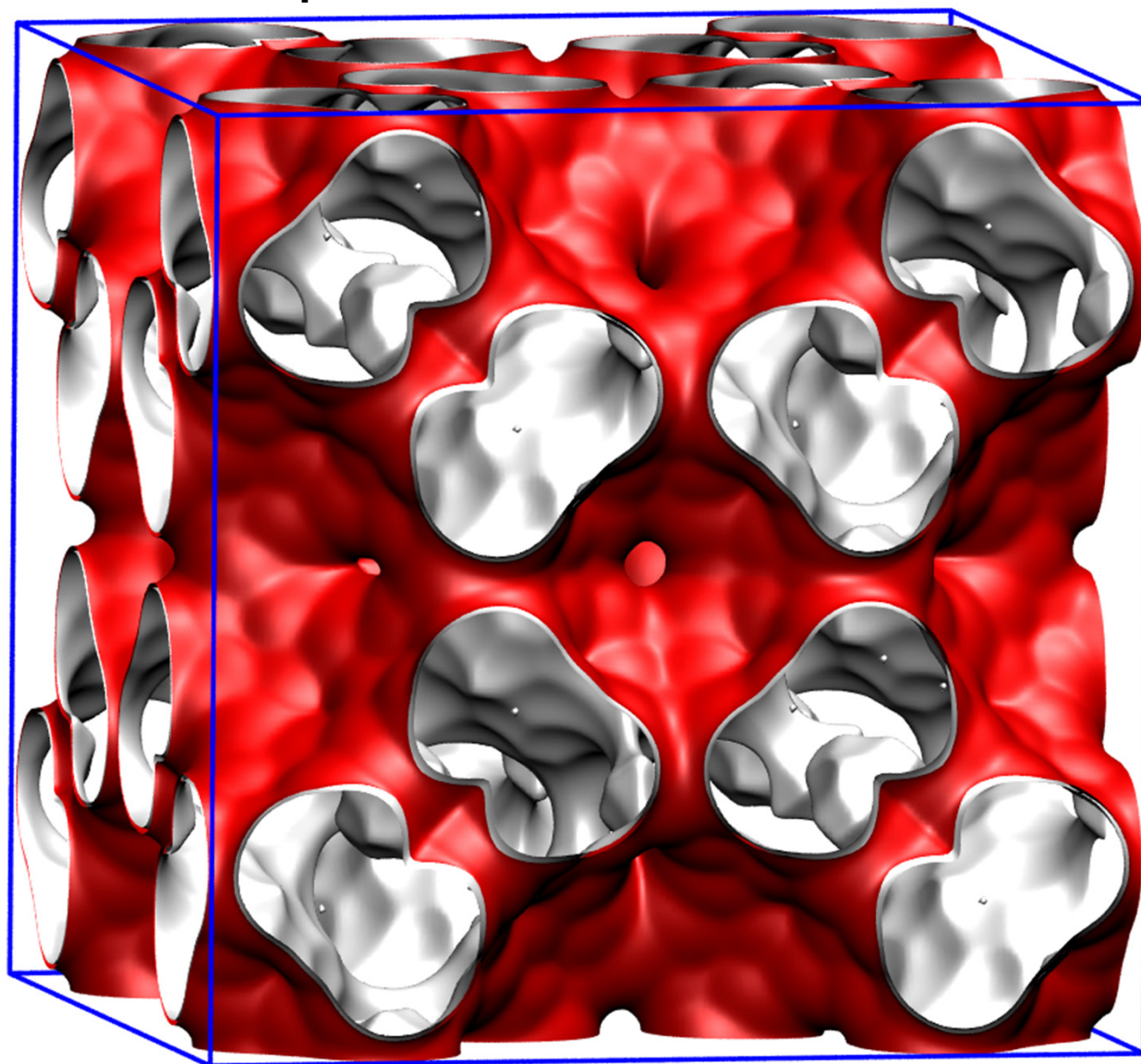
The window dimension calculated using the van der Waals diameter of framework atoms = 2.7 Å is indicated above by the arrow.

Note that the Na⁺ ions partially block the windows and therefore the diffusivities in LTA-4A are significantly lower than that for LTA Si. These cannot be determined from MD.

	LTA-4A
<i>a</i> / Å	24.555
<i>b</i> / Å	24.555
<i>c</i> / Å	24.555
Cell volume / Å ³	14805.39
conversion factor for [molec/uc] to [mol per kg Framework]	0.0733
conversion factor for [molec/uc] to [kmol/m ³]	0.2991
ρ [kg/m ³] (with cations)	1529.55
MW unit cell [g/mol(framework+cations)]	13637.27
ϕ , fractional pore volume	0.375
open space / Å ³ /uc	5552.0
Pore volume / cm ³ /g	0.245
Surface area / m ² /g	
DeLaunay diameter / Å	4.00

TSC landscape

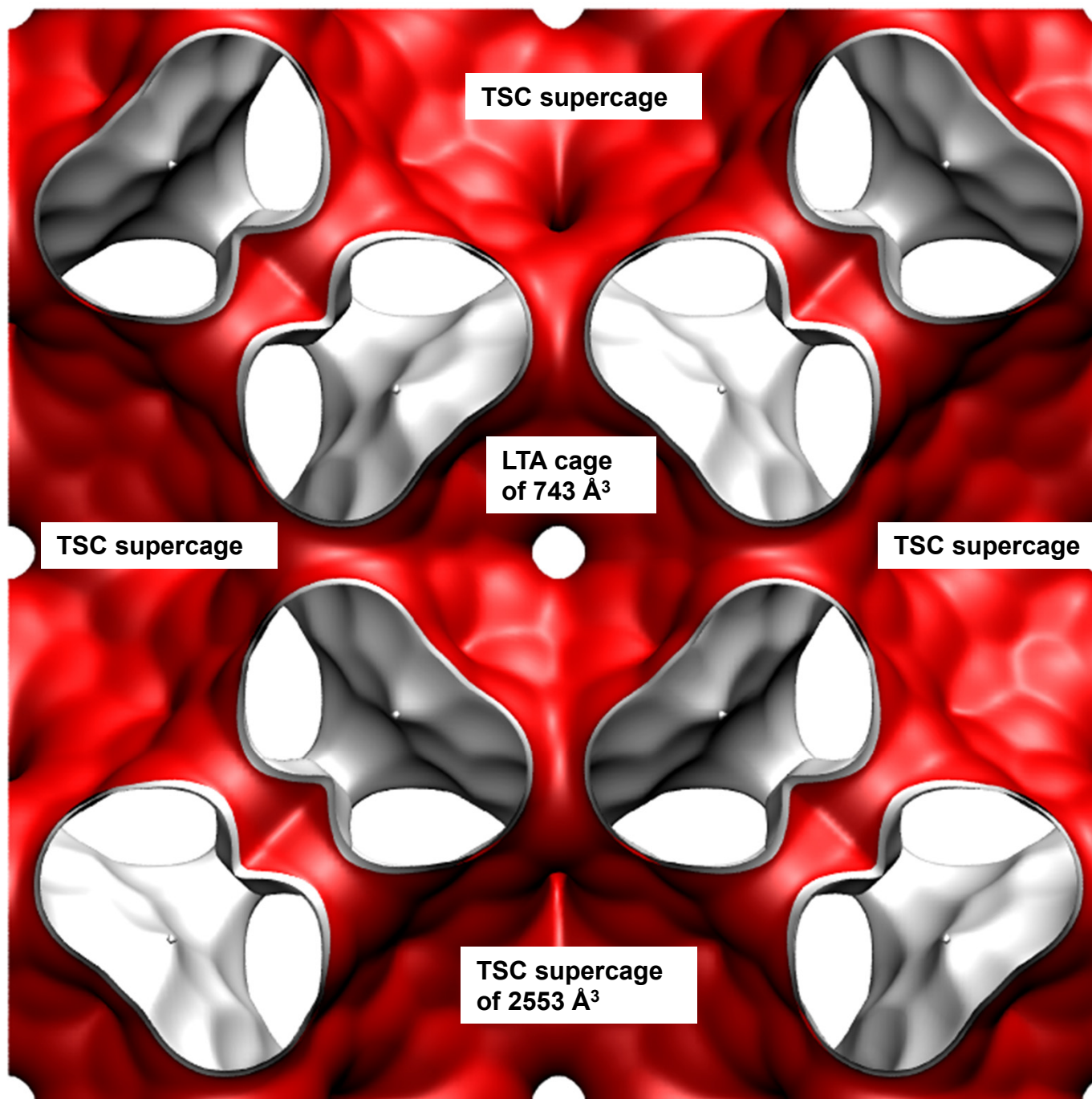
Fig. S33



**Unit cell
of TSC**

Structural information from: C. Baerlocher, L.B. McCusker, Database of Zeolite Structures, International Zeolite Association, <http://www.iza-structure.org/databases/>

Fig. S34

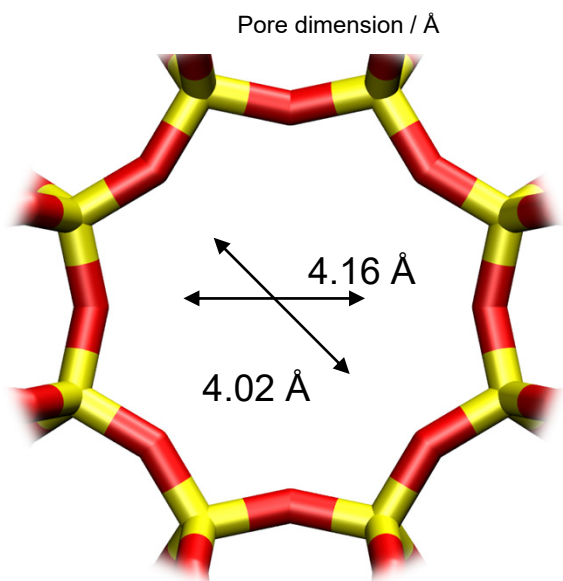
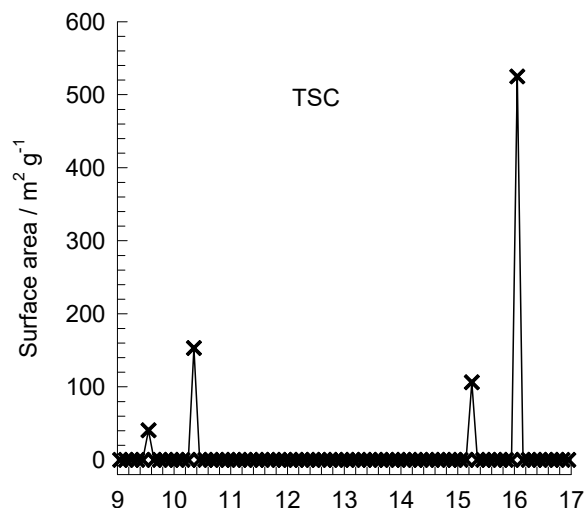


8-ring windows of two sizes:
4.2x4.2 Å along [100]
3.1x5.6 Å along [110]

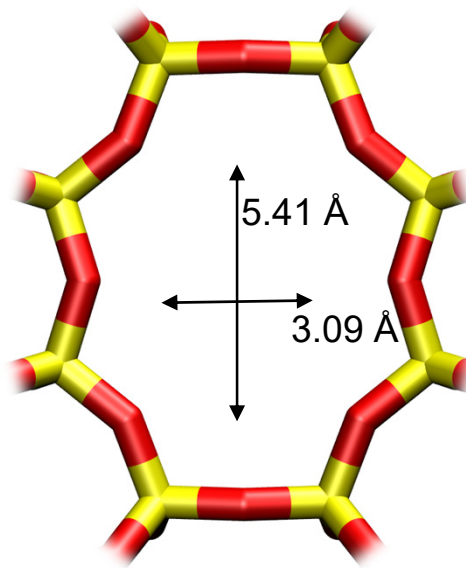
**Front
plane of
unit cell
of TSC**

TSC window and pore dimensions

Fig. S35



TSC
(supercage - cage)



TSC
(supercage - pocket)

	TSC
$a / \text{Å}$	30.742
$b / \text{Å}$	30.742
$c / \text{Å}$	30.742
Cell volume / Å^3	29053.36
conversion factor for [molec/uc] to [mol per kg Framework]	0.0433
conversion factor for [molec/uc] to [kmol/m ³]	0.1260
ρ [kg/m ³]	1318.729
MW unit cell [g/mol(framework)]	23072.56
ϕ , fractional pore volume	0.454
open space / $\text{Å}^3/\text{uc}$	13182.6
Pore volume / cm^3/g	0.344
Surface area / m^2/g	829.0
DeLaunay diameter / Å	4.02

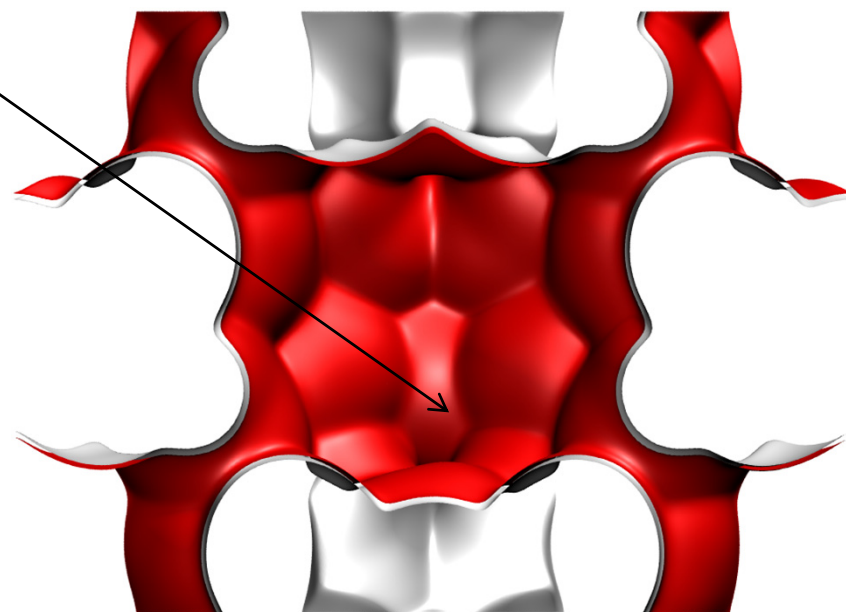
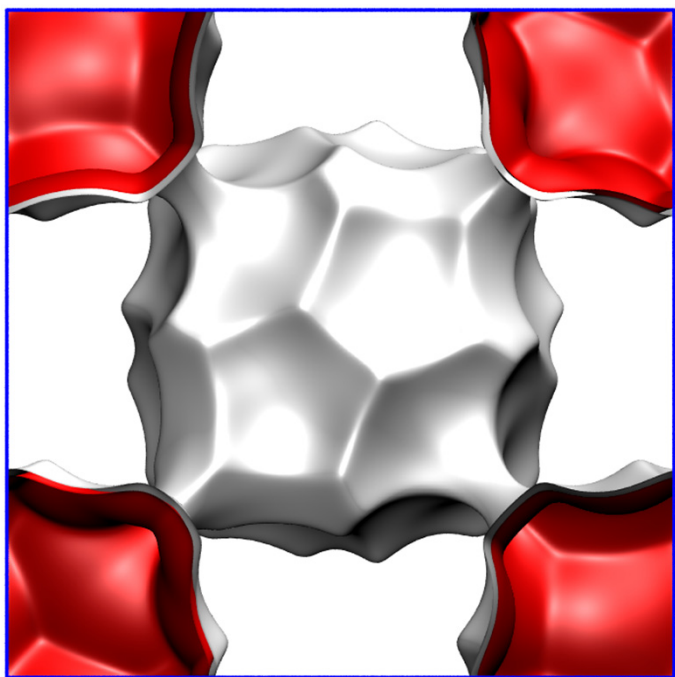
The window dimension calculated using the van der Waals diameter of framework atoms = 2.7 Å are indicated above by the arrows. It is likely that the pockets are inaccessible due to the narrow constriction of 3.092 Å. Another point to note is that the dimensions provided in the IZA website do not appear to be correct for the window on the left.

ZIF-8 pore landscapes

Fig. S36

There are 2 cages per unit cell. To convert from molecules per cage to mol kg⁻¹, multiply by 0.7325.

There are 2 cages per unit cell.
The volume of one ZIF-8 cage is 1168 Å³, significantly larger than that of a single cage of DDR (278 Å³), or FAU (786 Å³).



ZIF-8 dimensions

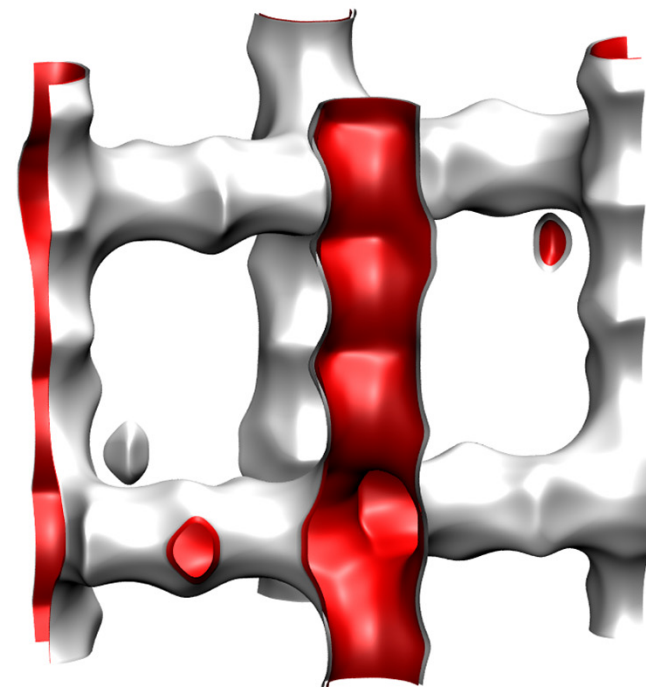
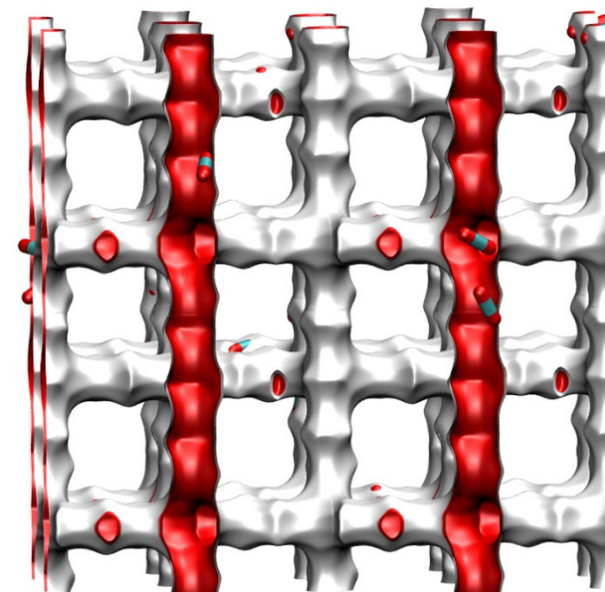
Fig. S37

	ZIF-8
$a / \text{\AA}$	16.991
$b / \text{\AA}$	16.991
$c / \text{\AA}$	16.991
Cell volume / \AA^3	4905.201
conversion factor for [molec/uc] to [mol per kg Framework]	0.3663
conversion factor for [molec/uc] to [kmol/m ³]	0.7106
ρ [kg/m ³]	924.253
MW unit cell [g/mol(framework)]	2730.182
ϕ , fractional pore volume	0.476
open space / $\text{\AA}^3/\text{uc}$	2337.0
Pore volume / cm ³ /g	0.515
Surface area /m ² /g	1164.7
DeLaunay diameter / \AA	3.26

MFI pore landscape

Fig. S38

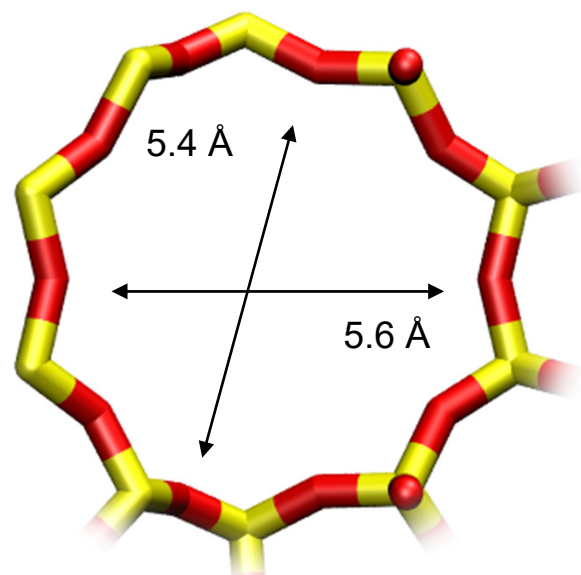
	MFI
$a / \text{\AA}$	20.022
$b / \text{\AA}$	19.899
$c / \text{\AA}$	13.383
Cell volume / \AA^3	5332.025
conversion factor for [molec/uc] to [mol per kg Framework]	0.1734
conversion factor for [molec/uc] to [kmol/m ³]	1.0477
ρ [kg/m ³]	1796.386
MW unit cell [g/mol(framework)]	5768.141
ϕ , fractional pore volume	0.297
open space / $\text{\AA}^3/\text{uc}$	1584.9
Pore volume / cm^3/g	0.165
Surface area / m^2/g	487.0
DeLaunay diameter / \AA	5.16



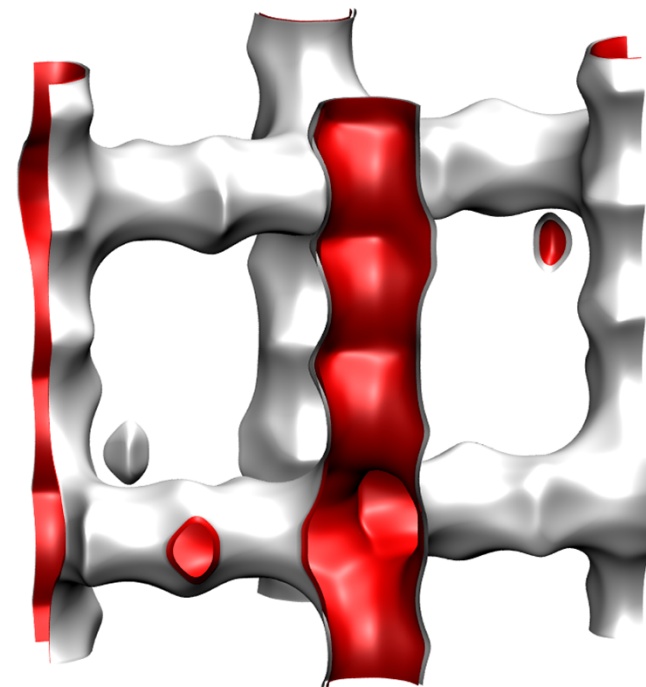
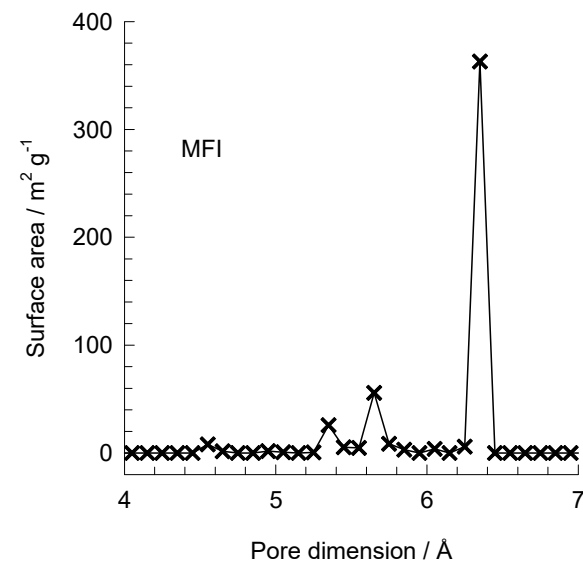
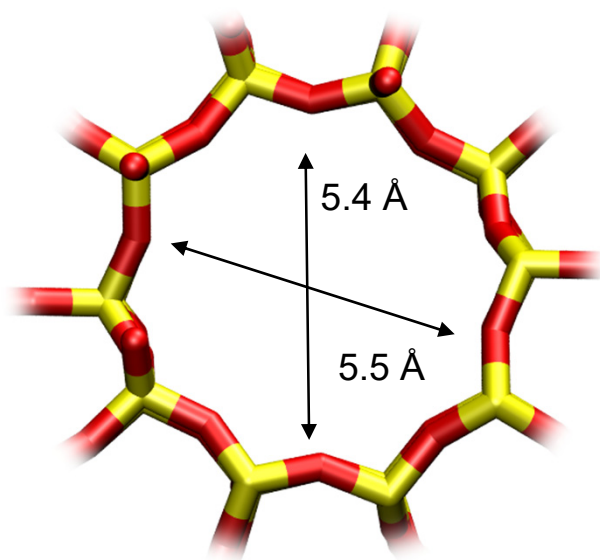
MFI pore dimensions

Fig. S39

10 ring channel
of MFI viewed
along [100]



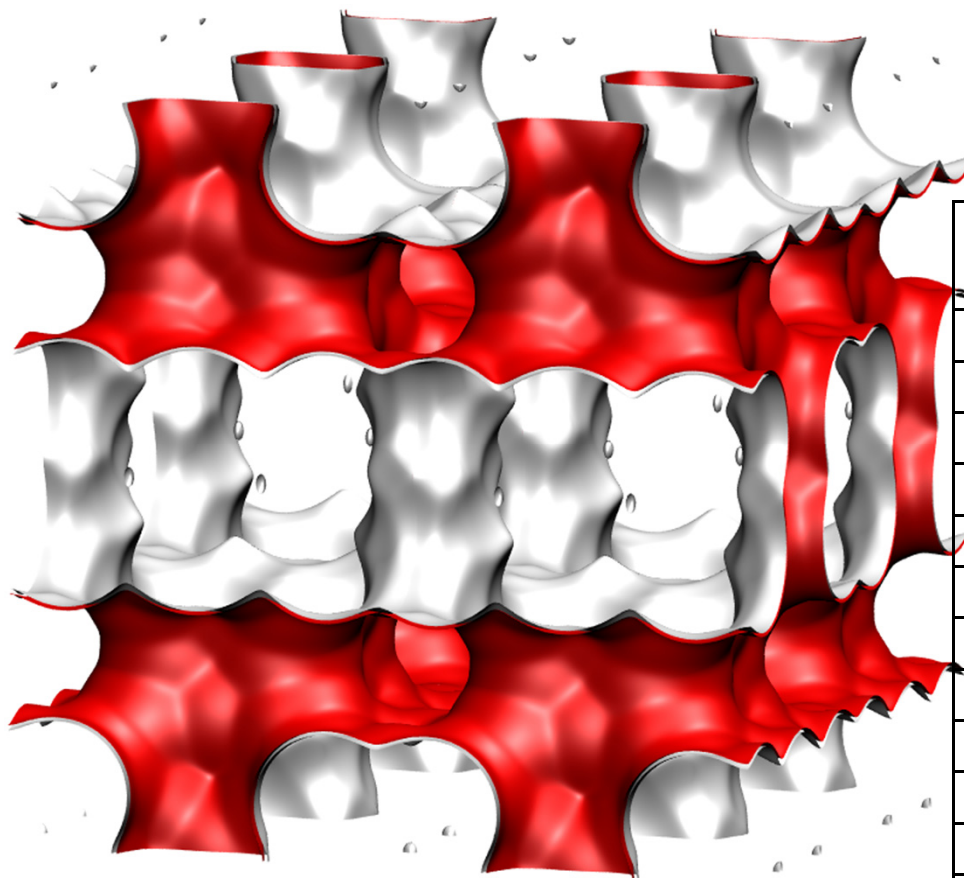
10 ring channel
of MFI viewed
along [010]



ISV pore landscape

Fig. S40

Intersecting 12-ring channels structure



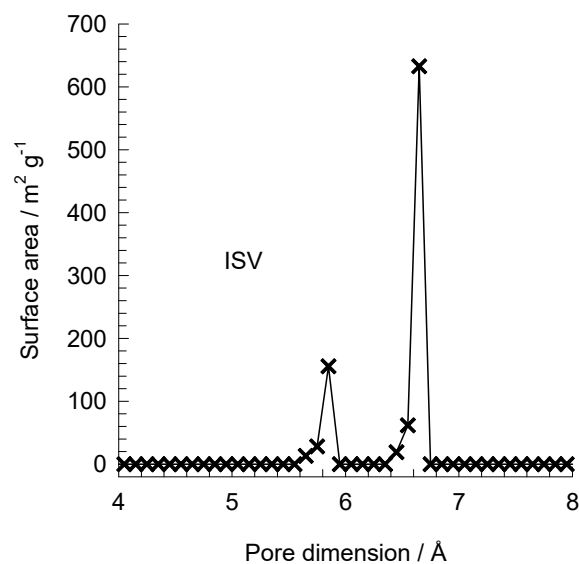
	ISV
$a / \text{\AA}$	12.853
$b / \text{\AA}$	12.853
$c / \text{\AA}$	25.214
Cell volume / \AA^3	4165.343
conversion factor for [molec/uc] to [mol per kg Framework]	0.2600
conversion factor for [molec/uc] to [kmol/m^3]	0.9361
ρ [kg/m^3]	1533.027
MW unit cell [g/mol(framework)]	3845.427
ϕ , fractional pore volume	0.426
open space / $\text{\AA}^3/\text{uc}$	1773.9
Pore volume / cm^3/g	0.278
Surface area / m^2/g	911.0
DeLaunay diameter / \AA	5.96

Structural information from: C. Baerlocher, L.B. McCusker, Database of Zeolite Structures, International Zeolite Association, <http://www.iza-structure.org/databases/>

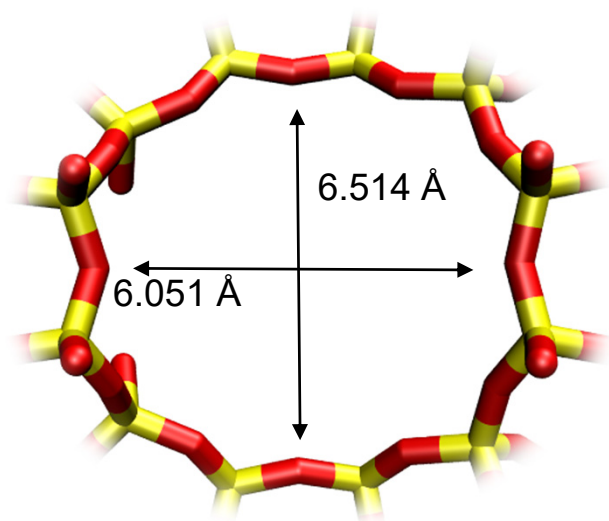
ISV pore dimensions

Fig. S41

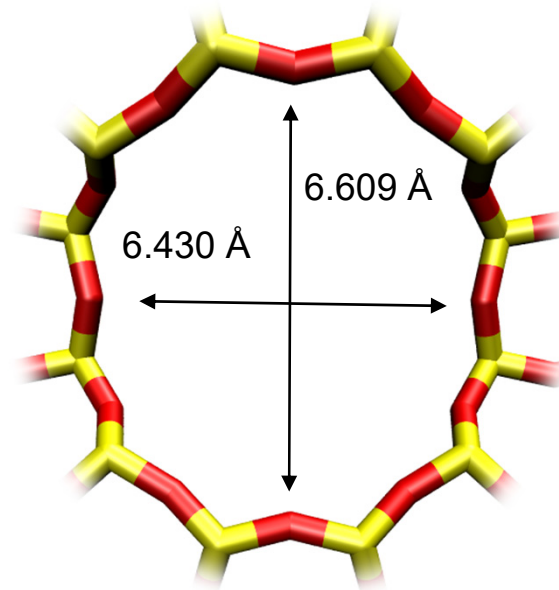
This plot of surface area versus pore dimension is determined using a combination of the DeLaunay triangulation method for pore dimension determination, and the procedure of Dürren for determination of the surface area.



Intersecting 12-ring channels structure



ISV [1 0 0]

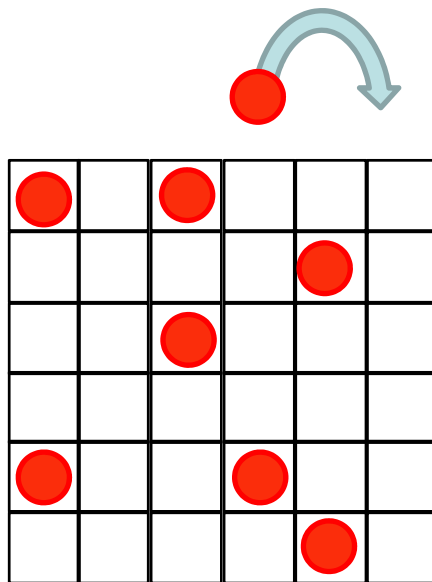


ISV [0 0 1]

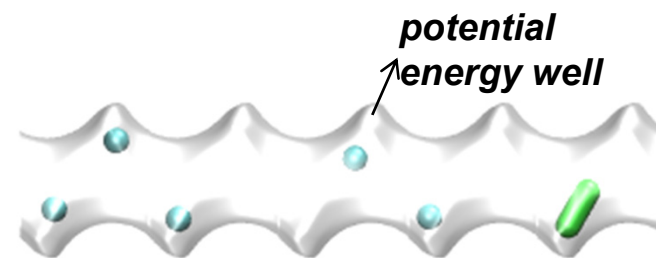
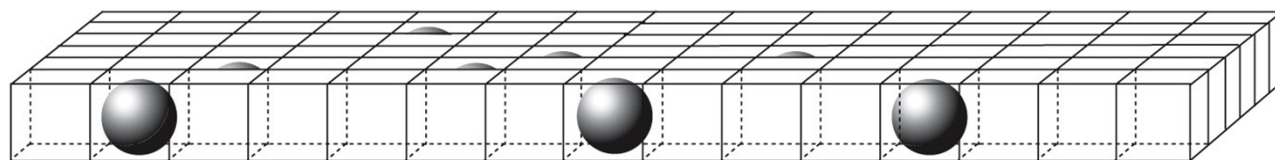
Langmuir isotherm



Irving Langmuir (1881-1957);
Nobel prize (1932)



No adsorbate-adsorbate interactions



TON zeolite

molar loading

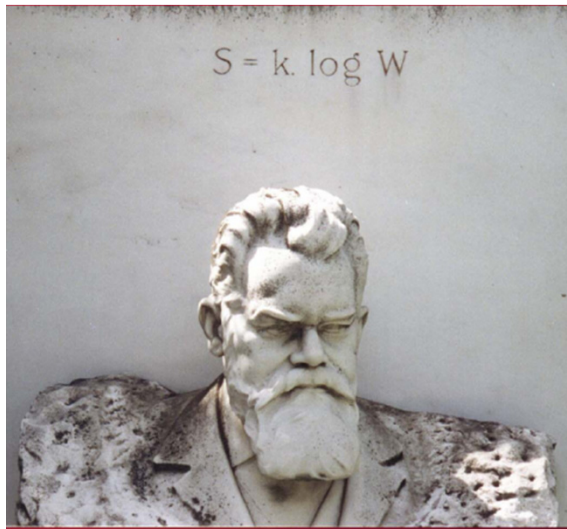
binding constant

$$\frac{q}{q_{sat}} = \theta = \frac{bp}{1 + bp}$$

fractional occupancy

$S = k_B \ln(\text{Wahrscheinlichkeit})$

Fig. S43



LVDWIG
BOLTZMANN
1844 - 1906

N = number of adsorbed molecules on surface per square meter

At equilibrium, $\mu_{\text{gas}} = \mu_{\text{surf}}$

μ_{gas} = chemical potential of adsorbate in the gas phase

μ_{surf} = chemical potential of adsorbate on the surface

Surface is assumed to be two - dimensional lattice of M sites per square meter

The fractional coverage $\theta = \frac{N}{M}$

At saturation, $\theta = 1$; $N = M$

The number of possible arrangements of the particles on the surface lattice

$$W = \frac{M!}{N!(M - N)!}$$

The translational entropy is given by

$$\frac{S}{k_B} = \ln(W) = \ln(M!) - \ln(N!) - \ln((M - N)!)$$

Use Stirling's approximation

$$\ln(M!) = M \ln M - M$$

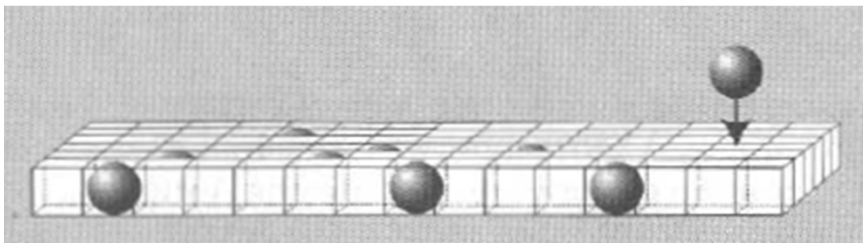
$$\ln(N!) = N \ln N - N$$

$$\ln((M - N)!) = (M - N) \ln(M - N) - (M - N)$$

$$\ln(W) = M \ln M - N \ln N - (M - N) \ln(M - N)$$

$$\frac{S}{k_B} = \ln(W) = -N \ln\left(\frac{N}{M}\right) - (M - N) \ln\left(\frac{M - N}{M}\right)$$

$$\frac{S}{Mk_B} = -\theta \ln(\theta) - (1 - \theta) \ln(1 - \theta)$$



Helmholtz free energy



Hermann Ludwig Ferdinand von Helmholtz
(1821-1894)

Helmholtz free energy $F = U - TS$

The binding energy contribution to the internal energy = Nw
where $w < 0$ is the binding energy change per molecule.

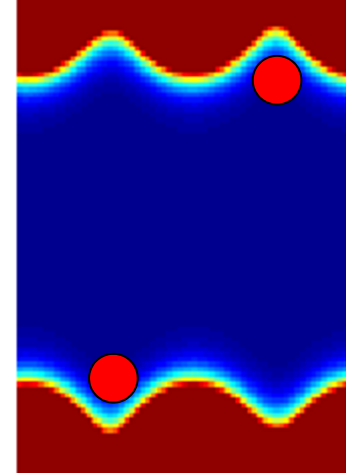
The other contributions to the internal energy are caused by
by adsorption to the surface, such as (a) changes in orientation,
(b) new modes of vibration, etc.

These contributions can be lumped = $-Nk_B T \ln Q_{surf}$

Q_{surf} = partition function for adsorbed molecule

Helmholtz free energy $F = U - TS$

$$\frac{F}{Mk_B T} = \frac{U - TS}{Mk_B T} = \theta \ln \theta + (1 - \theta) \ln(1 - \theta) + \left(\frac{w}{k_B T} \right) \theta - \theta \ln(Q_{surf})$$



Thermodynamic equilibrium: $\mu_{\text{gas}} = \mu_{\text{surf}}$

$$\frac{\mu_{\text{surf}}}{k_B T} = \left(\frac{\partial(F/k_B T)}{\partial N} \right)_{M,T} = \frac{1}{M} \left(\frac{\partial(F/k_B T)}{\partial \theta} \right)_{M,T}$$

$$\frac{\mu_{\text{surf}}}{k_B T} = \ln\left(\frac{\theta}{1-\theta}\right) + \left(\frac{w}{k_B T}\right) - \ln(Q_{\text{surf}})$$

$$\frac{\mu_{\text{gas}}}{k_B T} = \ln\left(\frac{p}{p_{\text{int}}^0}\right)$$

$$p_{\text{int}}^0 = k_B T \frac{Q_{\text{trans}}}{V} Q_{\text{vib}} Q_{\text{rot}} Q_{\text{elec}}$$

This represents properties internal to the molecule

At equilibrium

$$\ln\left(\frac{p}{p_{\text{int}}^0}\right) = \ln\left(\frac{\theta}{1-\theta}\right) + \left(\frac{w}{k_B T}\right) - \ln(Q_{\text{surf}})$$

$$\ln\left(\frac{p}{p_{\text{int}}^0}\right) = \ln\left(\frac{1}{Q_{\text{surf}}} \exp\left(\frac{w}{k_B T}\right) \frac{\theta}{1-\theta}\right)$$

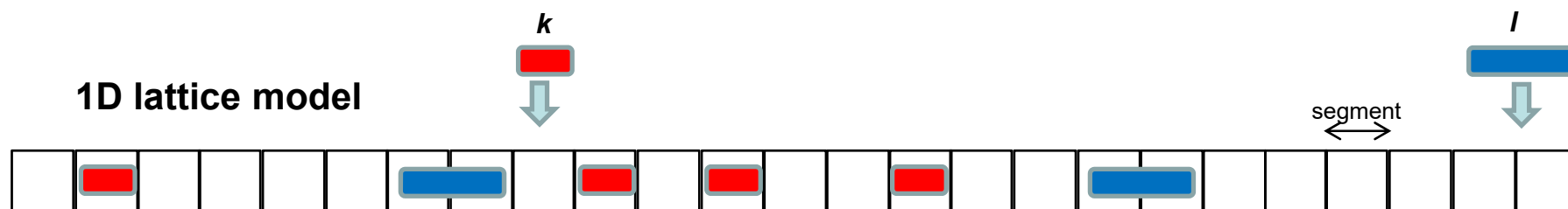
$$\frac{p}{p_{\text{int}}^0} = \frac{1}{Q_{\text{surf}}} \exp\left(\frac{w}{k_B T}\right) \frac{\theta}{1-\theta}$$

$$b = \frac{Q_{\text{surf}}}{p_{\text{int}}^0} \exp\left(-\frac{w}{k_B T}\right) = \text{binding constant}$$

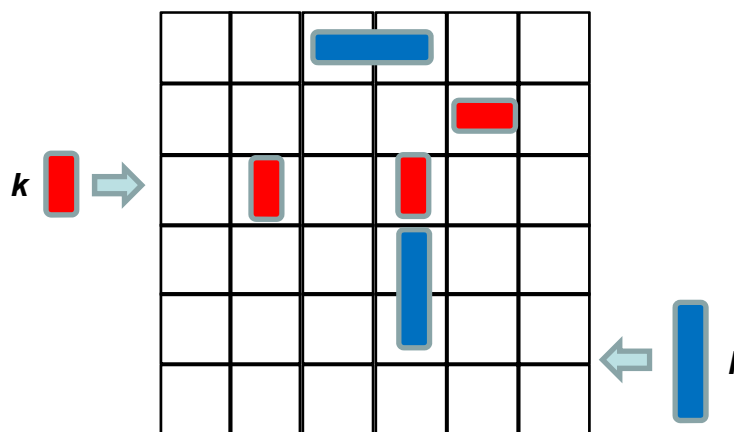
$$bp = \frac{\theta}{1-\theta}$$

$$\theta = \frac{N}{M} = \frac{bp}{1+bp}$$

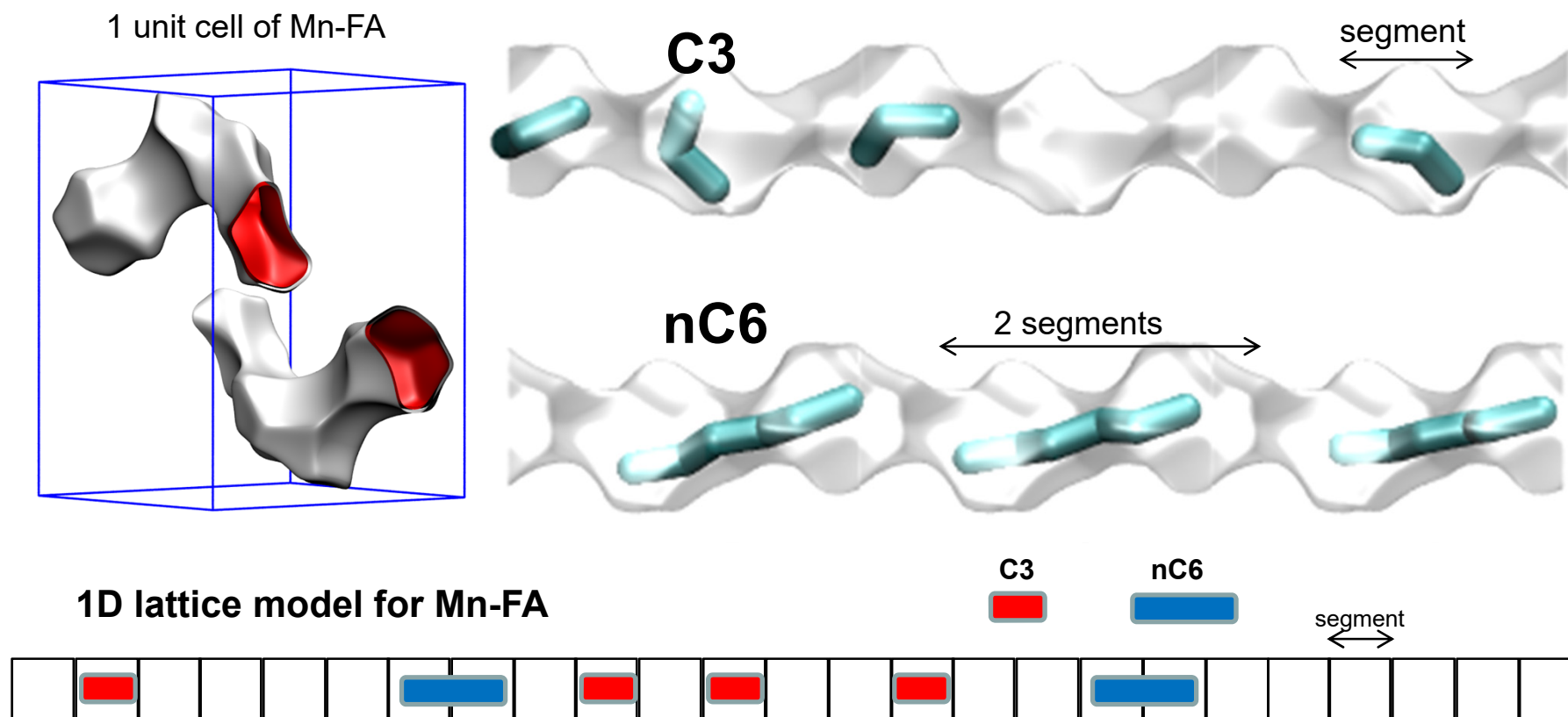
Lattice model



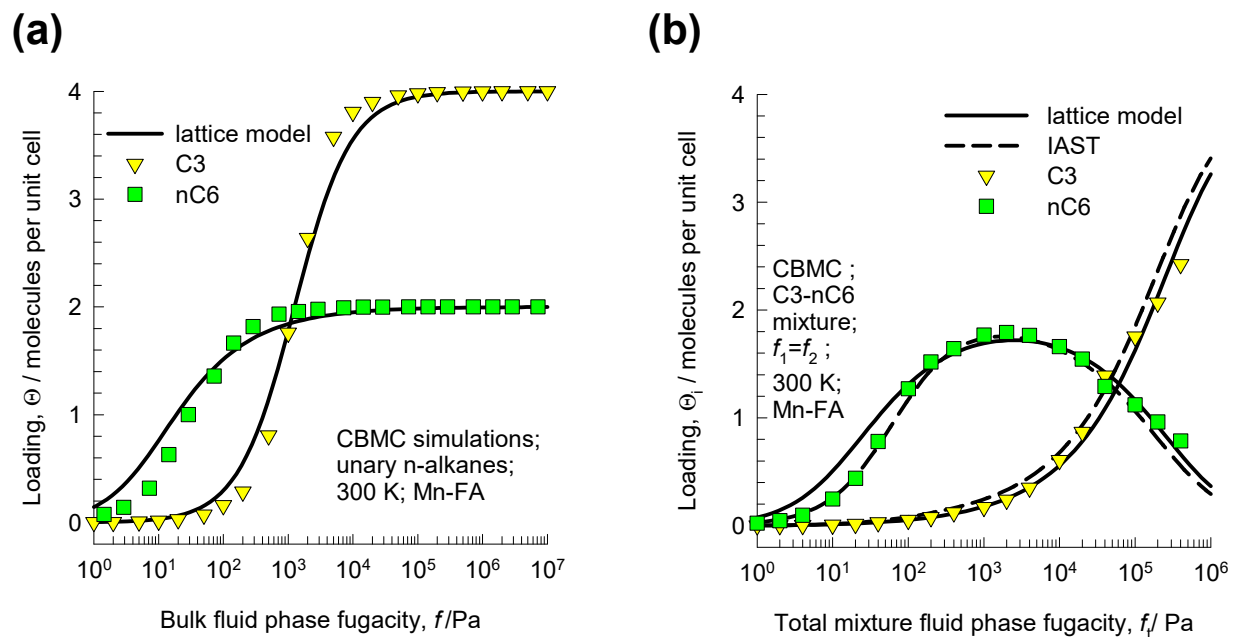
2D square lattice model



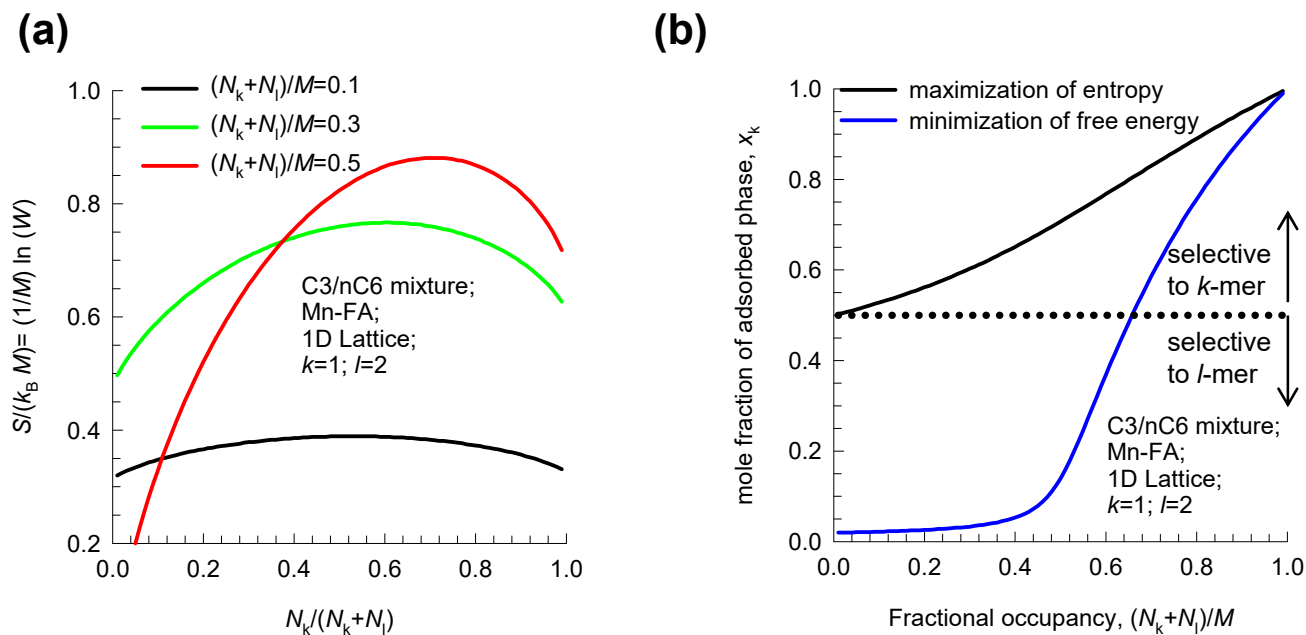
Adsorption of linear alkanes in Mn-Formate



Adsorption of linear alkanes in Mn-Formate

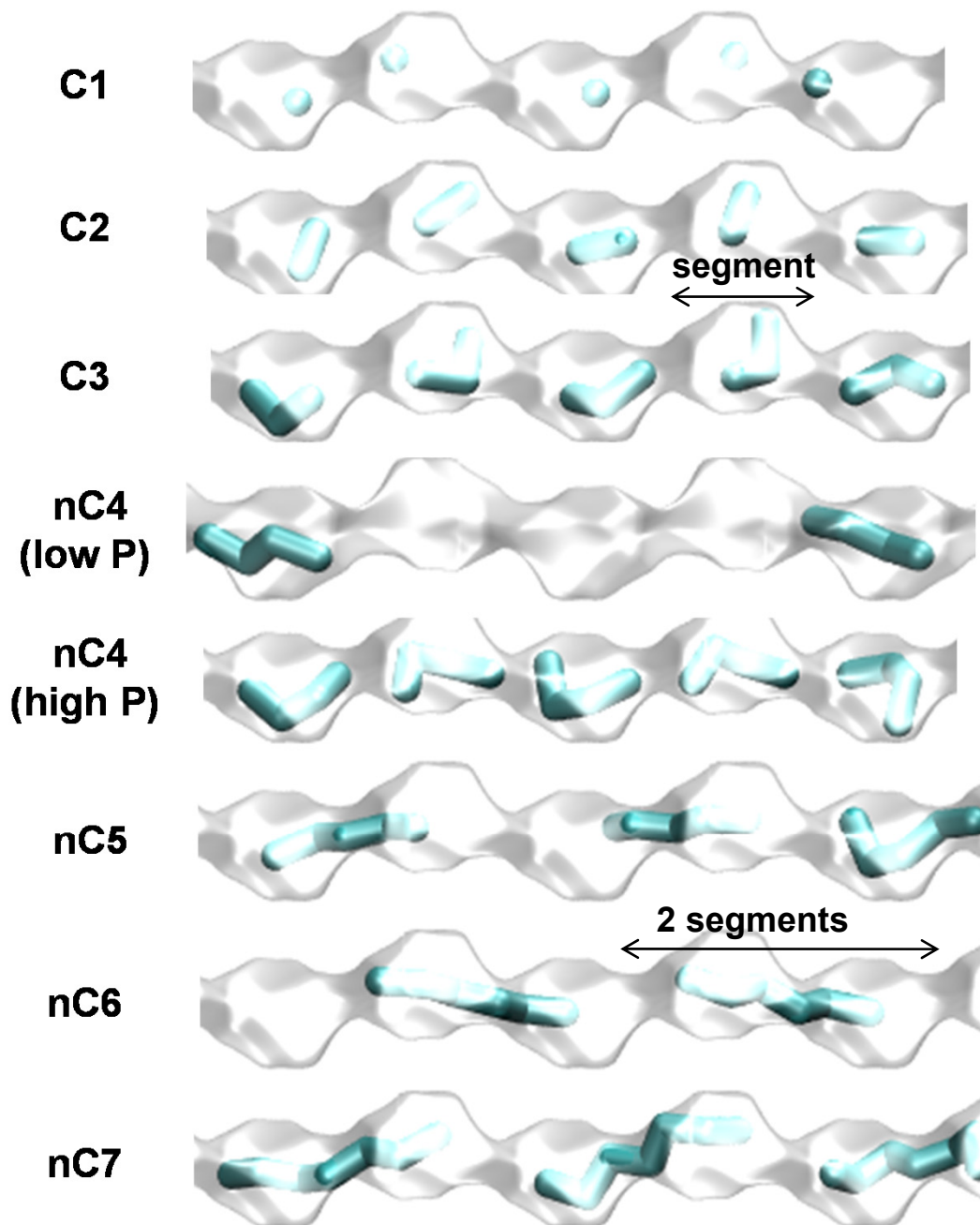
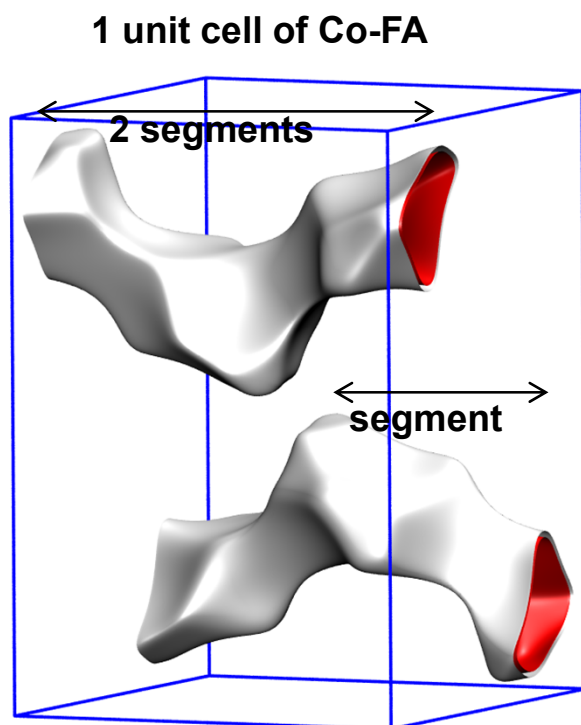


Adsorption of linear alkanes in Mn-Formate



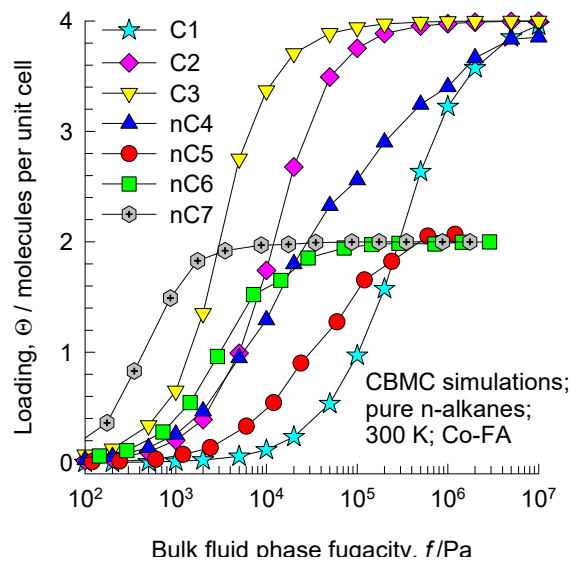
Snapshots of n-alkanes in Co-FA

Fig. S50

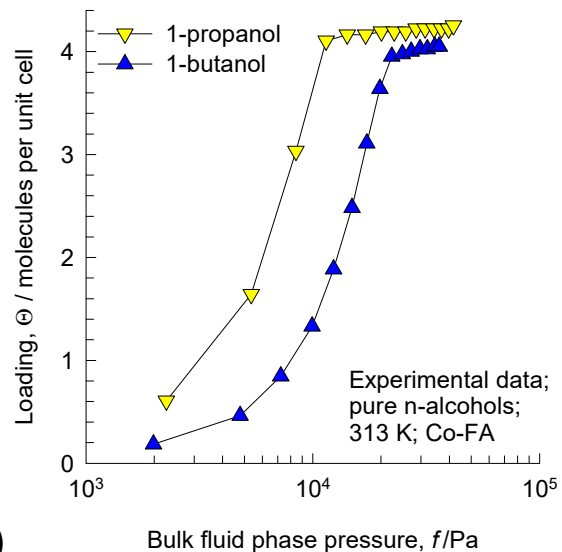


Adsorption and diffusion of n-alkanes in Co-FA

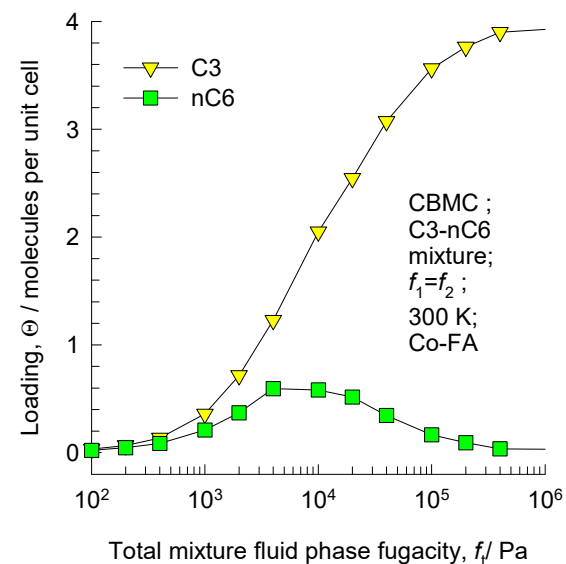
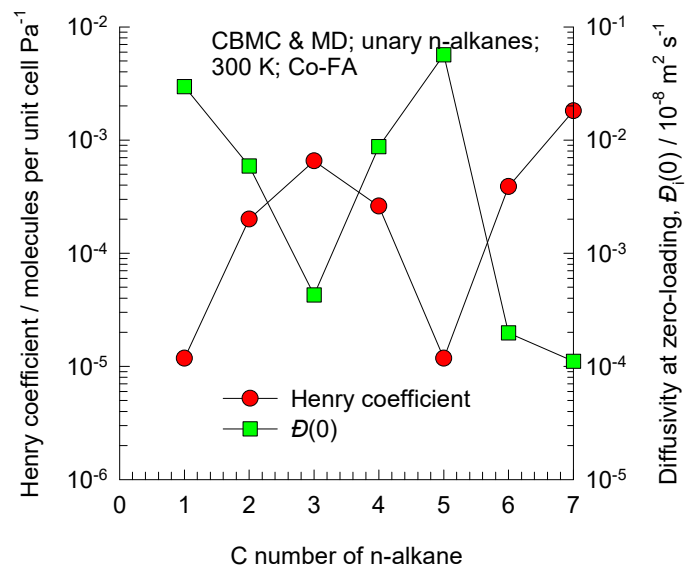
(a)



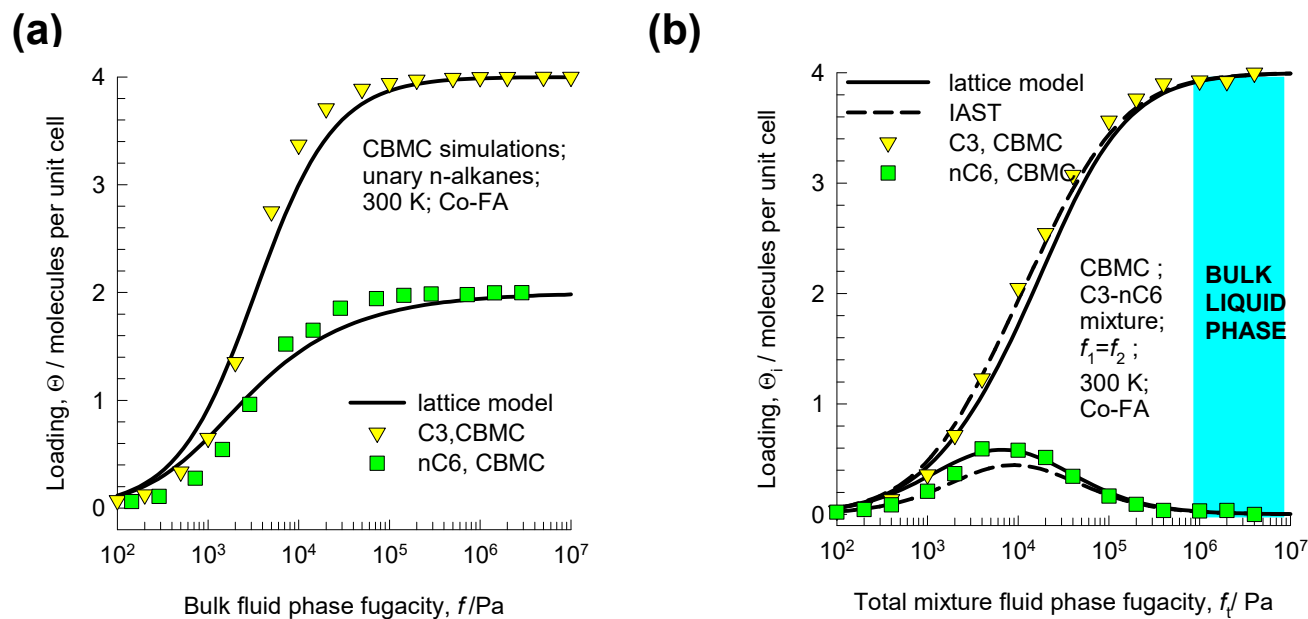
(d)



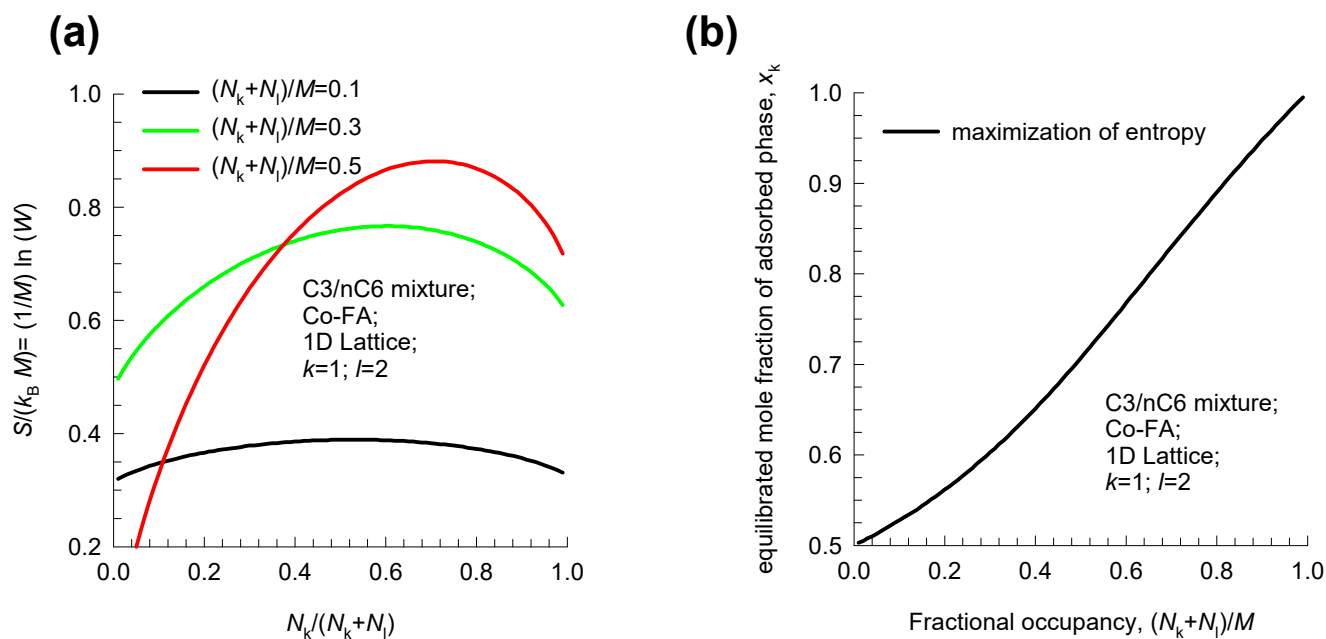
(c)



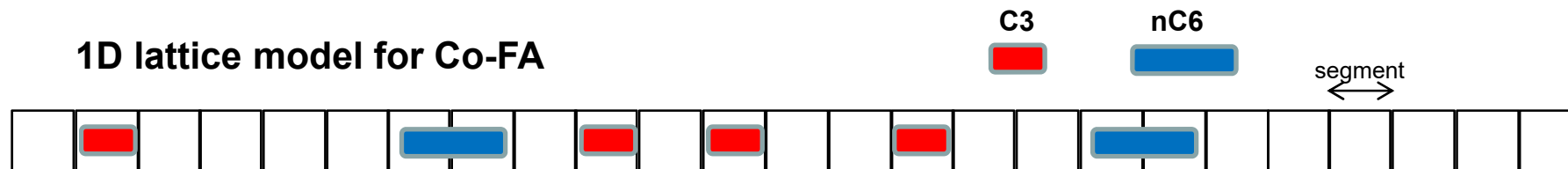
Adsorption of linear alkanes in Co-Formate



Adsorption of linear alkanes in Co-Formate

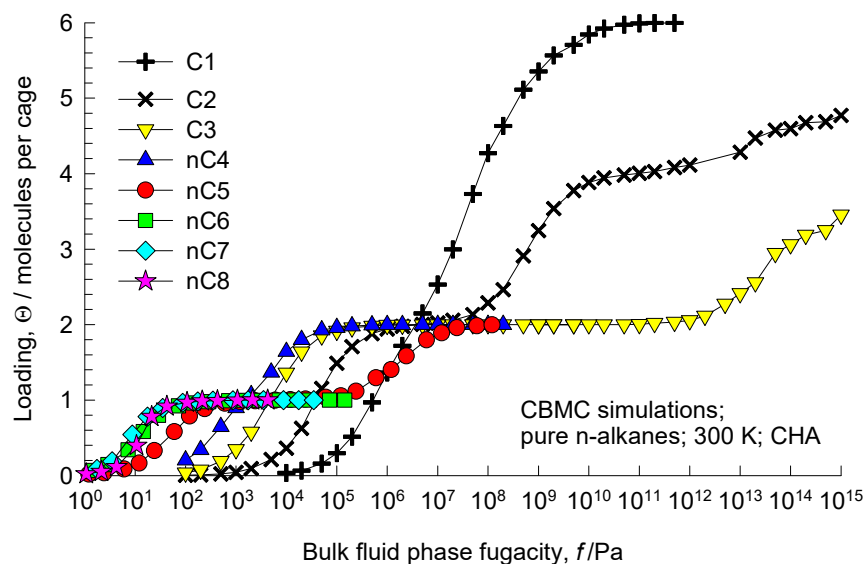


1D lattice model for Co-FA

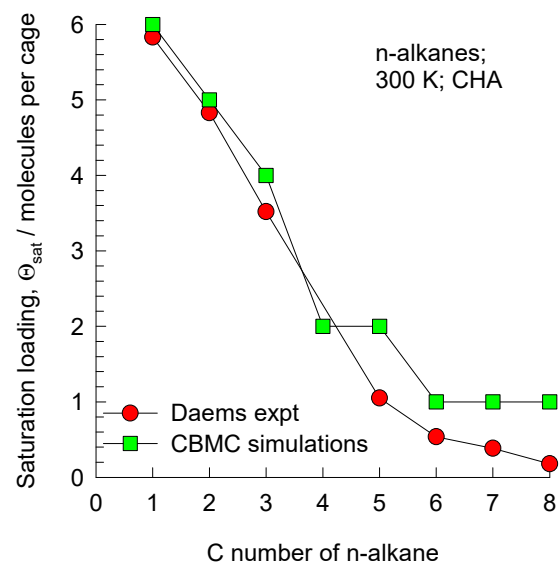


Adsorption of linear alkanes in CHA zeolite

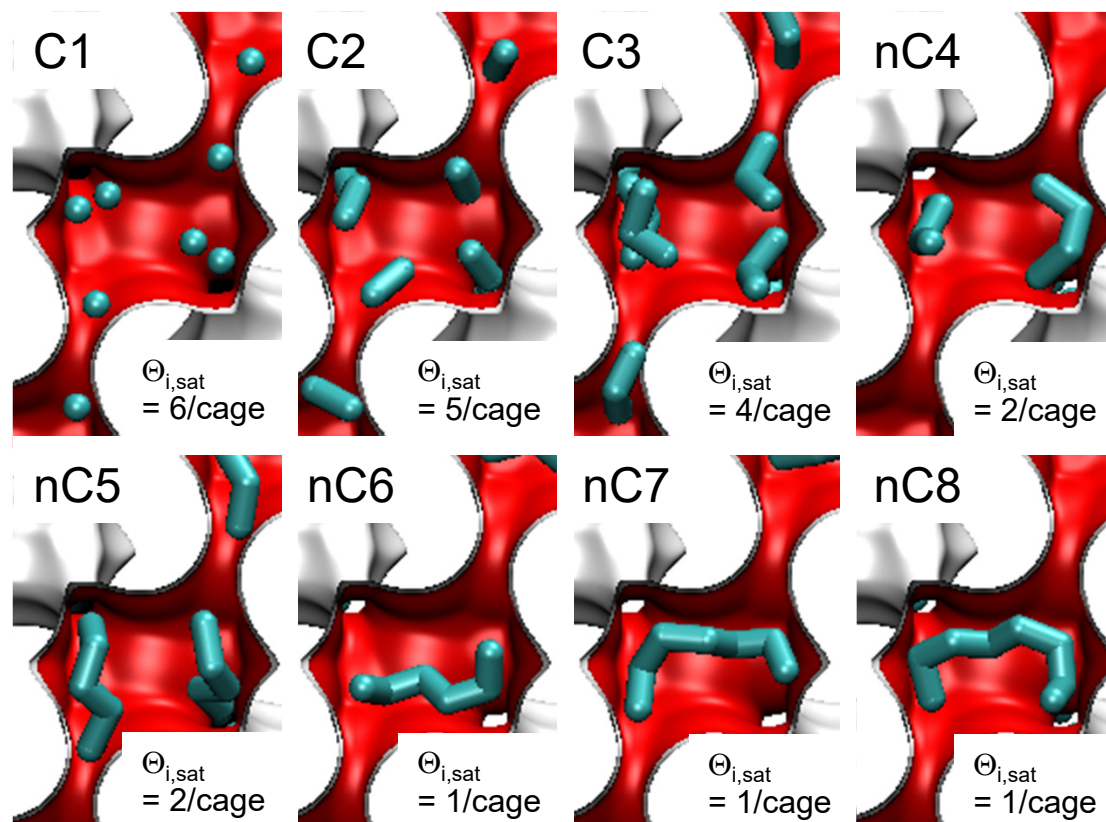
(a)



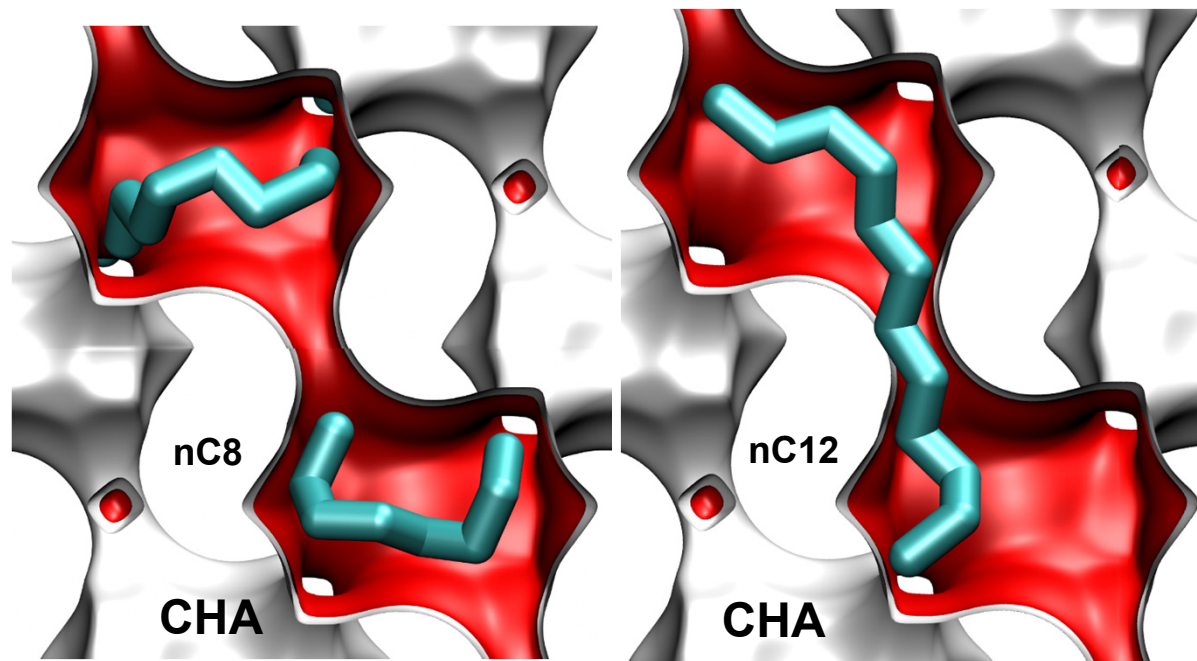
(b)



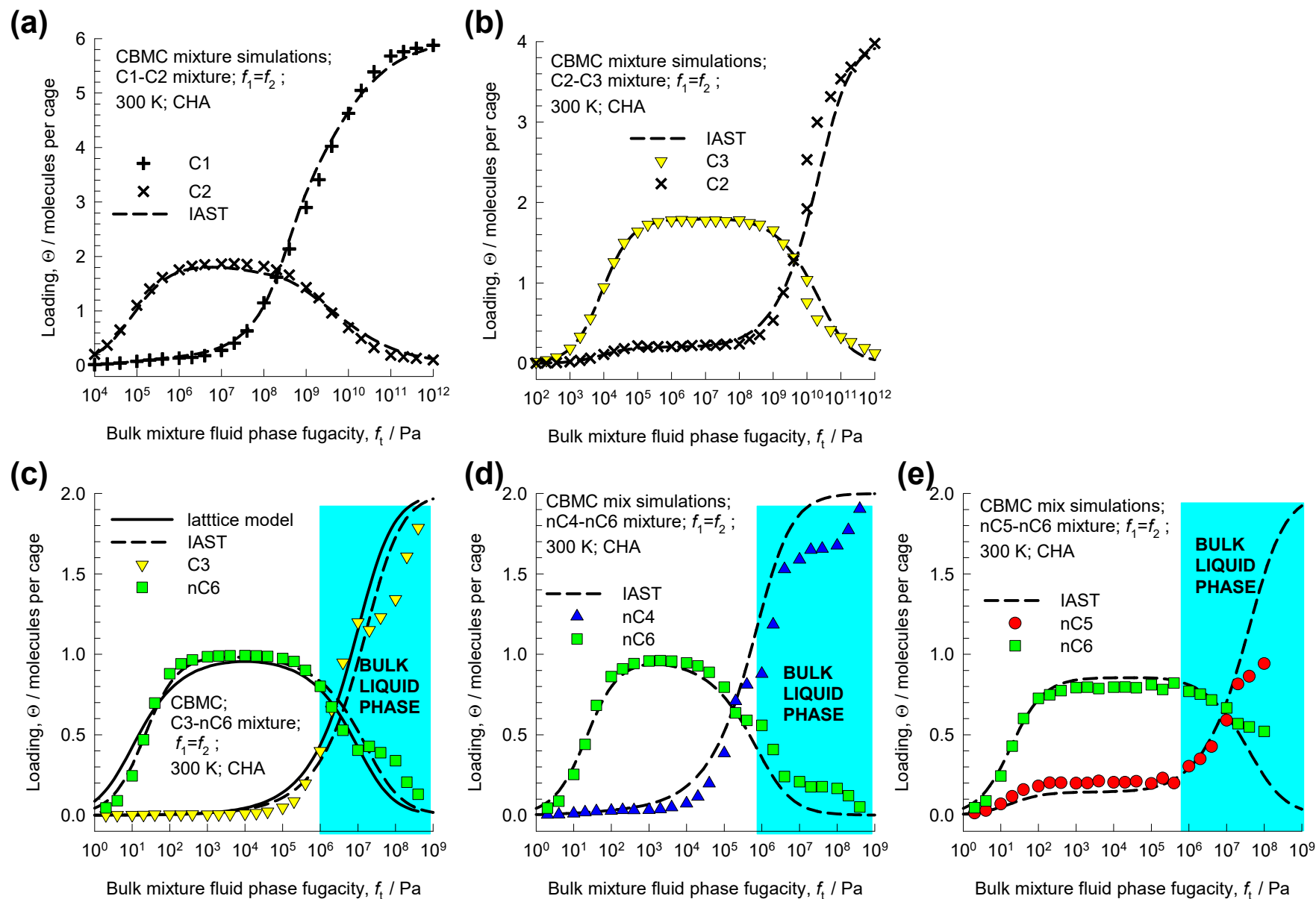
Adsorption of linear alkanes in CHA zeolite



Adsorption of n-alkanes in CHA zeolite

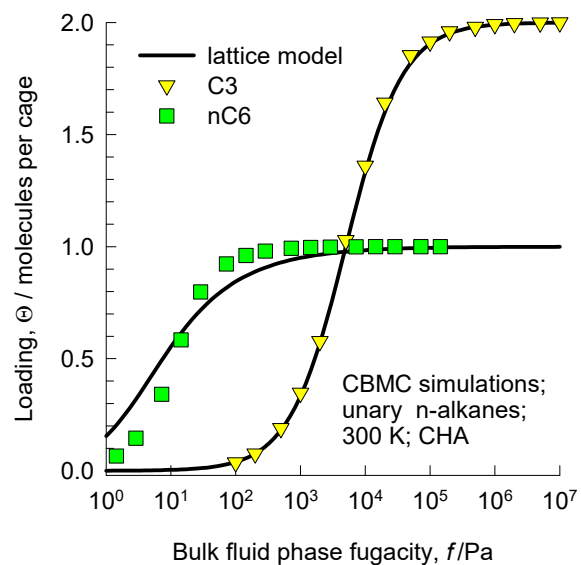


Adsorption of linear alkane mixtures in CHA

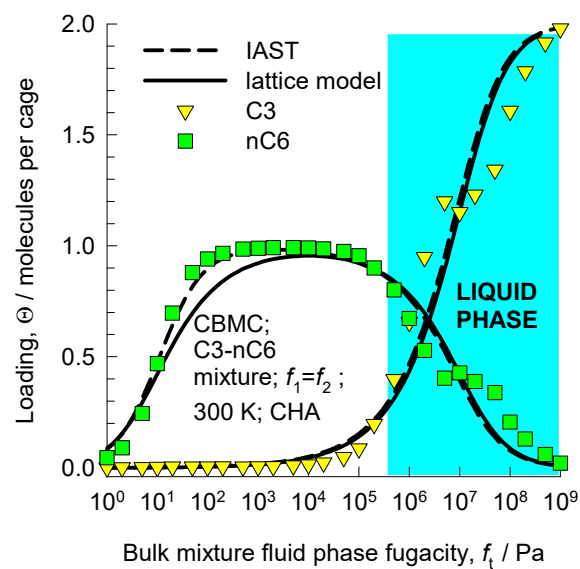


Adsorption of n-alkanes in CHA zeolite

(a)

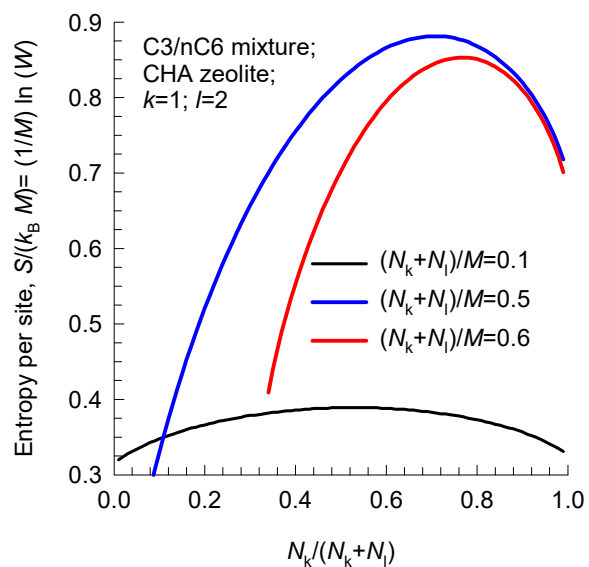


(b)

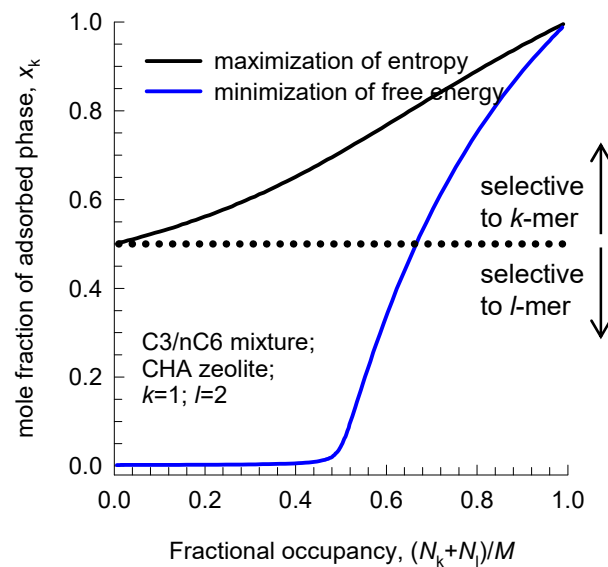


Adsorption of n-alkanes in CHA zeolite

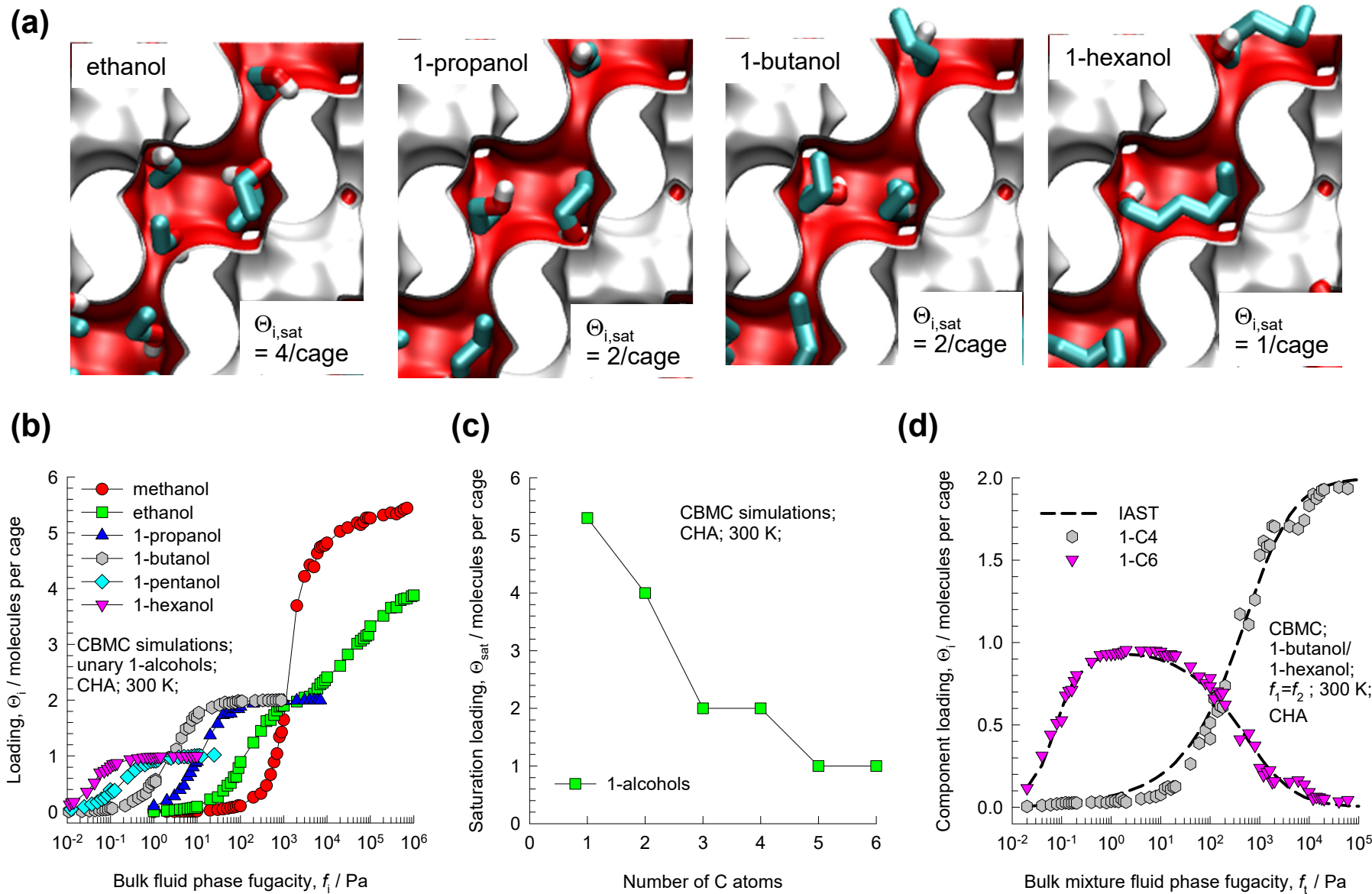
(a)



(b)

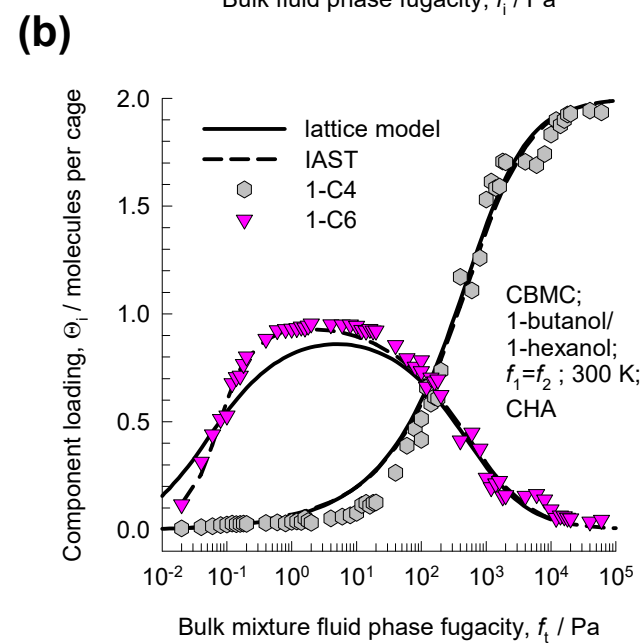
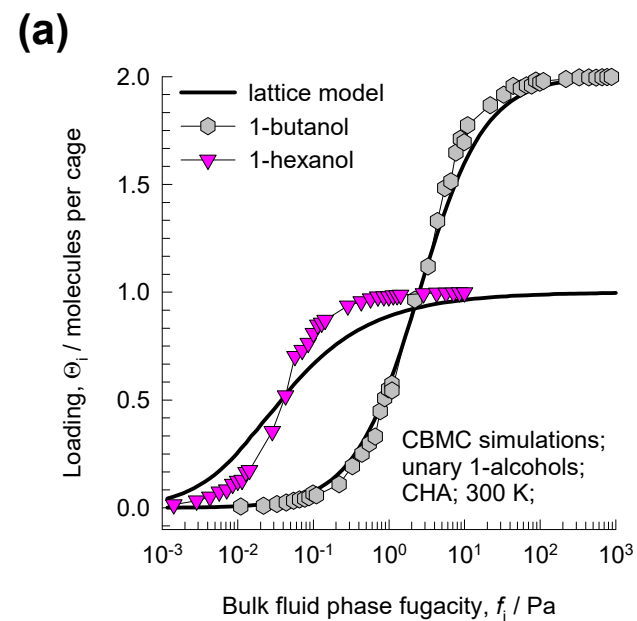
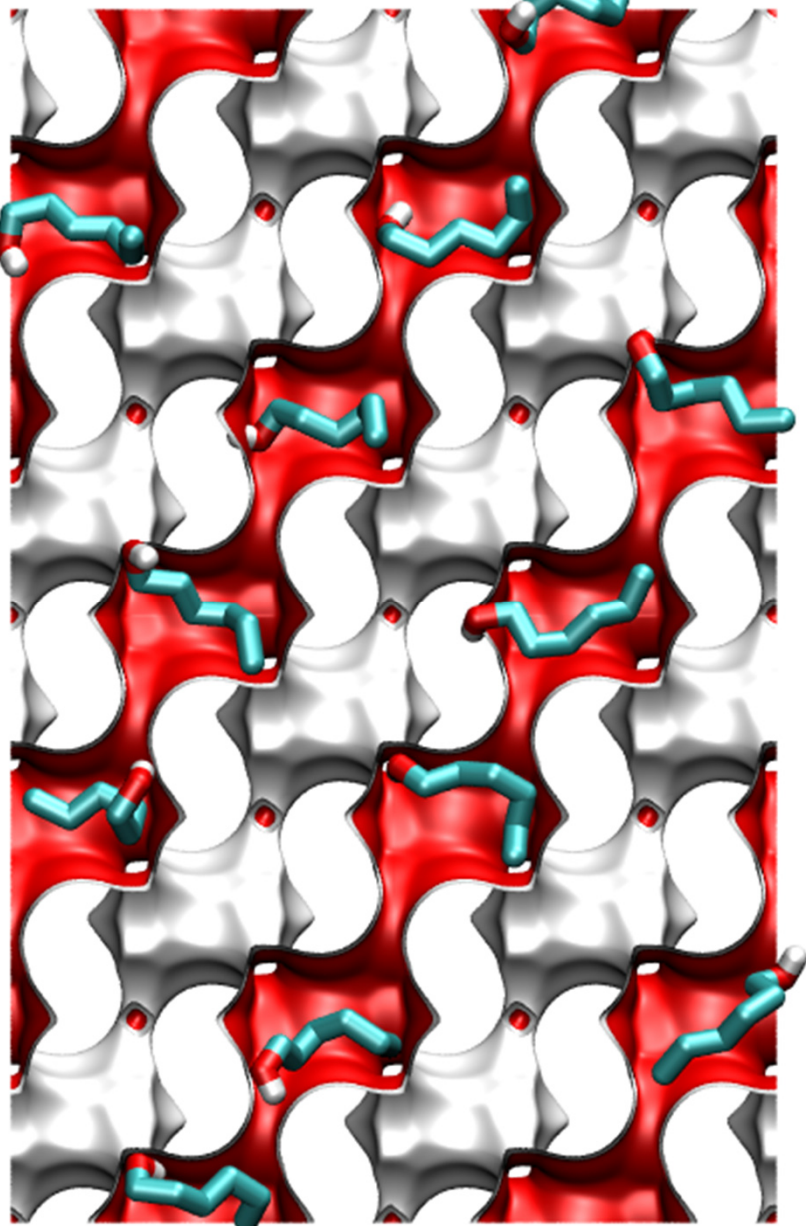


Adsorption of 1-alcohols in CHA zeolite



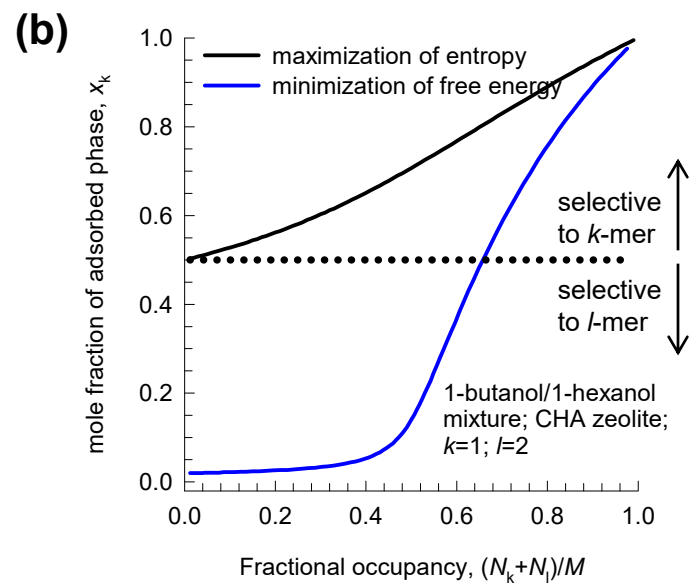
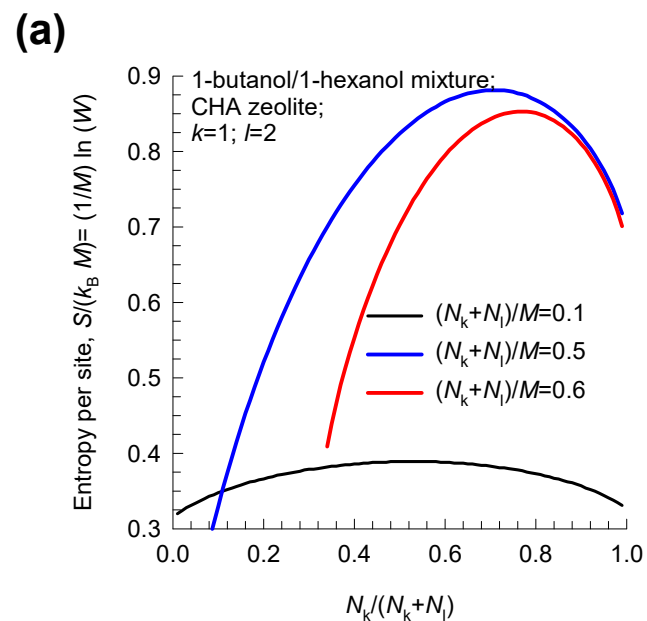
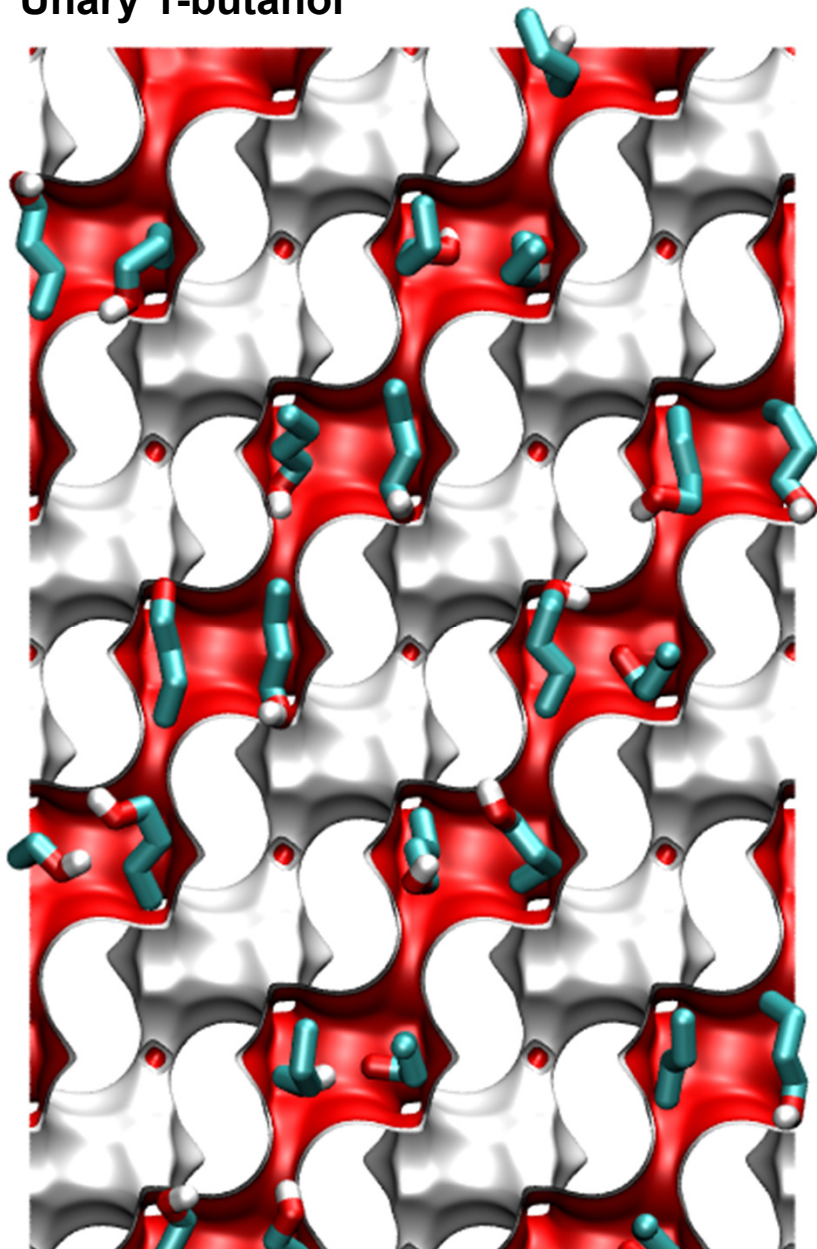
Adsorption of 1-alcohols in CHA zeolite

Unary 1-hexanol



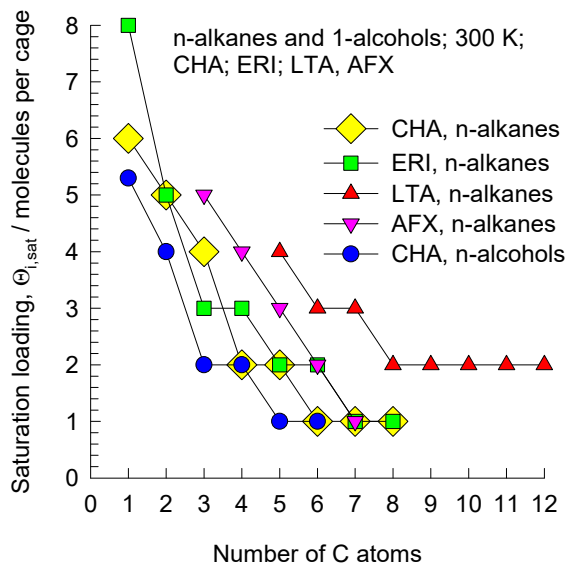
Adsorption of 1-alcohols in CHA zeolite

Unary 1-butanol

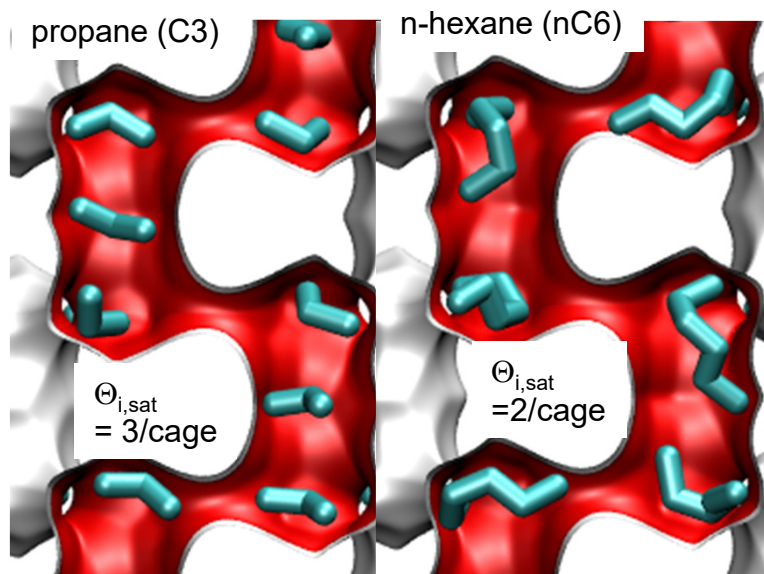


Adsorption of n-alkanes in ERI zeolite

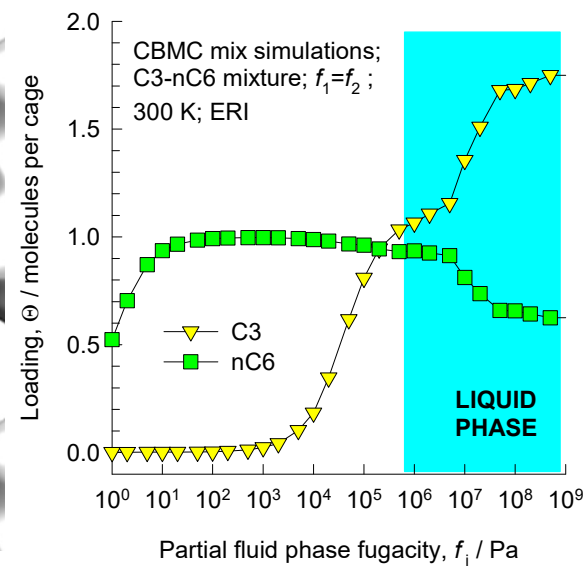
(a)



(b)

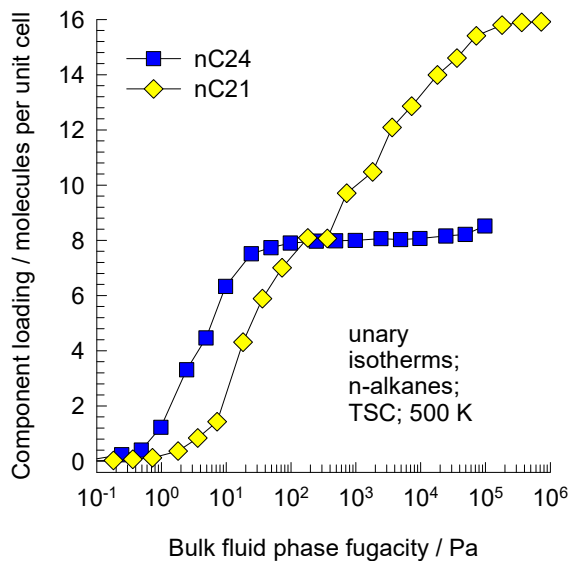


(c)

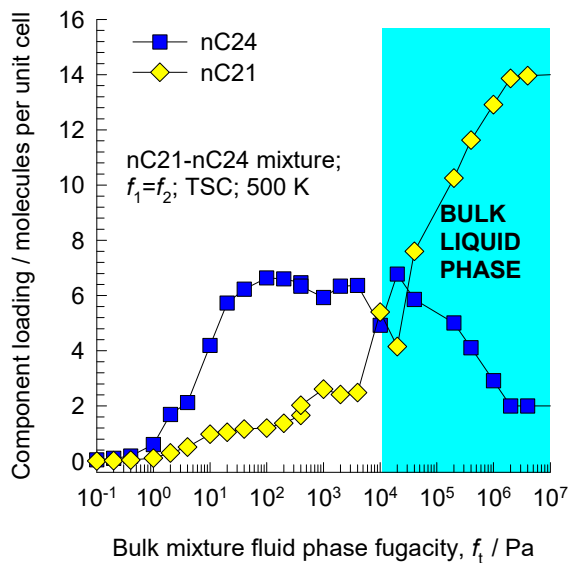


Adsorption of n-alkanes in TSC zeolite ^{Fig. S64}

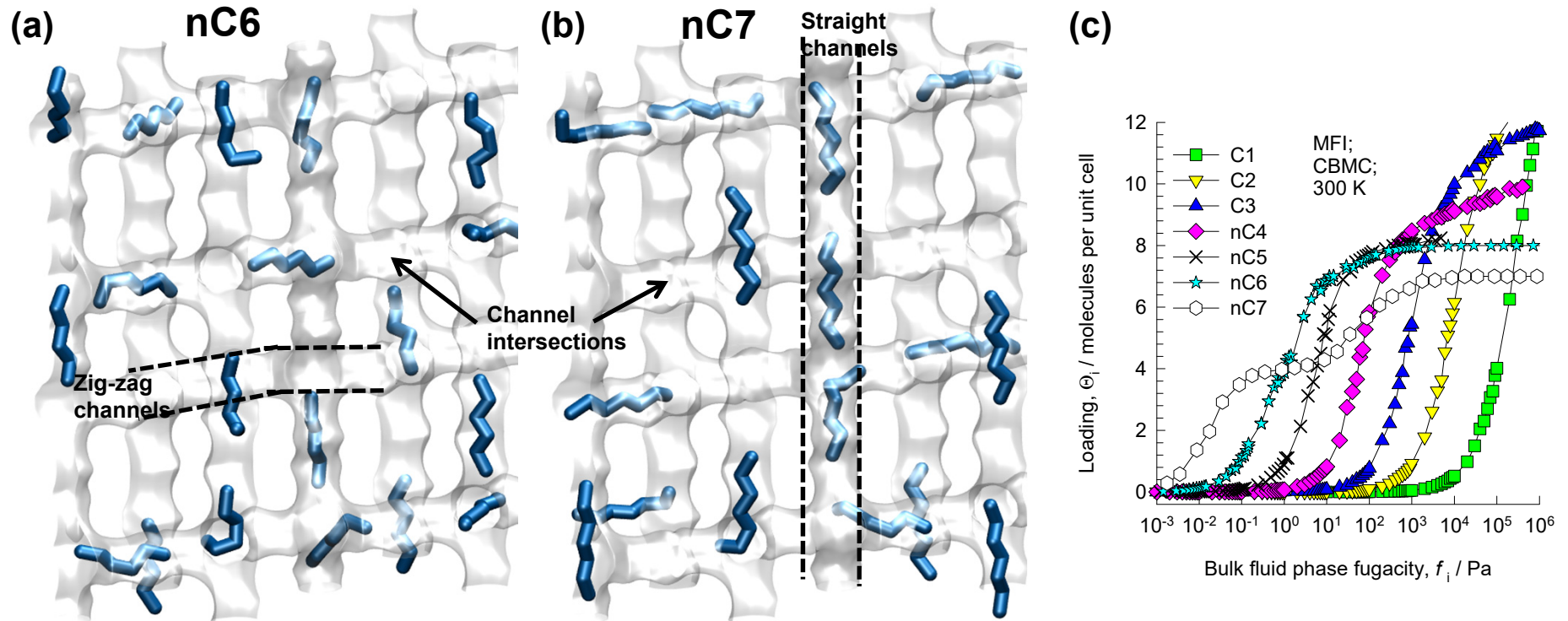
(a)



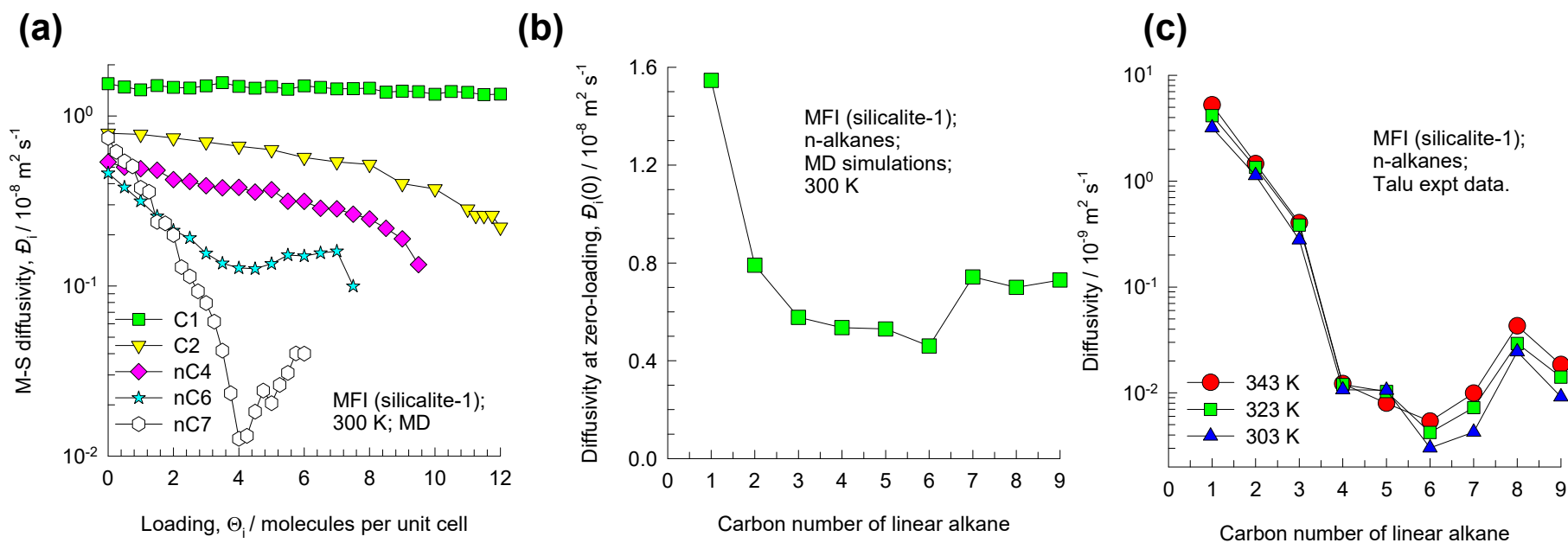
(b)



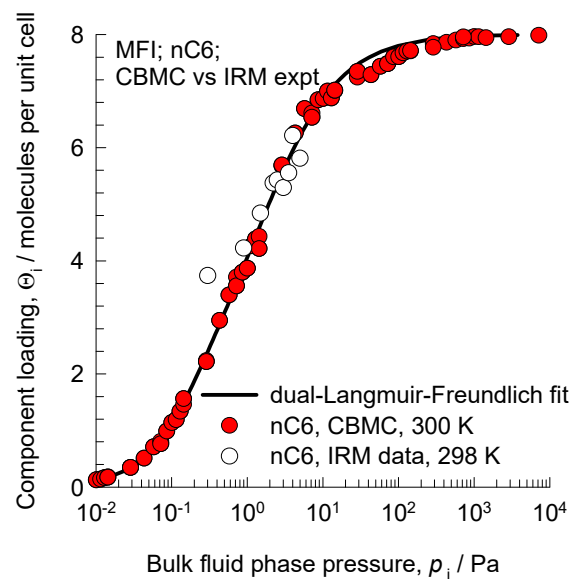
Adsorption of n-alkanes in MFI zeolite ^{Fig. S65}



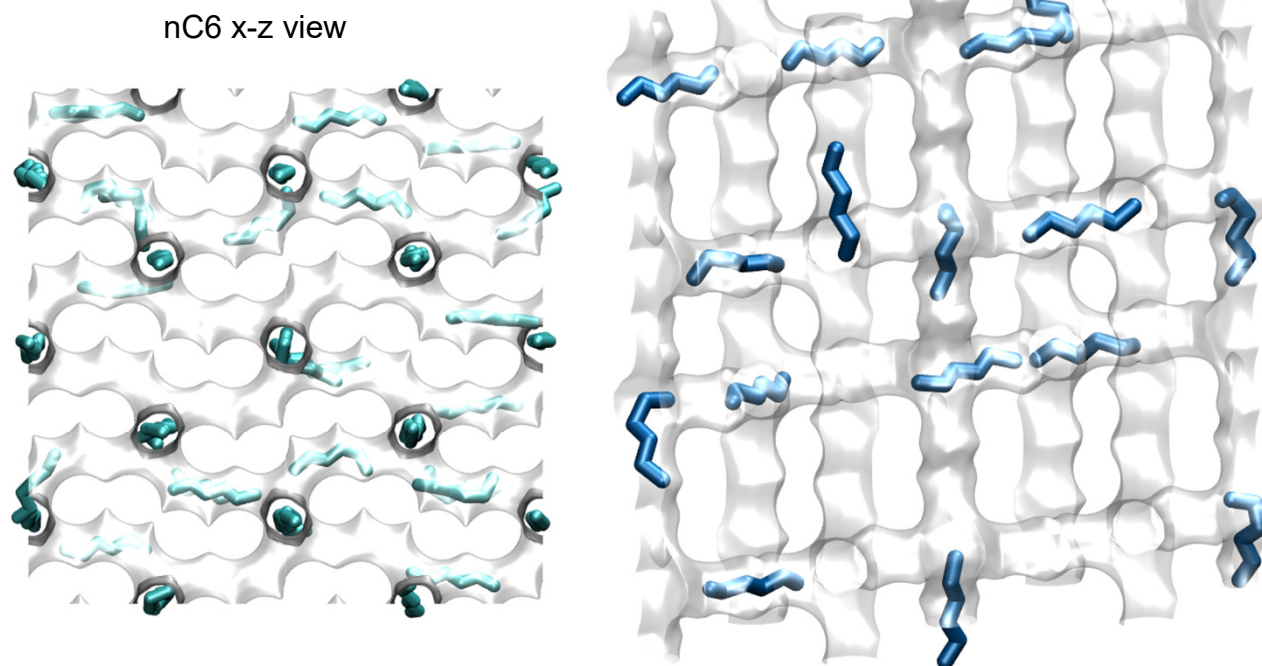
Diffusivity of n-alkanes in MFI zeolite Fig. S66



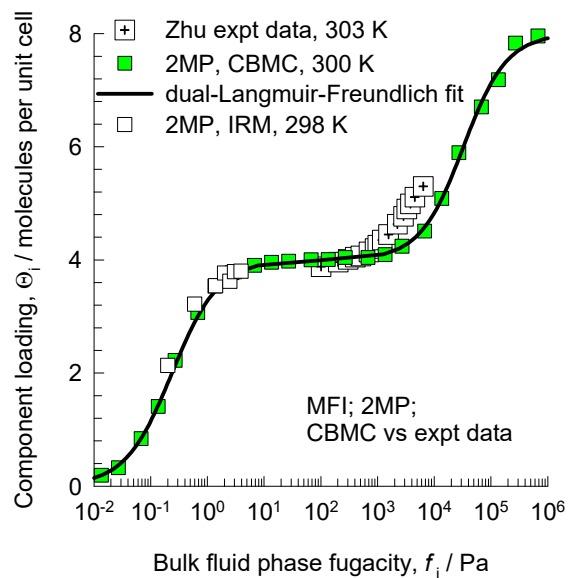
Adsorption of nC6 in MFI zeolite



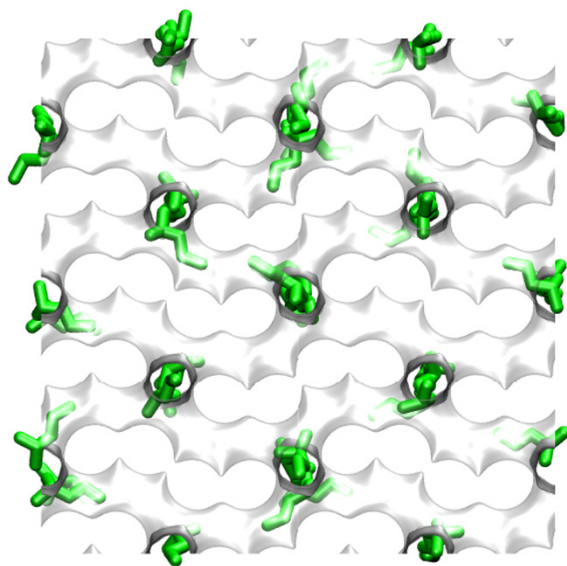
nC6 at loading of 4 molecules/uc
x-y view



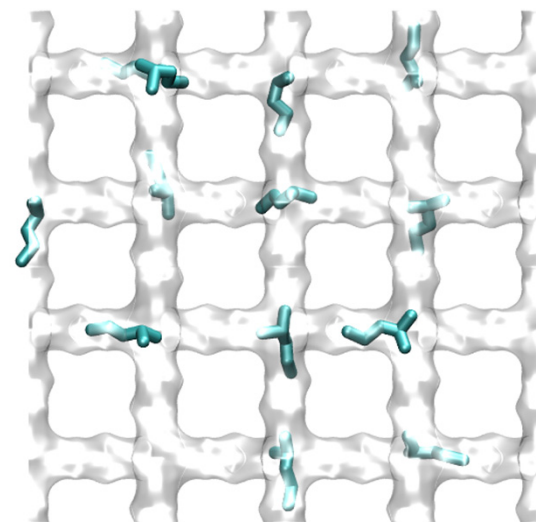
Adsorption of 2MP in MFI zeolite



x-z view of 2MP molecules

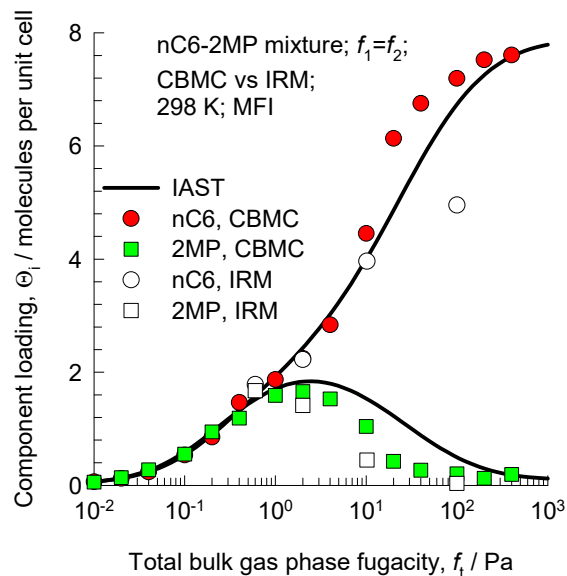


x-y view of 2MP molecules

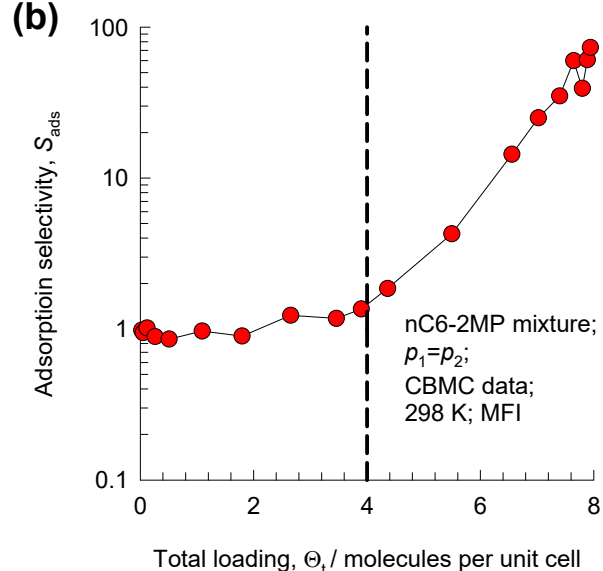


Adsorption of nC6/2MP in MFI zeolite Fig. S69

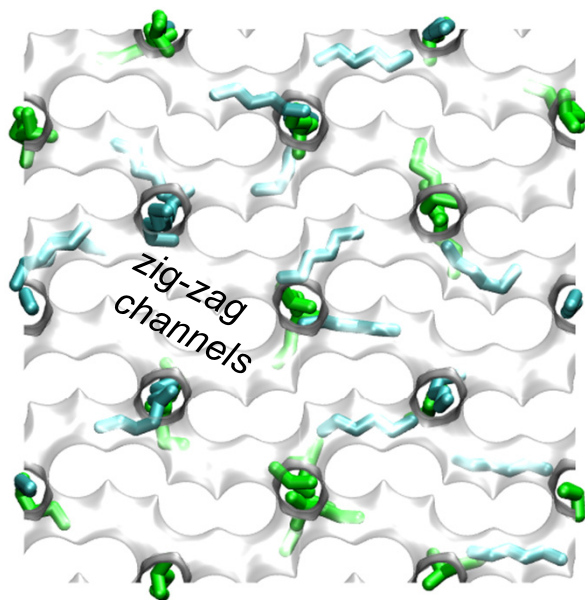
(a)



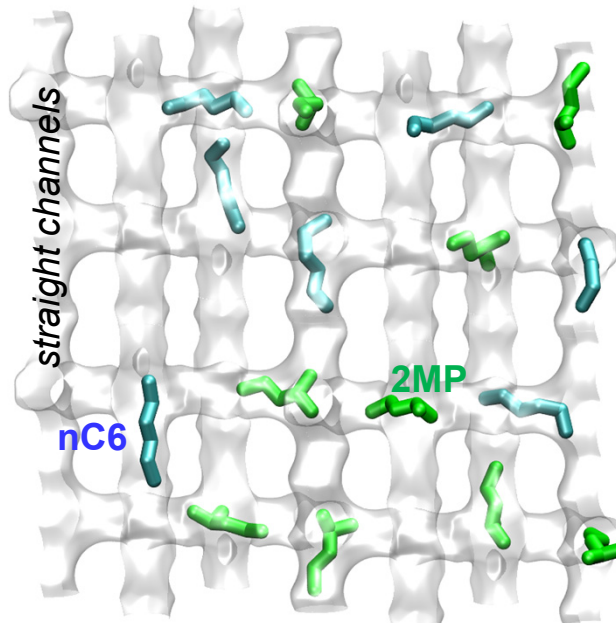
(b)



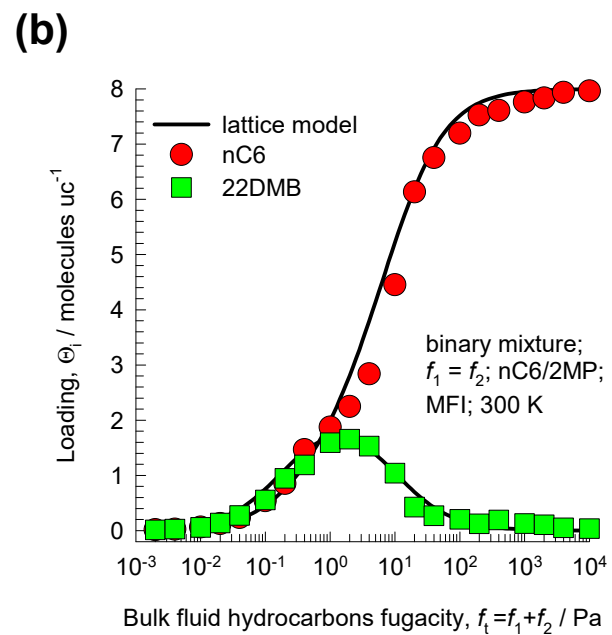
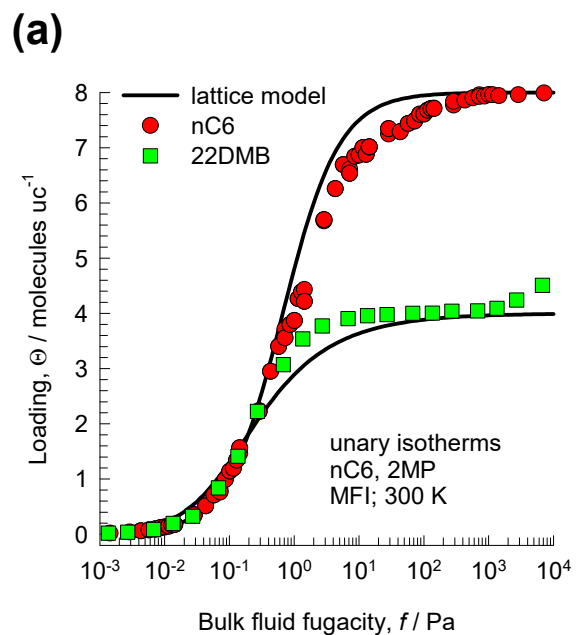
x-z view



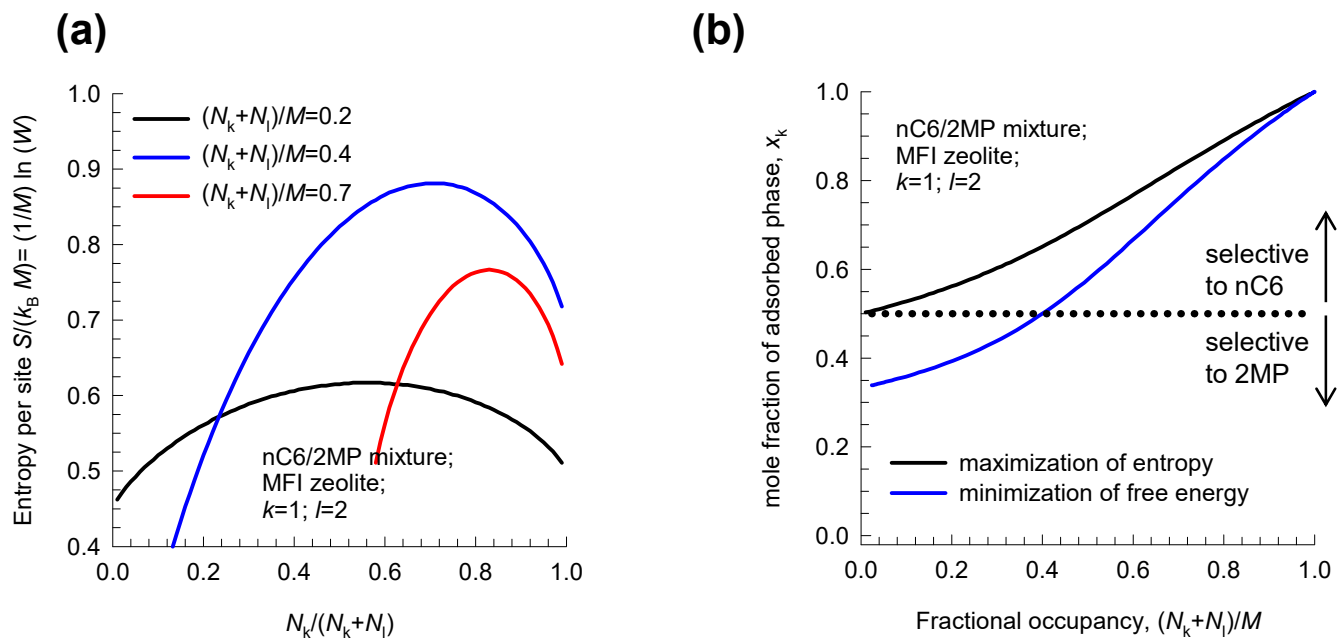
x-y- view



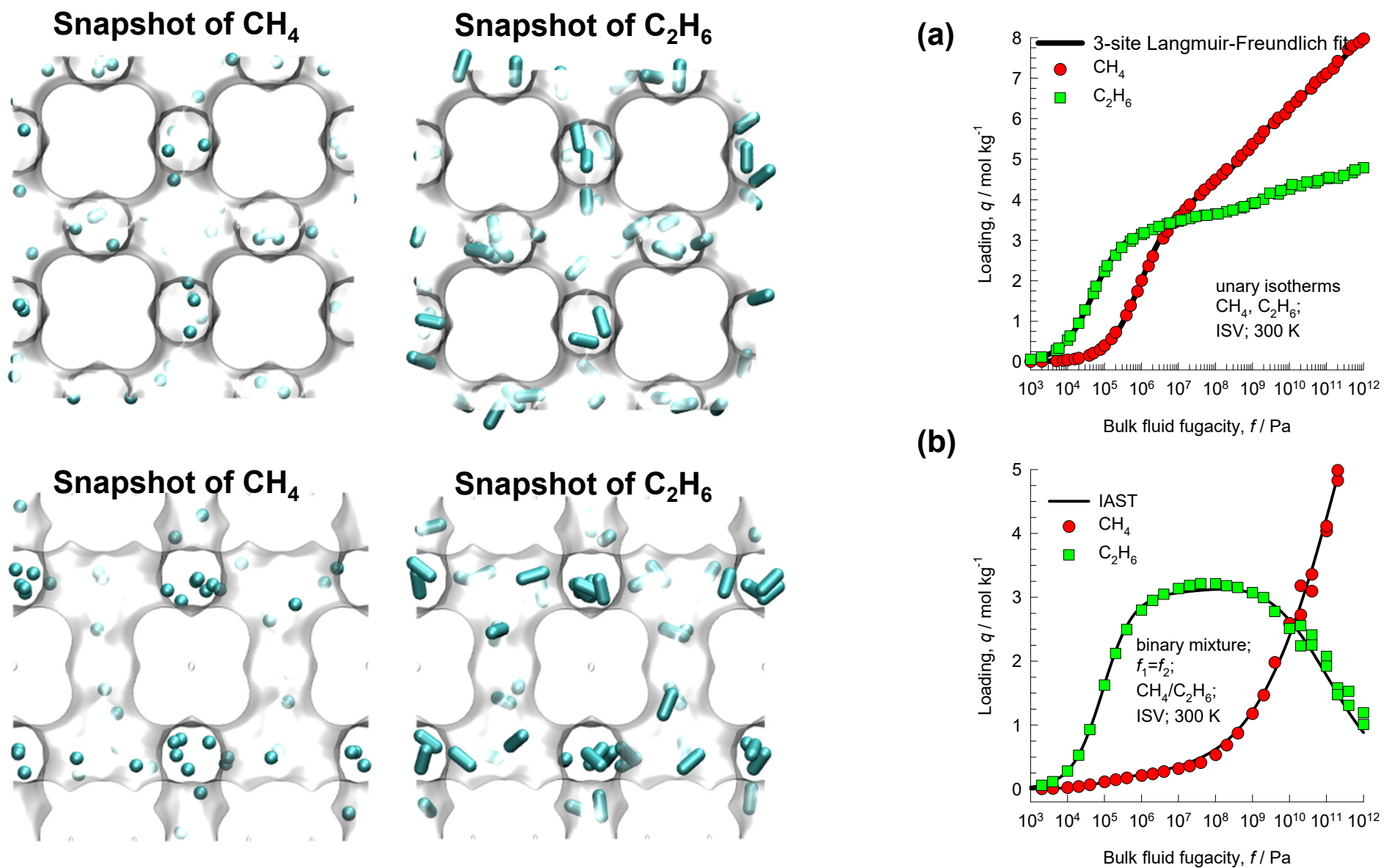
Adsorption of nC6/2MP in MFI zeolite Fig. S70



Adsorption of nC6/2MP in MFI zeolite Fig. S71

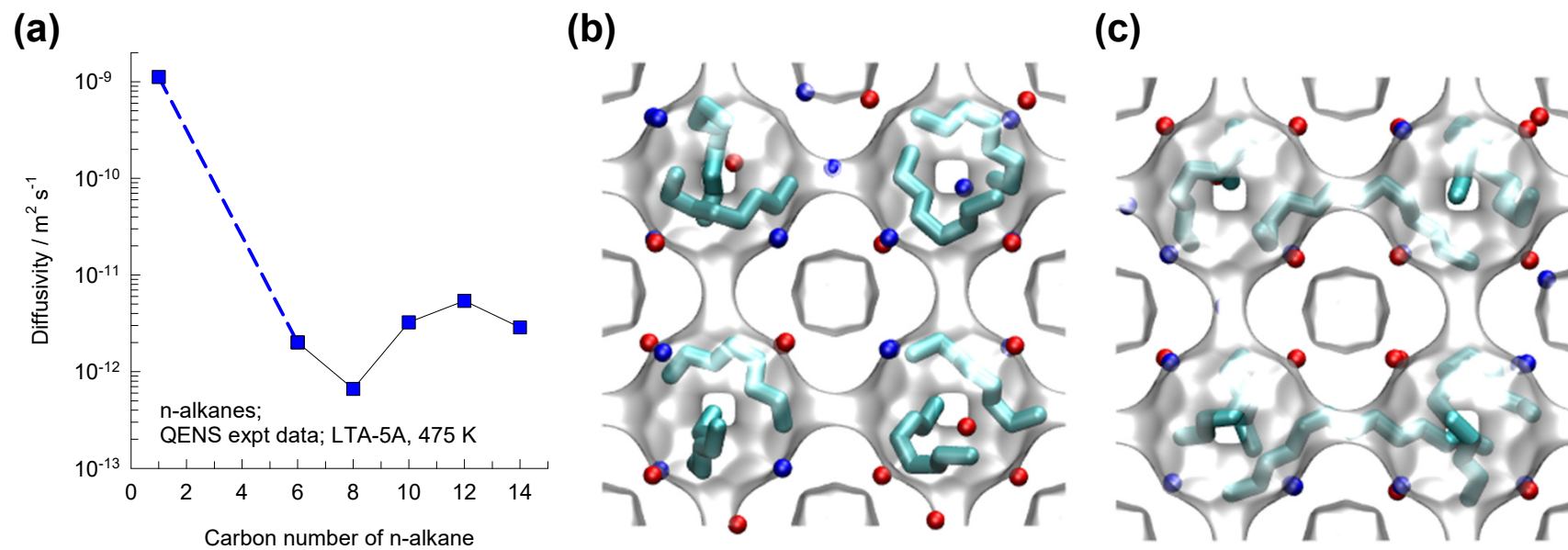


Entropy effects for CH₄/C₂H₆ mixtures in ISV zeolite



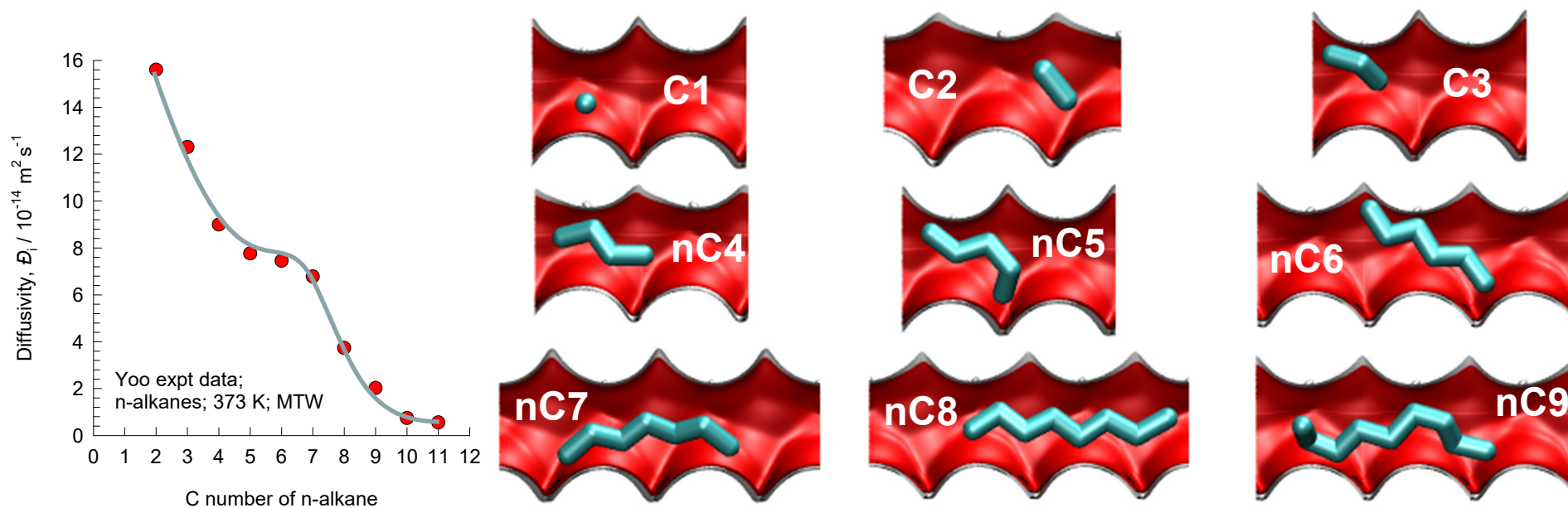
Diffusivity of n-alkanes in LTA-5A

Fig. S73



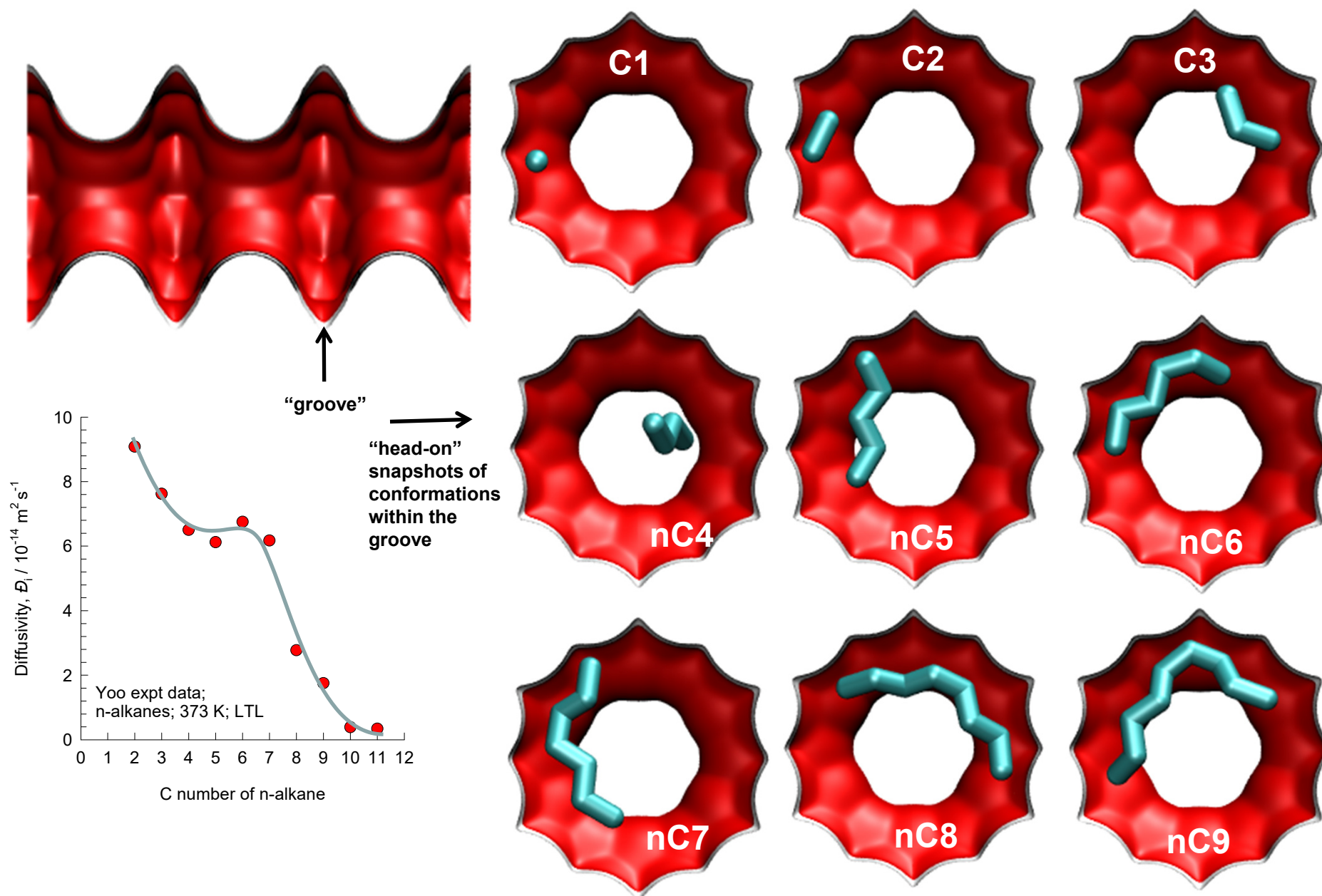
Diffusivity of n-alkanes in MTW

Fig. S74

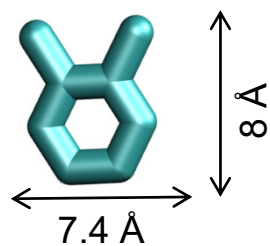


Diffusivity of n-alkanes in LTL

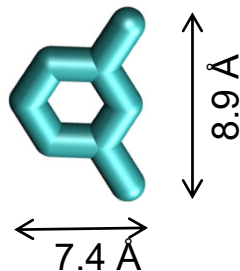
Fig. S75



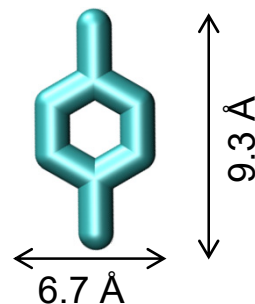
Molecular dimensions of Aromatic Molecules ^{Fig. S76}



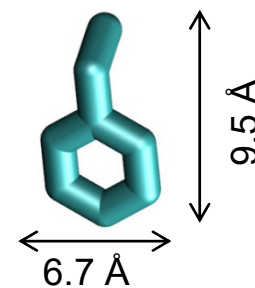
o-xylene (oX)



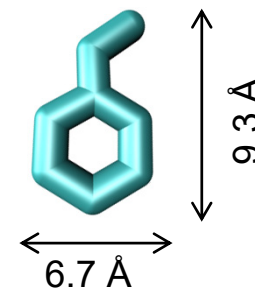
m-xylene (mX)



p-xylene (pX)



Ethylbenzene (EtBz)



Styrene (St)

Boiling point

417.6 K

412.3 K

411.5 K

409 K

418.3 K

Freezing point

248 K

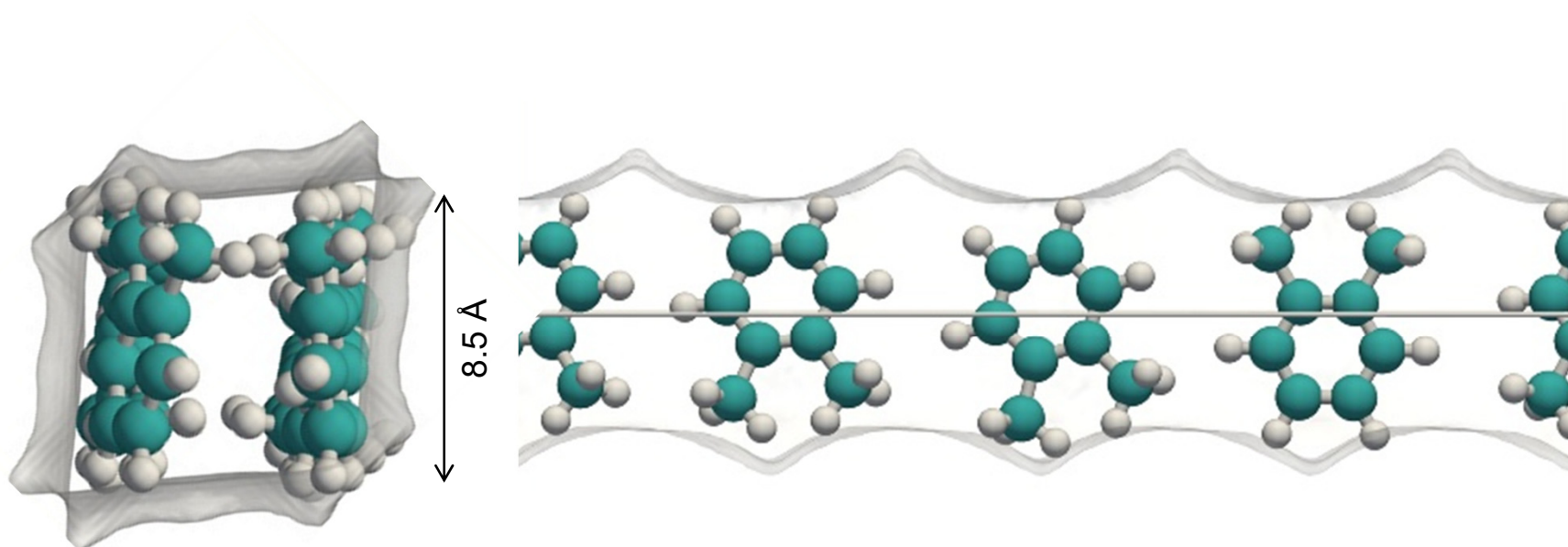
222 K

286 K

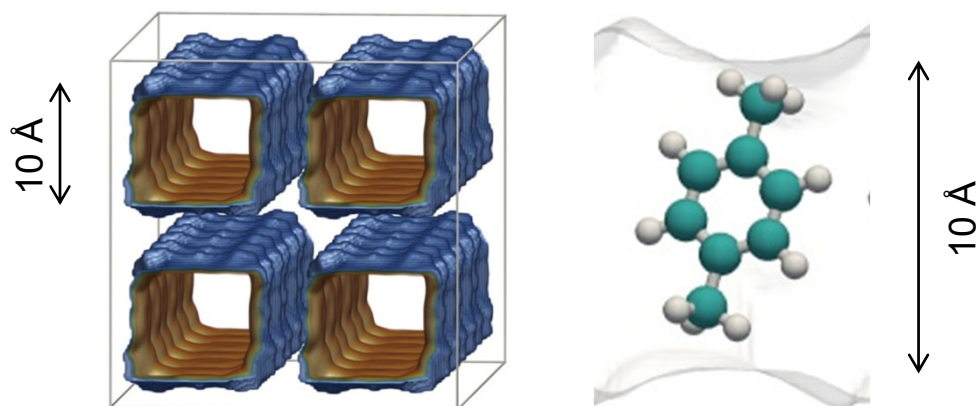
178 K

242.5 K

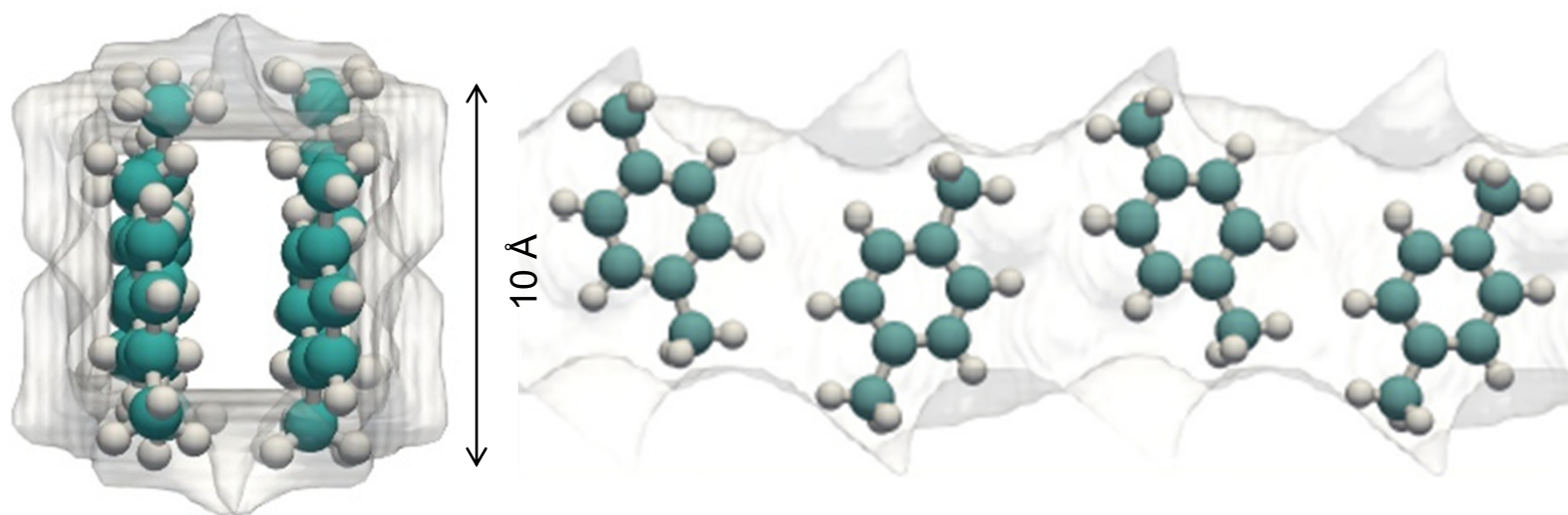
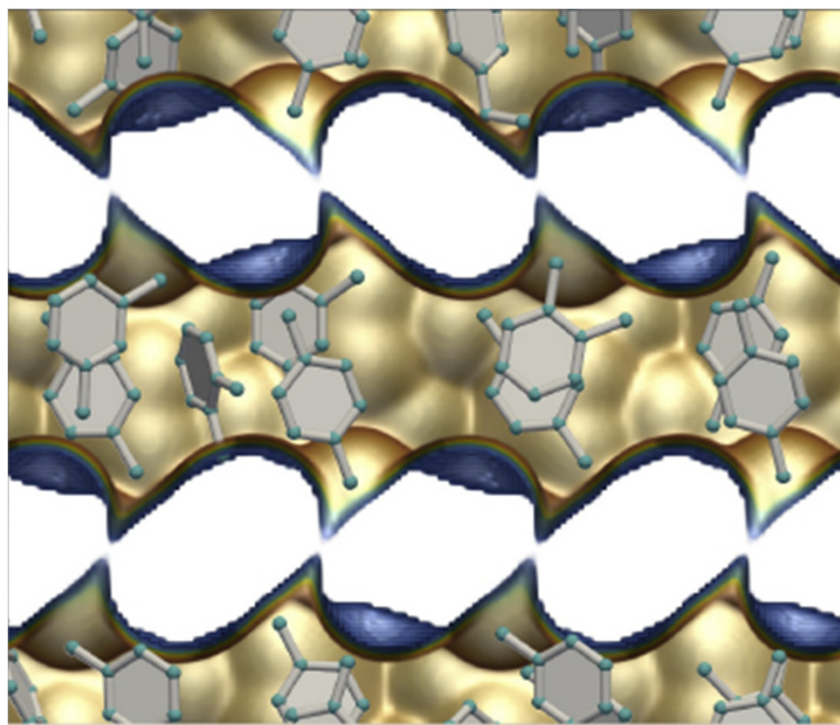
Commensurate stacking of o-xylene in MIL-47^{S77}



Commensurate stacking of p-xylene in Co(BDP)



Commensurate stacking of p-xylene in MAF-X8



AFI zeolite: Pore landscape; Xylenes adsorption

Fig. S80

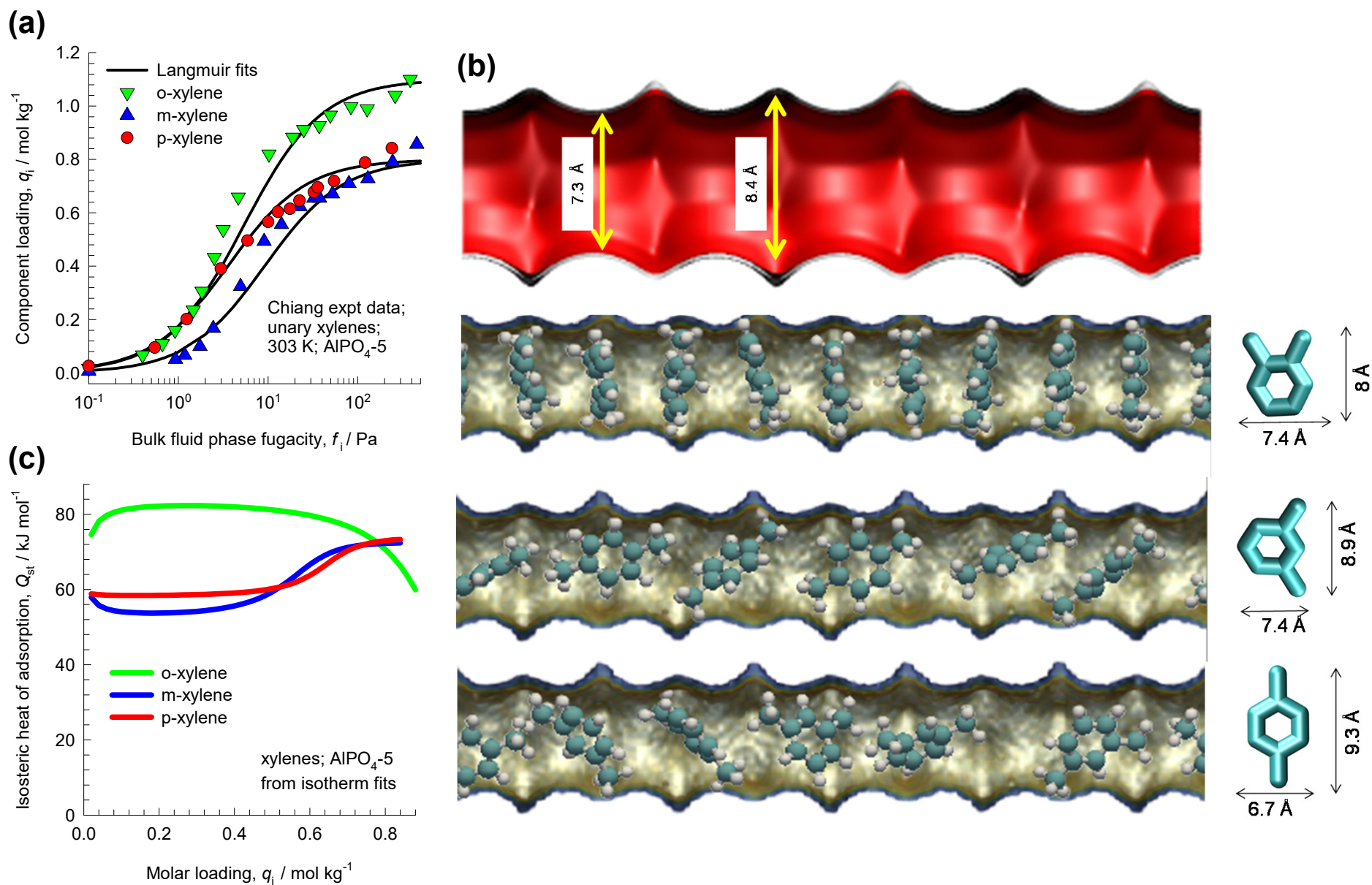
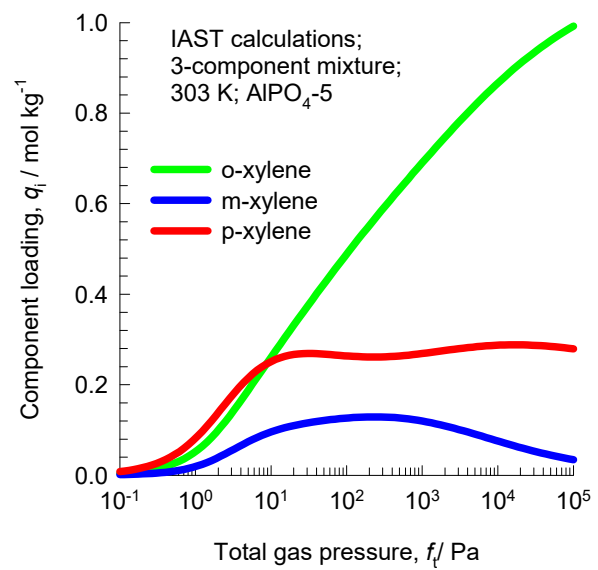
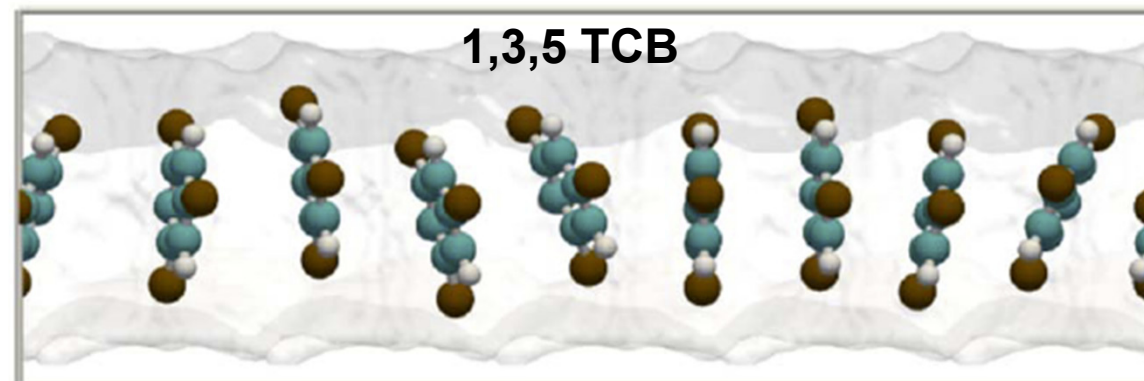
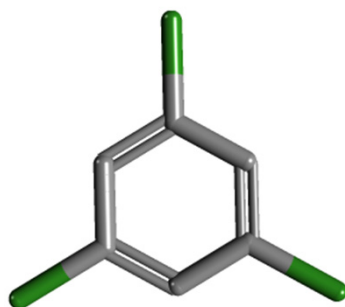
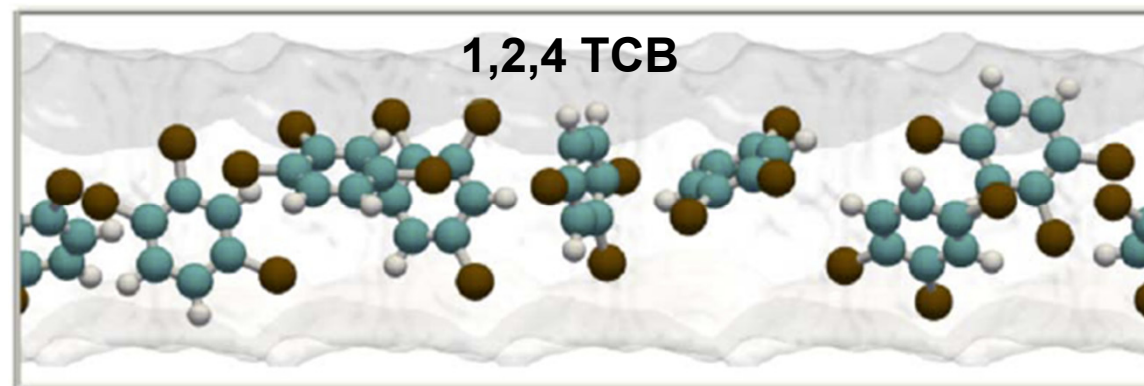
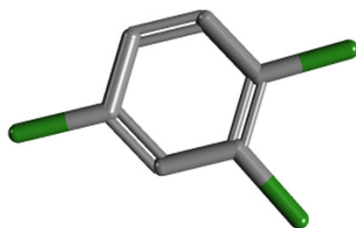
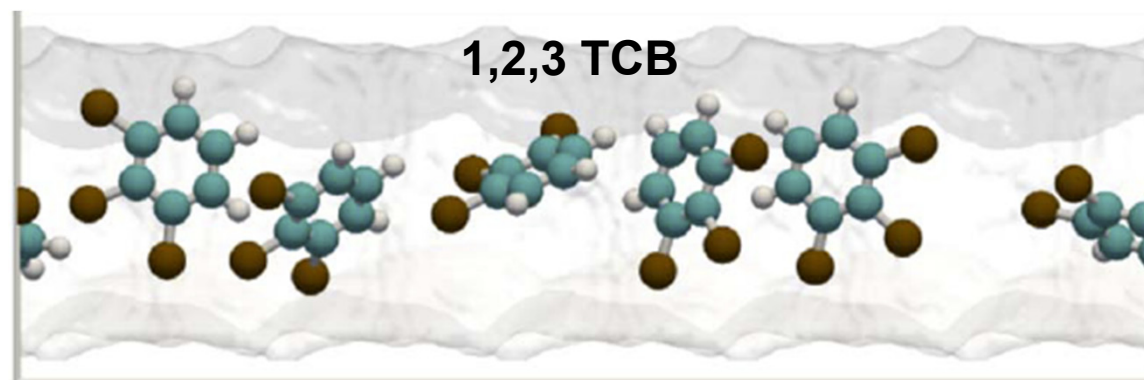
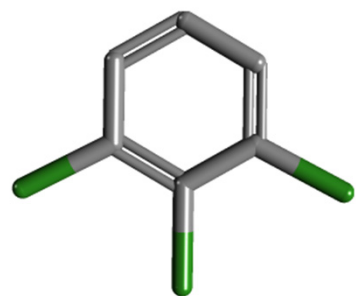


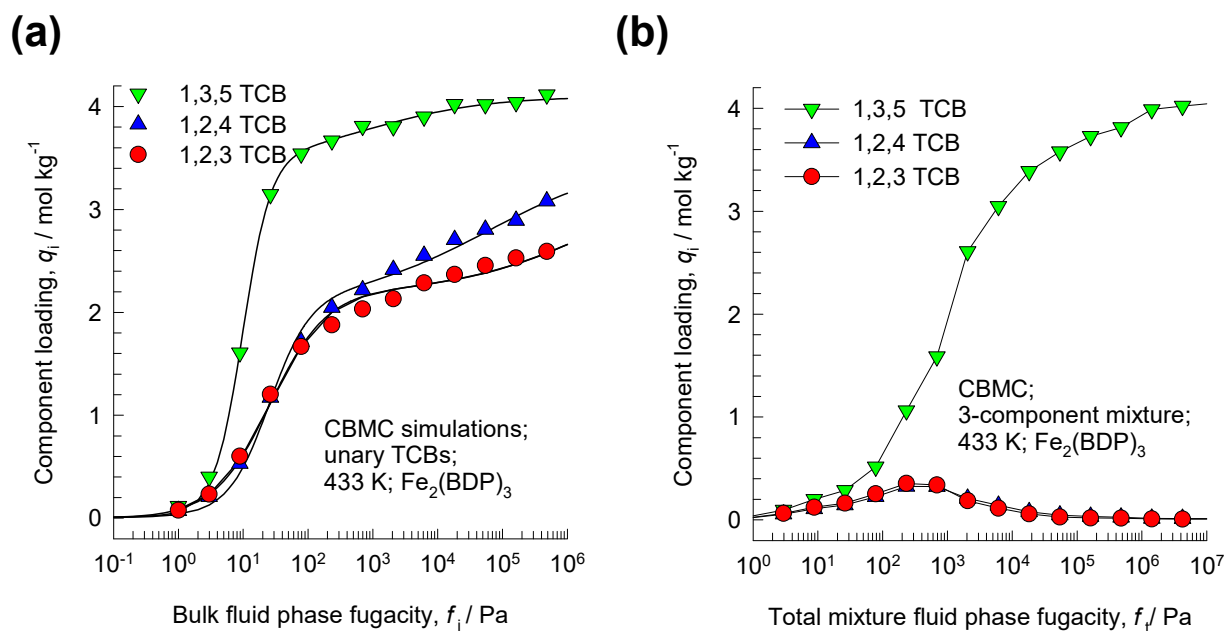
Fig. S81



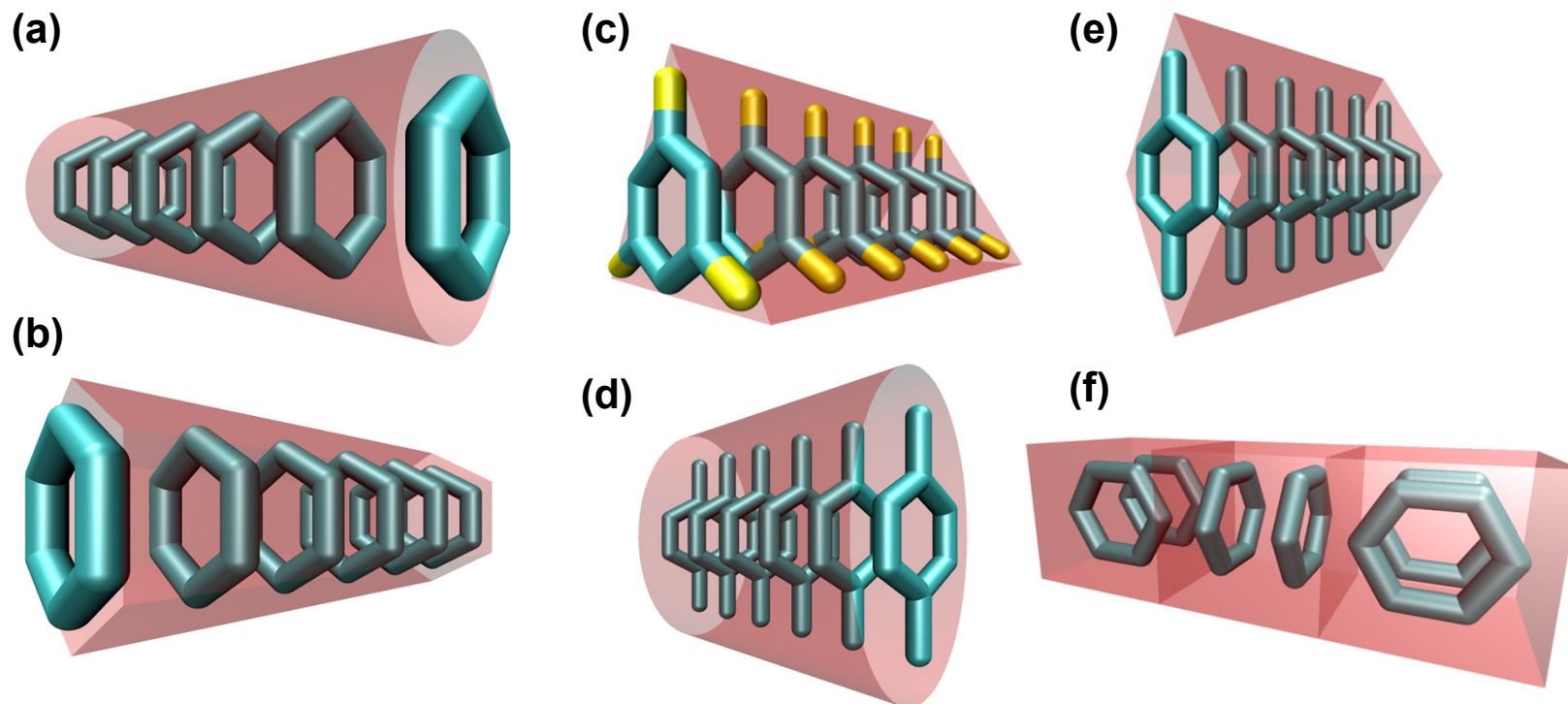
TCBs stacking in $\text{Fe}_2(\text{BDP})_3$



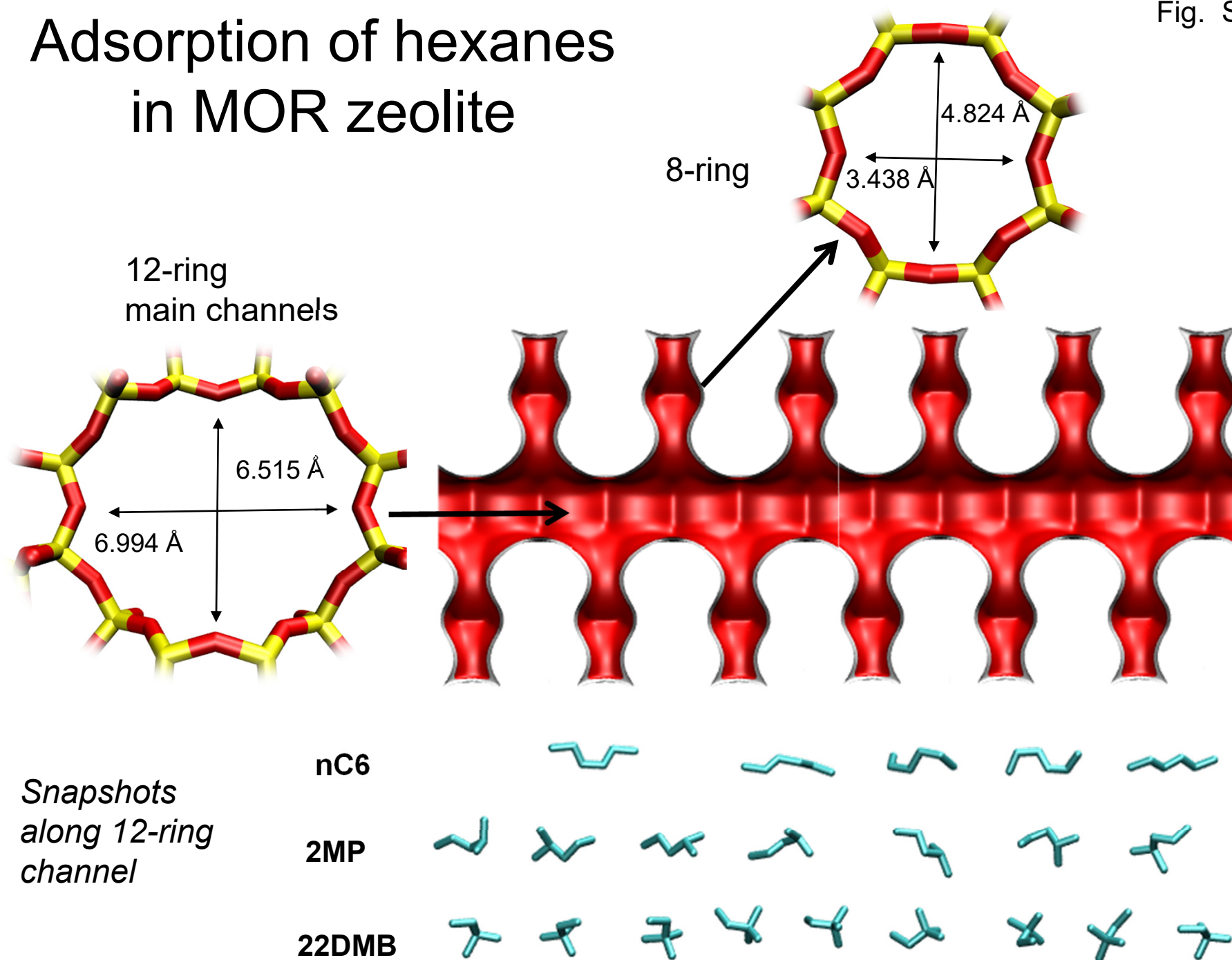
Separating TCBs using $\text{Fe}_2(\text{BDP})_3$



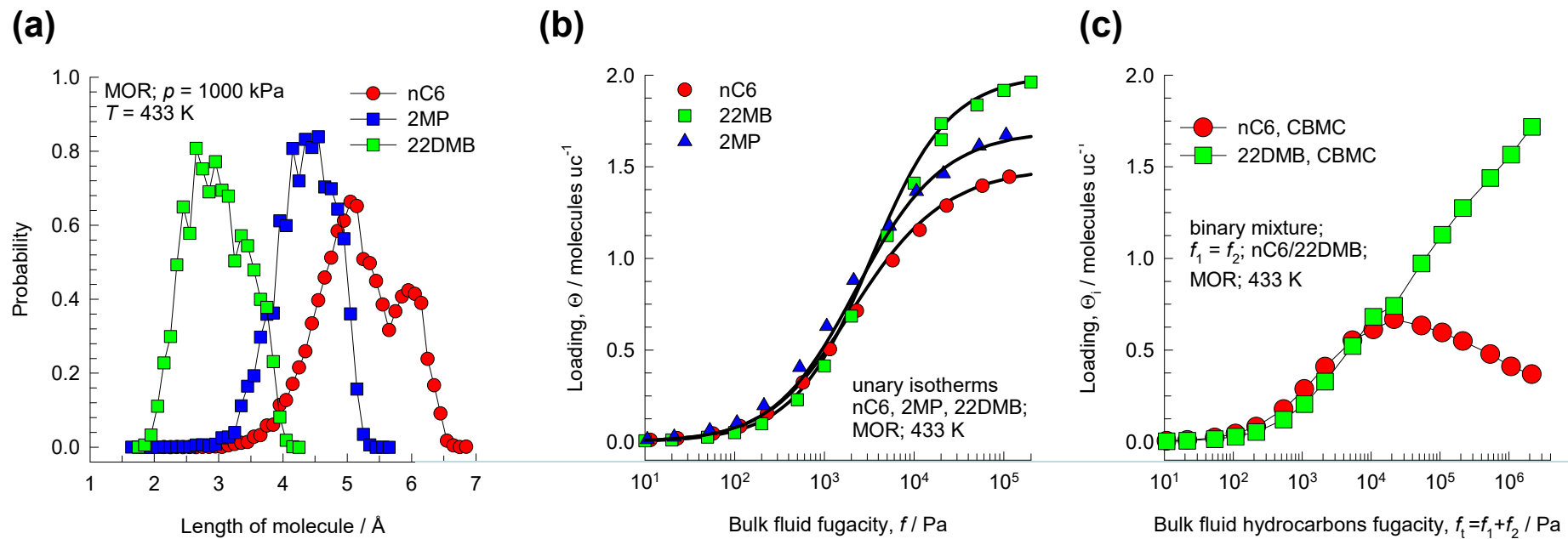
Face-to-Face Stacking



Adsorption of hexanes in MOR zeolite

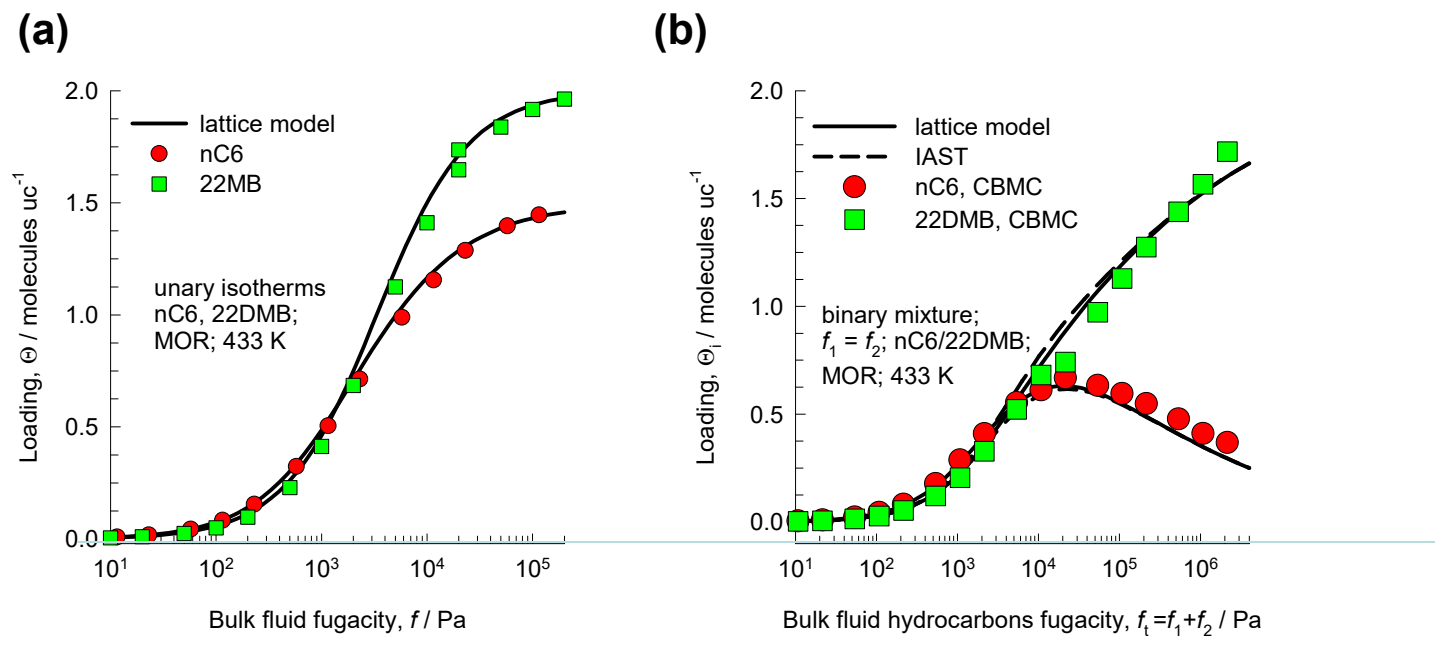


Adsorption of hexane isomers in MOR zeolite

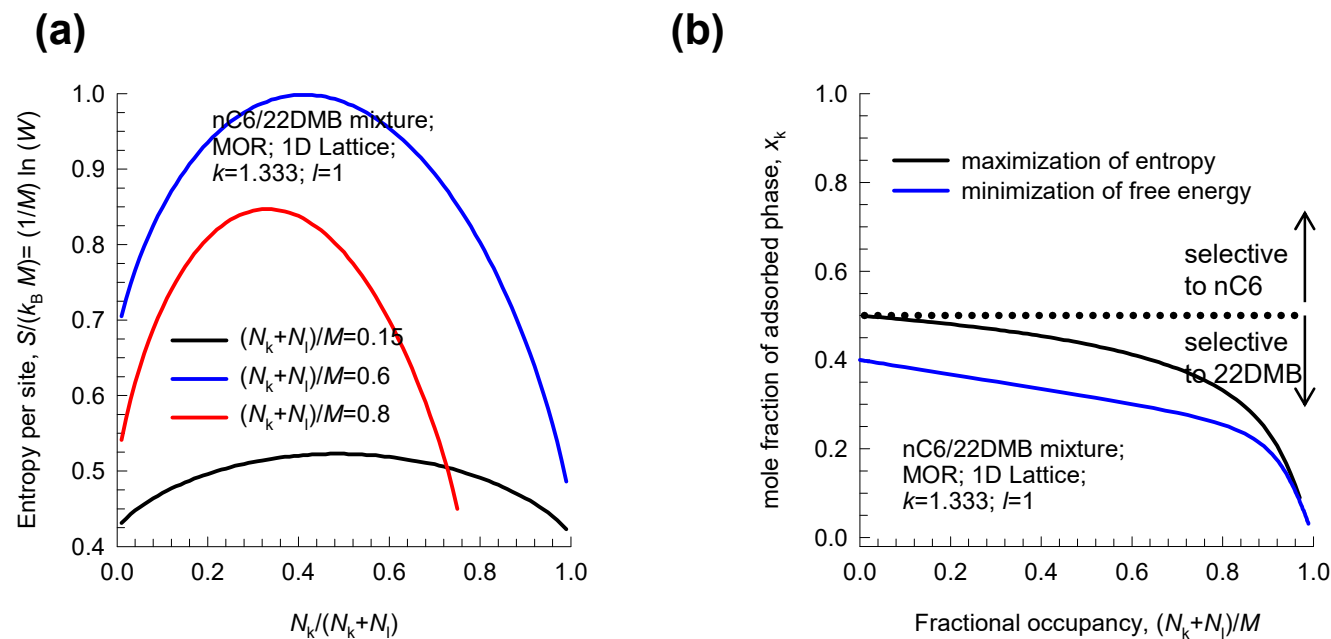


Entropy effects in hexanes adsorption in MOR Fig. S87

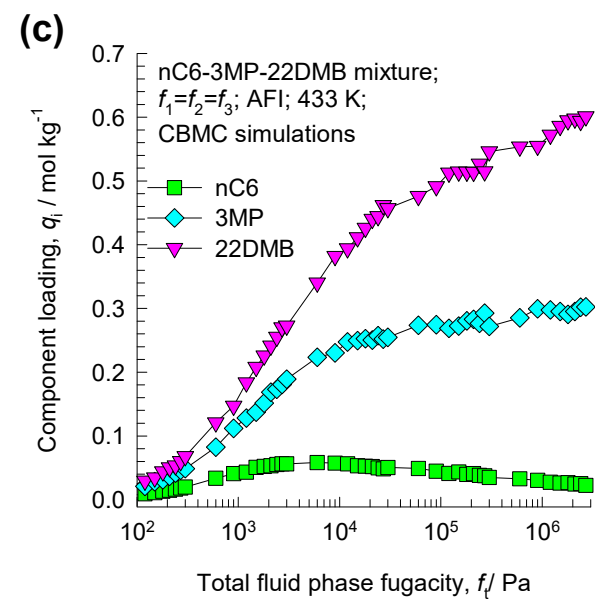
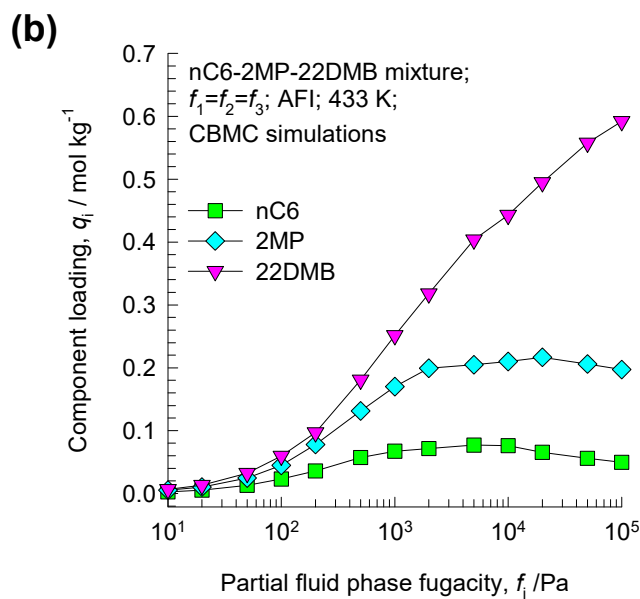
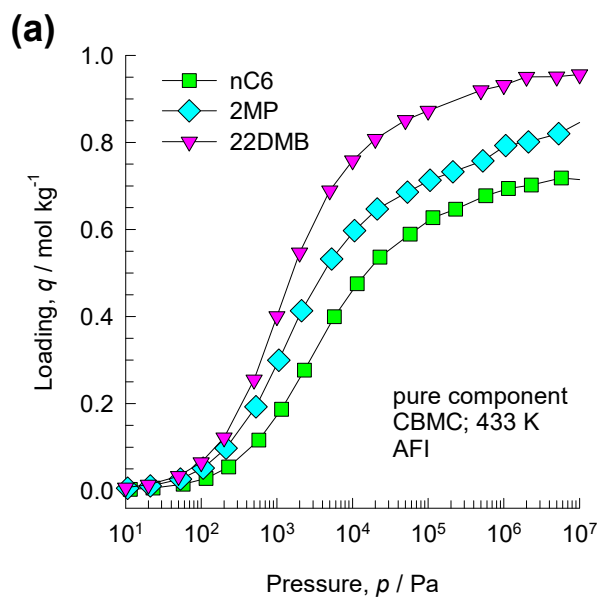
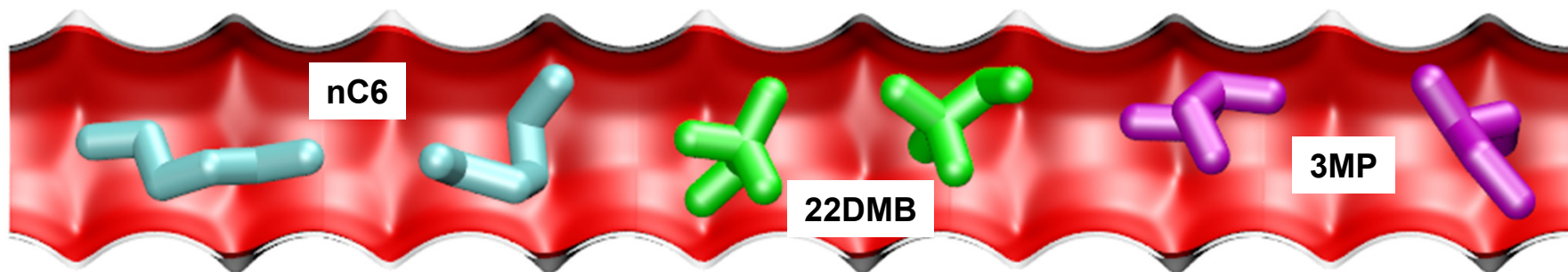
MOR



Entropy effects in hexanes adsorption in MOR



Adsorption of hexane isomers in AFI zeolite



Adsorption of heptane isomers in TON zeolite

